Chemical and Electrical Impact of Alkali Fluoride Post Deposition Treatments on Cu(In,Ga)Se_2 Solar Cells

Zur Erlangung des akademischen Grades eines

DOKTORS DER NATURWISSENSCHAFTEN

(Dr. rer. nat.)

von der KIT-Fakultät für Chemie und Biowissenschaften

des Karlsruher Instituts für Technologie (KIT)

genehmigte

DISSERTATION

von

M. Sc. Alexander Eslam

1. Referent: Prof. Dr. Clemens Heske

2. Referent: Prof. Dr. Michael Powalla

Tag der mündlichen Prüfung: 27.10.2022

Abstract

The alkali fluoride post deposition treatment (AlkF PDT) of Cu(In,Ga)Se_2 (CIGSe) thin films represents the most important process step in the last 20 years to boost the efficiency of CIGSe solar cells. The PDT has a distinct impact on the electrical properties of the CIGSe bulk material, but also on the chemical properties of the most vital interface of the device, the CdS/CIGSe interface. Substantial improvements, but also vast deteriorations of cell efficiency depend on the PDT process. The PDT is a multiparameter process, with the substrate temperature during PDT (T_{PDT}), the Se-rate, and the AlkF-rate, as important process parameters. To date, the precise influence of T_{PDT} and the Se-rate has not been examined, yet and only empirical results are published. Moreover, many previous PDT experiments are performed on alkali-containing substrates (e.g., like soda lime glass), so that the effects of alkalis from the substrate and from the PDT cannot be separated from each other.

The study in hand elaborates the dependence of the electrical properties of complete CIGSe solar cells on T_{PDT} (in the range from 105 to 315 °C) at a fixed AlkF- and Se-rate, and explains the trends found, with a change in alkali concentration in the CIGSe layer, and a detailed chemical analysis of the CIGSe surface with X-ray and ultraviolet photoelectron spectroscopy (XPS, UPS). The alkali fluorides used are sodium fluoride (NaF) or potassium fluoride (KF). Especially for this work, alkali free substrates were used, the CIGSe layers were grown in the so called “singe-stage process”, are free from silver or sulfur additives and are treated solely with one alkali fluoride (either NaF or KF). The resulting CIGSe cells thereby are similar to industrially applied cell structures but exhibit a reduced complexity in their “architecture” and serve as simplified model systems. Within this simplified model-system, it is easier to analyze the working- and failure-principle of PDT-treated CIGSe solar cells. The acquired results can then be applied to the more complex industrially used cell structures, to enable a more targeted improvement of the CIGSe technology.

For the NaF-treated CIGSe solar cells, a monotonous dependence between T_{PDT}, the Na concentration in the CIGSe layer, and cell efficiency is found, leading to an improvement of all NaF PDT cells, compared to the untreated, alkali-free reference cell. For KF-treated CIGSe solar cells also an improvement of the electronic properties with T_{PDT} is observed. However, a severe drop in efficiency is observed, when a KF PDT at T_{PDT} < 150 °C is applied, leading to device performances even worse than for the untreated, alkali-free reference cell.

The chemical analysis of the CIGSe surfaces after PDT with XPS reveals a pronounced change of the surface stoichiometry and formation of secondary components only in case of a KF PDT. For a KF PDT at high T_{PDT} (315 °C) a K-Se-In(-O) component is found on the CIGSe-surface, whereas at low T_{PDT} (105 °C) a Cu-rich component is found on the CIGSe surface. The formation of these secondary components after a KF PDT change the electronic properties of the CIGSe surface drastically, as revealed by UPS measurements: At high T_{PDT}, the formation of a K-Se-In(-O) component is accompanied by a slight downshift of the valence band maximum (VBM) relative to the Fermi energy. This VBM downshift is believed to create a beneficial band alignment at the CdS/CIGSe interface and to reduce charge carrier recombination, leading to enhanced efficiencies. At low T_{PDT}, the formation of the Cu-rich component is accompanied by a strong upshift of the VBM (relative to the Fermi energy). This strong upshift, in contrast, is assumed to increase charge carrier recombination at the CdS/CIGSe interface and thus can lead to the observed severe drop in efficiency.

The reason for the formation of a Cu-rich CIGSe surface on the low T_{PDT} KF-treated sample surface, lies in the simultaneous formation of Ga-F and In-F species: After rinsing, the Ga-F and In-F species are washed away, and consequently a Ga- and In-depleted surface results,

relatively enriched in Cu. Different, however, from the KF PDT samples, for the NaF PDT CIGSe surfaces, no change in surface composition and no secondary components were detected. In this respect, it is very noteworthy that the reactivity of KF and NaF differ so greatly on the CIGSe surface.

The Se-rate during the PDT also had a great impact on the effectiveness of the PDT. If the KF PDT is performed without Se supply, the diffusion of K into the CIGSe layer is strongly decreased and lower amounts of KF are detected on the CIGSe surface, than after a KF PDT with Se supply. Additionally, also lower amounts of K-Se-In(-O) are found on the KF PDT 315 °C sample and lower amounts of Cu-S-Se-O are found on the KF PDT 105 °C sample, when no Se is supplied during PDT. Consequently, without Se supply, due to lower amounts of KF at the CIGSe surface the reactivity of KF is decreased and therefore, the formation of secondary components is reduced.

Overall, the observed electrical trends with T_{PDT} could be explained by a thorough chemical analysis of the CIGSe surface after PDT with XPS and UPS. It was elucidated, that NaF and KF show distinctly different impacts on CIGSe solar cells, by means of both, electrical and chemical changes. Theoretical predictions that secondary components form more easily in case of the heavier alkali metal K, were confirmed experimentally. Additionally, it was found out that Se influences the amount of KF on the CIGSe surface, and therewith controls the chemical reactivity of KF. The here presented study reveals, that (the influence of) all process parameters of the PDT must be understood, and carefully adjusted, to ultimately evolve an improvement of CIGSe solar cell performance.

Zusammenfassung

Die Nachbehandlung frisch gewachsener Cu(In,Ga)Se_2 (CIGSe)-Schichten mit Alkalifluoriden (engl. *alkali fluoride post deposition treatment*, AlkF PDT) gehört zu den wichtigsten Errungenschaften der CIGSe Dünnschicht-Solarzellen Technologie der letzten 20 Jahre. Mit ihr ließen sich in dieser Zeit erhebliche Wirkungsgrad-Steigerungen erreichen. Der AlkF PDT hat immense Auswirkungen sowohl auf die elektrischen Eigenschaften des CIGSe-Halbleiters als auch speziell auf die Bildung des CdS/CIGSe-Heteroübergangs, dem Herzstück der Solarzelle. Mit dem PDT Prozess kann die Solarzelle als solche stark optimiert und verbessert werden, doch genau so einfach können auch noch nicht sorgfältig erforschte Prozessparameter die Zelle zerstören. Ganz allgemein ist der AlkF PDT ein Multiparameter-Prozess, der von vielen Einflussgrößen abhängt, wie zum Beispiel von der Substrattemperatur (engl. *PDT temperature*, T_{PDT}), der Se-Rate, oder der AlkF-Rate. Bisher hat man den genauen, chemischen Einfluss dieser Größen aber noch nicht ausreichend erforscht, und bedient sich eher empirischer Erfahrungen, die einem das ungefähre „Prozessfenster“ vorgeben, in dem gute Zellen resultieren. Hinzu kommt das Problem, dass in vielen Studien alkalimetallhaltige Substrate für den PDT-Versuch verwendet werden. Die Alkalimetalle diffundieren dann aus dem Substrat in die CIGSe-Schicht hinein und überlagern ihre Effekte mit den Alkalimetallen aus dem AlkF PDT. Dies hat die chemische Untersuchung des PDT bisher immens erschwert.

Die vorliegende Arbeit klärt daher auf, wie die elektrischen Eigenschaften kompletter CIGSe Solarzellen von der Substrattemperatur (T_{PDT}) abhängen (im Bereich von 105 bis 315 °C), bei konstant gehaltener AlkF- und Se-Rate. Als Alkalifluoride werden Natriumfluorid (NaF) und Kaliumfluorid (KF) untersucht. Die beobachteten Trends werden dann erklärt anhand von Änderungen der Alkalikonzentration innerhalb der CIGSe-Schicht, als auch mithilfe einer umfangreichen chemischen Analyse der CIGSe-Oberfläche durch die Röntgen- und Ultraviolett-Photoelektronen-Spektroskopie (XPS und UPS). Die untersuchten CIGSe-Zellen wurden speziell auf alkalifreiem Substrat abgeschieden, im sogenannten Einstufen-Prozess hergestellt, sind frei von Silber- oder Schwefelzusätzen und wurden nur mit einem AlkF (NaF oder KF) nachbehandelt. Die entstandenen CIGSe-Solarzellen orientieren sich dadurch grundlegend an der industriell hergestellten Zellstruktur, weisen jedoch eine deutlich reduzierte Komplexität des Materialsystems auf, und stellen damit ein vereinfachtes Modellsystem dar. An diesem vereinfachten Modellsystem kann durch ausgeprägte elektrische und chemische Analysen der Wirkungs- und Fehlmechanismus im PDT besser untersucht werden. Diese Erkenntnisse lassen sich dann auf die komplexeren industriellen Zellstrukturen übertragen, womit eine zielgerichtetere Verbesserung bestehender Technologie erreicht wird.

Für die mit NaF behandelten CIGSe Solarzellen wird eine monotone Abhängigkeit zwischen T_{PDT}, der Na-Konzentration in der CIGSe-Schicht, und der Zelleffizienz gefunden. Dieser Umstand führt zu einer Verbesserung der NaF PDT Zelle im Vergleich zur unbehandelten, alkalifreien Referenzzelle. Bei den mit KF behandelten CIGSe Solarzellen wird ebenfalls eine Verbesserung der elektrischen Eigenschaften mit T_{PDT} verzeichnet. Diese Verbesserung verläuft jedoch nicht „monoton“: Wird speziell ein KF PDT bei $T_{PDT} < 150$ °C durchgeführt, so bricht der Wirkungsgrad der CIGSe Solarzelle massiv ein. Dieser Einbruch ist so stark, dass die entsprechende, mit KF behandelte Zelle schlechter ist als die unbehandelte, alkalifreie Referenzzelle.

Durch die Analyse der CIGSe-Oberflächen nach dem KF PDT mit XPS konnte eine ausgeprägte Änderung der chemischen Zusammensetzung und die Bildung von Fremdphasen aufgedeckt werden: Im Falle eines KF PDT bei hohen T_{PDT} (315 °C) wurde eine K-In-Se(-O)-Komponente auf der CIGSe-Oberfläche entdeckt, wohingegen bei niedrigen T_{PDT} (105 °C) die Bildung einer Cu-reichen Komponente nachgewiesen wurde. Diese Sekundär-Komponenten

wiederum führen zu einer drastischen Veränderung der elektronischen Eigenschaften der CIGSe-Oberfläche, wie mit UPS-Messungen bestätigt wurde: Bei hohen T_{PDT} führt die Bildung der K-In-Se(-O)-Komponente zu einer leichten Absenkung des Valenzbandmaximums (VBM) an der Oberfläche (relativ zur Fermi-Energie). Diese Absenkung des VBM kann dann zu einer günstigeren Bandanpassung an der CdS/CIGSe-Grenzfläche führen, was die Ladungsträgerrekombination verringert, und damit letztendlich den Wirkungsgrad der Zelle verbessert. Bei niedrigen T_{PDT} wiederum führt die Bildung einer Cu-reichen Komponente zu einer starken Anhebung des VBM an der Oberfläche (relativ zur Fermi-Energie). Diese starke Anhebung verschlechtert möglicherweise die Bandanpassung an der CdS/CIGSe-Grenzfläche und erhöht dort die Ladungsträgerrekombination. Damit kann der massive Einbruch im Wirkungsgrad erklärt werden.

Die chemische Ursache für die Ausbildung einer kupferreichen Oberfläche auf der KF PDT 105 °C Zelle wird mit der gleichzeitigen Bildung von Ga-F und In-F Bindungen erklärt: Die beim KF PDT 105 °C gebildeten Ga-F und In-F- (Ver-) Bindungen sind wasserlöslich und werden in der darauffolgenden wässrigen Nachbehandlung (engl. *rinse*) weggewaschen. Damit resultiert eine Ga- und In-verarmte CIGSe-Oberfläche, die dadurch relativ an Cu angereichert ist. Anders, als für die KF PDT Proben wurde bei den NaF PDT Proben keine drastische chemische Veränderung der CIGSe-Oberfläche beobachtet und ebenso keine Bildung von etwaigen Fremdphasen. In dieser Hinsicht ist es sehr verwunderlich, dass sich die chemisch so ähnlichen Alkalimetalle Na und K so stark in ihrer Reaktivität auf der CIGSe-Oberfläche unterscheiden.

Wie schon eingangs erwähnt, ist auch die Se-Rate während des PDTs ein wichtiger Prozessparameter, der die Effektivität des PDT (mit-) bestimmt. Wird ein KF PDT ohne Se-Angebot (d.h. Se-Rate = 0) durchgeführt, so wird auf den CIGSe-Oberflächen weniger KF nachgewiesen, und auch die Eindiffusion von K in die CIGSe-Schicht fällt schwächer aus als bei einem KF PDT mit Se-Angebot (d.h. Se-Rate ≠ 0). Zusätzlich wird auch dort die Bildung der Fremdphasen beobachtet (K-In-Se(-O) bei KF PDT 315 °C und Cu-S-Se-O bei KF PDT 105 °C), jedoch in deutlich geringerem Ausmaß als auf einer Probe, die einen KF PDT mit Se-Angebot durchlaufen hat. Ohne Se im KF PDT ist durch die geringere KF-Konzentration auf der CIGSe-Oberfläche die chemische Reaktivität des KF herabgesetzt, und die Menge an gebildeter Fremdphase nimmt etwas ab.

Zusammenfassend konnten alle beobachteten Abhängigkeiten der elektrischen Effekte auf Basis einer chemischen Analyse der CIGSe-Oberfläche mit XPS und UPS geklärt werden. Es konnte gezeigt werden, dass sich NaF und KF stark voneinander unterscheiden in ihren Auswirkungen auf die elektrischen und chemischen Eigenschaften der CIGSe Solarzelle. Theoretische Vorhersagen, das schwerere Alkalimetalle wie K auf der CIGSe-Oberfläche eher zur Fremdphasen-Bildung neigen (als leichtere wie Na), konnten experimentell bestätigt werden. Weiterhin konnte eindeutig gezeigt werden, dass das Se-Angebot im PDT die Menge an KF auf der CIGSe-Oberfläche beeinflusst, und damit auch indirekt die chemische Reaktivität des KFs mitbestimmt. Im Allgemeinen zeigen die Ergebnisse dieser Arbeit auf, dass alle Prozessparameter des PDT verstanden, und fein aufeinander abgestimmt werden müssen, damit die Effizienz der entstehenden CIGSe Solarzelle davon profitieren kann.

1 Introduction

The undeniable necessity for renewable energies is more topical then ever in the current public debate. Renewable energies are not only important to reach the climate goals, as set by the “Fit for 55“ package by the European union [1], but also in view of unfortunate geopolitical dependencies [2,3]. The stable and reliable supply of energy is not just a technologically demanding problem, but has recently also become a weapon in modern warfare. The only way, to gain control over this problem in the long run, is to expand wind power and photovoltaics drastically. In this respect, highly efficient and cheap solar modules are needed, which convert sun light into electrical energy.

For this purpose, the $Cu(In,Ga)Se_2$ (CIGSe) thin-film solar cell technology plays a special role, as it combines low material and energy consumption with very high efficiencies. Taking the maturity level of the comparably young CIGSe technology into account, CIGSe clearly outperforms the silicon solar cell technology by far. On its way to very high efficiencies, the CIGSe technology was stepwise improved by the introduction of new features such as the double Ga-gradient [4] or the alkali fluoride post deposition treatment (PDT) [5]. Together with the optimization of the whole solar cell device, Solar Frontier accomplished a new world record in 2019 with a Cd-free non-toxic CIGSe thin-film solar cell reaching 23.35 % [6].

Like for most improvements in the CIGSe thin film technology, many progresses have been made on an empirical base, which is evident due to the complexity of the CIGSe material system and solar cells in general. The implementation of the alkali fluoride PDT represents the latest “new feature“ that led to a substantial increase in CIGSe efficiency. However, due to the rapid development, the full scientific understanding of the PDT lags somewhat behind. Therefore, the elucidation of the effect of the alkali fluoride PDT in the CIGSe technology is of special interest and will be addressed in this work.

The alkali fluoride PDT is a process, in which an alkali fluoride like NaF, KF, or RbF is evaporated together with selenium (Se) onto a freshly prepared, heated CIGSe sample surface under vacuum conditions. Within this process, the CIGSe sample surface is chemically modified, and alkali metals diffuse into the CIGSe layer. Many consequences have already been observed and explained, like the improvement of the electrical properties of the CIGSe layer itself [7] or the improvement of the chemical properties of the CIGSe surface [8]. Due to these structural and chemical changes, the electrical conductivity of the CIGSe layer is increased and charge carrier recombination is reduced, both culminating in higher cell performances.

As illustrated above, the PDT leads to complex chemical reactions of the CIGSe surface with NaF (or KF), and Se. Moreover, the PDT is a multiparameter process, with many critical parameters, i.e., the substrate temperature during PDT (the PDT temperature), the AlkF rate, or the Se supply, whose explicit chemical effects have not elucidated so far. It is known that a PDT temperature about 315 °C together with a low Se coevaporation rate leads to excellent cell efficiencies, but the exact reason for these quantities remains unknown. It is therefore the aim of this work to analyze the impact of the PDT temperature on the CIGSe solar cell. Thereby, the electrical properties of a full solar cell device will be examined in dependence of PDT temperature and the chemical properties of the CIGSe surface will be investigated for different PDT temperatures. It will be examined how different PDT temperatures affect the chemical reactivity of the alkali fluorides on the CIGSe surface and what role the simultaneous evaporation of Se plays in this context.

Concerning the alkali fluorides, both, NaF and KF PDTs led to improved efficiencies for CIGSe thin-film solar cells. Despite their chemical resemblance, their electrical impact on CIGSe cell properties is distinctly different [9]. To examine the different chemical and electronic effects the NaF PDT is compared to the KF PDT especially with respect to the PDT temperature.

The superior goal of this scientific work is that results and insights contribute to improvements in the commercial production of CIGSe cells and modules, to further develop the CIGSe solar cell technology. Typical “benchmark” CIGSe cells, however, offer a high degree of complexity by means of their structural composition and processing factors and are thus very hard to analyze and understand. To overcome this problem, the work in hand uses CIGSe cells, which are close to industrial CIGSe cells, but show a great reduction in their complexity. This leads to more defined boundary conditions and makes an analytical analysis of processing steps, such as the PDT, more feasible. The following “modifications” are applied to reduce the complexity of the CIGSe solar cell architecture: The CIGSe layers are exclusively grown on alkali free substrates, to decouple alkali effects coming from the substrate or the PDT. Further, the quaternary system $Cu(In,Ga)Se_2$ is applied as light absorbing material and Ag or S are left out, to reduce the compositional complexity. Moreover, the CIGSe layers are grown by a single stage process, so that no compositional gradients exist within the layer. Additionally, a defined rinsing step is applied together with the use of the well-known CdS buffer layer. Finally, with a careful packing and shipping procedure, cross-contamination of the valuable samples can be ruled out. With all these considerations, the use of electrical and surface analytical methods becomes more profitable and insights from our simple material system can be applied to more complex industrial CIGSe systems. Thereby, the improvement of the CIGSe solar cell technology becomes more targeted.

The work in hand is built up as follows:

Chapter 2 gives a short summary about the CIGSe thin film technology, current techniques, the evolution of the PDT, and the most important achievements of this field.

Chapter 3 introduces theoretical aspects, which are needed to understand the working principle of a CIGSe solar cell and to understand the measuring principle of photoemission spectroscopy (PES), a versatile tool used to chemically characterize the CIGSe surfaces.

Chapter 4 then presents the experimental setup, how the CIGSe solar cells were fabricated, the tools for the electrical analysis and how sample preparation and packaging was achieved especially for the surface sensitive PES measurements at KIT.

Chapter 5 illustrates the electrical properties of CIGSe solar cells, which underwent a NaF PDT or a KF PDT, in dependence on PDT temperature. This chapter serves as a rough, but solid basis to establish some general trends but also to spot some unexpected, and new detrimental alkali effects after a KF PDT at low PDT temperature.

Chapter 6 then explains the trends made for the electrical properties from Chapter 5 on a chemical basis. Therewith, X-ray (XPS) and ultraviolet photoelectron spectroscopy (UPS) are used to unravel the chemical and electronic structure of the CIGSe surface. As the CIGSe surface represents the site where the p/n junction of the solar cell is formed, its properties and quality distinctly influence device performance. Hereby, the main differences between NaF and KF PDTs and the detrimental alkali effect at low KF PDT temperature are elucidated. As nondestructive, surface sensitive methods, XPS and UPS are excellently suitable to probe such samples.

Chapter 7 investigates the need for the simultaneous evaporation of Se during PDT, again with XPS and UPS measurements. Therewith, KF PDT samples, which underwent a KF PDT without Se supply, are investigated and the results will be compared to the KF PDTs with Se

supply from Chapter 6. Thereby, the influence of Se on the chemical reactivity of KF on the CIGSe surface can easily be examined.

Chapter 8 summarizes the results made in Chapter 5-7, discusses comparisons to literature, and offers possible models to explain the made results. Finally, the results are put in a wider context and an outlook for future experiments is given.

2 The CIGSe Thin-Film Solar Cell Technology

2.1 Historical development and general properties of the $Cu(In,Ga)Se_2$ compound semiconductor

The first interest for Cu-containing heterojunctions was aroused in the 1960s with the Cu_2S-CdS system [10,11]. In that time, the rectifying properties of such a heterojunction (i.e., for transistor applications) were of main interest and the observed photovoltaic effect was secondary, and rather weak. Just in the 1970s the Cu_2S-CdS heterojunction received considerable attention for photovoltaic energy conversion [12,13]. It began in 1974, when the first $CuInSe_2$/CdS heterojunction was described, being suitable for photovoltaic applications, because of its remarkably high optical absorption coefficient [14]. In 1985, Boeing prepared a coevaporated $CuInSe_2$-CdS solar cell with a Cu-poor composition, creating an efficiency leap up to 11.4 % [15]. At this stage, the $CuInSe_2$ solar cell technology gradually improved throughout the years [16]: A wet-chemical CdS-deposition led to thinner CdS layers and reduced absorption losses. In the 1990s, alloying of the $CuInSe_2$ absorber material with Ga led to the recently used $Cu(In,Ga)Se_2$ material system. Together with the use of Na-containing soda lime glass substrates, the efficiency was further boosted (This special role of Na will be addressed in Chapter 2.2). After the development of a multi-stage coevaporation process in the early 1990s [4], the electrical properties of the $Cu(In,Ga)Se_2$ layer, such as the conductivity, were further improved. Subsequently, the post deposition treatment (PDT) of the $Cu(In,Ga)Se_2$ layer with alkali fluorides under Se atmosphere was developed [17], pushing the power conversion efficiency up to 23.35 % nowadays [18]. Great success in high efficiencies has not only been reached on lab-scale cells in the order of some cm^2, but also on a module level: E.g., in 2021 AVANCIS realized a $30 \times 30\ cm^2$ solar module with a certified efficiency of 19.64 % [19]. For many commercial $Cu(In,Ga)Se_2$ solar cells, and also (with slight changes) in the scope of this work, the layer stack in Figure 2.1, shown as a cross section image a) and schematically b) [20], is often applied:

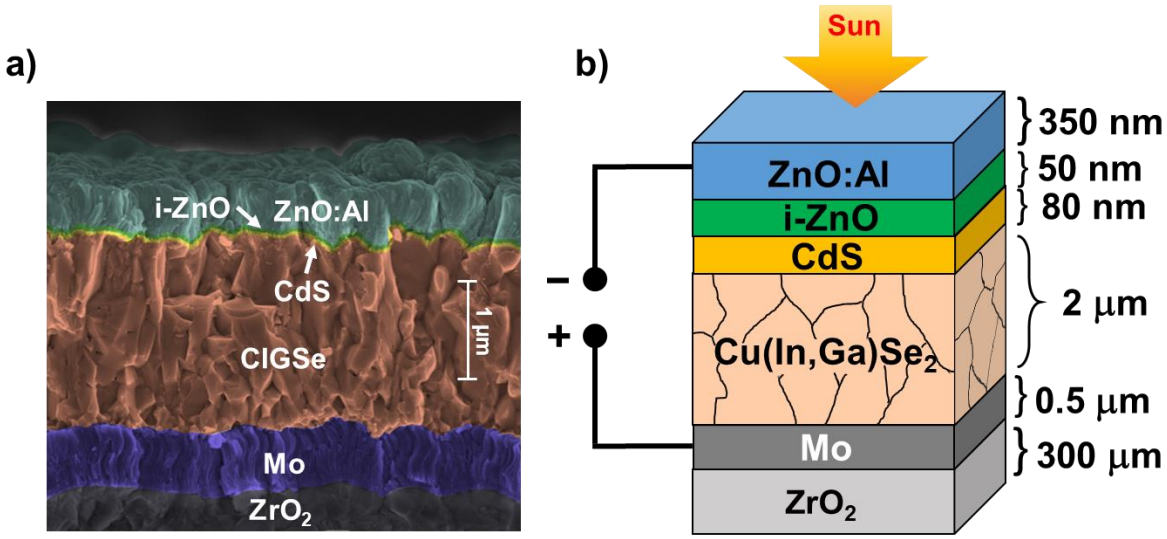

Figure 2.1 a) Scanning electron microscopy cross section image of the CIGSe solar cell stack prepared and used in this work. b) Schematic illustration of the CIGSe solar cell stack and thicknesses of the several layers. Reference see text.

In this layer stack, different materials with precisely tuned physical and chemical properties contribute to the functioning of the CIGSe solar cell: Soda lime glass is used as substrate, thermally and chemically stable, serving as mechanical support of the solar cell and working as a Na source. Thereover, the Mo layer is applied, serving as the plus pole of the solar cell and exhibiting high electrical conductivity, as well as a smooth surface, and a good chemical resistance towards a corrosive Se atmosphere. The CIGSe layer itself must be a good light absorber, show a high conductivity for electrons or holes, and a low concentration of structural defects to reduce charge carrier recombination. The CdS and intrinsic (i-ZnO) layers serve as "buffer" layers that enable a good electrical band alignment between CIGSe and front contact, along with a suitable lattice matching to prevent structural defects. The Al-doped ZnO layer (ZnO:Al) serves as the front contact, the minus pole of the cell, and above all should be highly transparent, and a very good electrical conductor. Both aspects, however, cannot be maximized at the same time, so that the thickness and the doping level of the ZnO:Al layer must be carefully adjusted. On top of the CIGSe cell, a metallic Ni/Al/Ni grid is applied (not shown), which collects the current from the ZnO:Al layer, and transports it to the electrical contacts of the cell.

As was mentioned before, the properties of all layers must be specially tailored and well matched, so that very high efficiencies can be reached. Especially in this work, the alkali fluoride PDT was investigated, which takes place on the CIGSe surface. Therefore, some more structural and physical properties about the CIGSe layer itself are given in the following.

$Cu(In,Ga)Se_2$ is a quaternary I-III-VI, direct, compound semiconductor, and exhibits a high optical absorption coefficient up to 10^5 cm^{-1} in a wide spectral range [21]. Layers, only several µm thick, therefore allow for a sufficient absorption of light. $Cu(In,Ga)Se_2$ crystalizes in the tetragonal chalcopyrite crystal structure (α-phase), which can be derived from the zinc blende structure. In this chalcopyrite crystal structure, every atom is tetrahedrally coordinated by its binding partners. $Cu(In,Ga)Se_2$ can be viewed as solid solution of $CuInSe_2$ and $CuGaSe_2$, in which Ga and In are interchangeable on their lattice sites. Depending on the Ga/In ratio, the lattice constants of the unit cell can be varied and the bandgap energy of the material can be tuned between 1.0 eV (pure $CuInSe_2$) and 1.7 eV (pure $CuGaSe_2$) [22]. Most CIGSe thin films are polycrystalline and are grown with an overall Cu-deficiency (meaning a final Cu amount of less than 25 %). The CIGSe films prepared in this work show an average grain size about 100 nm. At the surface of the CIGSe thin film, the formation of a Cu-poor region is observed, possibly only one monolayer thick. Most CIGSe thin films for PV applications are polycrystalline with hence many intrinsic structural defects, present in the material. These can be zero-dimensional defects like point defects such as vacancies, interstitial atoms, or substitutional defects. All these structural defects influence the electrical properties of the material, and in case of CIGSe, a highly compensated, p-conducting semiconductor is created. The grain boundaries (GBs) in polycrystalline CIGSe thin films can be seen as two-dimensional structural defects. At these boundaries between neighboring grains in the crystal structure, unsaturated chemical bonds ("dangling bonds") are present, which possess a high chemical reactivity. It is believed that GBs act as barriers for charge carrier transport and therefore crucially influence the electrical mobility of charge carriers (across them) [23]. Consequently, the intrinsic defects in the grain interior (GI) as well as the defects at GBs of polycrystalline CIGSe need to be passivated for the application of the CIGSe material in solar cells.

2.2 Doping of CIGSe layers with alkali metals

The beneficial doping of CIGSe solar cells with Na was discovered coincidentally, as common window glass (soda lime glass) was used as a substrate. At elevated temperatures (i.e., during the CIGSe deposition process) Na diffuses from the glass substrate through the Mo layer into the CIGSe layer and improves its electrical properties. This effect was first observed by Hedström et al. in 1993 [24]. Upon this incorporation of Na, the charge carrier density is increased [25], and grain boundaries and bulk-related defects are passivated, as Na is located at both, in the GI and at GBs [26]. In this respect, Heske et al. found, that, independent of the Na source, Na changes the surface dipole and reduces the work function at the CIGSe surface, and possibly also at grain boundaries [27]. The passivation of grain boundaries improves the charge carrier mobility and the conductivity of the CIGSe layer. Both effects lead to an improvement in open circuit voltage (V_{OC}) and fill factor (FF), two very important properties, which characterize the performance of the solar cell (see Chapter 4.2). Problems arising from an "indirect" Na supply from the substrate are a lack of controllable Na doses (depending highly on the glass), smaller grain sizes of the CIGSe absorber, a reduced interdiffusion of Ga and In [28], and a higher density of stacking faults [29]. To better control the crystal quality and the Ga/In composition profile throughout the CIGSe layer, it is better to decouple CIGSe growth and Na supply. Thereby, the post deposition treatment was developed are presented in the next chapter.

2.3 The alkali fluoride PDT as key step to very high efficiencies – advantages, benefits, and open questions

The positive effect of the in-diffusion of Na especially after CIGSe growth was described by Rudmann et al. in 2003, enabling an improvement of the efficiency from 10 to 14 % [30]. The so-called post deposition treatment with NaF (NaF PDT) led to an incorporation of Na into the CIGSe layer, and thereby improved the solar cell characteristics without any influence on crystal growth or interdiffusion. Upon a NaF PDT, mainly the V_{OC} and the FF of the solar cell are improved, similar to the case when Na is supplied from the glass substrate. Other alkali fluorides were also used and consequently the first pure KF PDT was applied by Lämmle et al. in 2013 [31]. The application of a KF PDT directly after a preliminary NaF PDT led to a strong boost in cell efficiency on polyimide substrate up to 20.4 % [32]. This achievement was followed by another boost in cell efficiency on glass substrates up to 21.7 % and 22.6 % by application of a RbF PDT and a CsF PDT in 2015 and 2016 respectively, both by Jackson et al. [33,34]. Thereby, the device performances of CIGSe solar cells were steadily increased up to the current record efficiency of 23.35 % [18]. A schematic illustration of the alkali fluoride post deposition treatment is given in Figure 2.2.

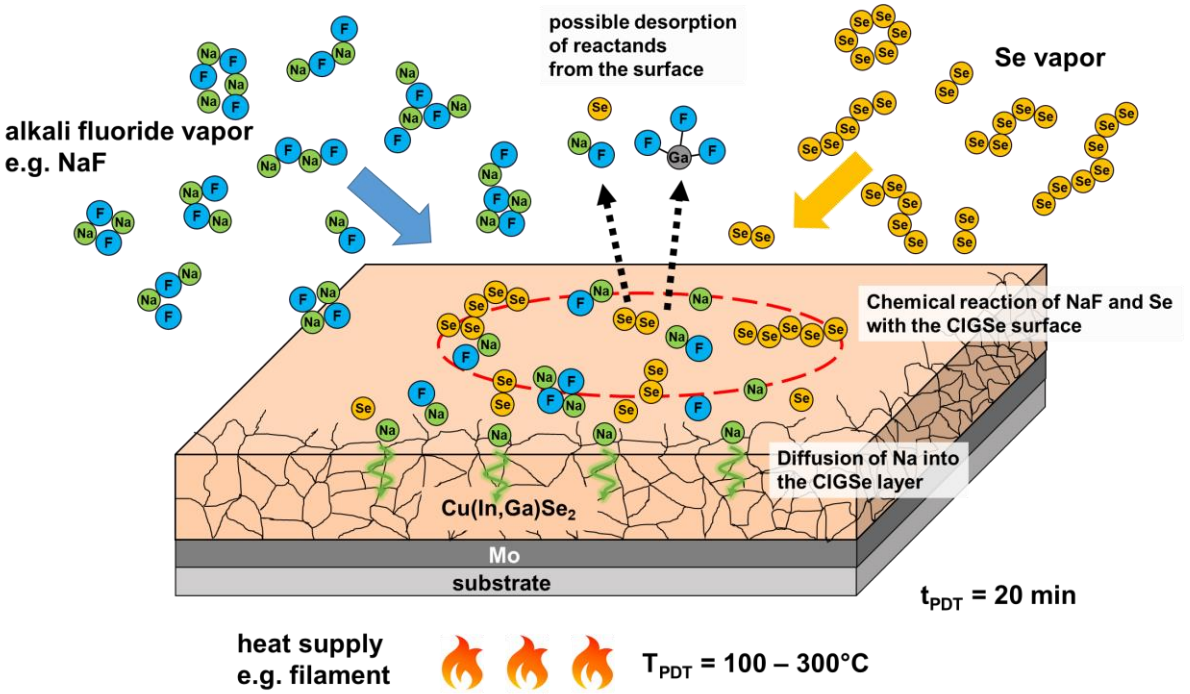

Figure 2.2 Model scheme for a NaF PDT on a CIGSe surface shown on a molecular level.

The PDT takes place right after the CIGSe deposition step and is done in the same deposition chamber, as the CIGSe preparation. The sample is cooled down to the so called "PDT temperature, "T_{PDT}" and then annealed for a certain time in presence of an alkali fluoride and elemental Se vapor. Consequently, NaF (as in the example in Figure 2.2) and Se react on the CIGSe surface, and also with the CIGSe surface, and form a number of volatile and non-volatile intermediates and components. Some reactants stay on the surface and some desorb into the gas phase, as the PDT is done in the CIGSe deposition chamber with gas pressures in the 10^{-7} mbar range. The chemical reactions, which occur on the CIGSe surface are very complex and depend sensitively on many process parameters like T_{PDT}, the CIGSe surface composition, the type of alkali fluoride, the duration of the PDT, or the rates, at which the alkali fluorides and Se are evaporated. At the same time, also other atomic processes, like the reconstruction or relaxation of the CIGSe surface may take place, also in dependence of T_{PDT} and other parameters. Therefore, the exact chemical mechanism of the alkali fluoride PDT on CIGSe surfaces is not fully understood, and many opposed observations have been made (e.g., for a KF PDT [35]). A circumstance, which worsens this problem is that there is no standard CIGSe and PDT process, and that every research group applies a slightly different procedure. This makes the comparison of different results even more difficult. For example, besides beneficial effects of a PDT on cell efficiency, also detrimental effects of a PDT have been reported [36]. Nevertheless, there is also a significant amount of consent in the scientific community: Generally, the alkali fluoride PDT changes the CIGSe surface chemically and electronically, and leads to the incorporation of alkali metals into the CIGSe layer.

For the chemical structure of the CIGSe surface, often a depletion in Ga is observed [37,38], together with the formation of a secondary component, being composed of the respective alkali metal, In and Se (Alk-In-Se). However, there is still no absolute certainty for the existence of these secondary phases, and also their exact composition is not clear (therefore mentioned as "Alk-In-Se"). This secondary phase (e.g., K-In-Se as published by Handick et al. [38]) possesses beneficial electrical properties and assumingly leads to an improved band alignment at the CdS/CIGSe interface [8]. Thereby, the charge carrier recombination at the interface is reduced and the V_{OC} of the solar cell is increased. A general trend exists that heavier alkali metals like K, Rb and Cs do form the Alk-In-Se secondary component much

easier, than lighter alkali metals like Na. This trend is explained with theoretical calculations by Malitckaya et al., by the lowered solubility of Alk-In-Se (Alk= K, Rb, Cs) in the CIGSe surface [39]. However, not in every case a Ga-depleted surface and the formation of an Alk-In-Se (Alk= K, Rb, Cs) component is observed: Kreikemeyer-Lorenzo et al. found that a RbF PDT only led to a slight reduction of Cu content at the CIGSe surface, no change in Ga content and increased formation of Ga- and In-oxides, rather than selenides (as was expected for Alk-In-Se) [40]. Another benefit resulting from the changes in chemical surface composition is an improved growth of the CdS layer onto the CIGSe surface after a RbF PDT, reported by Friedlmeier et al. [41]. With a denser coverage of the CIGSe surface with CdS, the deposition of a thinner CdS layer is possible, leading to an increase in carrier collection [37]. Another interesting observation is made, when the alkali fluoride dose, e.g., in a NaF or RbF PDT, is too high: The device properties, such as the FF, decrease [42]. It is speculated that secondary components with rather detrimental electrical properties (like a high electrical resistance) form during PDT, so that a thicker secondary component layer would deteriorate the device performance [43]. Moreover, too high amounts of alkali fluoride at the CIGSe surface could also lead to an in-diffusion and doping of the CdS layer, which could affect the type inversion at the CdS/CIGSe interface (the transition between n- and p-type layers in the cell) [44,45].

Despite the formation of secondary components at the surface, a part of the alkali metals also diffuses into the CIGSe layer. As mentioned in Chapter 2.2, alkali metals inside the CIGSe layer segregate at grain boundaries, but can also diffuse into the grain volume [42,46]. It is observed that at both locations, alkali metals improve the electrical properties of the $Cu(In,Ga)Se_2$ material [47,48]. However, no clear experimental proof exists, how alkali metals exactly work as dopants.

Until now, treatments of a CIGSe sample with double alkali PDTs lead to the highest cell efficiencies. Therewith, the properties of light and heavy alkali metals are combined: Light alkali metals diffuse into the grain volume more easily and also segregate at the GBs, whereas heavy alkali metals mainly segregate at the surface, or at GBs. Heavy alkali metals, which segregate at GBs, are able to push lighter alkali metals away from the GBs [49]. Additionally, heavier alkali metals are able to form secondary phases [50]. Thereby, lighter alkali metals mainly seem to improve the conductivity of the material, and thus the FF of the solar cell, whereas heavy alkali metals better passivate GBs, and thereby reduce charge carrier recombination, and improve the V_{OC} of the solar cell [51].

Overall, the PDT has a vast impact on the chemical and electronic properties of the whole CIGSe layer, including the surface, and the bulk region. However, many questions regarding the principal “working mechanism“ of alkali metals within the CIGSe layer are unsolved and also processual details, e.g., reasons for the need of a Se supply during PDT, have not been explored so far. These questions are addressed in the work in hand.

3 Theoretical Background

In Chapter 3, some theoretical aspects are presented which describe the working principle of a CIGSe solar cell (Chapter 3.1) and the characterization technique used especially for CIGSe surfaces (Chapter 3.2).

3.1 General working principle of a CIGSe solar cell and analytical description of its current-voltage dependence

A solar cell can be understood as a thermal engine, which converts radiation energy into chemical energy, and subsequently converts chemical energy into electrical energy. The particular steps of these energy conversions are presented in Figure 3.1 and take place in the following order [52,53]: First, light is absorbed in the respective semiconductor material (CIGSe) upon excitation of an electron from the valence band to the conduction band. The missing electron in the valence band is called a “hole“. Because of their opposed electrical charge, electron and hole can be bound to each other and form an “exciton“. This exciton pair, however, is only weakly bound together in a semiconductor like CIGSe. Consequently, electron and hole dissociate and diffuse independently from each other through the semiconductor. At this stage, radiation energy has been converted into chemical energy. It is this additional chemical energy, which “drives“ the electron and hole through the material. More precisely, the electrochemical potential of electron and hole in the semiconductor have been increased under absorption of a photon. This electrochemical potential is not constant throughout the semiconductor, but shows a gradient, which is steeper towards the boundaries of the CIGSe material. To create an electrical current with a defined direction eventually, the electrons and holes must selectively diffuse into opposite directions. This charge selective diffusion is realized by layers with different conductivities for electrons and holes (as can be thought of selective membranes). A p-doped layer e.g., mainly exhibits a good conductivity for holes, whereas an n-doped layer exhibits a good conductivity for electrons. Therewith, the n-doped layer lets electrons pass through, whereas holes are blocked. For the p-doped layer, this behavior is vice versa.

Figure 3.1 displays an exemplary band diagram of a CIGSe solar cell, in which a $Cu(In,Ga)Se_2$/CdS interface has been formed and for which Morkel et al. have found a flat-band alignment at the interface [54]. In this solar cell structure, the CIGSe layer represents the light absorber and the p-doped layer at the same time. The CIGSe layer therefore mainly impedes the electron diffusion and blocks them in reaching the back contact, whereas holes pass through on their way to the back contact. The CdS layer represents the n-doped layer, which blocks holes and lets electrons pass through on their way to the front contact. Figuratively, these different types of conductivities in the CIGSe and CdS layer enable a selective carrier transport towards the contact poles of the solar cell (positive and negative pole, Mo back contact and ZnO:Al front contact, respectively). With these different layer-properties, a macroscopic electrical current flow can be established and chemical energy is ultimately transformed into electrical energy.

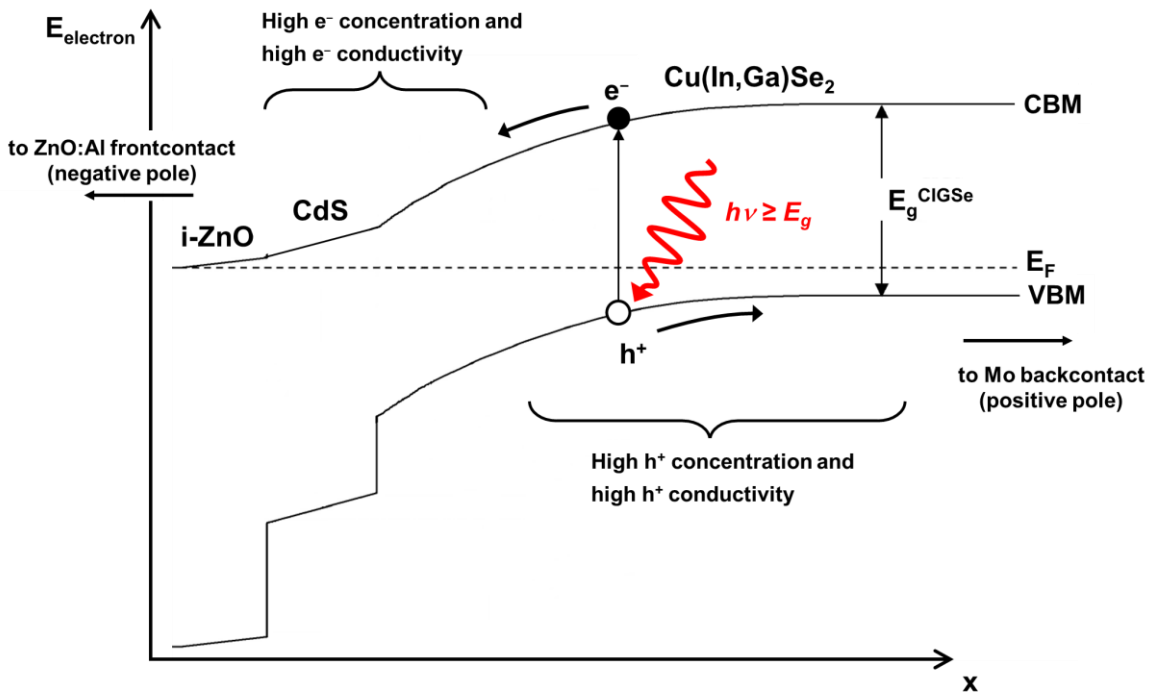

Figure 3.1 Schematic band diagram of an exemplary CIGSe solar cell (Mo back contact and ZnO:Al front contact left out) as a function of the position x within the cell, where only the CIGSe layer, the CdS layer and the i-ZnO layer are shown. In case of an CdS/Cu(In,Ga)Se_2 interface, a flat-band alignment was found at the CdS/Cu(In,Ga)Se_2 interface (i.e. the conduction band offset is zero). E_V denotes the valence band maximum, E_C denotes the conduction band minimum and E_F denotes the Fermi energy. The incoming photon (red) is absorbed in the CIGSe layer, where it creates an electron-hole pair. Electron (e^-) and hole (h^+) dissociate and diffuse through the CIGSe layer. Because of the high p-conductivity of the CIGSe layer, mainly holes will wander through the CIGSe layer and reach the back contact (direction indicated with an arrow in the diagram). Electrons, however, will travel in the opposite direction through the CdS layer towards the front contact, because of the high n-conductivity of the CdS and front contact layers.

Electrically, the p/n junction in the solar cell works as a diode, so that the solar cell shows a voltage dependent resistance. The equivalent circuit diagram of the solar cell can be modeled with a diode, two resistors, and a direct current source. Under inclusion of other assumptions and in case of an ideal solar cell with a continuous band diagram, the current density-voltage characteristic (I-V) under illumination can be described by Eq.1:

$$I(V) = I_0 \left(e^{\frac{q(V-IR_S)}{AkBT}} - 1\right) + \frac{V - IR_S}{R_P} - I_{sc} \qquad \text{(Eq.1)}$$

The variables in Eq.1 are denoted as follows: I_0 denotes the dark saturation current, q denotes the elementary charge, R_S denotes the series resistance, A denotes the diode quality factor, k_B is the Boltzmann constant, T is the temperature, R_P is the parallel resistance, and I_{sc} is the short-circuit current. The equivalent circuit diagram of the solar cell in the one-diode model, and the derivation of Eq.1 including all its approximations can be found elsewhere [55,56].

3.2 Photoelectron Spectroscopy

In X-ray photoelectron spectroscopy (XPS), a material interacts with soft X-rays with an energy ranging from 50 to 1500 eV. Therewith, electrons of the material are excited from an occupied state to an unoccupied state (e.g., the conduction band), or can also leave the surface (= excitation into the vacuum). In a XPS-spectrum, the number of the emitted photoelectrons is recorded as a function of their kinetic energy (E_{Kin}) with an electron energy analyzer. For a subsequent characterization, the kinetic energy of the photoelectron is then converted into its former binding energy (E_{Bin}) according to Einstein´s photoelectric equation in Eq.2 [57]:

$$E_{Bin} = h\nu - E_{Kin} \qquad \text{(Eq.2)}$$

The excitation energy for XPS measurements is provided by a Mg or Al X-ray tube. The energy value for Mg K_α radiation is 1253.6 eV and for Al K_α 1486.6 eV [58]. For ultraviolet photoelectron spectroscopy (UPS), the sample surface is irradiated with ultraviolet radiation, coming from a He discharge lamp. The energy of the UV radiation is much lower, for example He I radiation (21.2 eV) and He II radiation (40.8 eV). With a FWHM of 0.02 eV, the UV excitation width is much narrower than that of Al K_α or Mg K_α radiation (0.83 eV and 0.68 eV, respectively) [59]. Figure 3.2 schematically illustrates the photoemission process in a band diagram (adapted from [60]) :

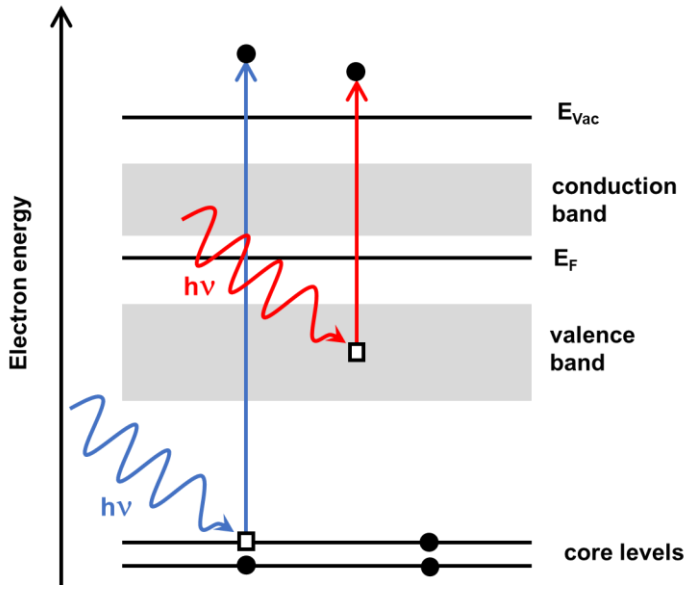

Figure 3.2 Scheme for the excitation processes of XPS measurements (blue) and UPS measurements (red) within the band diagram. White squares illustrate holes, and black circles present electrons. The scheme is adapted from Moulder et al. (reference see text).

Photoelectrons at common kinetic energies of an XPS or UPS experiment (0-1500 eV) are very surface sensitive due to their very short inelastic mean free paths λ (IMFP, definition see Figure 3.3, in the “universal curve“ for electrons in solids) [61]. Thereby, these photoelectrons are very suitable for probing the surface region of a material (IMFP approx. 1 – 3 nm), being able to investigate the occupied core and valence level states in the surface region of the sample. Consequently, detailed information about the band structure of the valence band (in case of UPS) or about the chemical environment of an elemental species (in case of XPS) can be obtained.

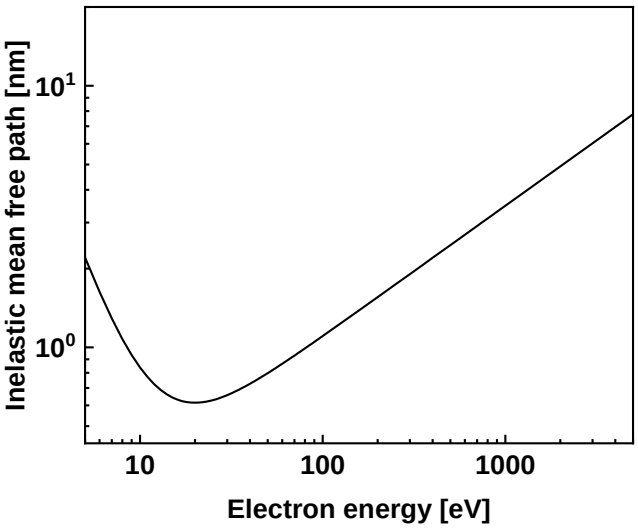

Figure 3.3 Inelastic mean free path (IMFP) of electrons in a solid, as a function of their kinetic energy. The figure is adapted from a publication by Seah and Dench (reference see text). The inelastic mean free path is defined as the distance, which electrons have to travel through a solid, so that their intensity is reduced to 1/e (~63%) of its initial value by inelastic scattering.

Another very valuable process, which follows the emission of a photoelectron, is the Auger transition [62]. In this de-excitation process of the atom, the core hole is filled with another electron, which relaxes from a higher energy level. Upon this relaxation, energy is transmitted from the relaxing electron (green). The emitted photon energy hν can then be transferred to a third electron, which can leave the atom. This (the third one) emitted electron is called the Auger electron and it carries valuable information about the specific, chemical state of the atom it was emitted from. An schematic illustration for the Auger process is shown in Figure 3.4 (adapted from [60]).

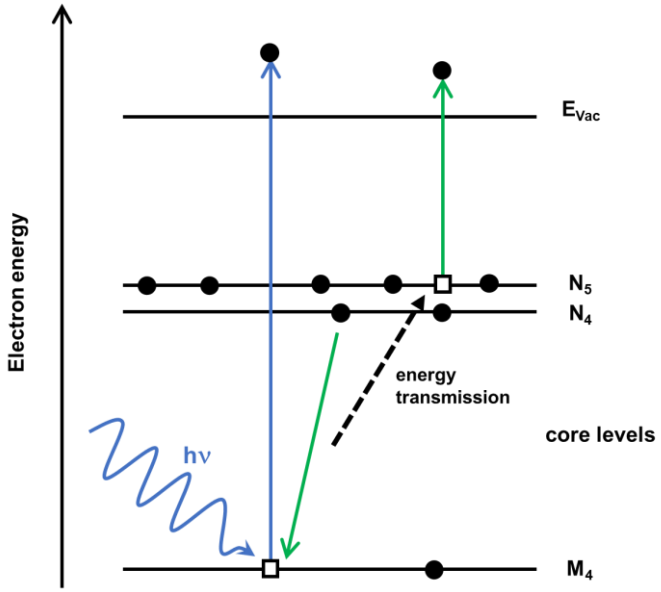

Figure 3.4 Schematic illustration of the In $M_4N_{4,5}N_{4,5}$ Auger process (green) in an energy diagram. Electrons are illustrated as black circles and holes are illustrated as white squares. The scheme is adapted from Moulder et al. (reference see text).

Because in the Auger process two core holes are present in the final state of the process, Auger electrons in most cases (but not always) are more sensitive towards chemical changes of the respective atom than photoelectrons, where only one core hole is present in the final state of the atom. This fact makes the evaluation of Auger spectra very complex, but the

chemical information they carry is substantial. The analysis of Auger electrons in the context of an XPS experiment is called X-ray excited Auger electron spectroscopy (XAES). Auger transitions are denoted by the quantum numbers of the involved electronic states during the Auger process: The first letter marks the principal quantum number of the state, from which the core hole was generated, the second letter marks the state, from which the second electron relaxed into the core hole, and the third letter marks the state, from which the Auger electron was emitted, for example "In $M_4N_{4,5}N_{4,5}$."

All photoemission experiments have to be carried out in an ultra-high vacuum (UHV) chamber to prevent coverage of the sample surface with residual gas particles. At gas pressures in the UHV range (~ 10^{-10} mbar); the number of collisions of residual gas particles with the surface is sufficiently low, so that it takes several hours to fully cover a freshly prepared surface. In the meantime, all surface sensitive experiments like XPS or UPS can be accomplished. The same circumstance is indispensable for the emitted photoelectrons: Only at sufficiently low residual gas pressures, the photoelectrons do not collide with gas particles in the analysis chamber and are able to reach the electron analyzer, where they are detected.

To determine the chemical environment of an elemental species, the so-called modified Auger parameter (α') can be calculated. With the help of the modified Auger parameter, the results of different photoemission experiments can be compared more easily [63]. The modified Auger parameter of a chemical species is defined as the sum of the kinetic energy of the sharpest Auger feature of this species and the binding energy of the most intense photoelectron line, as stated in Eq.3:

$$\alpha' = E_{Kin}(\text{Auger}) + E_{Bin}(\text{Photoelectron}) \qquad \text{(Eq.3)}$$

The modified Auger parameter has the advantage that it is independent on many circumstances like the excitation source of the photoemission experiment, sample charging, band bending, doping, and more. All these points influence the exact binding or kinetic energy positions of the photoelectron or Auger line and complicate the characterization of the chemical environment. With the help of the modified Auger parameter, these problems can be circumvented.

α' is displayed in the so called Wagner plot, where E_{Kin} of the Auger line is plotted on the ordinate and E_{Bin} of the photoelectron line is plotted negatively oriented on the abscissa. The α' values are then displayed as a linear function with slope +1. Throughout this work, the α'-values are attached on the right y-axis of the Wagner-plot (e.g., see Figure 6.1.2.3). This plot was first presented by C.D. Wagner, who also measured several components and calculated the respective α' value [64]. Thereby, his work is often used as reference. For a more detailed review about the unique usefulness of photoelectron spectroscopy (among other techniques using soft x-rays) especially for thin film surface properties, see [65].

4 Experimental Setup

In this chapter it will be illustrated, how the CIGSe solar cells are prepared (Chapter 4.1), and how they are characterized (Chapter 4.2). Furthermore, it will be described, how the CIGSe samples, especially for the XPS/UPS-measurements are prepared, packed and shipped to the Materials for Energy (MFE) lab at KIT (Chapter 4.3). Finally, details about the XPS and UPS measurements will be given (Chapter 4.4).

4.1 CIGSe solar cell preparation

The CIGSe solar cell is built of several layers with different properties, as was shown in Figure 2.1. The cell is prepared in a bottom up process, starting with the alkali-free substrate. The description of the particular preparation steps will be given in the same order in the following:

For an alkali-free substrate of the solar cell, zirconium dioxide (ZrO_2) substrates (CeramTech GmbH) with a thickness of 300 μm and a size 50 × 50 mm^2 of were used. The thermal expansion coefficient of these ZrO_2 substrates is 11 × 10^{-6} K^{-1}, similar to that of the CIGSe thin film (7 to 9 × 10^{-6} K^{-1}). Other merits for ZrO_2 as a substrate material are its high thermal, mechanical, and chemical resilience. The ZrO_2 substrates were cleaned with acetone and isopropyl alcohol successively in an ultrasonic bath and dried under a nitrogen purge.

Thereafter, a 500 nm thick Mo back contact was deposited onto the ZrO_2 substrates by direct current (dc) sputtering. Subsequently, the Mo-coated ZrO_2 substrates were loaded into a CIGSe coevaporation chamber (Octoplus 800, MBE Komponenten GmbH, base pressure 1 × 10^{-9} mbar) equipped with a cooling shroud and a load lock. A fine-grained CIGSe layer with a thickness of about 2 µm was deposited on the samples by coevaporation of Cu, In, Ga and Se in a single stage process. The evaporation sources were equipped with shutter lids for a precise control of the evaporation period. The substrate temperature during the CIGSe process was ~450 °C. The temperatures of the Cu, In, Ga, and Se sources were adjusted, to obtain CIGSe layers with a Cu content of [Cu]/([In]+[Ga]) = CGI = 0.79 – 0.81 and Ga content of [Ga]/([In]+[Ga]) = GGI = 0.3. The bulk composition of the CIGSe films was determined with X-ray fluorescence measurements and is approximately $Cu_{0.8}In_{0.7}Ga_{0.3}Se_2$. After deposition of the CIGSe layer, the alkali fluoride PDT was conducted *in situ*. Either a sodium fluoride PDT (NaF PDT) or a potassium fluoride PDT (KF PDT) was performed under low Se flux. The CIGSe samples were cooled down to the PDT temperature (T_{PDT}) in two steps under a constant co-evaporation of Se: One cool down ramp was applied from ~450 °C to 350 °C under a Se flux of ~6 Å/s within 4 min, and the final ramp to T_{PDT} was performed under a Se flux of ~ 2 Å/s within ca. 10 min. The PDT was then performed for 20 min under a Se flux of ~2 Å/s and an alkali fluoride flux of ~0.3 Å/s. After PDT, the alkali fluoride source was shut and the CIGSe samples yet were held at T_{PDT} for 2.5 min under a Se flux of ~2 Å/s. After that, he Se source was also shut and the sample was cooled down to 250 °C within 4 min under the ambient Se background pressure of the deposition chamber.

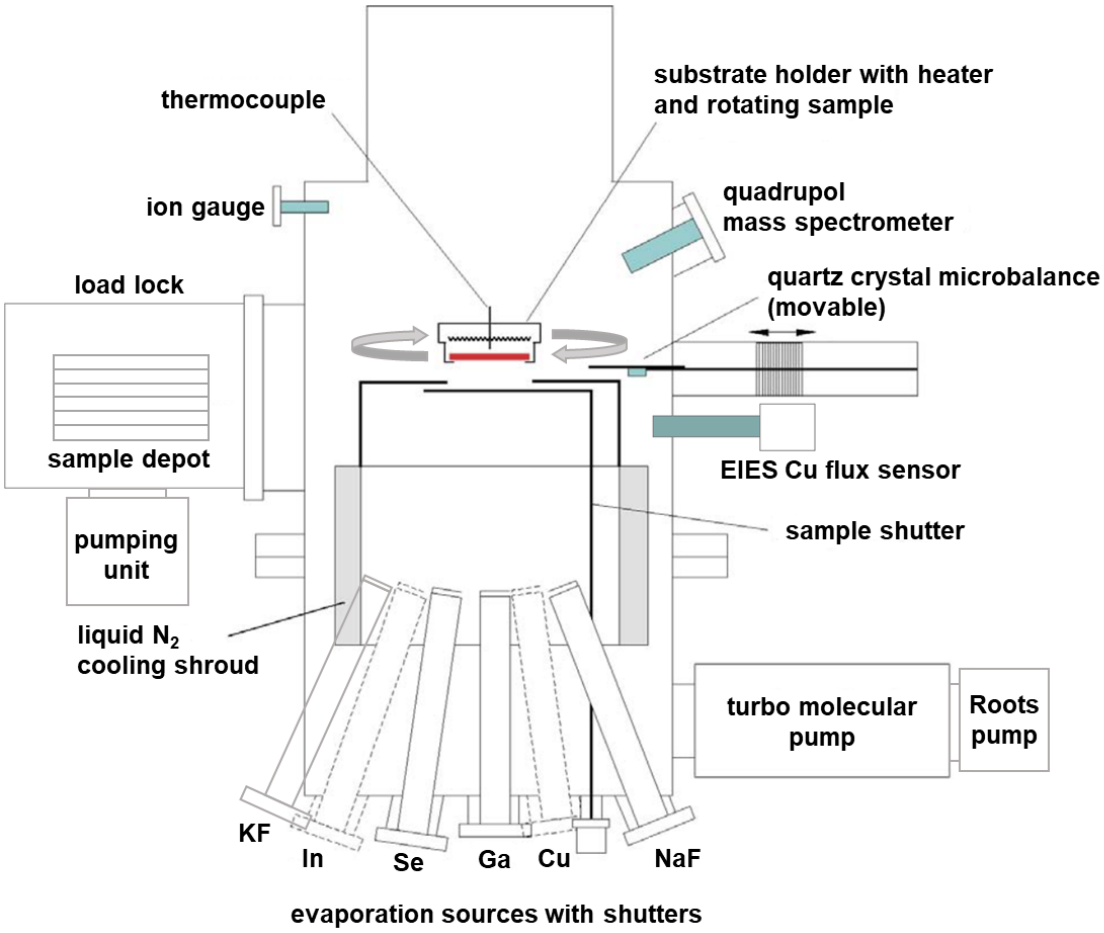

Figure 4.2 Schematic illustration of the coevaporation chamber at ZSW for preparation of the CIGSe layer and subsequent alkali fluoride PDT. Graphic adapted from Rudmann [13].

A detailed process diagram is shown in Figure 4.3. The evaporation rates of Se were controlled with the help of an optical quartz fiber sensor (MBE Komponenten GmbH) and calibrated with a quartz crystal microbalance (Inficon). The evaporation rate of the Cu source was monitored with an electron impact emission spectroscopy flux sensor (EIES-IV Guardian by Inficon). Residual and process gas analysis was conducted with a quadrupole mass spectrometer (Prisma Plus QMG 220 by Pfeiffer Vacuum).

After deposition of the CIGSe layer and subsequent PDT, the samples were unloaded from the deposition chamber and rinsed with an aqueous, 0.1 mol/L Na_2S solution for 30s. Thereafter, the rinsing solution was washed off the sample with deionized water and the samples were thoroughly dried under a nitrogen purge. Thereon, a CdS layer of ~50 nm thickness was applied onto the CIGSe samples via a chemical bath deposition (CBD) step. The chemical bath was prepared by a mixture of aqueous solutions of $CdSO_4$, thiourea, and ammonia, with a final concentration of 1.4 mmol/L, 0.1 mol/L and 1.5 mol/L, respectively, typically in a volume of ~200 mL. The temperature of the chemical bath was held at 65 °C. The chemical bath deposition took about 8 min and the CdS thickness was checked optically with a Mo-coated SLG stripe as a “reference“ sample. After the CdS deposition, the samples were washed thoroughly with deionized water, dried under a nitrogen purge, and kept at ambient conditions for about 1 h for residual traces of water to vaporize.

Subsequently, the front contact of the cell was deposited by radio-frequency sputtering of a ~80 nm thick i-ZnO layer and dc sputtering of a 350 nm thick ZnO:Al layer. The cells were completed by electron beam evaporation of a Ni/Al/Ni contact grid through a shadow mask. Finally, the cells were separated from each other by mechanical scribing. The resulting total area of the cells was ~0.5 cm^2. All cells were measured without antireflective coating.

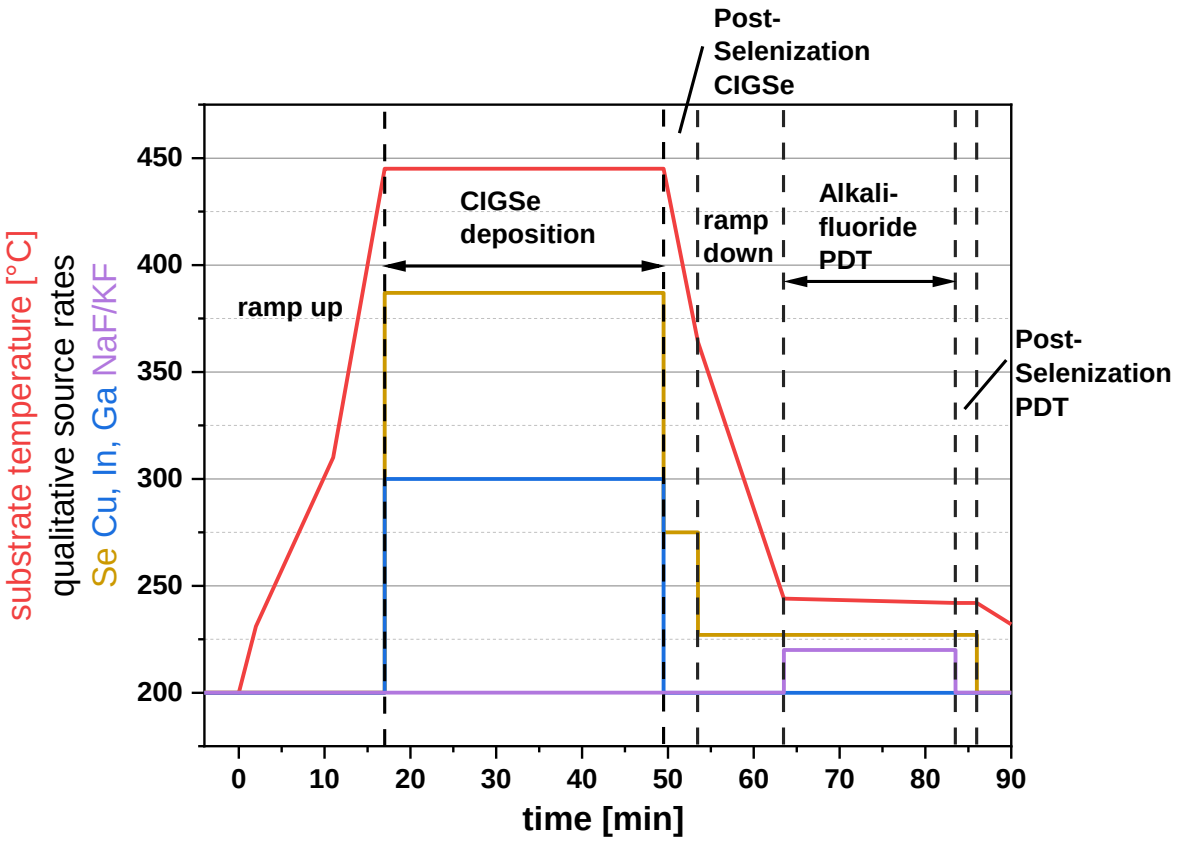

Figure 4.3 Scheme for the chronological sequence of the single-stage CIGSe deposition process and a subsequent alkali fluoride PDT.

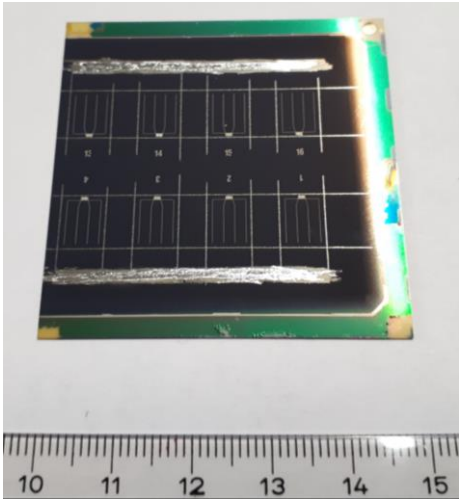

Figure 4.4 Photo of an array of 8 complete CIGSe solar cells on a 50 × 50 mm^2 ZrO_2 substrate.

4.2 Structural, chemical and optoelectronic characterization tools for CIGSe solar cells

The alkali depth distributions within the solar cell were determined with **Time-of-Flight secondary ion mass spectrometry (ToF-SIMS)**. Especially for the work in hand, alkali concentration profiles within the CIGSe layer were determined with this technique. A ToF-SIMS 5 system from IONTOF was used and Wolfram Hempel at ZSW conducted the measurements. The sputtering beam consisted of O^+ ions with a kinetic energy of 30 keV, which was scanned over a sample area of 150 μm × 150 μm with a resolution of 128 × 128 pixels. The analysis beam consisted of Bi^+ ions with a kinetic energy of 2 keV, which was scanned over a smaller area of 50 μm × 50 μm to avoid crater-edge effects. A depth profiling is achieved by a continuous switching between the analysis and sputter beam. To obtain absolute Na and K concentrations, the relative ToF-SIMS profiles had to be calibrated. The applied procedure is illustrated in the following with an exemplary depth profile shown in Figure 4.5.

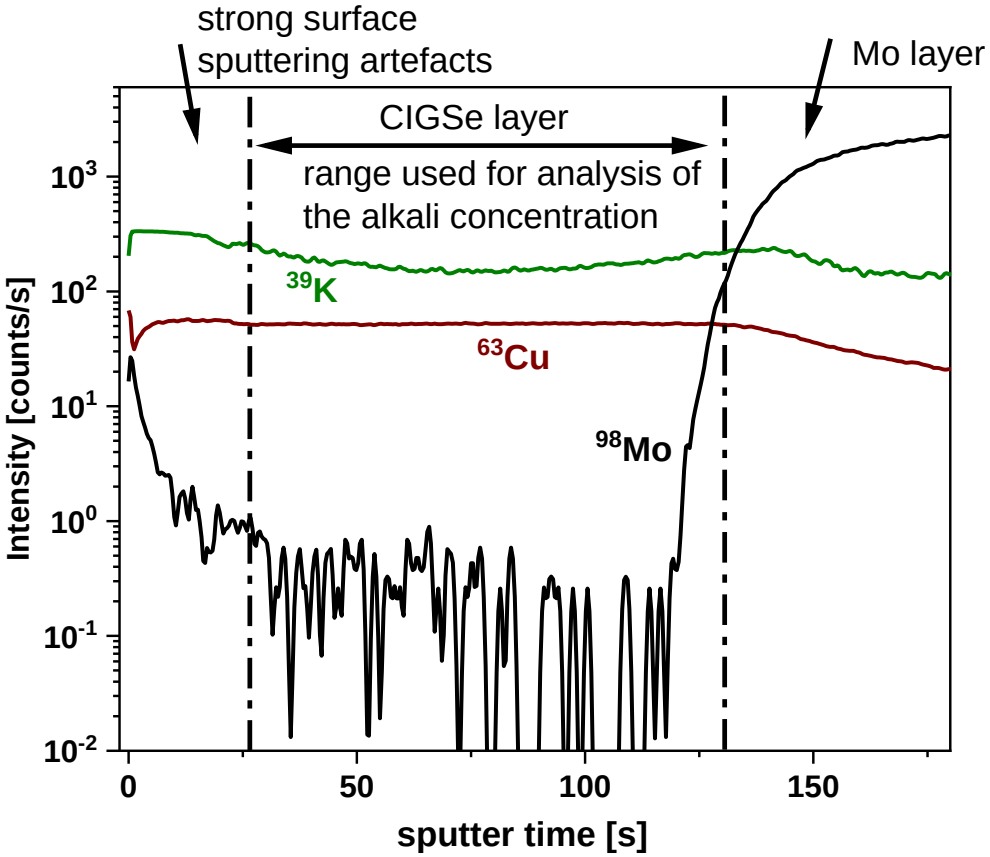

Figure 4.5 ToF-SIMS depth profiles for K, Cu and Mo of a CIGS layer after a KF PDT at T_{PDT} = 315 °C. Dashed-dotted lines mark the range for determination of the K concentration in the CIGSe layer.

Immediately before the ToF-SIMS measurements the ZnO and CdS layers were etched off in an aqueous HCl solution (w/w = 10%), rinsed with deionized water, dried with nitrogen, and then directly transferred into the SIMS setup. This etching step of the front contact layers strongly reduces knock-in effects and enhances depth resolution. In Figure 4.5 the ^{39}K, ^{63}Cu, and ^{98}Mo signals are plotted over the sputter time. Depending on the sputter time, different depths of the layers are analyzed. The ^{39}K signal slowly decreases at the surface of the CIGSe layer and shows a local maximum towards the Mo back contact, which are both SIMS artefacts: At the surface, it takes some time until a sputter equilibrium is achieved. Remnants of oxygen

can lead to enhanced signals for ^{39}K towards the surface due to an enhanced ionization probability. The increase of the K signal towards the Mo back contact can be explained partly by segregation of K at the interface CIGS/Mo and partly by a change of the ionization probability due to a change of the sputtering matrix**.** To exclude these sputtering artefacts, the K profile was evaluated in the range, where the Cu signal is constant. In this range, surface effects can be neglected, and only the pure CIGSe layer is analyzed (without the Mo layer). An alkali-free CIGSe sample implanted with ^{23}Na (dose = 1.2 x 10^{14} cm^{-2}, energy = 380 keV) and a sample implanted with ^{39}K (dose = 1.6 x 10^{14} cm^{-2}, energy = 700 keV) were used to calibrate the relative ToF-SIMS profiles to obtain absolute Na and K concentration profiles, respectively. To account for daily variations in absolute signal intensity the K (Na) signal is referenced to the Cu signal as follows to determine the alkali concentration in the CIGS layer in Eq. 4 and 5:

$$c(Na) = \frac{I(^{23}Na^{+})}{I(^{63}Cu^{+})} \times 261 \text{ ppm} \qquad \text{(Eq.4)}$$

$$c(K) = \frac{I(^{39}K^{+})}{I(^{63}Cu^{+})} \times 173 \text{ ppm} \qquad \text{(Eq.5)}$$

The ToF-SIMS system is able to detect alkali metal concentrations as low as 1 ppm.

Energy-dispersive **X-ray fluorescence measurements (XRF)** were conducted for a non-destructive analysis of the composition of the CIGSe layer with a FISCHERSCOPE® X-RAY XDV®-SDD system. In this method, the sample is excited with X-rays generated by a W anode operating at voltages up to 50 kV, whereupon the emission of characteristic fluorescence radiation takes place. The emitted radiation (X-rays) is then detected by a Si-drift detector with a resolution better than 140 eV. The data is analyzed with the built-in Fischer WINFTM® software. In this software, the area beneath the peaks of the K-Lines is determined and the atomic concentrations of Cu, In, Ga, and Se are examined, based on the Fundamental Parameter method [66]. The diameter of the analysis spot was 3 mm.

Another important characterization tool for solar cells are measurements of **current density-voltage curves (J-V curves).** As solar cells generate a voltage and a current under illumination, the dependence between these values expresses a characteristic measure of the solar cell. All J-V measurements were conducted at standard testing conditions at a temperature of 25 °C and under illumination with an “Air Mass 1.5” (AM 1.5) sun spectrum with a power density of 1000 W/m^2. The “Air Mass” is the ratio of the distance, which light travels through the atmosphere, until it reaches the ground, to the shortest way when it travels vertically through the atmosphere [67]. Depending on the path length light travels through the atmosphere, the solar irradiation is attenuated, respectively. For J-V measurements a WACOM sun simulator together with a Keithley 238 power supply was used. The solar cells were measured with Kelvin tips in a four-point probe configuration. Figure 4.6 shows exemplary J-V curves of a NaF PDT CIGSe solar cell under illumination (red) and in dark (blue).

As a solar cell can be understood as a diode, which is illuminated, the shape of its J-V curves also shows a typical electrical diode behavior: A blocking of the current can be observed at reverse bias (or at low forward bias) and an exponential increase of the current is observed at increasing forward bias. Both of these features are depicted for the J-V curves in Figure 4.6. Although the shape of the whole J-V curve discloses very valuable information about the cell, prominent points of the J-V curve are defined, which serve as “characteristic“ solar cell parameters. These specific points of the J-V curve are the open circuit voltage (V_{OC}) at j = 0, the short circuit current density (j_{SC}) at V = 0, and the fill factor (FF). The fill factor is determined as a dimensionless value between 0 and 100 %, which defines the maximum power, which

can be generated by the solar cell under illumination. As illustrated in Figure 4.6, the maximum power point of operation (V_{MPP} | j_{MPP}) of the cell is met, when the area of the gray rectangle between J-V curve (red) and coordinate axes becomes maximal.

The fill factor in Eq.6 can then be expressed as:

$$FF = \frac{V_{MPP} \times j_{MPP}}{V_{OC} \times j_{SC}} \qquad \text{(Eq.6)}$$

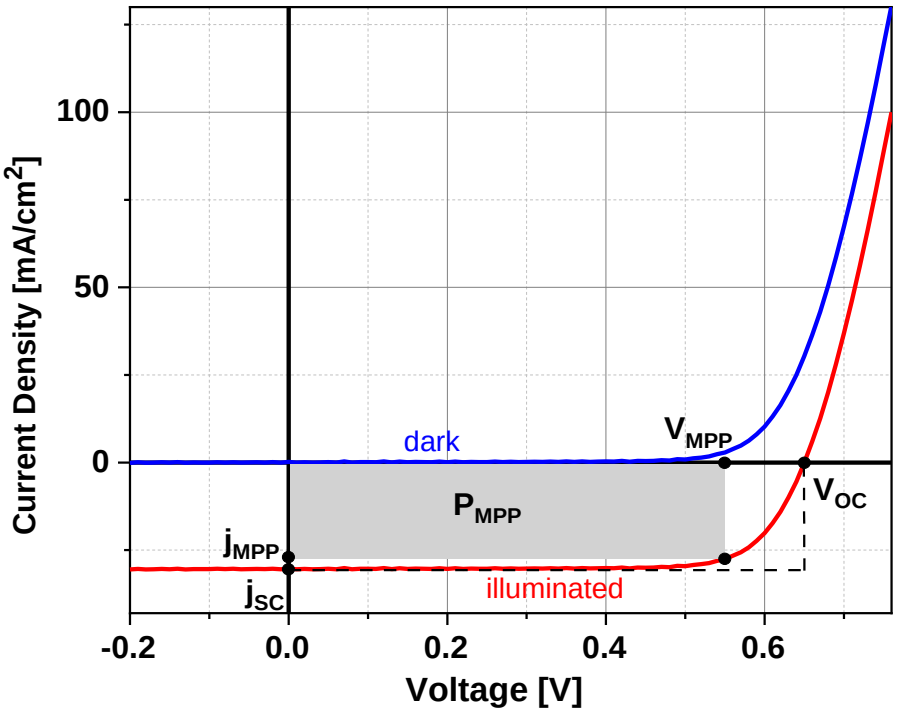

Figure 4.6 Current density-voltage (J-V) curves of a CIGSe solar cell with NaF PDT at 275 °C measured in the dark (blue line) and under illumination (red line). Shown in the diagram are the open circuit voltage (V_{OC}) at j = 0, the short circuit current density (j_{SC}) at V = 0, and the point of maximum power generation (MPP).

The resulting efficiency of the solar cell is defined as the ratio between the maximal generated energy (at MPP) and the power of the irradiation $P_{irr.}$ shone on a defined area of the solar cell. The mathematical expression for this definition is given in Eq.7:

$$\eta = \frac{V_{MPP} \times j_{MPP}}{P_{irr.}} \qquad \text{(Eq.7)}$$

To examine, how effectively which part of the sunlight contributes to the generated photocurrent, the **External Quantum Efficiency (EQE)** of the solar cells are measured. The external quantum efficiency is defined as the ratio of the number of generated electron-hole pairs in the solar cell to the number of irradiated photons, in a defined wavelength interval. EQE measurements were performed on a commercial BENTHAM PVE300 QE setup including a lock-in amplifier, a Xe-lamp, a monochromator, and a Si- and Ge-solar cell to calibrate the photon flux. The EQE measurements were conducted at room temperature under bias light.

The charge carrier density (N_A) of the CIGSe solar cells was estimated with **Capacitance-voltage (C-V)** measurements. The C-V curves were recorded with a HP 4192A LF Impedance Analyzer at room temperature in the dark. The measurements were carried out at a frequency of 100 kHz to prevent signal contributions from defect charge carrier states. With the exclusion

of defect states it is possible to determine a more accurate value for N_A. The DC bias voltage was varied from −1.5 V to 1.0 V, and the AC modulation voltage was set to 50 mV to prevent a significant contribution to the DC bias signal. The analysis of the C-V data and the theoretical model used for it is described in Chapter 5 on page 21.

4.3 Preparation of CIGSe layers for surface-sensitive XPS and UPS measurements

For the analysis of the CIGSe surface, special samples have been prepared, which were shipped to the MFE lab at KIT. These samples do not consist of complete cell stacks, but only of the CIGSe layer, which is deposited on the Mo-coated ZrO_2 substrate. On these CIGSe surfaces, different PDTs were applied, including an untreated reference cell.

In order to examine the chemical impact of the PDT and the subsequent rinse on the CIGSe surface, two identical sample sets were prepared. One sample set, on which the CIGSe surface is analyzed directly after PDT is called “as-grown“. The other sample set, which analyzes the influence after PDT and rinse is called “rinsed“. For very surface sensitive measurements like XPS and UPS, the surface of the CIGSe samples has to be kept from ambient atmosphere, as it has been observed by Heske et al., that humidity from the air strongly interacts with the CIGSe surface which can lead to a reduction of the Na content on the CIGSe surface [68]. Therefore, the “as-grown“ sample set was sealed under N_2 atmosphere directly after the preparation, without any contact to ambient atmosphere (This requirement was accomplished by attaching a separate glove bag at the load lock of the deposition chamber, which could be pumped out and flushed with an additional pumping stand). For the “rinsed“ sample set, the samples had to be unloaded from the deposition chamber and had to be rinsed at ambient atmosphere. After rinse (which was done similar as for cell preparation), the samples were directly transferred into coarse vacuum, and then loaded into a N_2 filled glove box, in which they were also sealed. It is estimated that rinsed samples were exposed to ambient atmosphere about 5 min in sum. Both sample sets (“as-grown“ and „rinsed“) were shipped to the MFE lab at KIT, and were transferred into the UHV system, without any exposure to air. The complete shipping procedure took about 4 – 5 hours (from glove box to glove box).

4.4 Specifications for the XPS and UPS measurements at the MFE lab

At the MFE lab at KIT the different samples were analyzed with XPS and UPS. XPS was performed with non-monochromatized Mg K_α radiation from a DAR 450 twin anode X-ray source (Omicron) and monochromatized Al K_α radiation from an SIGMA Surface Science MECS X-ray source. UPS spectra were taken by use of a He II discharge lamp. The photoelectrons were detected with a Scienta Omicron Argus CU electron analyzer. A FOCUS FDG 150 ion source at a sample current density of ~300 nA/cm^2 was used for low energy (50 eV) Ar^+-ion treatments. XPS and UPS spectra were calibrated with the Fermi Energy of a sputter-cleaned Au-foil. The base pressure of the analysis chamber was ~ 1×10^{-10} mbar.

All samples were measured twice: At first all spectra were taken from the samples in the condition in which they arrived at the MFE lab, this sample condition is called “as-received“. Afterwards the samples have been Ar^+-ion cleaned (50 eV) for 10 min, to remove common

surface contaminants. This sample condition is called “Ar^+-ion cleaned“. To evaluate the impact of the Ar^+-ion cleaning on the composition of the CIGSe surface, all photoelectron and Auger spectra have been compared prior (as-received) and after the Ar^+-ion cleaning (not shown). This comparison has been done for all samples. In Figure 4.7 exemplary spectra for the effect of the Ar^+-ion cleaning are shown. The Ar^+-ion cleaning mainly removed some carbon from the

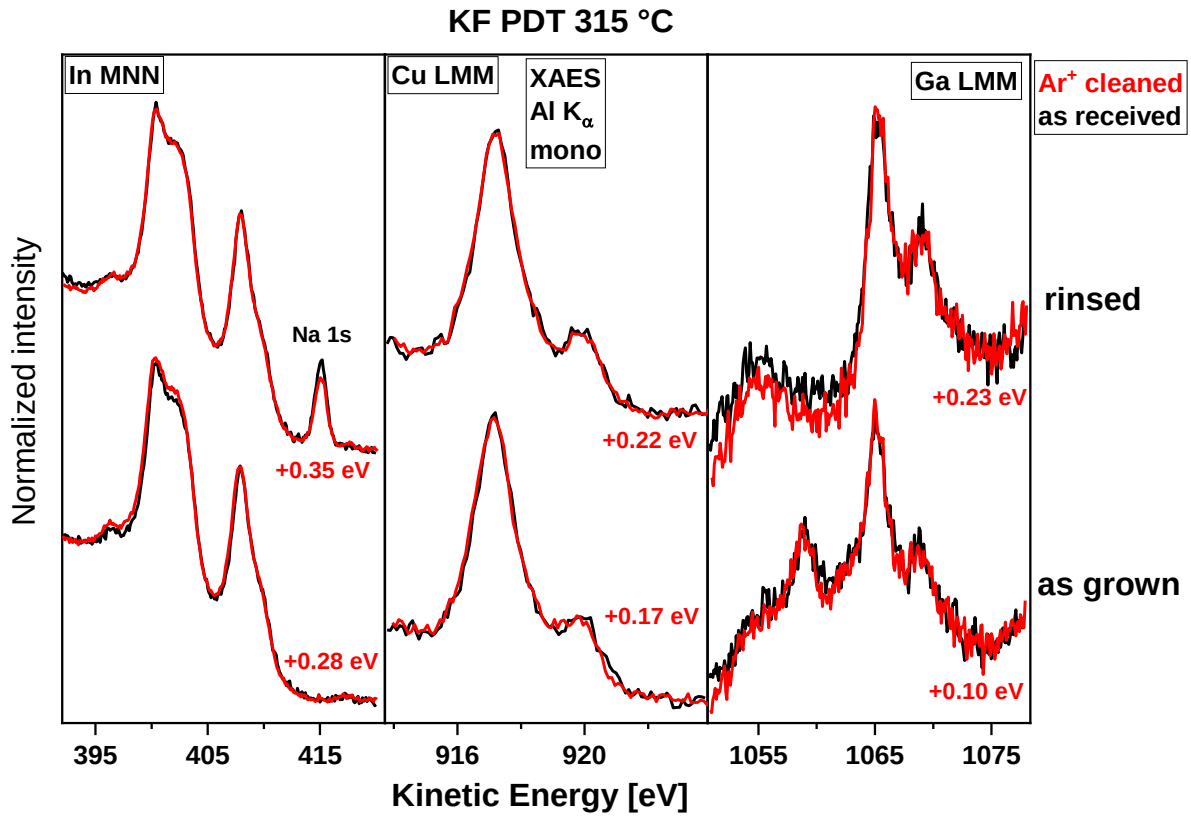

Figure 4.7 Normalized Al K_α excited In MNN, Cu LMM and Ga LMM Auger spectra of the KF PDT 315 °C samples „as-grown“, directly after PDT (bottom spectra) and „rinsed“, after PDT and subsequent rinsing (upper spectra). To highlight the impact of the Ar^+-ion cleaning, spectra taken prior Ar^+-ion cleaning (as-received, marked in black) and after Ar^+-ion cleaning (marked in red) are aligned. The spectra were normalized by setting the high kinetic energy background to zero and the peak maximum to one (for the In MNN spectra, the peak maximum at E_{Kin} ~ 407 eV was set to one). The Ar^+-ion cleaned spectra (red) were shifted on the x-axis, to allow for a better comparison of their shapes. Respective shifts are given in the diagram.

surface but did not change the CIGSe composition. No additional signals due to the Ar^+-ion cleaning were detected, no strong peak shifts were observed, and the intensity ratios of prominent CIGSe signals were preserved. A slight peak shift of ~0.2 eV is detected, together with a faint increase of the signal-to-noise ratio (SNR) for CIGSe-related signals. Therefore, it is concluded that the Ar^+-ion cleaning does not alter the chemical composition of the CIGSe surface, and that it does not lead to the formation of sputter-induced secondary phases (like metallic species, e.g., as observed by higher Ar^+-ion energies [69]. The Ar^+-ion cleaning should therefore not affect the results for the chemical impact of the PDT on the CIGSe surface. Consequently, exclusively spectra taken from Ar^+-ion cleaned samples are shown throughout the work in hand (unless otherwise stated). To demonstratethat the Ar^+-ion cleaning did not change the CIGSe composition severely, the In MNN, Cu LMM and Ga LMM Auger spectra of the KF PDT 315 °C samples (as-grown and rinsed) are plotted in Figure 4.7. In this diagram, these Auger spectra from as-received and Ar^+-ion cleaned samples can be compared.

Without further analysis of the Auger spectra, the spectral changes upon Ar^+-ion cleaning are very small. This comparison has been made for all other samples and no significant changes due to Ar^+-ion cleaning were observed.

For technical reasons, non-monochromatized Mg K_α radiation was not available for some samples (which explains why the Auger spectra in Figure 4.7 are measured with Al K_α radiation). Therefore, some spectra with different excitation sources will be compared throughout this work.

5 Impact of PDT temperature on optoelectronic properties of CIGSe solar cells: NaF PDT versus KF PDT

The electrical effects of alkali metals as dopants in CIGSe thin-film solar cells depends on the amount of alkalis incorporated in the CIGSe layer. To study this coherence, cell and layer properties, in literature, are often displayed as a function of the alkali concentration within the CIGSe layer. Following this manner, the inherent assumption is that all samples are prepared under the exact same process conditions and only differ in their alkali concentration.

This assumption, however, is not true, since equal alkali concentrations in two different CIGSe layers do not necessarily result from two equal PDT processes. For example, the same alkali concentrations can result from a PDT either at high T_{PDT} and short PDT process duration, or from a low T_{PDT} and a long process duration. Certainly, the chemical reactions at the CIGSe surface will be different in these both cases, due to the different thermal activation energies. Hence, the alkali concentration itself does not reflect the “full information“ about the CIGSe layer, and examining the cell properties in dependence on alkali concentration can be misleading. Therefore, the PDT process duration and the AlkF-rate (as well as the Se-rate) is kept constant, and only T_{PDT} is varied, as T_{PDT} mainly affects surface reactions, and the diffusion on alkali metals.

The here presented electrical properties of NaF- and KF PDT cells as a function of T_{PDT} in Chapter 5 will therefore serve as a rough, but solid basis for more detailed examinations in Chapters 6 and 7.

5.1 Cell parameters after NaF PDT or KF PDT as a function of PDT Temperature

The solar cell power conversion efficiencies (PCEs) in dependence on T_{PDT} are depicted in Figure 5.1.1. Untreated, alkali-free cells are taken as a reference, and show PCEs around 10%. Upon treatment of alkali-free absorbers with a NaF PDT, the PCEs rise monotonously with T_{PDT} and reach 16.3 % at T_{PDT} = 315 °C. In contrast, for KF PDTs a big drop in PCE for T_{PDT} < 150 °C is observed, resulting in cells with even lower PCEs than the alkali-free reference. At T_{PDT} > 150 °C the PCEs of the KF PDT cells increase and reach up to 15 % at T_{PDT} = 330 °C. Generally, at T_{PDT} > 150 °C both PDTs create cells with higher PCEs than the reference sample. Comparing NaF and KF PDTs, at a given T_{PDT} a NaF PDT results in cells with equal or higher PCEs than a KF PDT. The drop in PCE for KF PDT cells is no coincidence and was easily reproducible.

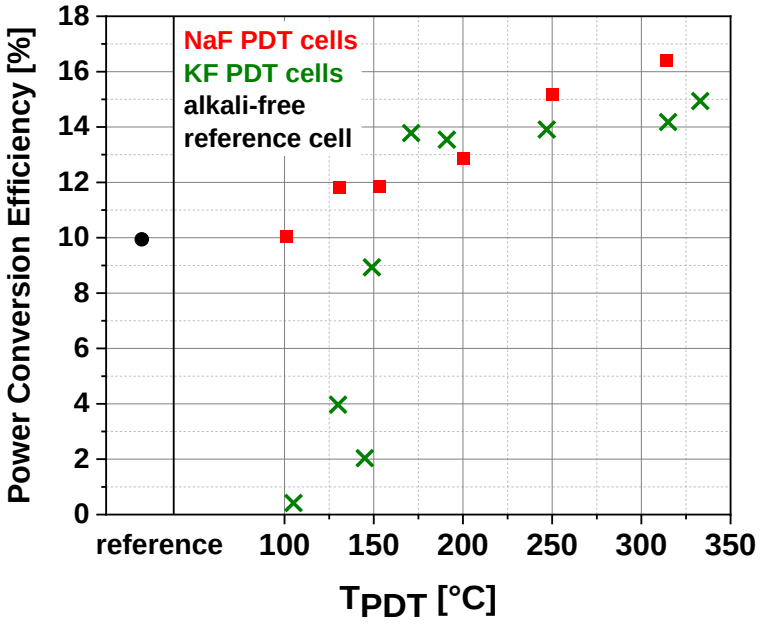

Figure 5.1.1 Power conversion efficiency (PCE) of the CIGSe solar cells after a NaF (red) or KF (green) PDT as a function substrate temperature during the PDT (T_{PDT}). The values are given as mean values of up to eight cells per sample, without the inclusion of shunted cells.

Despite this interesting observation, no report in literature about the influence of T_{PDT} in case of KF PDTs exists, so far. To have a closer look at the device characteristics of the resulting solar cells, the open-circuit voltage (V_{OC}) and fill factor (FF) are shown as a function of T_{PDT} in Figure 5.1.2. Generally, the dependencies of V_{OC} and FF on T_{PDT} resemble those of the PCEs on T_{PDT}: Cells with a NaF PDT show a monotonous rise in V_{OC} and FF with increasing T_{PDT}. At T_{PDT} = 315 °C NaF PDT cells show 79% FF and 675 mV V_{OC}. For a KF PDT at comparable T_{PDT} or higher, the resulting V_{OC} and FF are lower. Equal to the dependence of the PCE on T_{PDT}, a huge drop in V_{OC} and FF at T_{PDT} < 150 °C is observed in case of a KF PDT, leading to lower values for V_{OC} and FF than for the reference cell. Moreover, for T_{PDT} > 150 °C after KF PDT, the resulting V_{OC} does not rise steadily with rising T_{PDT}, but rather decreases slightly. It is speculated that this observation has no physical origin, but is due to statistical variance. For the dependence of the short circuit current density (j_{SC}) on T_{PDT} for NaF PDT or KF PDT cells no clear trend is being found. The only remarkable observation (not shown) was a drop in j_{SC} at T_{PDT} < 150 °C for KF PDT cells. This is very unusual for the electrical effects of alkali metals in CIGSe thin films because most studies only report an effect on V_{OC} and FF, rather than on

j_{SC} [5,31]. Therefore, the strong drop in j_{SC} for low KF PDT temperatures is conspicuous and worth exploring.

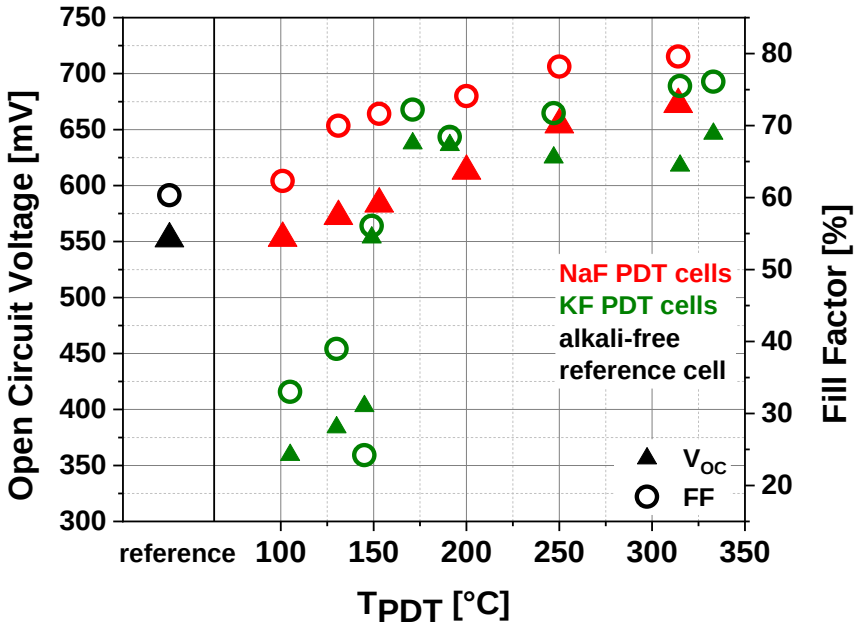

Figure 5.1.2 Open circuit voltage (V_{OC}, triangles, left ordinate) and fill factor (FF, open circles, right ordinate) of the CIGSe solar cells after a NaF PDT (red symbols) or KF PDT (green symbols), as a function of T_{PDT}. The values are given as mean values of up to eight cells per sample, without the inclusion of shunted cells.

To generally explain the rise in V_{OC} and FF with increasing T_{PDT}, the amount of alkali within the CIGSe has to be taken into account. As will be shown in Chapter 5.2, the resulting alkali concentration within the CIGSe layer will rise with increasing T_{PDT}. A higher alkali concentration will increase the charge carrier density (N_A), which will result in a rise in V_{OC} [70]. Besides, it is known that Na and K electrically passivate defects at grain boundaries and inside the grain of the CIGSe layer. Upon passivation, charge carriers then would not be trapped and their mobility μ would increase. By increasing μ, the charge carrier recombination is believed to be decreased and the electrical conductivity of the CIGSe layer is increased. This should lead to an improved V_{OC} and FF, respectively [48,71].

Closing the first section, the attention will be shifted from a very general dependence that of device performance on T_{PDT}, to a more distinct correlation, which obviously is of great importance, too: The dependence of the resulting alkali concentration and, subsequently, the generated charge carrier density, on T_{PDT}.

5.2 Charge carrier density as function of T_{PDT} and alkali concentration: NaF PDT versus KF PDT

Different T_{PDT} lead to different amounts of incorporated alkali metals within the CIGSe layer as shown in Figure 5.2.1. The alkali concentration was determined with the help of ToF-SIMS measurements and details can be looked up in Chapter 4.2 of this work.

Reference cells, which underwent no PDT, contain no alkali metals and their alkali concentration is lower than 1 ppm, since this is the detection limit of our ToF-SIMS setup. Nevertheless, small traces (< 1 ppm) of alkali metals could be existent within the CIGSe layer of the reference cells due to cross-contamination from some parts of the deposition chamber. However, it is speculated that these low alkali concentrations have no impact on the electrical properties.

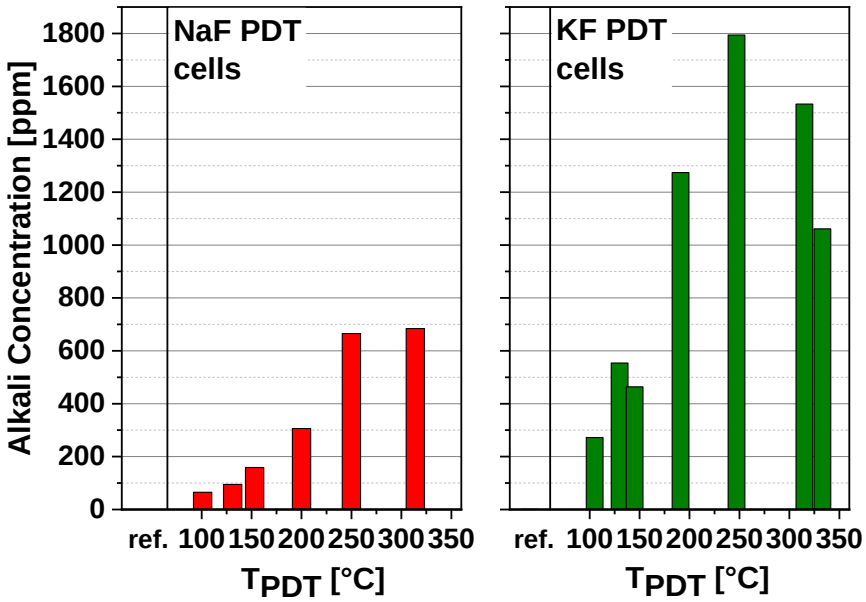

Figure 5.2.1 Na (left, red) and K (right, green) concentration within the CIGSe layers, derived from ToF-SIMS measurements, as a function of the corresponding substrate temperature during PDT (T_{PDT}).

For NaF PDTs a rise in T_{PDT} leads to a monotonous increase in Na concentration within the CIGSe layer. The increase is but non-linear and seems to reach a plateau from T_{PDT} = 250 °C on. At T_{PDT} = 315°C a Na concentration of 700 ppm can be found.

For KF PDTs the dependence of K concentration on T_{PDT} is non-monotonous. At T_{PDT} = 250 °C a maximum K concentration of 1800 ppm is found within the CIGSe layer, which then decreases for KF PDTs at higher T_{PDT}, leading to a K concentration of ~1100 ppm at T_{PDT} = 330 °C. The existence of a maximum K concentration could be explained by a partial desorption of K (e.g., as KF or K_2Se) at elevated T_{PDT}: Less K is available at the CIGSe surface and subsequently the amount of incorporated K might be lower.

For comparable T_{PDT}, the resulting K concentrations are always higher than the resulting Na concentrations within the CIGSe layer. This can be explained with the difference in lattice energy for NaF and KF. 920 kJ/mol of energy is needed to break a NaF lattice, whereas for KF only 816 kJ/mol are needed [72]. Consequently, less energy is needed to break the bonds in KF so that more K^+ is available to diffuse into the CIGSe layer.

At this point it is important to mention that the diffusion and incorporation of alkali metal fluorides in the CIGSe layer are complex processes, which are not clarified yet. Different

molecular steps, like thermalization of KF clusters on the CIGSe surface, diffusion along steps or terraces, physisorption or chemisorption at distinct sites and dissociation into K^+- and F^- ions have to be taken into account; all of them with a distinct dependence on temperature. Additionally, Se is evaporated synchronously onto the CIGSe surface, so that the existing reactions get more complex. Although the base pressure of the deposition chamber is better than 2×10^{-9} mbar, the pressure during the PDT is two orders of magnitude higher ($p \sim 2 \times 10^{-7}$ mbar) and the gas pressure directly above the CIGSe surface, during PDT, is believed to be even higher, e.g., in the order of 10^{-5} mbar. With such a high spatial density of particles, the CIGSe surface might be directly covered with the reactants and the proceeding chemical reactions on this surface get very difficult to examine and to explain.

Studies on adsorption and diffusion of alkali fluorides on some surfaces do exist, but can only minorly contribute to a better understanding of the PDT, mainly because of the missing comparability: Different, than in most surface science studies, the CIGSe surface is polycrystalline and therefore not well-defined. Moreover, as stated above, the particle densities during PDT can be several orders of magnitude higher than in common molecular beam epitaxy experiments.

Nevertheless, a thorough analysis of some of these special surface- “complications“ will be presented in Chapter 6 and 7. For now, these issues will be neglected and the focus kept more on CIGSe bulk-related properties.

An electrical consequence of doping with alkali metals in CIGSe layers is the generation of new charge carriers. To examine this effect, one will analyze how the resulting charge carrier densities N_A vary with T_{PDT}. It must be mentioned that the values for N_A are extracted from capacitance-voltage measurements (C-V). Because C-V measurements are difficult to evaluate, for a first glance the estimated N_A values are compared, and afterwards closer attention is paid the entire C-V results. The extracted N_A values are displayed as a function of T_{PDT} in Figure 5.2.2.

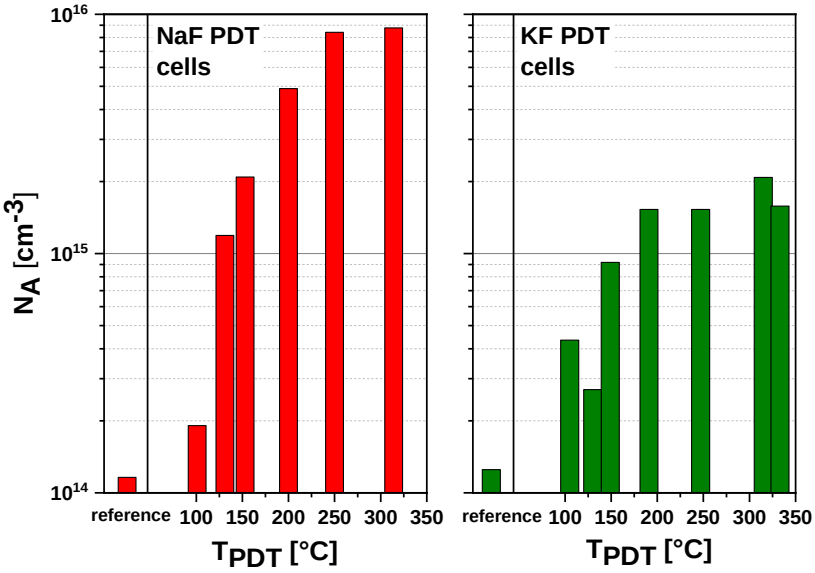

Figure 5.2.2 Charge carrier densities (N_A) after a NaF PDT (red, left) and KF PDT (right, green) as a function of the corresponding PDT substrate temperature T_{PDT}, extracted from CV measurements.

The alkali-free reference cell shows a $N_A = 1.2 \times 10^{14}$ cm^{-3}, which is created by intrinsic doping of the highly compensated CIGSe material with a high concentration of copper vacancies. Upon rise of T_{PDT} the N_A starts to rise. For Na, this rise in N_A with T_{PDT} is monotonous and at

the highest T_{PDT} = 315 °C a charge carrier density $N_A = 8.8 \times 10^{15}$ cm^{-3} is created. For K, the rise in N_A with T_{PDT} exhibits a slight maximum again, where at T_{PDT} = 315 °C, a $N_A = 2 \times 10^{15}$ cm^{-3} is created. At nearly all given T_{PDT} examined in this work, the introduction of Na leads to a higher N_A than with K. The only exception from this trend is visible at T_{PDT} ~ 105 °C, where the N_A after KF PDT is higher than after NaF PDT. Further specifics concerning the low T_{PDT} sample(s) will be discussed in the following.

Now that a rough trend in N_A has been observed with T_{PDT} between NaF and KF PDT cells, the entire C-V measurement will be analyzed, which yields additional information about the width of the space charge within the CIGSe layer. Figure 5.2.3 shows the determined relation between N_A and the width of the space charge region (SCW) for NaF and KF PDT cells.

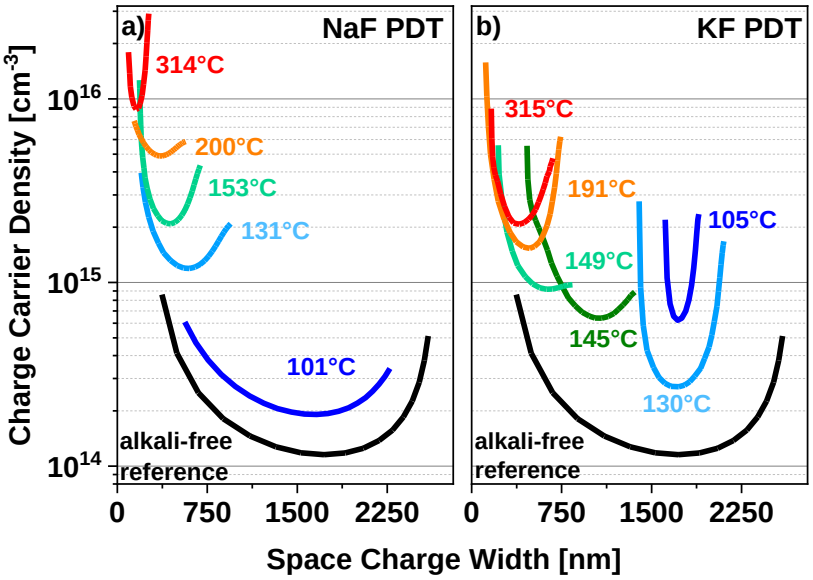

Figure 5.2.3 Relation between the charge carrier density N_A and width of the space charge region SCW in the CIGSe layer of a) NaF- and b) KF-treated CIGSe solar cell devices.

C-V measurements are a well-established technique to analyze charge carrier densities in semiconductor materials [73,74]. To evaluate the data, the solar cell is modeled as a capacitor in parallel-plate geometry. Further, it is assumed in this model that one side of the capacitor is highly n-doped, which could correspond to the window layers in the CIGSe cell (CdS/i-ZnO/ZnO:Al). The other side of the capacitor is relatively lowly p-doped, which could correspond to the CIGSe layer. The width of the space charge region, which forms at the p/n-junction in the real cell, is varied by application of a dc bias. Thereby, the space charge region is predominantly extending into the CIGSe layer. At the same time, the capacity C of the solar cell is measured. C is then a function of the width of the space charge region (SCW) and the charge carrier density N_A in the CIGSe layers. Following this model, N_A and SCW depend on the applied dc bias and the measured capacity C and are estimated with Eq.8 and Eq.9:

$$N_A = -\frac{C^3}{q\,\varepsilon\,A^2\,(\frac{dC}{dV})} \qquad \text{(Eq.8)}$$

$$SCW = A\,\frac{\varepsilon}{C} \qquad \text{(Eq.9)}$$

This model is called the Mott-Schottky model, which assumes a uniformly doped space charge region and the absence of a significant density of states, which are located “deeper” within the bandgap [55,75]. Here, q is the elementary charge, ε the dielectric constant of CIGSe, and A

the area of the cell. The resulting values for N_A for each sample are shown as a function of SCW in Figure Figure 5.2.3 5.2.3.

In the case of thin-film solar cells, the N_A-SCW curves oftentimes show a U-shape [76,77]. Unfortunately, this U-shape is affected by metastable states and other defects, which are not included in this model. Because the minimum of the U-shape is least impacted by these defects, these points are used to estimate the N_A- and SCW-values of our samples.

Figure 5.2.3 shows that with increasing T_{PDT}, the N_A increase and SCW decrease for both, the NaF PDT and KF PDT. This coherence between N_A and SCW can be explained with the fact that charge carrier neutralization is needed at the p/n-junction. The depletion of charge carriers in the p- and n-field must be balanced, so that the resulting internal electric fields compensate each other. If the doping densities of CIGSe and CdS layers are different (which is assumed to be true), different sized regions of the material will be charge carrier depleted. In our case, like it is stated above, most of this depletion region will extend into the CIGSe layer.

For the same cause it can be explained why the u-shaped curves become broader at lower N_A: To create an internal electric field which can account for the applied bias voltage, more charge carriers in the CIGSe layer must be depleted, so that the variation of SCW with bias voltage increases (and therefore the broadness of the u-shaped curve).

Exceptions from the general trend between N_A and SCW with T_{PDT} can be found for the low T_{PDT} 105 and 130 °C KF cells. Despite these samples show N_A higher than for the alkali-free reference cell and the u-shaped curves are narrower, the corresponding SCWs are larger than expected. What is furthermore striking, is that the N_A of the 105 °C KF PDT cell is higher than that of the 130 °C KF PDT cell, but still shows the widest space charge region. With SCW ~ 1800 nm, it is possible that the space charge region of the KF PDT 105 °C sample is extending throughout the cell all the way to the back contact.

These “deviations“ from the trend might be ascribed to metastable effects or other defects, not included in the Mott-Schottky model. One drastic possibility could be a deterioration of the p/n-junction. The theoretical background of most capacitance spectroscopy models demands a well-established p/n-junction and a pronounced diode behavior of the examined cells. Something within the 130°C and 105 °C KF PDT cells seems to change this diode behavior. At this point, the need not only for an electrical but also chemical-structural characterization of the p/n-junction becomes evident.

Comparing NaF and KF PDT cells, one finds that the N_A after NaF PDT is considerably higher than after a KF PDT (e.g., by a factor of 5 at T_{PDT} ~315 °C). With regard that the Na concentration within the CIGSe layer is less than the K concentration for all T_{PDT} (see Figure 5.2.1) it is concluded that Na is more “doping efficient“ than K. To better illustrate this finding, the charge carrier density N_A is plotted against the alkali concentration within the CIGSe layer in Figure 5.2.4.

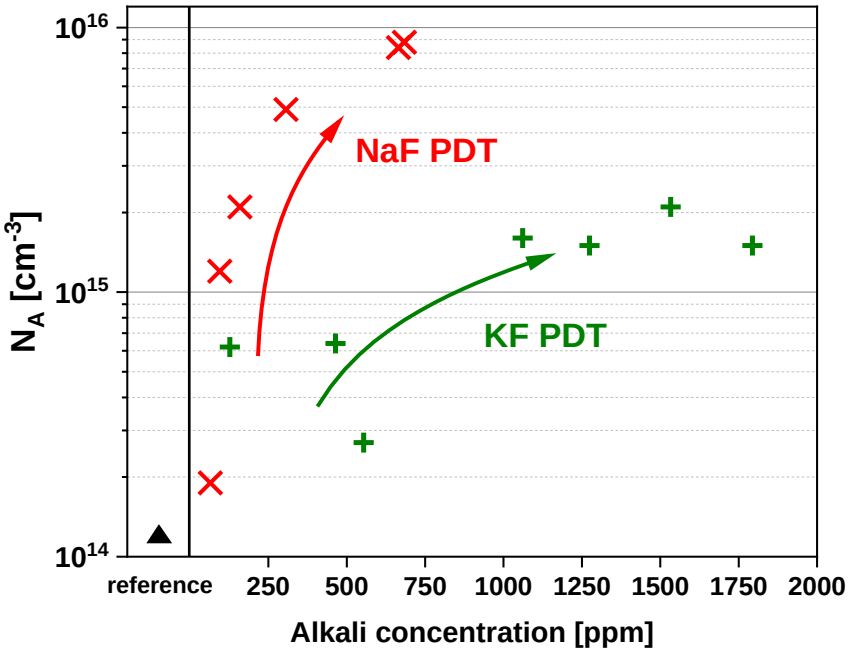

Figure 5.2.4 Charge carrier density N_A, derived from C-V measurements as a function of the alkaliconcentration within the CIGSe layer shown for NaF PDT cells (red) and KF PDT cells (green). The charge carrier density of the reference cell is depicted as a black triangle.

The charge carrier density in NaF PDT cells (red) increases with the Na concentration up to nearly 10^{16} cm^{-3} at a Na concentration of ~750 ppm. For KF PDT cells (green), the charge carrier density also rises with K concentration, but does not exceed ~ 2×10^{15} cm^{-3} at K concentrations around 1500 ppm (which is twice of the maximum Na concentration). Thereby, even with a lower Na concentration in a NaF PDT cell (compared to the K concentration in a KF PDT cell), a higher charge carrier density is achieved with a NaF PDT, than with a KF PDT.

This result was also reported before and can be explained with a model by Yuan et al. [78]: During PDT Na ions diffuse into the CIGSe layer and repel Cu ions from their lattice site. Upon this, Na_{Cu} substitutional defects are formed. The formation of these defects is believed to critically depend on temperature. By cooling down the sample after PDT, Na_{Cu} defects might “decompose“, and Na ions will leave the copper sites. In that way, additional copper vacancy sites (V_{Cu}) are generated, which formally could be classified as electron “holes“. This increased hole concentration contributes to N_A of the CIGSe layer. To explain the differences in resulting N_A between NaF and KF PDT samples, one has to take into account the different formation energies to create Na_{Cu} or K_{Cu}. Formation energies were calculated [39] and are 1.6 eV for K_{Cu} and 0.4 eV for Na_{Cu}. Therefore, the concentration of Na_{Cu} substitutional defects can be higher. Following thereof, the V_{Cu} and hole concentration after a NaF PDT would be higher than after a KF PDT and so N_A.

To conclude our comparison of the electrical properties due to NaF and KF PDTs, the most significant differences are briefly summarized:

- NaF PDTs at all (here examined) T_{PDT} lead to an improvement of PCE, as compared to the alkali-free reference cell

- KF PDTs also lead to an improvement of the PCE, but for T_{PDT} < 150 °C a huge drop in PCE was observed, leading to a massive deterioration of the cell

- Comparable T_{PDT} lead to higher K concentrations in a KF PDT, than Na concentrations in a NaF PDT

- Comparable T_{PDT} lead to higher N_A in case of a NaF PDT than for a KF PDT and therefore Na is more doping efficient than K

- Electrical properties for KF PDT cells with $T_{PDT} < 150$ °C deviate considerably from their behavior at $T_{PDT} > 150$ °C

Summing up, for KF PDT cells the variation of electrical properties with T_{PDT} are less steadily than for NaF PDT cells. To obtain some more insights about these peculiarities, now one will focus on KF PDT cells and have a look at the j-V curves and quantum efficiency measurements. Therewith, additional information about shunt resistances, electron transport barriers and charge carrier collection can be estimated. The following Chapter 5.3 will address these measurements.

5.3 Peculiarities of IV- and EQE-behaviors after KF PDT at low T_{PDT}

Depicted in Figure 5.3.1 are the current-density-voltage (j-V) curves for solar cell devices, resulting from KF PDTs at different T_{PDT}. Solar cells with the highest PCE of 15 % (red) result from a KF PDT at T_{PDT} = 333 °C. The shape of the respective j-V curve resembles that of an ideal diode. The black and green j-V curves look very similar; they correspond to the 149 °C KF PDT sample and the reference sample, which is alkali-free. By comparing the green and black curve with the red one, it can be recognized that a reduction in T_{PDT} leads to lower V_{OC} and FF.

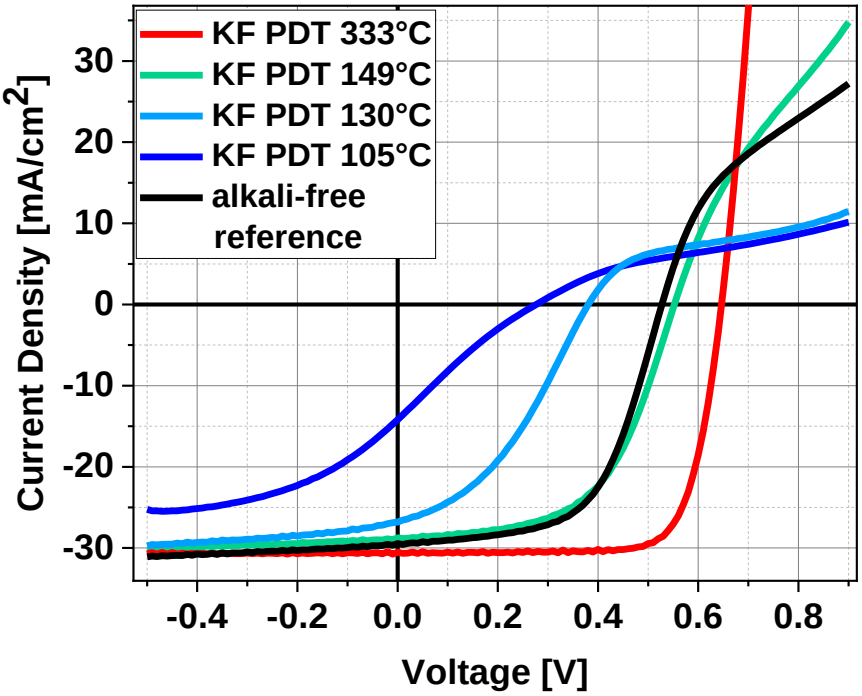

Figure 5.3.1 Current-density-voltage curves under illumination of an alkali-free reference (black curve) and KF PDT cells with different T_{PDT} (as listed in the legend).

At a bias voltage of 0.6 V and higher, the current of the diode starts to differ from the expected exponential increase, which results in lower current densities. This “downward bending“ of the j-V curve is called “roll over“ and is interpreted as a saturation-like behavior of the current. It can be explained with an electrical barrier, which is located at the back contact and acts as a “second diode“ (in the equivalent circuit diagram), which is directed in reverse [76].

For the low T_{PDT} cells at 130 and 105 °C a significant decrease in both, the V_{OC} and j_{SC} is observed. For these samples, all cell parameters are lower than for the reference cell. Remarkably for the 105 °C KF PDT cell, the photocurrent starts to drop quite “early“ at bias voltages around −0.4 V, which causes a low j_{SC}. The resulting j-V curve deviates significantly from ideal diode behavior and shows a so-called “kink“ at ca. −0.2 to +0.2 V. This kind of anomaly is typically related to an electrical barrier at the absorber/buffer interface [79].

Overall, it is surprising, how the different T_{PDT} can change the shape of the j-V curves. Until now it is anticipated that alkali metals only affect V_{OC} and FF of the CIGSe solar cell. The reported impacts on j_{SC}, however, are only minor so far. It is concluded that for T_{PDT} < 150 °C additional electron barriers might arise, which drastically change the diode behavior. Because of these strong deviations, it can be concluded that the p/n-junction in the low T_{PDT} KF PDT cells must be detrimentally affected.

J-V measurements reveal information about the integral current, which is collected by the solar cell. To qualitatively analyze the wavelength-dependent absorption of incident light into the CIGSe layer, and subsequent charge carrier generation and collection, external quantum efficiency measurements (EQE) are applied. The EQE is the ratio of the number of electron-hole pairs generated to the number of photons incident on the solar cell.

With EQE measurements one gains insight into the origins of current losses inside the cell [80]. Current loss can stem from optical reasons like reflection at internal interfaces or from absorption by the window layers. Additional electrical losses are also possible, which stem from charge carrier recombination. Because of the wavelength-dependent penetration depths of the incident light into the CIGSe layer, one can roughly locate the origin of the current loss.

EQE curves from the corresponding KF PDT cells (see Figure 5.3.1Figure 5.3.1) are shown in Figure 5.3.2.

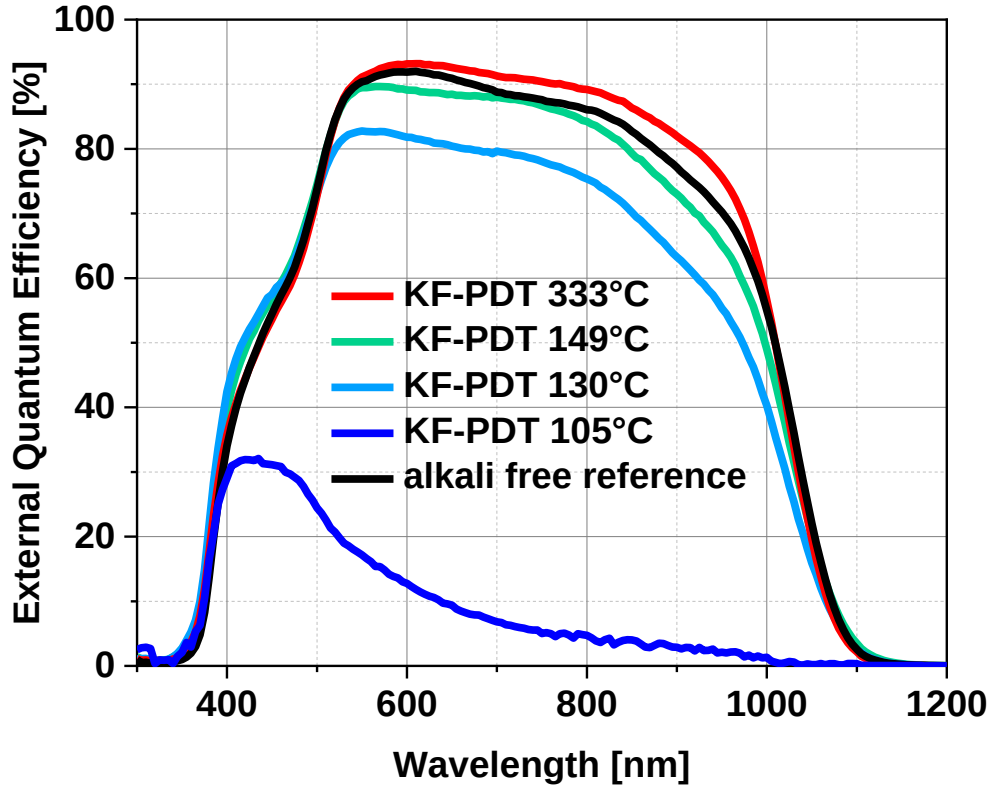

Figure 5.3.2 External quantum efficiency (EQE) curves of an alkali-free reference (black curve) and KF PDT cells with different T_{PDT} (as listed in the legend). The EQE was measured under white bias light.

The KF PDT cell at T_{PDT} = 333 °C (red) shows the highest EQE at nearly all wavelengths and therefore generates the highest j_{SC} = 30.4 mA/cm^2. Compared to the reference cell (black curve), the EQE of the KF PDT 333 °C sample is slightly higher in a wide wavelength regime between ~550 nm and 1000 nm. This increase of the EQE of the KF PDT 333 °C sample, compared to the reference sample, can be due to a higher number of passivated defects and therefore a higher charge carrier density. The comparison of the EQE of the reference cell to the EQE of KF PDT cells at T_{PDT} < 150 °C, however, shows an opposed trend:

For T_{PDT} < 150 °C (green and light blue), the EQE decreases in the range between ~520 nm and 1000 nm (including a slight increase in ultra-violet (UV) absorption range between ~380 nm and 480 nm), and the EQEs are lower, than for the reference cell. For the KF PDT cell prepared at T_{PDT} = 105 °C (dark blue) the EQE is severely decreased over the entire

wavelength regime. Only a narrow span of the incident light in the UV regime is still absorbed and contributes to the cell current.

The interpretation of these two opposed observations is rather complex: On one hand, the KF PDT is beneficial for the cell and improves the charge carrier collection (as observed for the KF PDT 333 °C sample), on the other hand, however, the KF PDT is detrimental for the cell and deteriorates the charge carrier collection (as observed for the KF PDT samples with T_{PDT} < 150 °C).

One reason for these observations could be that alkali metals somehow evolve detrimental electrical effects at low T_{PDT} in the CIGSe layer. However, taking our previous results into account (Chapter 5.1 and 5.2), this reason seems unlikely.

Another reason could be that the decreased EQE might not depend specifically on alkali metals as dopants but on a more global property of the solar cell: the quality of the p/n-junction. The following arguments will try to give a possible explanation:

The increased UV-absorption (in CIGSe) for the KF PDT 130 °C and 149 °C samples in the regime between 380 nm and 480 nm could indicate a different (e.g., thinner) CdS layer, since less UV light is being absorbed by CdS. This should be reasonable, since CdS deposited on CIGSe in most cases has an optical band gap of ~2.4 eV, [81] which corresponds to a wavelength of 516 nm. Thus, light with a wavelength of ~516 nm or shorter will be absorbed (partially) by the CdS layer. Therefore, one can conclude that a different CdS layer has formed on the KF PDT 130 °C and 149 °C sample. With a different CdS layer in turn, a different interface to the CIGSe layer and therefore, a different p/n-junction might be created in case of T_{PDT} < 150 °C. If (e.g.) the doping density of the resulting CdS layer is too low, an only weakly pronounced type inversion at the CdS/CIGSe interface will result. Consequently, the internal electric field inside the CIGSe layer will be very weak. This weak electric field can explain the poor charge carrier collection throughout the whole depth of the CIGSe layer. This low collection efficiency (i.e., the ineffective transport of generated charge carriers to the p/n-junction) finally leads to a decrease of EQE over the whole wavelength spectrum. For the sample at T_{PDT} = 105 °C the charge carrier collection within the CIGSe layer is so inefficient that only those electron hole pairs are collected, which are generated near the p/n-junction. Therefore, only a weak EQE ~ 30 % is measured in the UV-regime, which corresponds to photons, which are absorbed mainly in the front part of the CIGSe layer. Overall, a weak internal electric field due to a different (possibly worse) p/n-junction and the resulting weak charge carrier collection are only one possible reason for the j_{SC} drop at T_{PDT} < 150 °C. Other causes, such as a high defect density in the CIGSe layer or high transport barriers at the front or back contact interfaces are possible reasons, as well.

Nonetheless, it is concluded that at low T_{PDT} KF PDT, a different CdS layer (e.g. a thinner one) is observed, than for the high T_{PDT} KF PDT. Because the CdS layer is grown on the surface of the underlying CIGSe layer, the CIGSe surface itself must be the reason for the different CdS growths. Therefore, one has to ask for the differences of the CIGSe surface formed after a KF PDT at T_{PDT} < 150 °C.

To check, if the KF PDT at 105°C only damages the surface or also the bulk of the CIGS layer, a KCN etching step was used as a different surface treatment in comparison to the rinse with Na_2S. An etching of the CIGSe surface with an aqueous KCN solution is known to remove copper selenides as well as surface oxides from the surface [82] and thereby to “clean” the surface. In Figure 5.3.3 J-V curves of KF PDT 105 °C CIGSe solar cells are compared, which were treated with either the KCN etching step (w/w = 9%, t = 3min) or with the standard Na_2S rinsing step. For a better comparison the J-V curves, an untreated sample with standard Na_2S rinsing step is also included in Figure 5.3.3 as a reference cell.

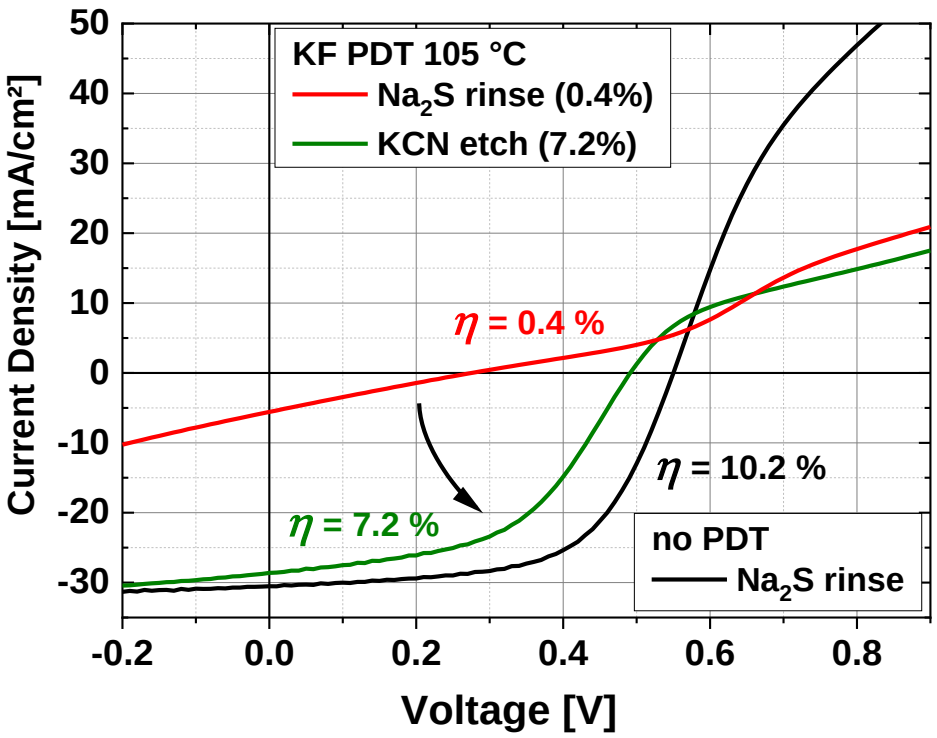

Figure 5.3.3 J-V curves of samples after a KF PDT at 105 °C after a standard rinsing with Na_2S solution (red curve) and after an etching with KCN solution (green curve) in comparison to the J-V curve of a reference sample without PDT (black curve).

The cell efficiency recovers from 0.4 % for the Na_2S rinsed KF PDT 105 °C sample (red) to 7.2 % for the KCN etched KF PDT 105 °C sample (green). The KCN etching leads to a strong increase of all cell parameters when compared to the Na_2S rinsed sample. The comparison of the J-V curve for the KCN etched KF PDT 105 °C sample (green) to that of the untreated reference sample (black) shows that the cell parameters have recovered strongly, but not completely. This experiment has revealed that a KF PDT at low temperature (e.g., at T_{PDT} = 105 °C) has a strong, detrimental impact on the surface of the CIGSe layer.

Consequently, the electronic properties of a CIGSe surface at high and low T_{PDT} KF PDT will be analyzed and compared with the corresponding NaF PDT samples. Therewith, ultraviolet photoelectron spectroscopy (UPS) measurements will be presented in the next chapter.

5.4 Changes of the valence band structure at the CIGSe surface due to AlkF PDTs

To determine the effect of the PDTs on the electronic structure of the CIGSe surface, five CIGSe surfaces were subjected to UPS measurements after the rinsing step: The untreated reference sample, two KF and two NaF PDT samples, in each case at T_{PDT} = 315 and 105 °C. The resulting spectra are shown in Figure 5.4.1. To determine the position of the valence band maximum (VBM) with respect to the Fermi Level (E_F), a linear extrapolation was drawn (red) for the leading edges for each spectrum [83,84].

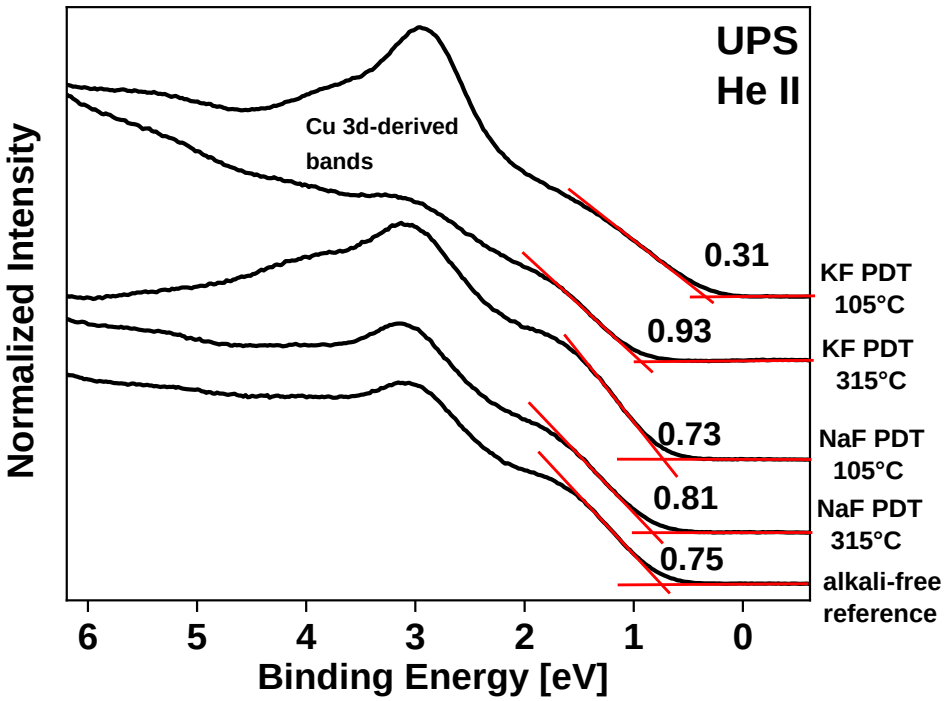

Figure 5.4.1 He II-excited UPS spectra of the rinsed CIGSe reference and four absorbers after NaF PDT (315 °C), NaF PDT (105 °C), KF PDT (315 °C), and KF PDT (105 °C), respectively. The binding energy is given with respect to the Fermi energy of an Au foil reference (not shown). Linear extrapolations of the leading edge are drawn for the determination of the valence band maxima (VBM). VBM values are given in eV.

The VBM for the NaF PDT (315 °C), NaF PDT (105 °C), KF PDT (315 °C), KF PDT (105 °C) and the alkali-free reference surfaces are determined to 0.81, 0.73, 0.93, 0.31, and 0.75 eV (± 0.10 eV), respectively. For both NaF PDT surfaces and the high T_{PDT} KF PDT surface, a downshift of the VBM (i.e., away from the Fermi level) is observed, related to the VBM of the alkali-free CIGSe surface.

For the two high T_{PDT} KF and NaF PDT surfaces, one observes a decrease in intensity for the Cu 3d-derived bands at ~3 eV, relative to the untreated CIGSe surface. In contrast, for both low T_{PDT} KF and NaF PDT surfaces one observes an increase in intensity for the Cu 3d-derived bands at ~3 eV. A number of other studies [8,85–87] observed a downward shift of the VBM after PDT as well and postulate that this shift leads to a decreased interface recombination of charge carriers and hence improved device performance.

The low-temperature KF PDT leads to an upward-shift of the VBM by −0.44 eV, resulting in an energetical distance between VBM and E_F of 0.31 eV. This small separation leads to a decreased band bending at the CIGSe surface. A decreased band bending in the absorber in

turn, can lead to enhanced charge carrier recombination at the buffer/absorber interface. Together with the finding that the spectral weight for Cu-related bands is strongly increased in the low-temperature KF PDT sample, it is suggested that a new Cu-containing phase has formed on the CIGSe surface.

A comparable observation was reported by Mezher et al., in which a KF PDT at lower T_{PDT} was applied: PCE decreases down to 2.8 % were observed, together with a Cu-enriched surface and a small separation between VBM and E_F of ca. 0.4 eV [88]. Contrary, the “low“ T_{PDT} was about 325 °C and good cells resulted from a similar KF PDT just at T_{PDT} ~ 333 °C. One ponders that it seems unlikely that 8 K in T_{PDT} difference are able to produce such different CIGSe surfaces. Nevertheless, the surface properties resemble each other and the resulting PCEs both are very low.

Concluding the UPS measurement, it has been observed that the CIGSe surface, electronically, is drastically altered after a KF PDT at low T_{PDT}. Some hints in our data and literature do also point out that there´s more a chemical transformation that has occurred upon PDT on the CIGSe surface.

Closing Chapter 5, distinct impacts of a NaF or KF PDT at different T_{PDT} on CIGSe solar cells and surfaces have been observed. It has been realized that Na is more doping efficient than K, and that the dependence of cell properties after a NaF PDT with T_{PDT} behaves more like it is expected, by means of electrical effects. For KF PDT cells, a kind of discontinuity in cell properties with T_{PDT} arises, and aside from electrical effects of alkali metals, significant chemical changes, specifically at the CIGSe surface, emerge during PDT. To further address this issue, a thorough chemical analysis of the CIGSe surface in dependence of PDT and T_{PDT} has to be established and will be presented in the next chapter.

6 Chemical reactions at the CIGSe surface during AlkF PDT

Besides the electrical effects of a NaF and KF PDT on the complete CIGSe layer, the CIGSe surface is also changed significantly. Depending on process parameters like T_{PDT}, these resulting chemical changes have a major contribution on device performance. To elucidate these changes and explain the difference between a NaF and KF PDT, XPS as a non-destructive, surface-sensitive technique is employed on the samples

A multitude of XPS-studies exist, studying CIGSe surfaces after different PDTs or rinsing treatments. Most of these studies are performed on multistage coevaporated CIGSe and Na-containing SLG substrates. Multistage CIGSe samples, however, show a different surface morphology than the single-stage CIGSe samples of this work. Moreover, Na from the SLG substrate diffuses through the CIGSe layer and segregates at the surface, also leading to a change of the chemical composition of the surface. Therefore, the CIGSe composition at the surface and further it`s chemical reactivity differs vastly between single stage and multi-stage samples. Therefore, single stage CIGSe layers serve as a less complex material system than multi-stage CIGSe layers, because they exhibit no compositional gradients. Like it was mentioned in the introduction, this simplification of the material system will help, to analyze and understand the impact of the PDT more easily.

XPS studies about PDTs on alkali-free grown CIGSe surfaces are also reported, for example [89]. Like in most cases, however, PDT and rinsing are done in a different procedure and sometimes in a different order. Accordingly, spectroscopic studies about PDTs on alkali-free CIGSe layer can be found in literature but their comparability to the here examined samples is rather low.

The work in hand therefore examines the chemical effects of a PDT, especially on alkali-free, single stage grown CIGSe samples, including the special rinsing treatment proved at ZSW.

Section 6 is structured as follows: In Chapter 6.1 the as-grown PDT samples are analyzed, as they are directly prepared after the PDT. Next, Sub-Chapter 6.1.1 will characterize the chemical composition of the no PDT CIGSe surface, and Sub-Chapter 6.1.2 will deal with the CIGSe-related core level signals and discuss possible secondary species. Chapter 6.1.3 will characterize non-CIGSe related elements and afterwards in Chapter 6.1.4, relative changes of the CIGSe stoichiometry are evaluated. At the end, in Chapter 6.1.5 the thickness of the adsorbate layer is estimated and in Chapter 6.1.6 the spatial distribution of the PDT reactants within the surface region is evaluated.

Chapter 6.2 finally will deal with the impact of the subsequent processing step on the PDT surfaces, the rinsing treatment.

6.1 Chemical reaction products formed on CIGSe surfaces by AlkF PDTs ("as-grown" samples)

6.1.1 Chemical constitution of CIGSe surfaces before AlkF PDTs (the reference sample without PDT)

To give an overview of the constituents of the untreated CIGSe surface, survey spectra are shown in Figure 6.1.1.1. An Ar^+-ion-cleaning treatment was applied to remove surface adsorbates and thus increases the intensity of the CIGSe signals. Additionally, information about adsorbate-induced band bending at the surface can be investigated.

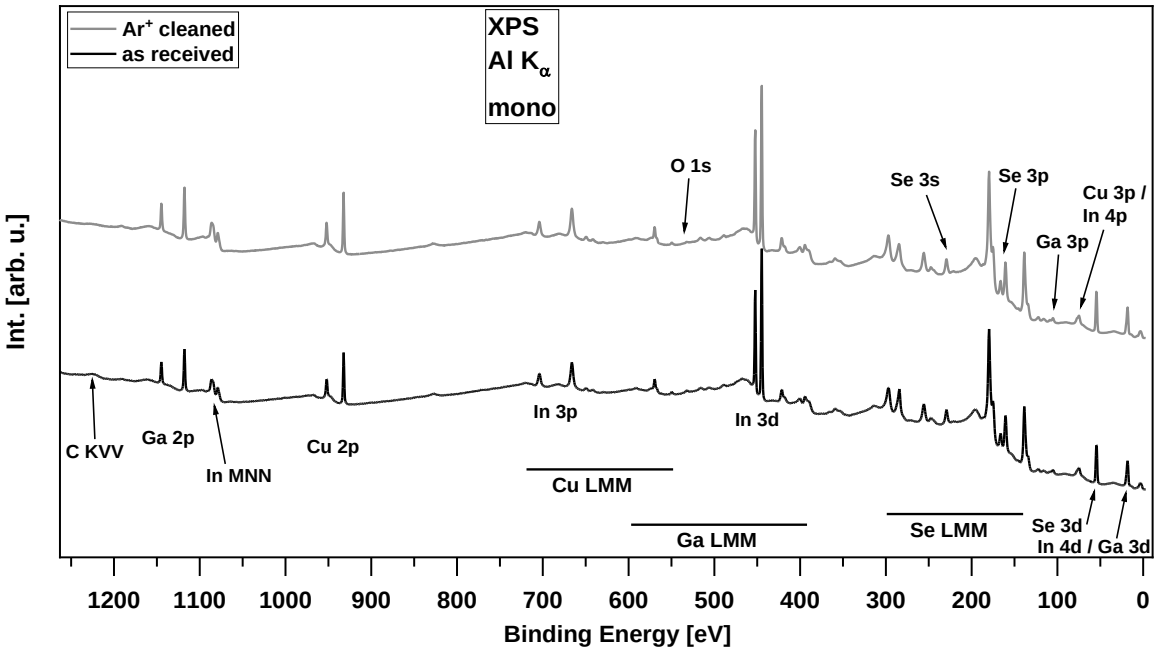

Figure 6.1.1.1 Al K_α excited XPS survey spectra of the no PDT CIGSe absorber surfaces as-grown (black) and after an Ar^+-ion-cleaning of the surface (gray). All prominent photoemission and Auger lines are labeled.

For the as-received CIGSe absorber surface, all expected photoemission and Auger signals (from the absorber) are observed in high intensity, including small surface contaminants of O. Since sample packing and transfer were elaborately planned and accomplished, a vanishingly small O 1s signal can be detected. Compared to other XPS studies on CIGSe, such low O 1s intensities are notable.

Upon Ar^+-ion cleaning of the as-grown CIGSe surface, C- and O-related signals decrease (not visible in the survey spectrum), whereas all CIGSe-related signal increase in intensity. The relative increase in intensity is most distinct for the Ga 2p line. Therefore, C and O should mainly exist at the CIGSe surface, loosely bound to the surface, possibly as remnants of H_2O or as carbonates, hydroxides. Accurate identification of the chemical component is difficult because of the small signal intensities for O 1s and C 1s core levels. Moreover, the C 1s signal is overlapping energetically with the Se $L_3M_{3,4}M_{4,5}$ Auger line.

The composition of the Ar^+-ion cleaned, untreated CIGSe surface was estimated by analysis of the Cu 3p/ In 4p, Se3d, and In 4d/ Ga 3d peak intensities. These photoelectron lines all lie in a similar range of kinetic energy (1400 – 1480 eV) and therefore differences in the inelastic mean free paths and analyzer transmission function are small. With the peak-intensities of the

mentioned photoelectron lines and values for photoionization cross-sections [90], the chemical formula $Cu_{0.37}In_{1.29}Ga_{0.72}Se_2$ is calculated for the CIGSe surface composition. The CIGSe surface appears to be Cu-depleted and In+Ga-enriched as observed in most XPS studies [91,92] and strongly deviates from the bulk composition of $Cu_{0.9}In_{0.8}Ga_{0.3}Se_2$ as measured by X-ray fluorescence spectroscopy. This result seems unlikely, since charge neutrality is not given, when assuming Cu, In, Ga and Se in oxidation states of +I, +III, +III and –II, respectively.

6.1.2 Chemical constitution of CIGSe surfaces after AlkF PDTs

In the following, the impact of the NaF and KF PDTs at two T_{PDT} on the chemical structure of the CIGSe surface is analyzed. All shown spectra were taken from Ar^+-ion cleaned surfaces as these spectra have a slightly better signal-to-noise ratio (SNR) than the samples in an "as-received" condition. At first, to give an overview of the elements present on the CIGSe surface after the PDT, survey spectra of the samples directly after the PDT (from now on called "as-grown") are presented in Figure 6.1.2.1.

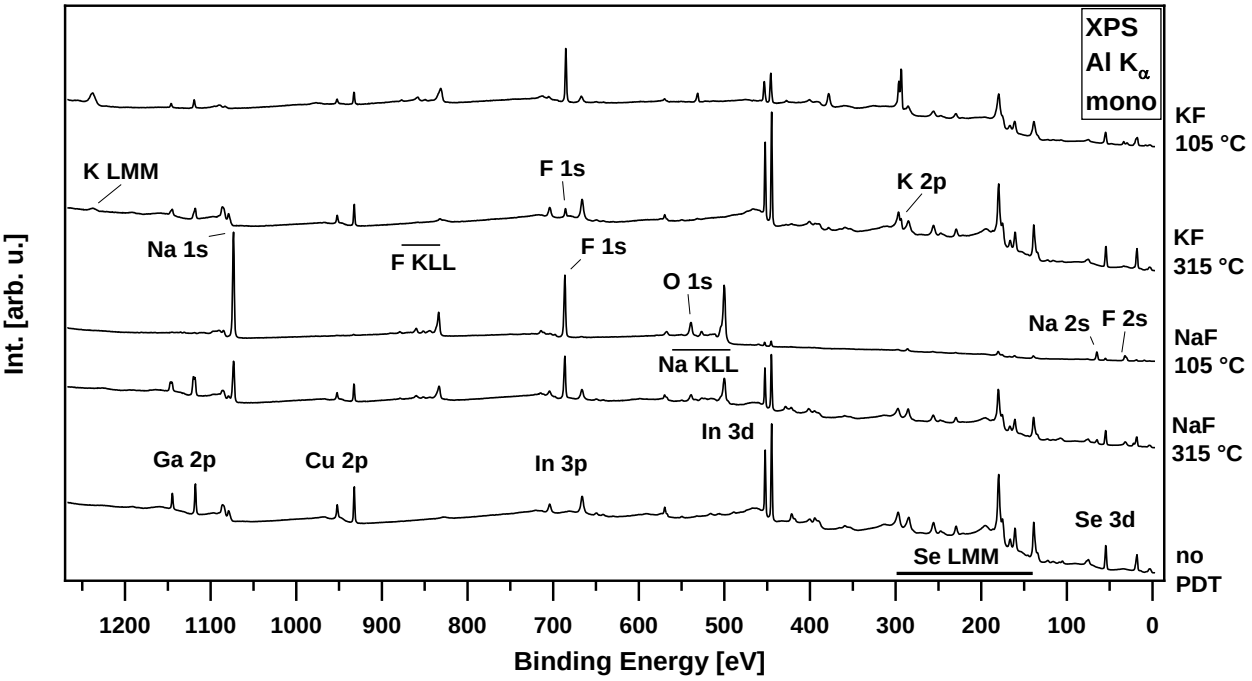

Figure 6.1.2.1 Al K_α XPS survey spectra of the CIGSe surfaces before and after different PDTs. Prominent photoemission and Auger signals are labeled.

In nearly all samples, all expected elements from absorber, PDT and common contaminants are observed. An exception is the NaF PDT 105 °C sample: No Ga- and Cu-related signals are visible. Depending on PDT and T_{PDT}, the absorber related signals are decreased and Na- or K- and F-related signals become visible.

For the NaF PDT 315 °C sample, all CIGSe photoelectron signals are decreased by approximately a factor of 2, compared to the untreated sample (no PDT). A strong F 1s and Na 1s signal emerged, with a peak height similar to that of In 3d. Furthermore, the O 1s signal increased in intensity, so that it now becomes visible in the survey spectrum. Like for all PDT samples presented herein, the CIGSe related peaks decrease (compared to the no PDT sample), so there must be attenuated, by adsorbates on top of the CIGSe surface. This adsorbate is composed of the alkali fluoride, which evaporated on the CIGSe surface during the PDT.

At lower T_{PDT}, the NaF-treated surface shows a stronger decrease in intensity for CIGSe related signals. The Ga 2p and Cu 2p signals are not visible anymore and the In 3d and Se 3d peaks are reduced in intensity by 5% of their initial intensity. Pronounced Na and F signals are observed with the highest intensity compared to the Na (or K) and F signals of all other PDT samples, together with a strong O 1s signal. Compared to NaF PDT 315 °C, the alkali fluoride cover layer is thicker (as will be shown in the following, see page 42 f.) and the resulting attenuation of the underlying CIGSe elements is more pronounced.

The KF PDT 315 °C survey spectrum shows all absorber signals together with K- and F related signals. Compared to the untreated surface, the intensity of Cu, Ga and Se has decreased, whereas the peak height for In 3d increased by ca. 25 %, compared to the untreated sample. This could be due to formation of a more In-rich surface region, possibly due to a depletion of other absorber elements, or a non-homogeneous coverage of the CIGSe surface with KF, leaving out In-terminated surfaces.

Similar to NaF, the KF PDT 105 °C surface shows an even weaker intensity for CIGSe-related signals and K and F related signals increase (compared to the KF PDT 315 °C sample). The attenuation of the signals is differently strong. These observations can be explained with a thicker cover layer (analogously to the NaF-treated sample), and a different composition of the KF PDT 105 °C surface, than the KF PDT 315 °C surface.

From this general view, the focus will now be on the analysis of the chemical components on the CIGSe surface in detail, starting with gallium, copper, indium, and then selenium.

Analysis of Ga-related photoelectron and Auger signals

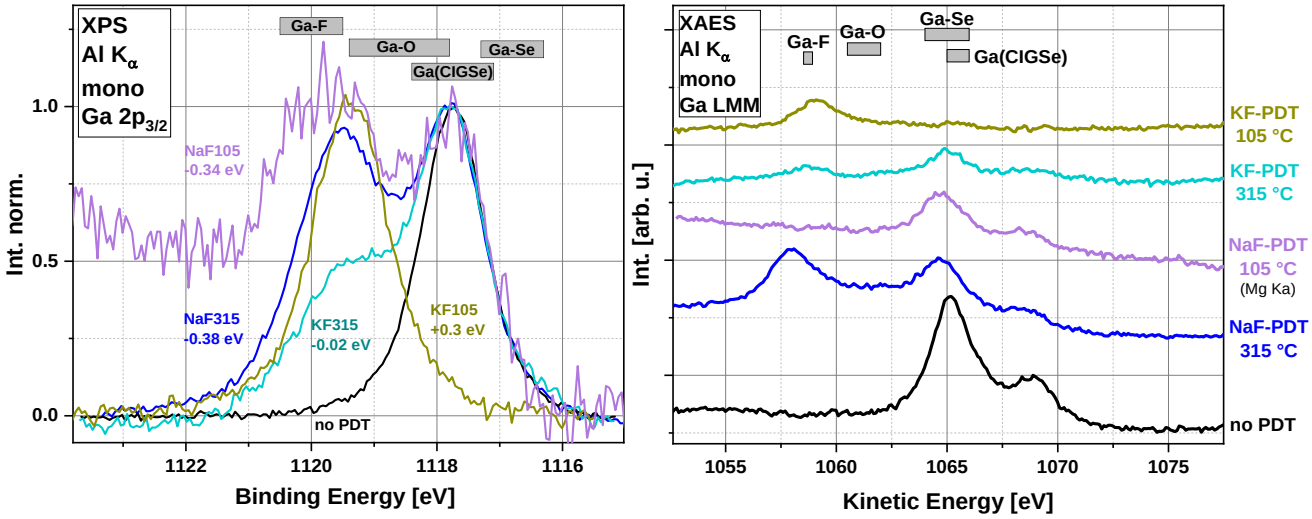

Figure 6.1.2.2 Ga $2p_{3/2}$ photoelectron spectra (left) and Ga LMM Auger spectra (right) for CIGSe samples, which underwent NaF or KF PDTs at different T_{PDT}. Ga $2p_{3/2}$ spectra are normalized by setting the low binding energy background at ~1115 eV to zero and the peak maximum to one. Additionally, the signals are shifted on the energy-axis to allow for a better comparison of the spectral shapes. Respective shifts are given in the diagram. Ga LMM spectra are displayed in absolute intensities. Note: All samples are excited by Al K_α radiation, except the Ga LMM Auger spectrum of the NaF PDT 105 °C sample, which is excited by Mg K_α radiation. Gray bars represent binding energy ranges of different Ga-bonds according from literature data.

In Figure 6.1.2.2, the shape of normalized Ga $2p_{3/2}$ signals is compared to identify additional Ga components. The Ga signal of the no PDT sample (black) is used as reference and this signal is assigned to Ga in a pure CIGSe environment when compared to literature data [92–94]. (From now on, and for the whole work in hand, Ga in a CIGSe-environment will be abbreviated as Ga(CIGSe)).

Additional Ga species located at higher binding energy arise for all PDT samples at E_{Bin} ~ 1119 – 1120 eV. The relative amount of secondary components to Ga(CIGSe) varies and ascends in the order KF PDT 315 °C < NaF PDT 315 °C ~ NaF PDT 105 °C < KF PDT 105 °C. For NaF PDT 105 °C, a lower SNR is observed, due to a thick NaF cover layer, as will be shown in Chapter 6.1.5. All signals can be fitted with two Voigt functions. The function at lower binding energy is kept constant in width and shape during the simultaneous fit and belongs to

Ga(CIGSe) and. The additional Ga-components are allowed to vary in width and shape, accounting for the possibly different chemical environments (compared to Ga(CIGSe)).

Comparing the positions of the additional Ga-components with literature data [94], suggests that mainly Ga-F bonds formed during the PDT, although Ga-O bonds lie within the same range of binding energy as the samples [94–97]. A look at the Ga Auger spectra will support these assumptions:

On all PDT samples, a signal at E_{Kin} ~1065 eV is visible, belonging to Ga(CIGSe). For some samples, however, an additional peak is observed at E_{Kin} ~ 1056 – 1059 eV, which could correspond to Ga-F bonds, clearly outside the range, where Ga-O bond can be expected. Since the Ga LMM Auger peaks are rather broad, additional Ga-O bonds, spectrally lying in between Ga(CIGSe) and Ga-F bonds, cannot fully be excluded. However, the relative amount with respect to Ga-F is very low.

Different from the Ga $2p_{3/2}$ spectrum of the NaF PDT 105 °C sample, no additional Ga species are observed in the corresponding Ga Auger spectrum, presumably because the Ga-F bonds are located at the very surface, as explained in Chapter 6.1.6, and the Ga LMM is less surface sensitive, than the Ga $2p_{3/2}$ signal.

Interestingly, the shape of the Ga LMM on the KF PDT 105 °C sample strongly deviates from that of the untreated sample, indicating a drastic chemical change for the KF PDT 105 °C sample.

To better analyze, which Ga-components formed during the PDT, and to subtract band bending effects, the Wagner plot of the modified Auger parameter α'_{Ga} is displayed in Figure 6.1.2.3.

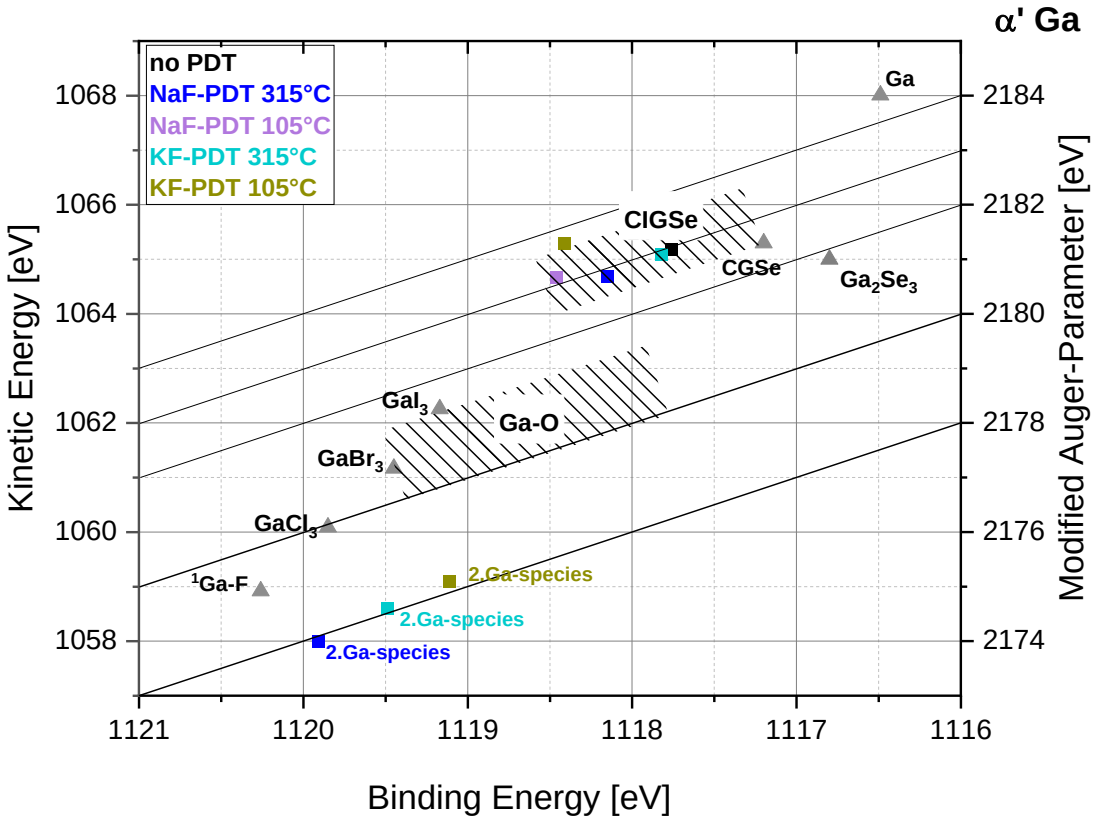

Figure 6.1.2.3 Wagner plot of the modified Auger parameter α'_{Ga} for the pristine CIGSe surface (black) and the differently treated PDT CIGSe surfaces. The shaded areas as well as the gray triangles show data points from literature for Ga in different bonding environments.

α'_{Ga} is calculated with $\alpha'_{Ga} = E_{Bin}(Ga\ 2p_{3/2}) + E_{Kin}(Ga\ LMM)$. The exact position of the Ga $2p_{3/2}$ signal was determined with Voigt fits and the position of the Ga LMM peak maximum was read from the spectra.

Two groups of chemical components are visible in the Wagner plot. The Ga species at α'_{Ga} ~ 2183 ± 0.7 eV belong to Ga(CIGSe), compared to literature values (α'_{Ga} ~ 2183.9 eV, (α'_{Ga} ~ 2182.3 eV). A deviation in α'_{Ga} is found for the KF PDT 105 °C sample: These Ga-atoms should still exist in a CIGSe-like environment, but the chemical situation of the Ga atoms has slightly changed on this surface. This could be due to changes in the coordination sphere of the Ga-atom, for example, it is bound to more fluorine atoms.

The second "group" of Ga-components is found at α'_{Ga} ~ 2178.0 ± 0.2 eV and is assigned to Ga-F bonds. Ga-O bonds can be excluded, since their α'_{Ga} values are ~2.5 eV higher. No literature values for Ga-F bonds were found, despite a speculation in the master thesis of A. Epprecht [94]. Compared with the data presented here, the kinetic energy of the Ga LMM are found in the same range from E_{Kin} ~ 1058 – 1059 eV, but the binding energy differs up to 1.5 eV. This difference is likely due to variations in the absorber growth and/or PDT process conditions. Thus, the Ga is surrounded by fluorine as well, but likely with more direct F bonding partners, so that the resulting α'_{Ga} becomes even lower than in case of A. Epprecht. Moreover, the α'_{Ga} values for Ga-F bonds follow the same trend as A. Epprecht's α'_{Ga} values in the row of Ga-halides: The stronger the electron affinity of the halogens, the lower the value for α'_{Ga}.

Analysis of Cu-related photoelectron and Auger signals

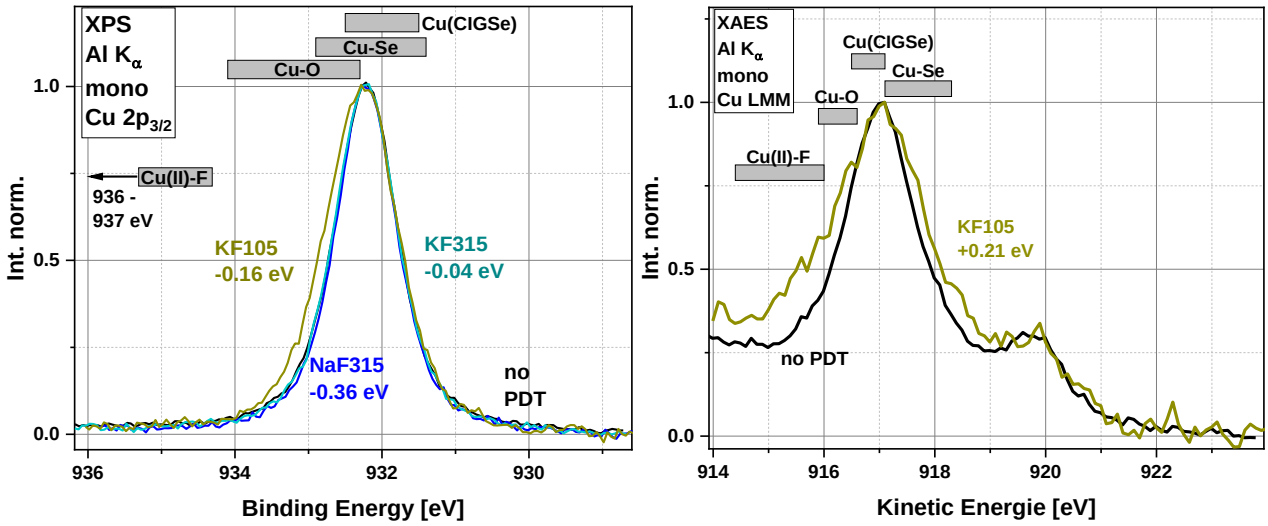

Figure 6.1.2.4 Cu $2p_{3/2}$ photoelectron spectra and Cu LMM Auger spectra for CIGSe samples, which underwent NaF or KF PDTs at different T_{PDT}. Cu $2p_{3/2}$ (Cu LMM) spectra are normalized by setting the low binding energy background at ~930 eV (high kinetic energy background at ~923 eV) to zero and the peak maximum to one. Additionally, the signals are shifted on the energy-axis to allow for a better comparison of the spectral shape. Respective shifts are given in the diagram. Gray bars represent binding energy ranges of different Ga-bonds according from literature data.

Figure 6.1.2.4 displays normalized Cu $2p_{3/2}$ spectra to identify additional Cu species. The peak shape of the no PDT sample represents Cu in a pure CIGSe environment, consisting of only one Cu species [92,94]. From now on, and for the whole work in hand, Cu in a CIGSe-environment will be abbreviated as Cu(CIGSe). The spectrum of NaF PDT 105 °C is omitted, due to the low SNR (similar to Ga $2p_{3/2}$). Nevertheless, the low SNR underlines that for the NaF PDT 105 °C sample a thick cover layer attenuated the CIGSe signals. Comparison of the

other Cu $2p_{3/2}$ peak shapes reveals that only for the KF PDT 105 °C sample an additional Cu-component has formed. This Cu-component is shifted to higher binding energies and indicates Cu-O bonds [98–100]. The same observation is made for the normalized Cu LMM signals: Only for the KF 105 °C sample, a deviation in Auger shape is observed as compared to the untreated sample. Additional intensity in Cu LMM at E_{Kin} ~915 – 916 eV could stem from a second Cu environment, e.g., Cu-O bonds.

For a better identification of the individual Cu components on the KF PDT 105 °C sample, the Cu LMM signal was fitted as shown in Figure 6.1.2.5.

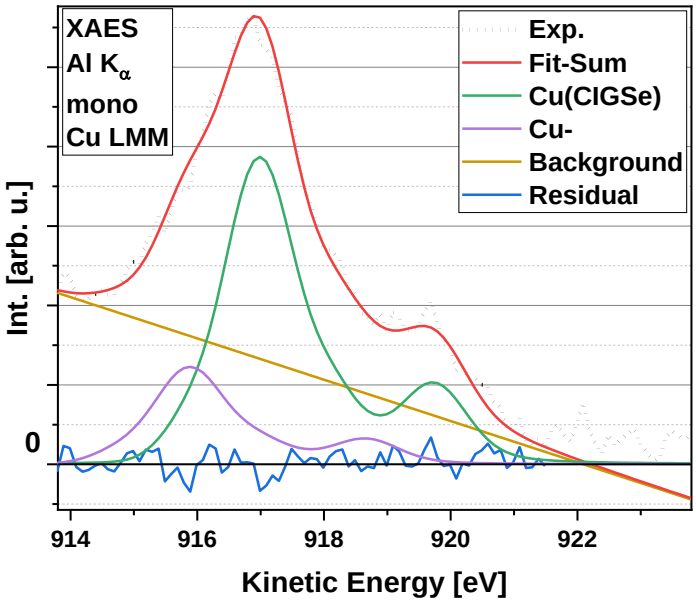

Figure 6.1.2.5 Cu LMM spectrum for the KF PDT 105 °C sample. The Cu LMM features is fitted by a sum of several shifted and scaled untreated Cu LMM spectra (green and pink). The differences between the measured points and the fitted lines are shown in the residuals. The different Cu species found are Cu in a CIGSe environment, labeled „Cu(CIGSe)“ and an additional Cu species labeled „Cu-“.

The no PDT Cu LMM was used as ”reference“ spectrum; two of those were independently scaled and shifted, and a linear background was used, to reproduce the Cu LMM Auger line of the KF PDT 105 °C sample (see Figure 6.1.2.5). Spectral broadening was not taken into account. The second Cu species (denoted as Cu- in the legend of Figure 6.1.2.5) is shifted ~1.5 eV to lower kinetic energy (pink). Together with the positions of the Cu $2p_{3/2}$ line, the modified Auger parameter is calculated and the respective data points are illustrated in the Wagner plot in Figure 6.1.2.6Figure 6.1.2.6 , together with some literature data for Cu-Se bonds [101,102].

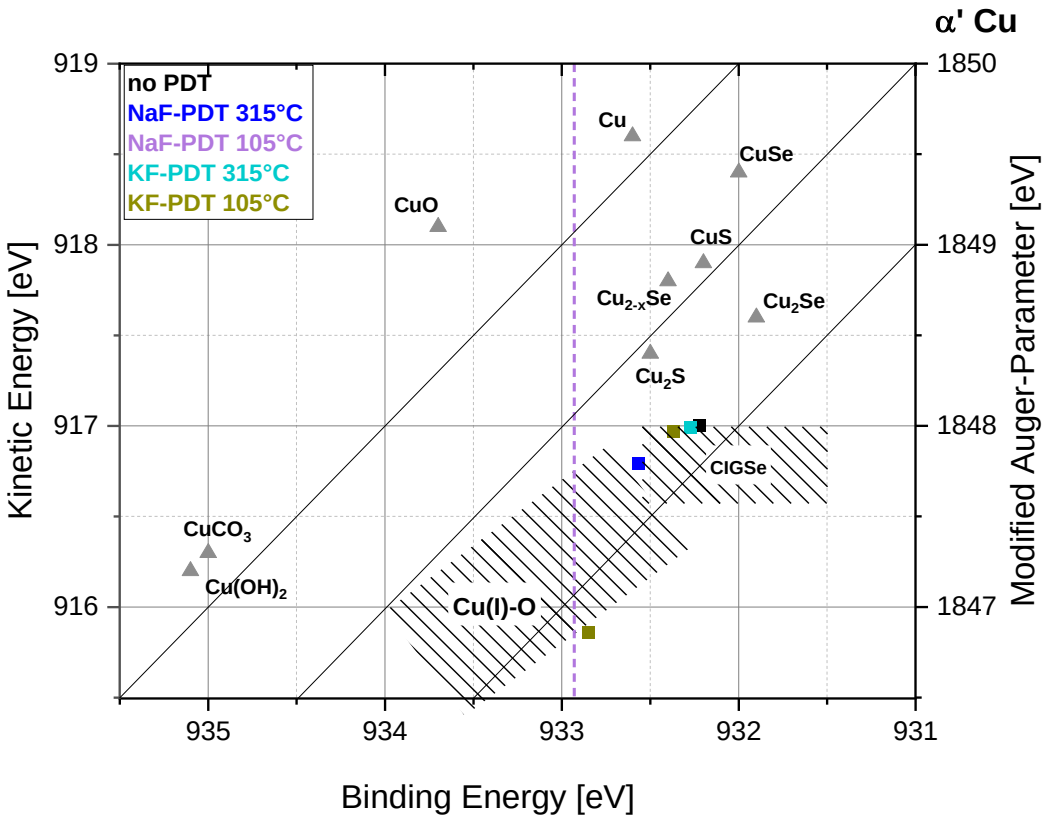

Figure 6.1.2.6 Wagner Plot of the modified Cu Auger parameter α'_{Cu} for the no PDT CIGSe surface (black) and the differently treated PDT CIGSe surfaces. The shaded areas include data points from literature given in the text. Gray triangles show data points from literature for Ga in different bonding environments. The two dark yellow points represent the two Cu species formed on the KF PDT 105 °C sample.

The data points for the Cu species on no PDT (black), NaF PDT 315 °C (dark blue), KF PDT 315 °C (light blue), and KF PDT 105 °C (dark yellow) all lie on the diagonal approximately for α'_{Cu} = 1849.3 ± 0.1 eV (diagonal not shown). A second data point (dark yellow) at E_{Bin} ~ 932.8 eV represents the additional Cu species on the KF PDT 105 °C sample.

At α'_{Cu} = 1849.3 ± 0.1 eV Cu(CIGSe) are found, which are similar to the Cu species from the no PDT sample (black) and lie within the area of literature values for CIGSe (hatched area).

The second Cu species for KF PDT 105 °C (dark yellow data point at E_{Bin} ~ 932.8 eV) shows a α'_{Cu} ~ 1848.7 eV and could be a Cu-oxide. Although the difference in α'_{Cu} is large (~0.6 eV), compared to α'_{Cu} of Cu(CIGSe), the value for KF PDT 105 °C coincides with the hatched area of Cu in a CIGSe environment. Thus, the partial formation of a Cu-Se-O species can be assumed.

Explicit formation of Cu-F bonds might be excluded, since Cu(I)-F components are believed to be thermodynamically instable and tend to disproportionate into Cu(0) and Cu(II) [103]. Cu(0) and Cu(II) but are not detected on the samples, and especially no Cu(II), since no Cu 2p shake up structure at higher binding energies is visible, which could indicate Cu(II) species [98,104–107].

For the NaF PDT 105 °C sample, the Cu LMM signal overlaps with the Na KLL Auger signal and due to a large Na amount on this sample no reliable value for the Cu LMM could be determined. Hence, only the position for Cu $2p_{3/2}$ is displayed as a dashed line (pink). No additional species was found for NaF PDT 105 °C in the Cu $2p_{3/2}$ spectrum. It is therefore speculated that this Cu species also belongs to Cu(CIGSe). The high binding energy of the

Cu 2p line might result from a strong band bending, possibly due to the large amounts of fluorine and/or sodium at the surface.

Analysis of In-related photoelectron and Auger signals

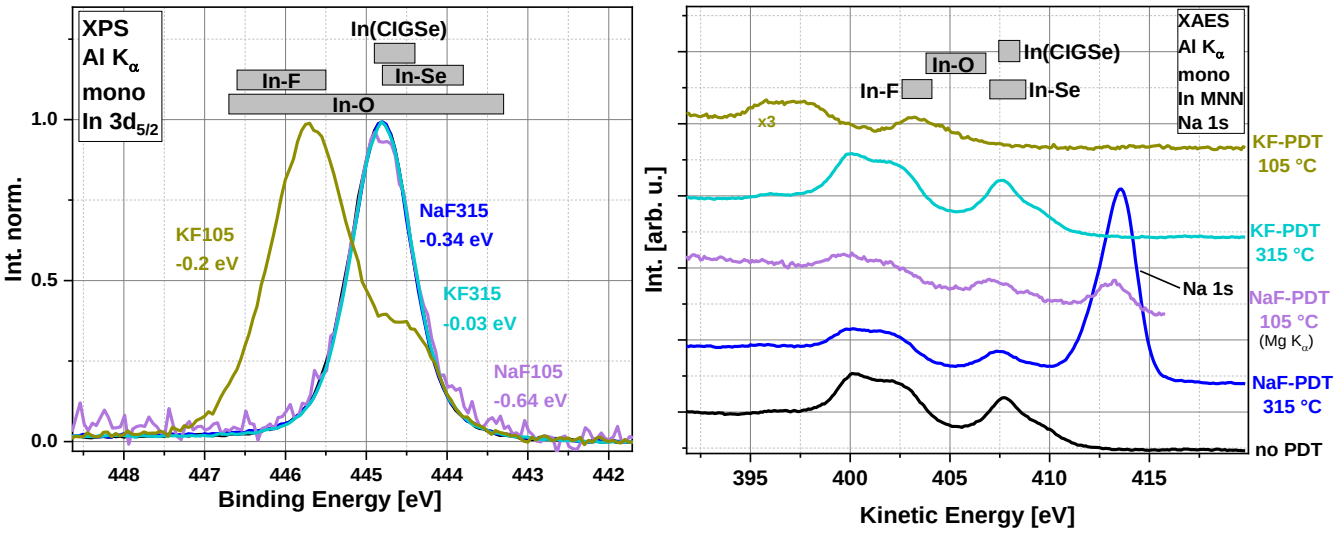

Figure 6.1.2.7 In $3d_{5/2}$ photoelectron and In MNN Auger spectra for CIGSe samples with different NaF or KF PDTs. In $3d_{5/2}$ spectra are normalized by setting the low binding energy background at ~442 eV to zero and the peak maximum to one. Additionally, the signals are shifted on the energy-axis to allow for a better comparison of the spectral shapes. Respective shifts are given in the diagram. In MNN Auger spectra are shown in absolute intensities. Note: All samples are excited with Al K_α radiation, except the In MNN Auger spectrum of the NaF PDT 105 °C sample, which is excited with Mg K_α radiation. Gray bars represent energy ranges of different In-bonds according from literature data.

The formation of different In species can be observed in the In $3d_{5/2}$ spectra in Figure 6.1.2.7: The In-components at E_{Bin}~444.8 eV all have the same shape and resemble In in the “no PDT“ absorber. Therefore, this In environment can be assigned to In in a CIGSe environment (from now on, and for the whole work in hand, In in a CIGSe-environment will be abbreviated as In(CIGSe)). [92,94].

The In $3d_{5/2}$ signal of the KF PDT 105 °C sample can only be reasonably fitted with three In-components. The three species appear at E_{Bin} ~ 444.7, 445.7 and 446.2 eV. Upon comparison with literature, these three In species can be ascribed to In(CIGSe), In-O and In-F, respectively [94,108,109],[47,48]. The ratio of In(CIGSe) : In-O : In-F is 1 : 2.4 : 1.5.

The In MNN Auger signal of the KF PDT 105 °C sample also deviates in its shape from the signal of the no PDT sample: On a closer inspection, a “flatter plateau” for the In $M_5N_{4,5}N_{4,5}$ feature at E_{Kin} ~ 396 – 398 eV is visible. Fitting the In MNN Auger with a superposition of reference In MNN spectra (like for Cu LMM) reveals the formation of two different In species at E_{Kin} ~ 404.6 and 403 eV. According to literature values, In-O species and In-F species lie in this range. The ratio of In-O : In-F is ~ 1 : 3. No In(CIGSe) Auger feature is detected at E_{Kin} ~ 407.5 eV, which can be explained by the lower surface sensitivity of In MNN Auger electrons compared to In $3d_{5/2}$ photoelectrons. This suggests that In-F only exist at the outermost surface of the KF PDT 105 °C sample, as will be discussed further in Chapter 6.1.6.

For a closer look at the high T_{PDT} samples, Figure 6.1.2.8Figure 6.1.2.8 shows the respective In MNN spectra, which have been normalized and shifted, to compare their spectral shapes.

The In MNN of KF PDT 315 °C and the untreated sample are very similar and show no difference in intensity, especially in the range about 405 eV ± 1 eV, where an “outgrowing“ of the valley-like structure would indicate In-O-bonds.

An analogous comparison of the NaF PDT 315 °C is difficult, since the intensity of the strong Na 1s signal increases the intensity of In MNN throughout the whole spectral range.

The comparison of the normalized In MNN spectra of the low T_{PDT} samples lead to no further insight. The SNR of both spectra was low and their backgrounds varied due to different excitation sources (non-monochromatized Mg K_α for NaF PDT 105 °C and monochromatized Al K_α for KF PDT 105 °C).

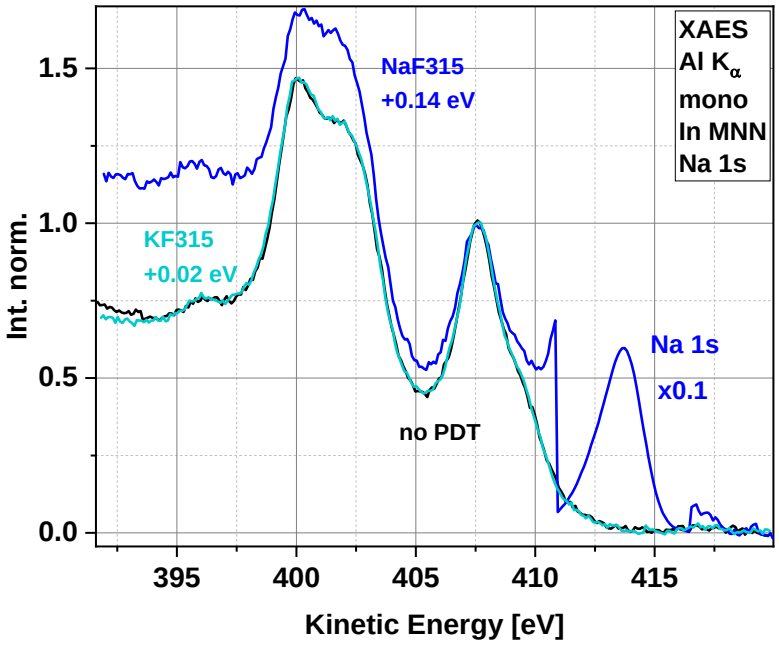

Figure 6.1.2.8 In MNN Auger spectra for high T_{PDT} NaF and KF PDT samples and the untreated „no PDT“ sample (black). The Auger spectra are normalized by setting the high kinetic energy background at ~418 eV to zero and the peak at ~407.5 eV to one. Additionally, the signals are shifted on the energy-axis to allow for a better comparison of the spectral shape. Respective shifts are given in the diagram.

The different In-environments found so far are In(CIGSe), In-O and In-F for the KF PDT 105 °C sample. For the other samples, In only appears in a CIGSe environment (In(CIGSe)).

It is speculated that, with these results, most of the present In-components are detected and only a few percent of additional In species are overlooked. To verify this assumption, one would have to fit the Auger signals, which was not done here.

Since the different In environments on the different samples are characterized, all data points are depicted in the Wagner plot for the modified Auger parameters α'_{In} in Figure 6.1.2.9.

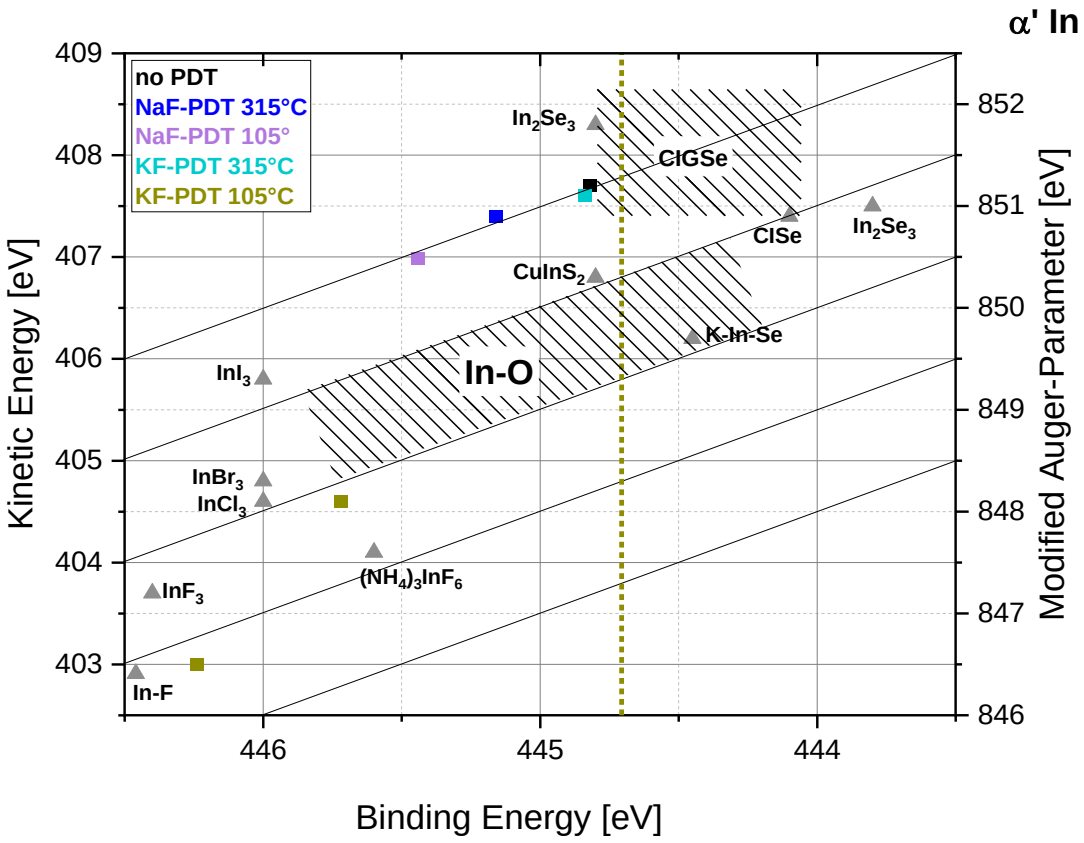

Figure 6.1.2.9 Wagner plot of the modified In Auger parameter α'_{In} for the pristine CIGSe surface (black) and the differently treated PDT CIGSe surfaces. For the KF PDT 105 °C sample, no In(CIGSe) contribution to the In MNN Signal was detected, therefore this species is marked as a dotted green line. Gray triangles show data points from literature for Ga in different bonding environments.

In the Wagner plot, the different In environments are illustrated. The modified Auger parameter for the In(CIGSe) species is α'_{In} = 852.5 ± 0.1 eV, which compares well with literature values. Small deviations show that the In environments on all samples must be very similar to each other by means of number, and type of binding partners. However, the difference in binding energy is nearly 0.9 eV. This points out that the overall chemical situation in turn is very different from sample to sample. The clearest example is the NaF PDT 105 °C surface, which is covered by NaF in largest amounts, as will be shown later. These high amounts of electron-pulling fluoride ions lead to an increase in binding energy for all surface constituents. It is speculated that these variations of alkali fluoride amount on the surfaces are the major reasons for the different surface induced band bending.

The position of the three In environments from the KF PDT 105 °C sample in the Wagner plot differ distinctly from each other. The first In species, which appears at E_{Bin} ~ 444.7 eV is assigned to In(CIGSe). This binding energy fits well to In(CIGSe) of the other samples and literature data, but no position Auger feature for In(CIGSe) could be detected.

The Auger parameter for the two other In species of the KF PDT 105 °C sample are in the region for In-O- and In-F environments. The In species at E_{Bin} ~ 445.7 eV lies in between reported regions for In-halides and $(NH_4)_3InF_6$, suggesting the formation of In-F. On the other hand, however, In-O bonds reported in literature also cover this region, and especially for In-F higher binding energies and a lower kinetic energy would be expected. Thus it seems that the In species at E_{Bin} ~ 445.7 eV is in an electron-pulling chemical environment, but not as pronounced as for the other In species at E_{Bin} ~ 446.2 eV. All in all, it is not possible to

determine the exact binding situation of the two In species, but it can be concluded that In-O and In-F bonds have formed on the KF PDT 105 °C sample.

Analysis of Se-related photoelectron and Auger signals

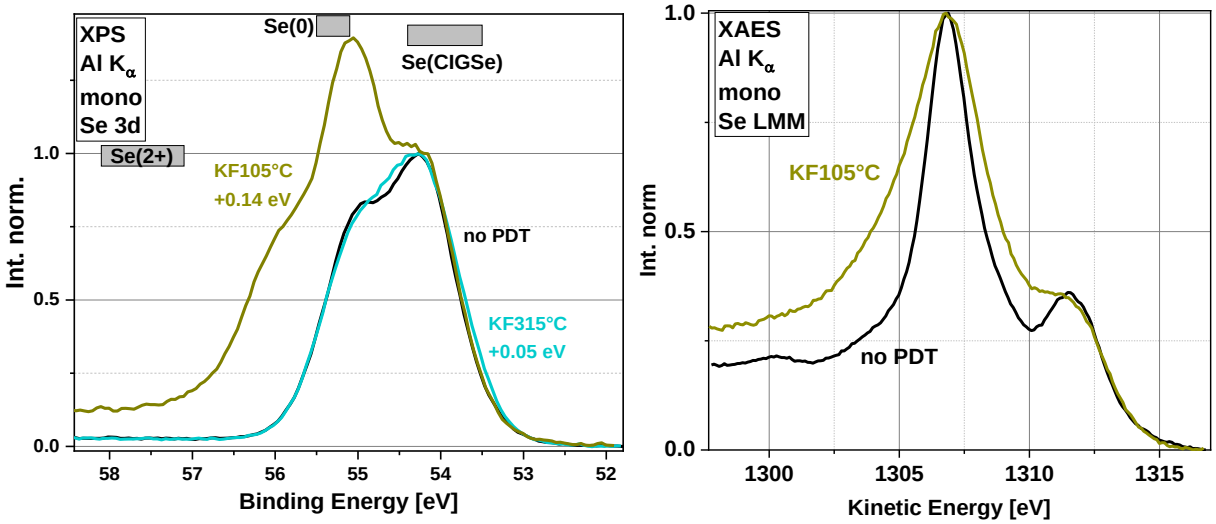

Figure 6.1.2.10 Al K_α excited Se 3d and Se LMM Auger spectra for an untreated sample „no PDT“ (black) and different NaF and KF PDT samples. The photoelectron (Auger) spectra are normalized to zero at the low binding energy background (high kinetic energy background) and to one at peak maximum (or E_{Bin} ~ 54.3 eV in case of Se 3d for the KF PDT 105 °C sample). For a better comparison of spectral shapes, the spectra are also shifted on the energy-axis. Respective shifts are given in the diagram. Gray bars represent binding energy ranges of different Se-bonds according from literature data.

The formation of different Se species can be determined with Figure 6.1.2.10. Distinct changes in peak shapes are observed for both, high and low T_{PDT} KF-treated samples. Again, it is assumed that the Se 3d signal of the untreated sample represents Se in a pure CIGSe environment. From now on, and for the whole work in hand, Se in a CIGSe-environment will be abbreviated as Se(CIGSe).

For the KF PDT 315 °C sample (light blue), additional intensity between Se $3d_{3/2}$ and Se $3d_{5/2}$ is observed and a “flatter“ shoulder at the low binding energy side of Se $3d_{5/2}$. This kind of broadening of the Se 3d peak shape can be reproduced by adding an additional Se species at E_{Bin} ~53.5 eV. This additional Se species, however, appears in very small amounts (4% relative to the main Se species), so that the certainty about its existence is rather low. For now, one will abstain from assuming the formation of an additional Se species on KF PDT 315 °C. A better reason for peak broadening could be an increase in peak width for Se $3d_{3/2}$ and Se $3d_{5/2}$, resulting from a not well-defined chemical Se environment. This seems reasonable, as Se plays a crucial role in the PDT process, as will be shown in Chapter 7.

The Se 3d signal of the KF PDT 105 °C sample (green) shows the typical envelop of two individual doublets, which results, when a Se $3d_{5/2}$ peak at higher binding energy overlaps with a Se $3d_{3/2}$ peak at lower binding energy. The fit with Voigt functions, however, was not very clear, since different peak widths and shapes were necessary, to obtain a modest result with two Se species. With some certainty it can be assumed that the two main components are located at E_{Bin} ~ 54.0 ± 0.3 and E_{Bin} ~ 55.0 ± 0.3 eV. Comparison with literature data indicates a possible existence of Se(CIGSe) [92,94] and elemental Se [60,110,111] at the surface.

An additional Se species on the KF PDT 105 °C sample is also detected in the Se LMM signal. The Auger signal is normalized and shifted for a better comparison with the untreated reference (black). The Auger signal of KF PDT 105 °C is broader than the “no PDT“ signal. The vanishing dip at E_{Kin} ~ 1310 eV and additional intensity at lower kinetic energy suggest existence of the additional Se species at lower kinetic energy. For an accurate determination of the position for the second Se species a fit of the Auger signal is needed. This fit did not yield very reliable results and therefore the error in the kinetic energy is 1 eV used in the following.

For the NaF PDT samples, no pronounced differences in peak shape compared to the untreated reference sample were found. The peak positions of the respective Se species are depicted in the Wagner plot for the modified Auger parameter α'_{Se} in Figure 6.1.2.11.

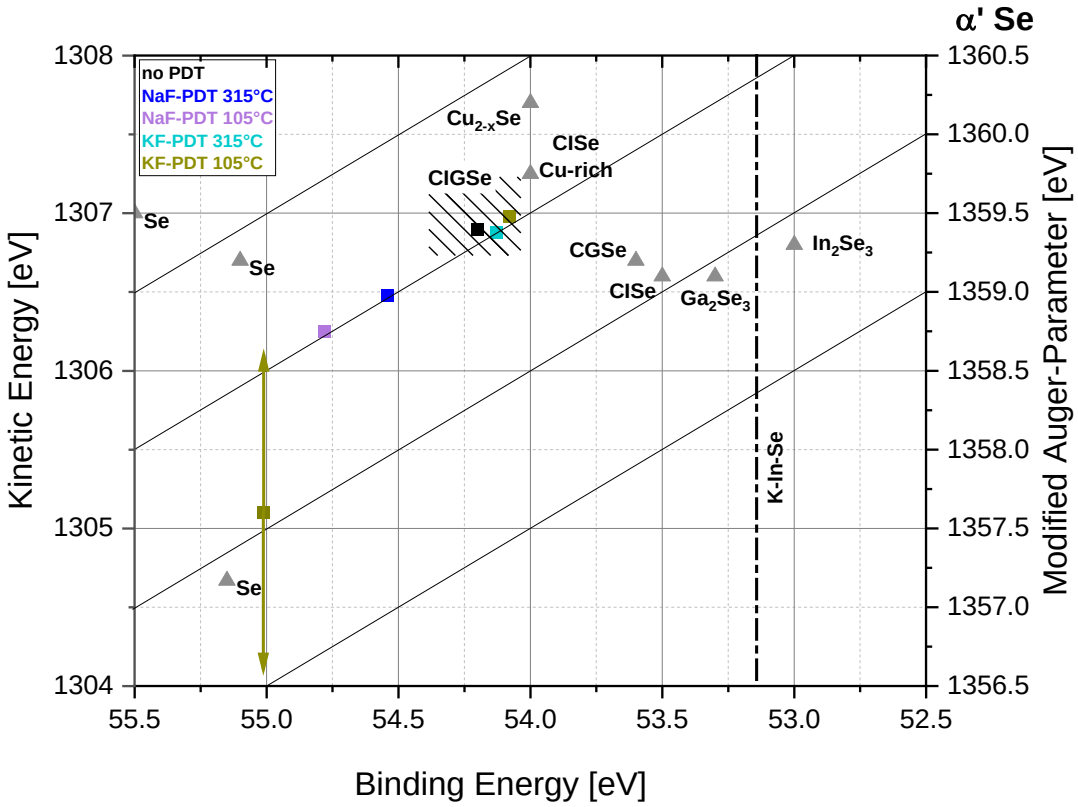

Figure 6.1.2.11 Wagner plot of the modified Se Auger parameter α'_{Se} for the pristine CIGSe surface (black) and the differently treated PDT CIGSe surfaces. Gray triangles show data points from literature for Ga in different bonding environments. The references are given in the text.

Two groups of Se species are visible in the Wagner plot. The Se species with α'_{Se} = 1361.0 ± 0.1 eV belong to Se(CIGSe) according to comparison with literature data and with the untreated reference sample (black). Again (like for In), shifts of the Se species for NaF PDTs to higher binding energies, up to ~ 0.7 eV are observed. A comparable shift was detected for In, and hence surface induced band bending is the likely reason for it. Therefore, both data points for NaF PDT 105 °C and NaF PDT 315 °C are far from Se(CIGSe) (hatched area) but might still be ascribed to the Se(CIGSe) species.

The second Se species on KF PDT 105 °C sample can likely be assigned to elemental Se. Although the value for the corresponding Se LMM position is not accurate, it is in accordance with other elemental Se literature values. Elemental Se could exist on an as-grown PDT CIGSe surface, since it is coevaporated together with KF during the PDT. As will be shown later, a KF layer, up to 4 nm thick, covers the CIGSe surface. This cover layer could contain the remaining, unreacted Se, which is then detected by XPS.

6.1.3 Non-CIGSe related elements after AlkF PDT on the CIGSe surface

To get a complete picture of the chemical environment on the CIGSe surfaces after PDT, the non-CIGSe related elements are analyzed as well. These are C, O, F, Na and K and they will be presented in the following.

Analysis of C-related photoelectron signals

The C 1s signal is overlapped by a strong Se $L_3M_{2,3}M_{4,5}$ signal. Identification of carbon components is therefore very difficult and was not done here. Nevertheless, C does exist on the samples and can partly be removed upon Ar^+-ion cleaning. The amount of carbon at the surface is estimated to be ≤ 5%.

Analysis of O-related photoelectron signals

Compared to other XPS studies, the O 1s signal on all PDT sample is very weak. For the high T_{PDT} NaF and KF samples, the intensity of O 1s signal is approximately equal and three times higher than for the untreated sample, respectively. The O 1s signal is very broad and still very small. Accurate identification becomes therefore very difficult, which is even complicated because many O-components fall within a narrow range in binding energy. For NaF PDT 315 °C a partial overlap of O 1s with Na $KL_1L_{2,3}$ Auger makes this condition even worse. Nonetheless, it is speculated about the formation of hydroxides, probably stemming from water molecules, which are bound to NaF or KF as crystal water, because of the high hygroscopicity of NaF and KF.

For the low T_{PDT} samples, the intensities of O 1s are not equal: Unexpectedly the O 1s signal of NaF PDT 105 °C is ~50% smaller than of the “no PDT“ sample. The O 1s signal on the KF PDT 105 °C sample, however, has the strongest intensity and is about 7 times higher than for the untreated reference. It sounds reasonable that the strongest O 1s signal is found on the KF PDT 105 °C sample, since the KF layer on the CIGSe surface is thicker at low T_{PDT} (as will be shown later) and the hygroscopicity is more pronounced for KF than for NaF. The smaller O 1s intensity on the NaF PDT 105 °C compared to NaF PDT 315 °C could be explained by different sample packing conditions. As the NaF PDT 105 °C sample was prepared and packed on another date, a lower humidity in the laboratory or improved vacuum sealing could be the reason.

Analysis of F-related photoelectron and Auger signals

Strong F 1s signals are present on all as-grown PDT samples. The peak intensity for F 1s increases in the order KF PDT 315 °C < NaF PDT 315 °C < KF PDT 105 °C < NaF PDT 105 °C.

To have a closer look at the different F species, the F 1s and F KLL spectra are displayed in Figure 6.1.3.1. Note that in these spectra the NaF PDT 105 °C sample was excited with Mg K_α radiation, whereas all other samples where excited with Al K_α radiation. Therefore, a comparison of intensities including the NaF PDT 105 °C sample is not directly possible.

To identify different F species, one would have to know the peak width and shape of a single, pure F-component. This kind of “reference“-component was existent in case of the CIGSe elements, where the untreated sample is believed to chemically represent the respective element in CIGSe. For the non-CIGSe related elements, this “reference signal“ is missing. A possible candidate for a reference-fluorine peak shape could be F 1s from the NaF PDT 105 °C sample. This peak has the least asymmetric shape and the corresponding F KLL signal shows

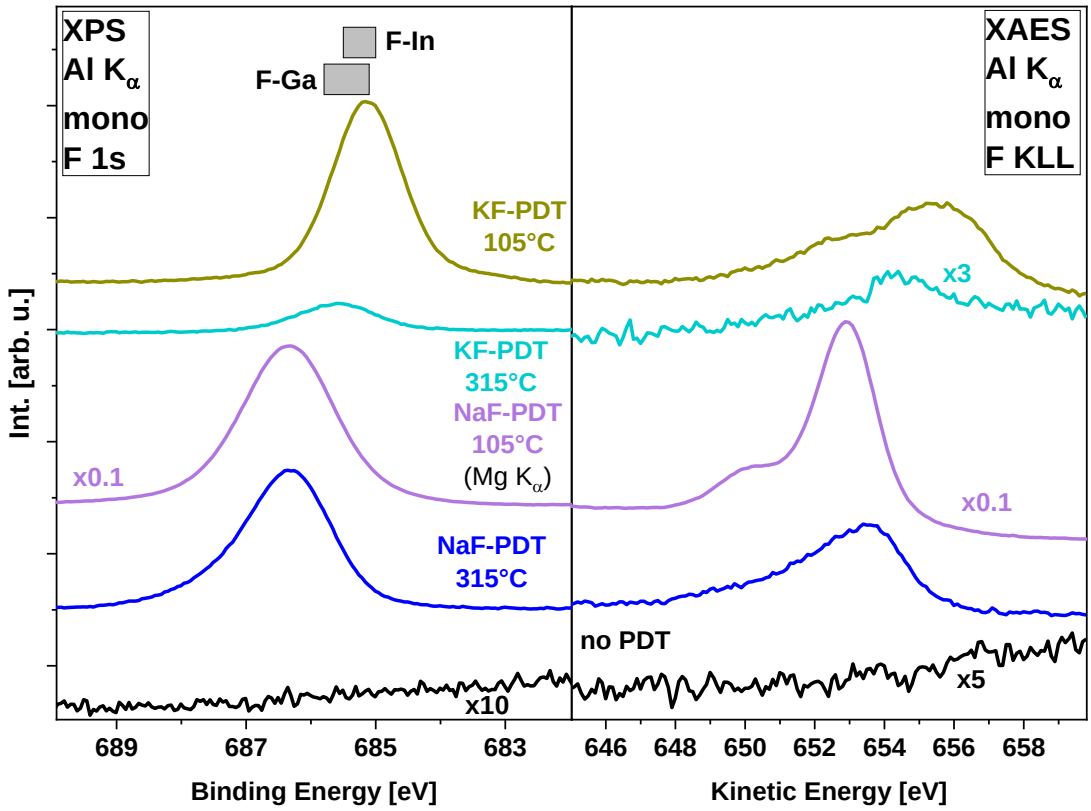

Figure 6.1.3.1 F 1s photoelectron and F KLL Auger spectra for CIGSe samples with different NaF or KF PDTs. Note: All samples except NaF PDT 105 °C are excited with monochromatized Al K_α radiation. The NaF PDT 105 °C sample is excited with non-monochromatized Mg K_α radiation. Gray bars represent binding energy ranges of different F-bonds according to literature data.

the best resemblance to an F KLL Auger found in literature for LiF. Fitting the other F 1s signals with the same width and shape, as for the NaF PDT 105 °C signal, however, fails, probably because of the different spectral widths of the excitation sources. Therefore, only the peak shapes of F 1s and F KLL are compared and some assumption about possible F species are made.

The F 1s signal for NaF PDT 315 °C shows a spectral broadening at the high-binding energy shoulder of the main peak at E_{Bin} > 687 eV. A similar broadening, analogously at lower kinetic energy, is seen for the F KLL signal (if compared to the F KLL shape of NaF PDT 105 °C). Fitting of F 1s with Voigt functions reveals two F-components at E_{Bin} ~ 686.3 and E_{Bin}~687.6 eV, possibly belonging to F-Na and F-Ga. Literature values are 683.5 and 685.8 eV for a NaF and GaF_3 crystal, respectively [112]. A direct comparison is difficult, since the surface induced band bending varies from sample to sample and in the here examined case a thin film is analyzed, and not a bulk material. Despite that, the binding energies do not agree a rough estimation can be made: F-Ga bonds might appear at higher binding energies, than F-Na bonds. Therefore, the minor F species on NaF PDT 315 °C could belong to F-Ga bonds.

For the F species on the NaF PDT 105 °C sample, it is assumed that mainly F-Na species have formed. As the NaF cover layer on this sample is the thickest (as will be shown later), the amount of F-Na bonds will strongly exceed the amount of any other F-bonds (like, e.g., F-Ga). This result is also in accordance with the binding energy of the F-Na species on the NaF PDT 315 °C sample, at E_{Bin} ~ 686.3 eV.

The F 1s signal for KF PDT 315 °C can be fitted with one single Voigt function. The respective F KLL Auger is small and has a too low SNR to evaluate, if additional F species were present. A comparison with literature values indicates possible formation of F-Ga bonds [105,112,113],

as already proposed in the analysis of Ga 2p photoelectrons. F-K bonds, however, can also not be excluded.

The KF PDT 105 °C sample shows an F 1s signal, which has a different shape and width than the KF PDT 315 °C sample. The F 1s signal of KF PDT 105 °C is narrower and shows higher proportions of Lorentzian shape. At the same time, additional intensity is detected at the tail of both sides of the signal at E_{Bin} ~ 683 and E_{Bin} ~ 686 eV. Compared to the main signal at E_{Bin} ~ 685 eV, each of the two smaller signals contributes ~3% to the whole F 1s peak. It can be speculated, whether these smaller signals really represent additional F species, or not. The F KLL Auger signal, however, shows a significant broadening, compared to the NaF PDT 105 °C sample. Therefore, the existence of more than one F-environment seems possible. Accordingly, the main contribution of the F 1s signal of the KF PDT 105 °C sample stems from F-K-bonds and the additional F species could exist as F-In-bonds or F-Ga-bonds, as already proposed in the analysis of the Ga 2p and In 3d signals.

Analysis of Na-related photoelectron and Auger signals

Na is only found in NaF PDT samples. Na 1s signals were fitted by Voigt functions and the partial overlap with the In MNN Auger makes a clear determination imprecise. The position of the Na KLL Auger was determined from the peak maximum in the spectra.

Two Na species were found for each NaF PDT sample in the Na 1s spectra, visible as an asymmetric Na 1s peak with a broader shoulder at higher binding energies (not shown). Since no “reference“ Na-spectrum is available, in which the Na KLL Auger shape for a pure, single Na-component is definitively obtained, an assignment is difficult. Nonetheless, for the NaF PDT 105 °C sample, additional intensity is observed at the high kinetic energy tail of the Na KLL signal, compared to NaF PDT 105 °C (not shown). This small additional signal indicated an additional Na species. The Wagner plot for the modified Auger parameter α'_{Na} is shown in Figure 6.1.3.2.

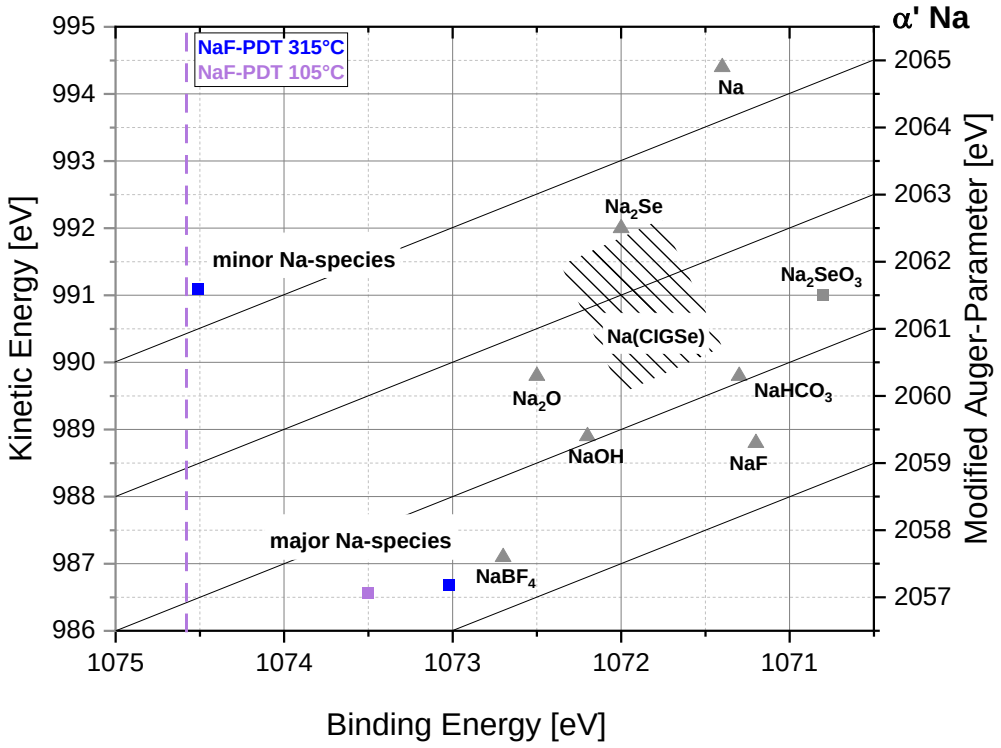

Figure 6.1.3.2 Wagner Plot of the modified Na Auger parameter α'_{Na} for the differently treated PDT CIGSe surfaces (pink and blue). Note, that for the second Na species on NaF PDT 105 °C no corresponding signal in Na KLL was observed. This additional species is therefore marked as a dashed line. Gray triangles show data points from literature for Na in different bonding environments.

The main Na species on both NaF PDT samples have a Auger parameter of α'_{Na} ~ 2060 ± 0.3 eV, which is similar to that of NaF and especially $NaBF_4$ [114]. One possible candidate therefore could be $Na[GaF_4]$, taking the previous results into account that Ga-F bonds could form. Interestingly, also no Na(CIGSe), as compared to literature values, is found on the here investigated surfaces [115–118]. This might be, because the Na(CIGSe) species reported in literature stem from the glass substrates and therefore are already present during CIGSe growth.

For the second Na species found on both samples, comparison with literature data leads to no conclusion about a possible chemical component. A combination of high binding energy and high kinetic energy is very unusual and therefore might imply that the wrong Na 1s and Na KLL values have been combined. Interchanging E_{Kin} and E_{Bin} for the two Na species on NaF PDT 315 °C makes no sense, since the intensity ratios of the two Na species in Na 1s and Na KLL do not match.

Analysis of K-related photoelectron and Auger signals

Like for C 1s, the K 2p signal is overlapped by a strong Se $L_3M_{2,3}M_{4,5}$ signal. A stronger K 2p signal is observed on the KF PDT 105 °C sample than on the KF PDT 315 °C sample. The peak maximum of K $2p_{3/2}$ is directly determined from the spectrum, as well as the peak maximum of the K LMM Auger signal. Only one K environments is found on both samples, possibly as K-F bonds. The Wagner plot for the modified Auger parameter α'_K is given in Figure 6.1.3.3.

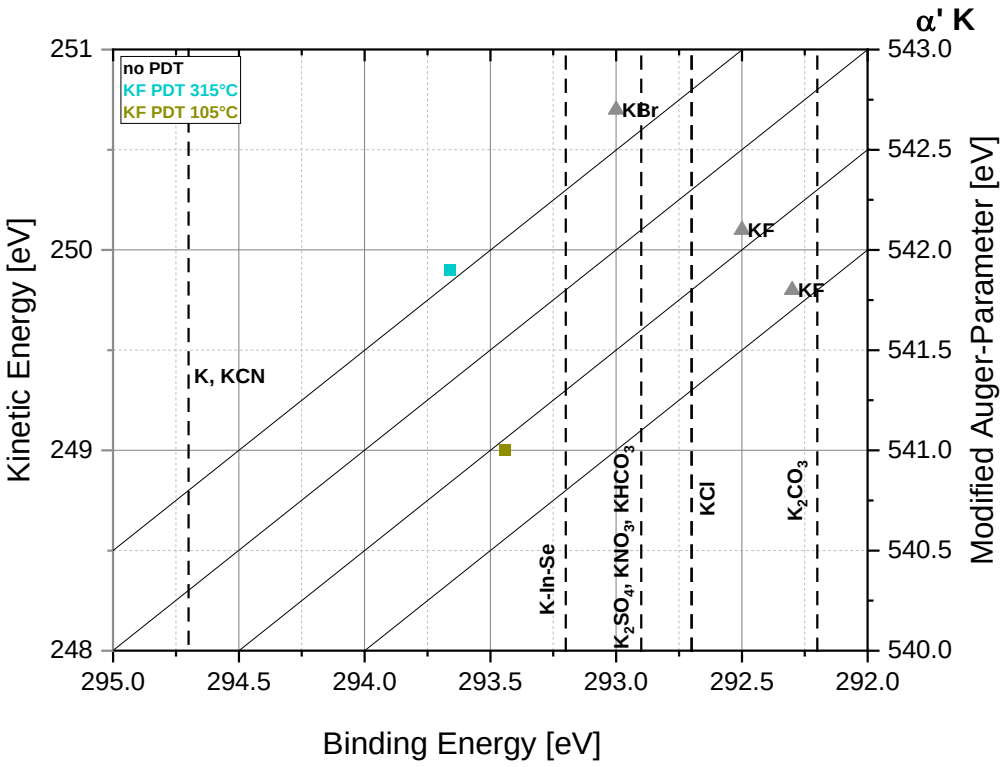

Figure 6.1.3.3 Wagner Plot of the modified K Auger parameter α'_K for differently treated PDT CIGSe surfaces (light blue and green). Note, that for many compounds, no K LMM values were reported in literature. These compounds are marked as dashed lines in the diagram. Gray triangles represent binding energy ranges of different K environments according to literature data.

Only very few values for α'_K were found in literature - most studies only report the position of K 2p. For the KF PDT 105 °C sample an α'_K ~ 542.4 eV is calculated, which could stem from K-F-bonds [105,114]. The difference in binding energy to literature values for KF is ≥ 1 eV and could be explained by a larger amount of fluoride on the sample surface, creating a stronger band bending at the surface.

The Auger parameter for KF PDT 315 °C is α'_K ~ 543.6 eV, resembling more an chemical environment which is comparable to KBr, according to literature [105]. Since bromine is a less electron affine halide than F, it can be speculated that the K species in KF PDT 315 °C is surrounded by less fluoride ions. This also makes sense, since the F 1s signal on KF PDT 315 °C is much smaller than on KF PDT 105 °C.

To summarize the chemical analysis of the CIGSe surfaces after different PDTs, all discovered chemical bonds and species will be presented in the sketch in Figure 6.1.3.4. No attempt to quantify the additional Cu-, In-, Ga- or Se-bonds was made, as the full characterization of the surfaces will be presented later.

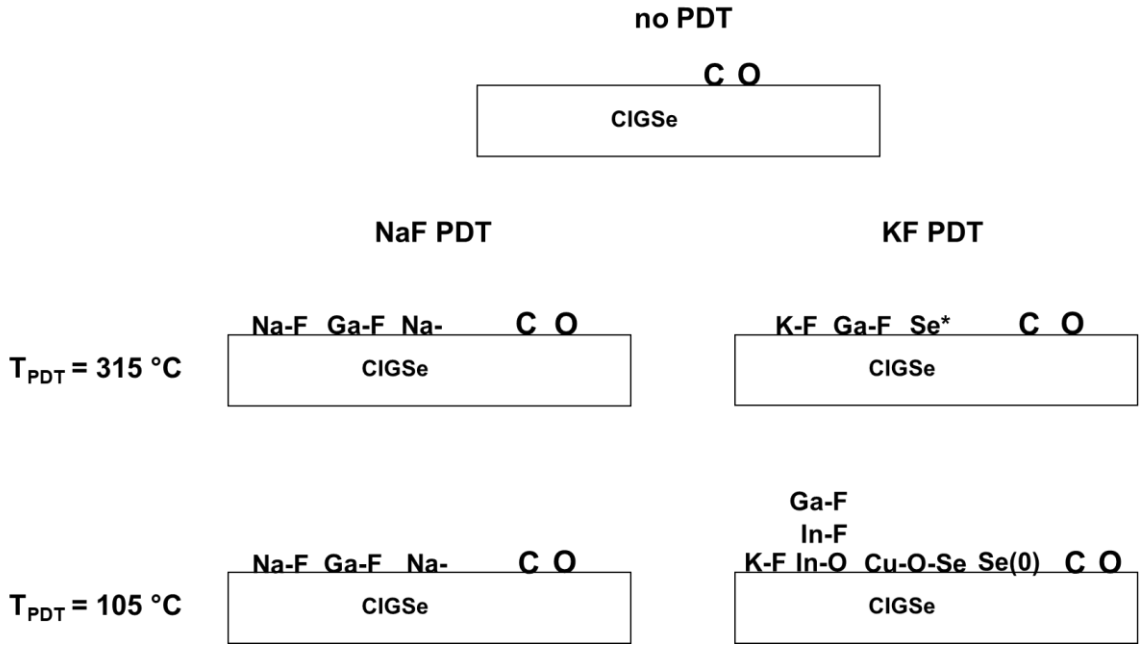

Figure 6.1.3.4 Summary of the found chemical bonds between the constituents of the CIGSe surfaces before (no PDT) and after PDT. The denotation „Se*“ on KF PDT 315 °C represents a chemically not well-defined environment for the Se atoms, rather than an additional Se species.

6.1.4 Relative changes in CIGSe surface stoichiometry due to AlkF PDTs

In the following the „low binding energy region“ of the XPS spectrum was analyzed to evaluate changes in composition of the underlying CIGSe phase. The „low binding energy region“ in the spectrum of CIGSe covers the binding energy range of ~80 eV to 0 eV. No absolute CIGSe stoichiometries were calculated, but the ratio of different peak areas was compared from sample to sample. Therewith the uncertainty for the individual photoionization cross section values was neglected. Generally, no absolute stoichiometries of the CIGSe surface with XPS data were calculated in this work, because the error margin for such calculations is too high, so that unreliable values would result. For a reliable calculation of absolute stoichiometries a very specific layer model would be needed, the values for the photoionization cross sections must be well known and excellent numbers for the IMFP are required. This, however, is not the case.

The kinetic energy of the here examined photoelectrons is therefore roughly equal, resulting in very similar inelastic mean free paths, which simplifies comparison of different signals. Moreover, the photoelectron signals show the same “sensitivity“, by means of signal attenuation, due to surface adsorbates. This is a very important property, since a lot of surface adsorbates exist on the CIGSe surface, as seen before.

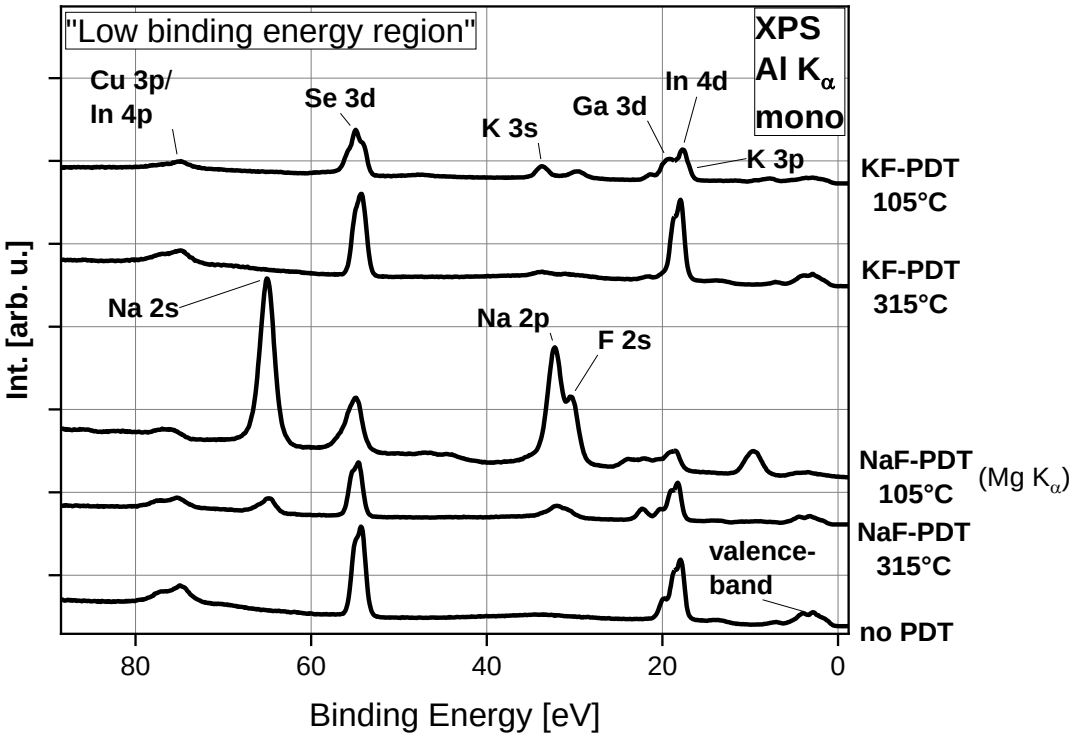

Figure 6.1.4.1 Low binding energy region, including Se 3d, In 4d, and Ga 3d. Note, that the NaF 105°C sample was excited with non-monochromatized Mg K_α radiation.

Figure 6.1.4.1 Figure 6.1.4.1 shows the “low binding energy region“ for all PDT samples and the untreated reference sample (no PDT). CIGSe-related photoemission lines are visible in this range, which makes the analysis of this part of the spectrum convenient. Additionally, Na-, K- and F-signals are also visible. For the evaluation the peak areas for the Se 3d, Ga 3d, and In 4d line will be used and solely the CIGSe-contribution of the signal is taken, to exclude secondary species. The analysis of the Cu 3p line is left out, since it is overlapped by the In 4p line, which shows a broad and complicated background structure.

The estimated peak areas and ratios are displayed in Table 1.

Sample	Peak-Areas [arb. u.]			Peak-Area Ratios	
	In $4d_{5/2}$	Ga $3d_{5/2}$	Se $3d_{5/2}$	$\frac{Ga}{In}$	$\frac{Ga+In}{Se}$
no PDT	2865	557	4186	0.19 ± 0.01	0.82 ± 0.03
NaF 315	1765	375	2565	0.21 ± 0.02	0.83 ± 0.04
NaF 105	60	13	88	0.22 ± 0.02	0.83 ± 0.04
KF 315	3964	162	3892	0.04 ± 0.00	1.06 ± 0.05
KF 105	946	501	1557	0.53 ± 0.04	0.93 ± 0.14

Table 1 Determined peak areas for In $3d_{5/2}$, Ga $3d_{5/2}$, Se $3d_{5/2}$ (solely the CIGSe part of the peak is included, secondary species are excluded here) and calculated peak area ratios for the untreated sample and the PDT samples. Note, that for a more accurate value of the peak area, the corresponding single spectra were evaluated, which were all measured with an Al K_α excitation. Delta is the error margin of the corresponding ratios.

The NaF-treated samples show a similar Ga/In and (Ga+In)/Se ratio, compared to the untreated sample. This indicated that the overall CIGSe-stoichiometry remains unchanged.

For the KF PDT 315 °C sample, a pronounced decrease of the Ga/In ratio is observed, stemming from a gain in In signal intensity and reduction of Ga intensity. A smaller Ga intensity sounds reasonable, since Ga-F bonds are formed, so that the amount of Ga(CIGSe) decreases.

The absolute increase in intensity for In is difficult to explain. One reason might be that Ga-F species leave the CIGSe surface, upon desorption, and expose the unreacted parts of the CIGSe surface. Therefore, the PDT could lead to a decreased atomic density of all Ga-atoms, no matter if Ga-F or Ga(CIGSe). Therewith, less photoelectrons from In might be inelastically scattered by their former Ga-neighbor atoms so that the absolute intensity for In increases.

Also, a slight decrease in Se 3d intensity is observed for the KF PDT 315 °C sample. This might result from partial Se-desorption or a too low Se supply during PDT, or could be a hint that Se(CIGSe) is consumed chemically during the PDT.

Different from this sample, the KF PDT 105 °C surface shows an increased Ga/In ratio. Absolute In- and Ga-intensities decrease for both signals (as compared to no PDT), since Ga-F, as well as In-F species form on this sample. The relative decrease, however, is more pronounced for In. It can be speculated that the reactivities of In and Ga are different, when the CIGSe surface is covered by a thick KF layer. The higher (Ga+In)/Se ratio is also not explainable, since a desorption of Se from the CIGSe surface seems unlikely, because of a thick, covering KF layer (as will be shown further below). All in all, however, the error margin for the peak areas of the KF PDT 105 °C sample is quite high and therefore the values are not very reliable.

Summing up this section, the overall CIGSe composition is not changed drastically after a NaF PDT, independent of T_{PDT}. For the KF PDT 315 °C sample a strong Ga-depletion is observed, and for the KF PDT 105 °C sample a depletion of both, Ga and In, is detected.

Hereby, the chemical characterization for the as-grown PDT samples is finished. In the next two sections, the thickness of the adsorbate films and the spatial distribution of Ga-F- and In-F species within the surface region is estimated.

6.1.5 Estimation of adsorbate layer thickness on the CIGSe surface after AlkF PDT

The thickness of an adsorbate layer was calculated in the context of a simplified model. In this model, a homogeneously thick, flat, and laterally uniform adsorbate layer on top of a flat substrate is assumed. Moreover, the transition between both layers is infinitely sharp and neglect photoelectrons that exit the surface apart from the surface normal. By supposing an exponential attenuation of the CIGSe signals, the following relation in Eq.10 between the intensity I_0 from a bare substrate and the damped intensity I, from a covered surface, can be made:

$$I(d) = I_0 \cdot e^{-d/\lambda(E_{Kin})} \qquad \text{(Eq.10)}$$

Where d is the thickness of the adsorbate layer and $\lambda(E_{Kin})$ is the inelastic mean free path of the respective signal. Especially for the here treated samples, one cannot assume a sharp transition between CIGSe and adsorbate, because the CIGSe layer chemically reacts within the PDT and thus changes. In this case the modified relation in Eq. 11 should be used [81]:

$$\frac{I'}{I''} = \frac{I_0' \cdot e^{-d/\lambda'}}{I_0'' \cdot e^{-d/\lambda''}} \qquad \text{(Eq.11)}$$

Where I‘ and I“ are two different lines from the same element and λ‘ and λ“ are the respective inelastic mean free paths. This equation only works well, when λ‘ and λ“ are sufficiently different.

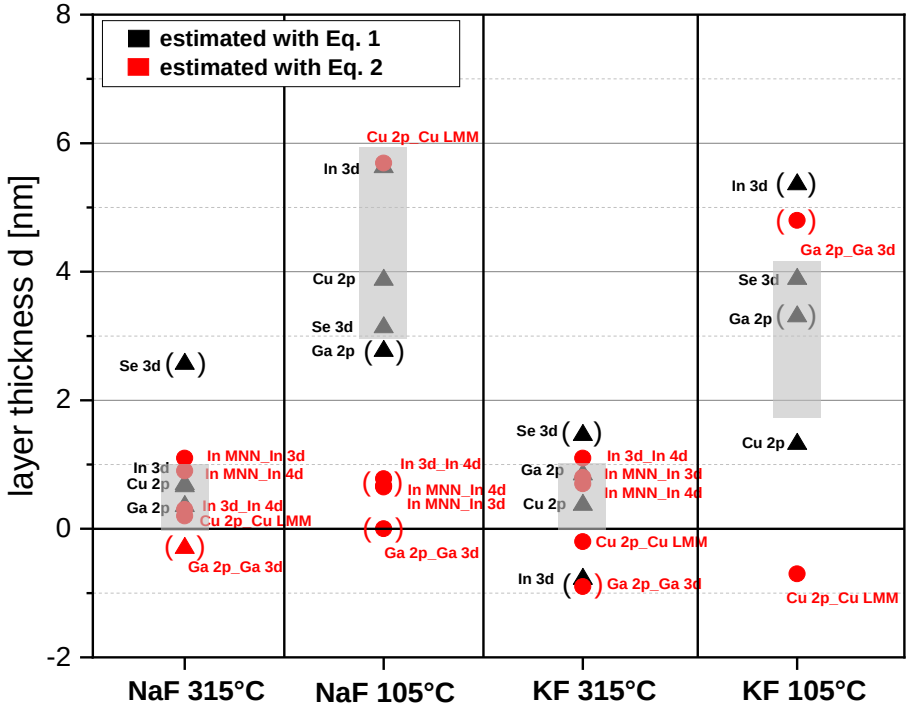

Figure 6.1.5.1 Adsorbate layer thicknesses d, estimated with the help of attenuation of the respective photoelectron and Auger signals, shown for the differently treated PDT CIGSe surfaces. d-values were estimated with two different models, in which Eq. 2 serves as a refinement for Eq. 1, taking into account, that a PDT modifies the surface chemically. For estimations with Eq.1, only photoelectron signals were evaluated, whereas for Eq.2 also the intensities from Auger signals were included. Values with expectably high uncertainty (mainly because of the existence of secondary components of the respective element) or outliers are set into brackets. The explanation for the exclusion of some estimated d-values is given in the text. The gray shaded areas mark the range, in which the thickness of the adsorbate layer is expected.

Different signals were evaluated, such as Ga 2p, Cu 2p, In 3d, In 3p, Se 3d, Se LMM and In MNN. The determined thicknesses d are depicted in Figure 6.1.5.1. Data points in black were derived with Eq.1, data points in red were derived with Eq.2.

The most striking fact is that d has a huge spread on all samples. This spread is most pronounced for the low T_{PDT} samples. Reasons for a huge spread in the values can be an inhomogeneous coverage of the surface with alkali fluorides. Thereby, some parts of the surface are covered with a thicker alkali fluoride layer, and other parts are covered with a thinner alkali fluoride layer, and the thickness values vary. This effect becomes substantially stronger when high amounts of alkali fluorides are present on the surface. This is just the case at low T_{PDT}.

For the NaF PDT 315 °C sample, an adsorbate layer thickness of 0 to 1 nm is estimated. The outlier at the higher thickness value belongs to a Se 3d signal. Although Se is believed to undergo no chemical reactions, this data point was excluded due to statistical considerations. The negative thickness value at d ~ is also excluded, since Ga is pronouncedly affected by the PDT. The uncertainties for the Ga signal intensity might therefore be very high.

The variation of d in KF PDT 315 °C is slightly more pronounced than for NaF PDT 315 °C. This could be explained by more drastic chemical changes during a KF PDT. The outliers at negative thickness values stem from In- and Ga-signals. Since Ga reacts away on the CIGSe surface, its signal intensity might be the most affected by the PDT and therefore this d-value is not reliable. Therefore, this value is excluded. Again, the farthest positive outlier stems from the Se 3d signal. One possible explanation could be that the KF layer indeed is thicker; especially on Se terminated CIGSe facets at the surface. Since KF only reacts with Ga (and at low T_{PDT} also with In), Se atoms would be rendered unchanged chemically. Therefore, no reactions would take place on Se-terminated surface sites and a slightly thicker KF layer builds up there. Overall, a similar thickness range for KF PDT 315 °C as for NaF PDT 315 °C is derived, i.e., 0 to 1 nm.

The NaF PDT 105 °C sample underwent the least chemical changes, with some formation of Ga-F. Still, the intensity of CIGSe-related signals on NaF PDT 105 °C was very low, and for Na- and F-related signals, the intensity was very high. It can therefore be expected that the estimated values < 1 nm are not correct. With all the remaining values (Se 3d, Cu 2p, In 3d, Cu 2p_Cu LMM) the adsorbate thickness is estimated to be > 4 nm.

On KF PDT 105 °C, Ga and In show the most pronounced chemical change, upon formation of Ga-F and In-F secondary components. Therefore, the Ga- and In-related estimations for d-values are excluded. For Cu, one also observes the formation of secondary components, but less pronounced than for Ga and In. The mean estimated d-value for Cu lies between 0-1 nm (the two lowest d-values). Se in turn might be the least affected chemically by the PDT, therefore it should be the best estimate for d. Considering both values (mean d-value for Cu, and d-value for Se), the adsorbate thickness is derived to be < 4 nm.

Some outlier d-values can be explained and together with other, uncertain values they are excluded, but even then, the resulting spread in thickness is still high, indicating that the assumptions are too simple, and both equations, 1 and 2, cannot describe the adsorbate-situation adequately. Nevertheless, qualitative insight is gained on how the adsorbate thicknesses could depend on PDT:

For high T_{PDT}, the resulting adsorbate thicknesses are ≤1 nm. To determine, if NaF or KF leads to a thicker cover layer, the calculated values are not accurate enough.

For the low T_{PDT} surfaces, the resulting adsorbate thicknesses are higher than for the high T_{PDT} surfaces, with >4 nm (NaF) and < 4 nm (KF), as illustrated with the gray shaded areas in

Figure 6.1.5.1. Therefore, tendentially, the adsorbate layer in case of a NaF PDT is thicker, than in case of a KF PDT.

The results that lower T_{PDT} lead to thicker cover layers, seem plausible, since the desorption rate of adsorbates from the CIGSe surface is less pronounced at lower T_{PDT}. Thicker cover layers in case of NaF PDT are also reasonable, since the lattice energy for NaF is slightly higher than for KF.

6.1.6 Depth distribution of Ga-F and In-F within the surface region

In this chapter, the location of Ga-F and In-F species within the surface region will be examined.

To gain depth-dependent information, photoelectron lines with large differences in IMFP are compared. Thereby, the peak area ratios of Ga-F to Ga(CIGSe) for the surface sensitive photoelectron Ga $2p_{3/2}$ are determined, as well as for the less surface sensitive photoelectron Ga $3d_{5/2}$. The peak area ratios are always referenced to Ga(CIGSe), and therefore the peak area of any Ga(CIGSe) peak is set to 1. Note that, because of this reason, comparisons from sample to sample are not possible. The ratios of Ga-F to Ga(CIGSe) and In-F to In(CIGSe) are given in the following Tables 2 and 3.

	Ga $2p_{3/2}$	**Ga $3d_{5/2}$**
Sample	**Ga-F : Ga(CIGSe)**	**Ga-F : Ga(CIGSe)**
no PDT	0 : 1	0 : 1
NaF 315	1.3 : 1.0	1.5 : 1.0
KF 315	0.7 : 1.0	0.75 : 1.00
NaF 105	2 : 1	0 : 1
KF 105	9 : 1	0.4 : 1.0

Table 2 Peak area ratios of Ga-F and Ga(CIGSe) contributions in Ga $2p_{3/2}$ signals and in Ga $3d_{5/2}$ signals. The peak area of Ga(CIGSe) is set to 1. The Ga $2p_{3/2}$ photoelectron is more surface sensitive than the Ga $3d_{5/2}$ photoelectron.

	In $3d_{5/2}$	**In $4d_{5/2}$**
Sample	**In-F : In(CIGSe)**	**In-F : In(CIGSe)**
KF 105	4.8 : 1.0	0.5 : 1.0

Table 3 Peak area ratios of In-F and In(CIGSe) contributions in In $3d_{5/2}$ signals and in In $4d_{5/2}$ signals. The peak area of In(CIGSe) is set to 1. The In $3d_{5/2}$ photoelectron is more surface sensitive than the In $4d_{5/2}$ photoelectron.

After the NaF PDT 315 °C, the ratio of Ga-F to Ga(CIGSe) is similar within the error margin for Ga $2p_{3/2}$ and Ga $3d_{5/2}$. Although this is within the error bar, a slight decrease is observed for the more surface sensitive Ga $2p_{3/2}$ signal. This observation could be explained by a desorption of Ga-F from the CIGSe surface into vacuum, which can only take place at the very surface. This indicated that the CIGSe layer reacts to form Ga-F from the upper most surface region throughout a depth of ~ 3 nm.

For the KF PDT 315 °C sample the trend is similar to NaF PDT 315 °C: The ratios of Ga-F to Ga(CIGSe) are comparable (within the error margin), but slightly higher for the less surface sensitive photoelectrons from Ga $3d_{5/2}$. Again, upon a possible partial desorption of Ga-F from the CIGSe surface, the Ga-F : Ga(CIGSe) -ratio for Ga $2p_{3/2}$ could have become lower. One must mention, however, that these small differences lie within the error bar and might therefore not be significant. A comparison between the two high T_{PDT} samples shows: The absolute Ga-F to Ga(CIGSe) ratios are lower for KF PDT 315 °C than for NaF PDT 315 °C. This could indicate that the reaction of KF with Ga(CIGSe) is (mainly) completed and the majority of the Ga-F species has desorbed from the CIGSe surface. The rate of the reaction of KF with Ga(CIGSe) is therefore higher than for NaF with Ga(CIGSe), which might be due to the easier "breaking" into K^+ and F^-.

For the low T_{PDT} samples, the ratio of Ga-F to Ga(CIGSe) is different: The ratio of Ga-F to Ga(CIGSe) is large for the Ga 2p and significantly smaller for the Ga 3d. This can be explained with Ga-F species, which form at the CIGSe surface, and then diffuse through the overlying NaF/KF layer to the top. A similar ion exchange process has already been observed between Na and Ga at the Mo/glass interface of a CIGSe solar cell [119].

The trend for In-F on the KF PDT 105 °C sample is similar to that of Ga-F on the KF PDT 105 °C sample: For the In 3d, the ratio of In-F to In(CIGSe) is larger than for the In 4d peak. Like for the Ga-F species, it can be assumed that In-F species are formed at the buried KF/CIGSe interface, and then diffuse through the KF layer to the upper most surface region.

6.1.7 Summary of reaction products due to the AlkF PDT on the CIGSe surface

The most important findings of the chemical characterization of the as-grown CIGSe surfaces after PDT are collected and presented in a sketch in Figure 6.1.7.1. For a better visibility, the relative quantities of F, C, and O, presented in Figure 6.1.7.1, are also given in Table 4.

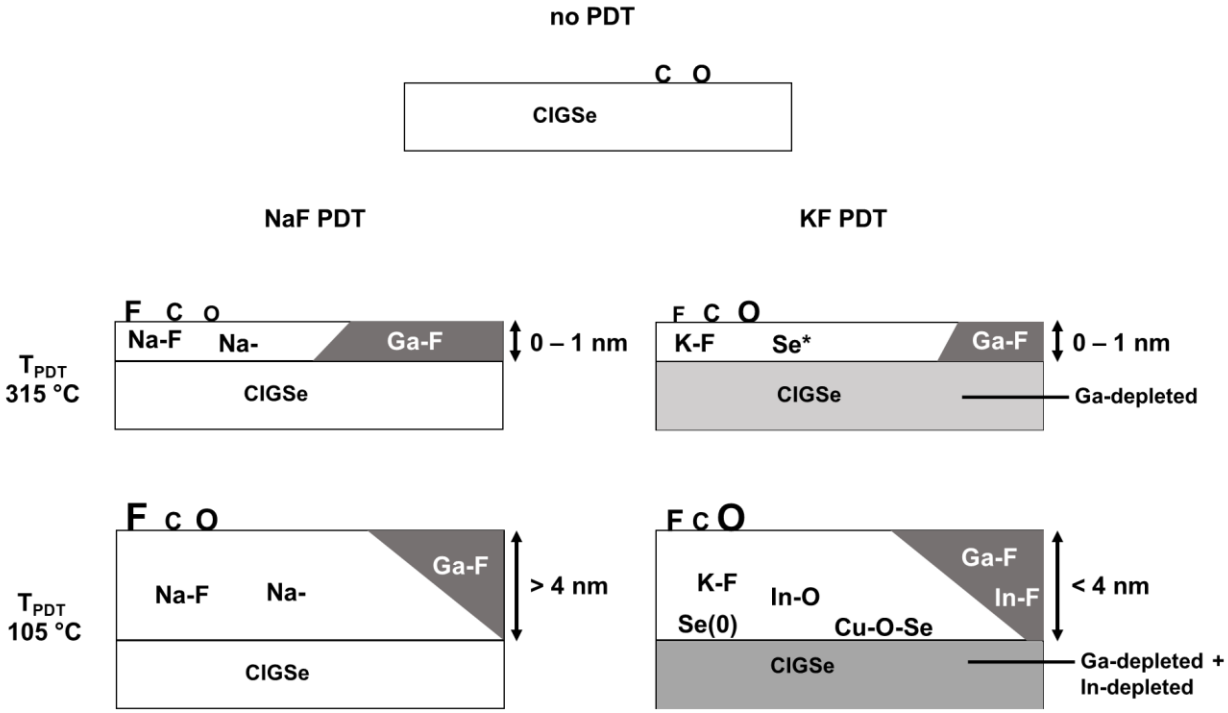

Figure 6.1.7.1 Simplified sketch of the measured samples with detected components. The font sizes for F, C and O indicate quantitative changes from sample to sample. For a better visibility, the relative F, C and O quantities are also provided in Table 4. No quantitative statements for CIGSe-related compounds (from sample to sample) are provided. Dark gray trapezia and a triangle schematically illustrate the distribution of Ga-F and In-F throughout the adsorbate layer. In this depiction the horizontal width of the trapezia or triangle indicate the concentration of Ga-F (or In-F) at a certain z-position in the adsorbate layer.

	F	C	O
no PDT		+	+
NaF PDT 315 °C	++	+	+
NaF PDT 105 °C	+++	+	++
KF PDT 315 °C	+	+	++
KF PDT 105 °C	++	+	+++

Table 4 Relative F, C and O quantities on the differently treated CIGSe surfaces directly after PDT. "+" marks the existence of the respective element and the number of "+" indicates the amount. The relative quantitites are given for the respective element from sample to sample, and no comparison between F,C and O –quantities on the same sample was made.

6.2 Cleaning of the CIGSe surface due to an aqueous Na_2S rinsing step ("rinsed" samples)

In this chapter, the chemical impact of the rinsing treatment will be evaluated. In this treatment, the as-grown PDT samples are put into an aqueous Na_2S-solution for 30 sec, are subsequently rinsed with water, and then dried under an N_2 stream.

The purpose of the rinsing treatment is to remove PDT reactants and byproducts with unwanted properties, especially the excess elemental Se, which is typically needed in CIGSe preparation and during PDT. Therefore, the rinse "conditions" the CIGSe surface for the subsequent CdS-deposition and affects the properties of the resulting interface. Some more rinsing agents like aqueous NH_3-, KCN- or NH_4OH-solutions have been employed [120,121]. The question is, if Na_2S only removes water-soluble PDT byproducts or also enables formation of additional components.

Section 6 is built up as follows: In Chapter 6.2.1 XPS survey spectra are presented to derive some general changes, like the existing elements on the surface. Then the individual core level spectra before and after rinse are compared to evaluate, which sample underwent significant chemical changes. Chapters 6.2.2 and 6.2.3 will then present the formation of secondary species on the KF PDT 315 °C and KF PDT 105 °C samples. Thereafter, Chapter 6.2.4 takes a short look at the resulting Na species that are formed during the rinse and in Chapter 6.2.5 the changes of the CIGSe stoichiometry are estimated and the findings are summarized.

Similar to Chapter 6.1, the spectra of Ar^+-ion cleaned sample surfaces are exclusively shown throughout Chapter 6.2. Upon Ar^+-ion cleaning, the SNR of CIGSe related signals increased slightly and data analysis therefore becomes more precise. Upon comparison of as-received and Ar^+-ion cleaned spectra (not shown), it can be confirmed that the Ar^+-ion cleaning does not alter the sample surfaces chemically, but only removes physisorbed C- and O-containing surface contaminants.

6.2.1 Change of the CIGSe surface constituents due to the rinsing step

Figure 6.2.1.1 shows the XPS spectra of a no PDT CIGSe layer without a PDT before and after the rinsing step.

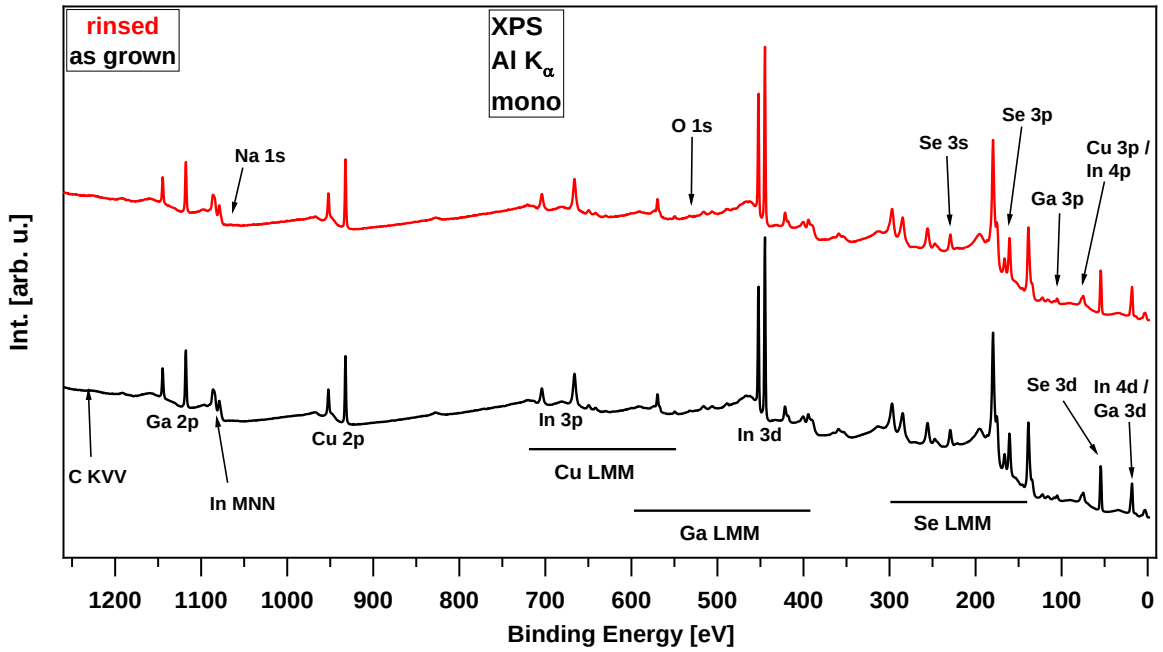

Figure 6.2.1.1 Al K_α excited survey spectra of the no PDT CIGSe absorber before (black) and after the rinsing treatment (red). All prominent photoemission and Auger lines are labeled.

Only a slight change of the surface composition is observed after rinsing (red spectrum): A very weak Na 1s signal appears at E_{Bin} = 1072 eV, and the whole spectrum shifts to lower binding energies by ~0.4 eV. This shift can possibly be related to a change of the surface dipole induced by the Na ions on the surface. The intensity of the Na 1s signal is very low, so that accurate determination of the chemical component is not possible. Comparison with literature values suggests that Na might exist in a Se- and O-containing environment, such as in the components Na_2Se or Na_2O.

The Ga $2p_{3/2}$ and Se 3d spectra (shown in Figure 6.2.1.3 , bottom line) reveal a slight decrease in intensity upon rinse. The same observation is made for the respective Ga- and Se- Auger signals. For Cu $2p_{3/2}$ and In $3d_{5/2}$, however, no change in intensity is observed. Therefore, the decrease in intensity cannot only be explained by a Na-containing cover layer. Moreover, Se 3d photoelectrons are the least surface sensitive of the compared peaks, which means that, if an adsorbate layer was the reason for the decrease in intensity, one would clearly see a decrease in Cu $2p_{3/2}$- and In $3d_{5/2}$-intensity, as well. However, this is not the case.

A probable explanation could be a partial dissolution of Ga and Se within the rinsing solution. Since the removal of excess Se is the actual purpose of the rinse, this interpretation for the intensity decrease sounds reasonable. The removal of Ga atoms within the short time span of a rinse also seems possible, as Ga is more reactive than In and Cu and so should also be removed first [82]. Moreover, an investigation of the rinsing solution after the rinsing step by inductively coupled plasma spectrometry (ICPS) revealed that Ga and Se (but not Cu and In) have been dissolved in the rinsing solution [122]. Hence, the ICPS observations confirm this explanation.

Rinsing the no PDT absorber thus removes some Ga and Se and covers the surface with a little of Na, which assumingly affects the band bending at the surface.

After this short characterization of the rinse-effect on a no PDT CIGSe surface, its effect on as-grown PDT surfaces will be analyzed in the following. Exemplarily, survey spectra of the NaF PDT 315 °C and KF PDT 315 °C samples, before and after the rinse, are presented in the next Figure 6.2.1.2.

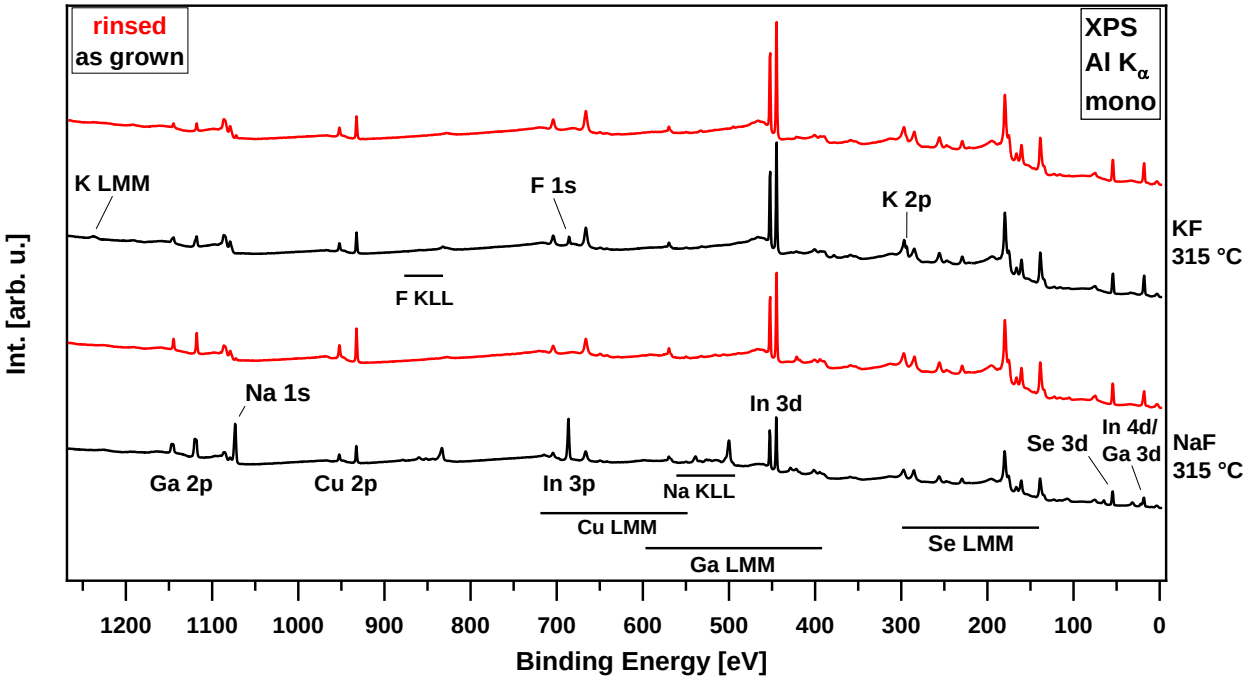

Figure 6.2.1.2 Survey spectra of the NaF PDT 315 °C and KF PDT 315 °C samples, as-grown (black) and after a rinsing (red).

After rinsing the samples, all F-related signals disappear. The O 1s signals do not increase after rinse, although one might expect additional water adsorption. Furthermore, a small Na 1s signal appears on all samples, indicating the formation of a Na species, which could stem from the rinsing solution.

For a closer look on the changes, the CIGSe core level spectra are plotted below in Figure 6.2.1.3, in which the as-grown and rinsed samples are compared.

In Figure 6.2.1.3 it can be ascertained that all Ga-F and In-F secondary components, which have formed on the surface after PDT (black), are removed due to the rinse (red). No Ga-F and In-F secondary components are detected at higher binding energies (compared to E_{Bin} of Ga(CIGSe) or In(CIGSe)) on the rinsed surfaces, and only one Ga or In species exists. The chemical analysis of these species (not shown) reveals that Ga and In are present in a CIGSe environment on every rinsed PDT sample.

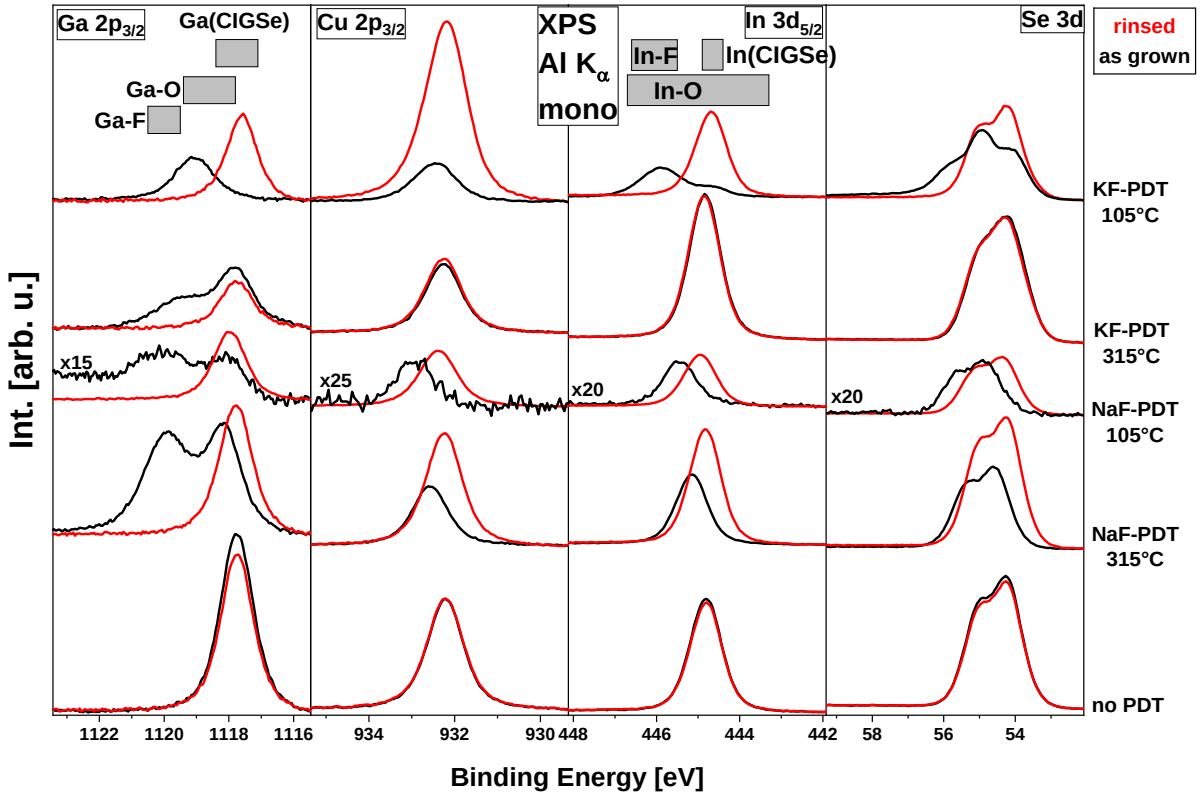

Figure 6.2.1.3 Al K_α excited CIGSe core-level spectra for the untreated and all PDT CIGSe surfaces. Spectra in black denote the as-grown samples, spectra in red denote the rinsed CIGSe samples. Note that the lower intensity for all spectra of the NaF PDT 105 °C sample probably is due to a larger distance between sample and X-ray tube. Gray bars represent binding energy ranges for different chemical species according to literature data.

Upon analysis of the Ga LMM and In MNN Auger spectra (not shown), neither Ga oxides, nor In-oxides could be detected. However, to identify additional Ga or In species, the Ga LMM and In MNN Auger spectra were not fitted, but only compared by means of their shape. Thereby, some percent of Ga-O or In-O might be overlooked. Yet, it is assumed that the relative amount of these additional Ga or In species is very low.

Another observation, which confirms that no Ga or In oxides have formed (or that their amount is very low) is the intensity of the O 1s signal. The intensity of the O 1s signal is very weak and does not increase upon rinse. Therefore, no additional oxides should be formed upon rinse.

The Cu-O-Se secondary phase (as observed on the as-grown sample in Chapter 6.1.2, Figure 6.1.2.5) on the as-grown KF PDT 105 °C sample is not completely removed and remains intact after rinse (not directly evident from Figure 6.2.1.3). This additional Cu species is detected at higher binding energies, compared to Cu(CIGSe) and can be noticed by the slightly asymmetric shape of the Cu $2p_{3/2}$ signal of the rinsed KF PDT 105 °C sample in Figure 6.2.1.3. Moreover, the intensity for the Cu $2p_{3/2}$ signal increased by nearly a factor of 2, compared to the untreated reference, so that a Cu-rich surface should have formed on the KF PDT 105 °C sample.

A more detailed analysis of the Cu signals will be given in Chapter 6.2.3.

For Se, a slightly broader shape for the Se 3d signal is detected for the rinsed KF PDT 315 °C sample (red), compared to the as-grown KF PDT 315 °C sample (black). In the analysis of the Se 3d signals of the as-grown samples in Chapter 6.1 (page 33), a broader Se 3d shape was ascribed to a not well-defined chemical environment for Se. This could also be the case for the

rinsed sample. Another reason might be the formation of an additional Se species. This circumstance will be discussed in Chapter 6.2.2.

The additional Se-component on the KF PDT 105 °C sample at E_{Bin} ~ 55 eV, which is believed to be elemental Se (as determined in Chapter 6.1.1 on page 34), is completely removed after the rinse.

For all other photoelectron signals (Ga 2p, Cu 2p, In 3d, and Se 3d) and the respective Auger signals (Ga LMM, Cu LMM, In MNN and Se LMM) not mentioned so far, no additional species are observed upon rinse. The signals of the rinsed NaF PDT samples are identical in shape and width, compared to signals of the untreated, rinsed sample. The chemical analysis is therefore continued for the two KF PDTs at 315 °C and 105 °C, where the spectra significantly differ from the untreated and NaF PDT samples after rinse.

6.2.2 Chemical impact of the rinsing step on the KF PDT 315 °C sample

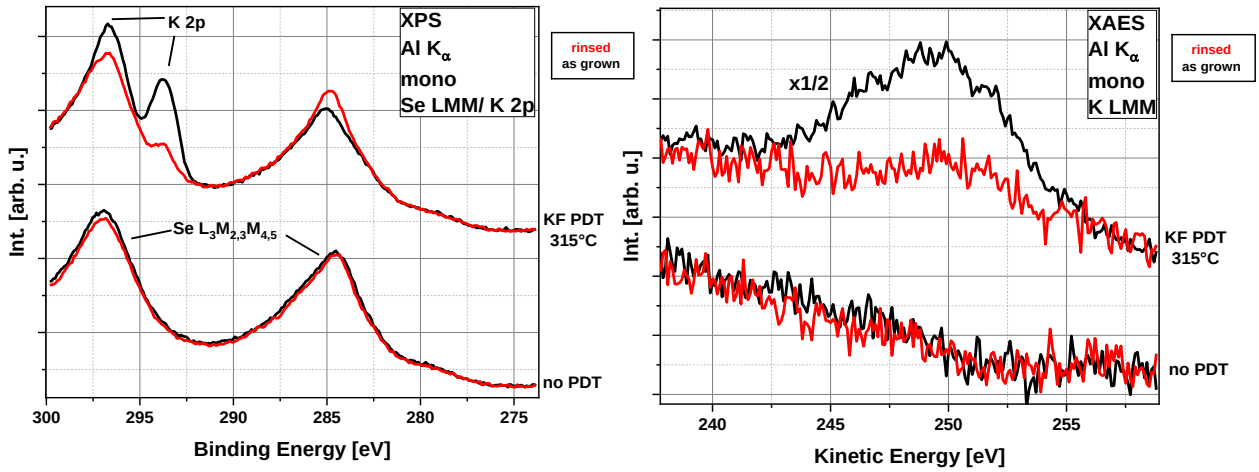

Figure 6.2.2.1 K 2p and K LMM spectra for the no PDT absorber surface (bottom spectra) and the KF PDT 315 °C sample (top spectra). Illustrated in black are the respective as-grown samples and in red the rinsed samples.

Upon rinse, 80 % of the K found at the surface of the as-grown KF PDT 315 °C sample, possibly existent as K-F, gets removed from the surface (shown in Figure 6.2.2.1 left).

Since the K 2p signal overlaps with the Se LMM Auger, and the K LMM Auger shows a low SNR, the exact chemical identification of the K-component is difficult. The position of K $2p_{3/2}$ is read from the peak maximum in the spectrum (at E_{Bin} ~ 294 eV), and the position of K LMM is roughly estimated by the peak region of K LMM. Estimated uncertainties for K $2p_{3/2}$ and K LMM are ±0.1 and ± 0.7 eV, respectively. Figure 6.2.2.2 shows the Wagner-Plot for the modified Auger parameter for K.

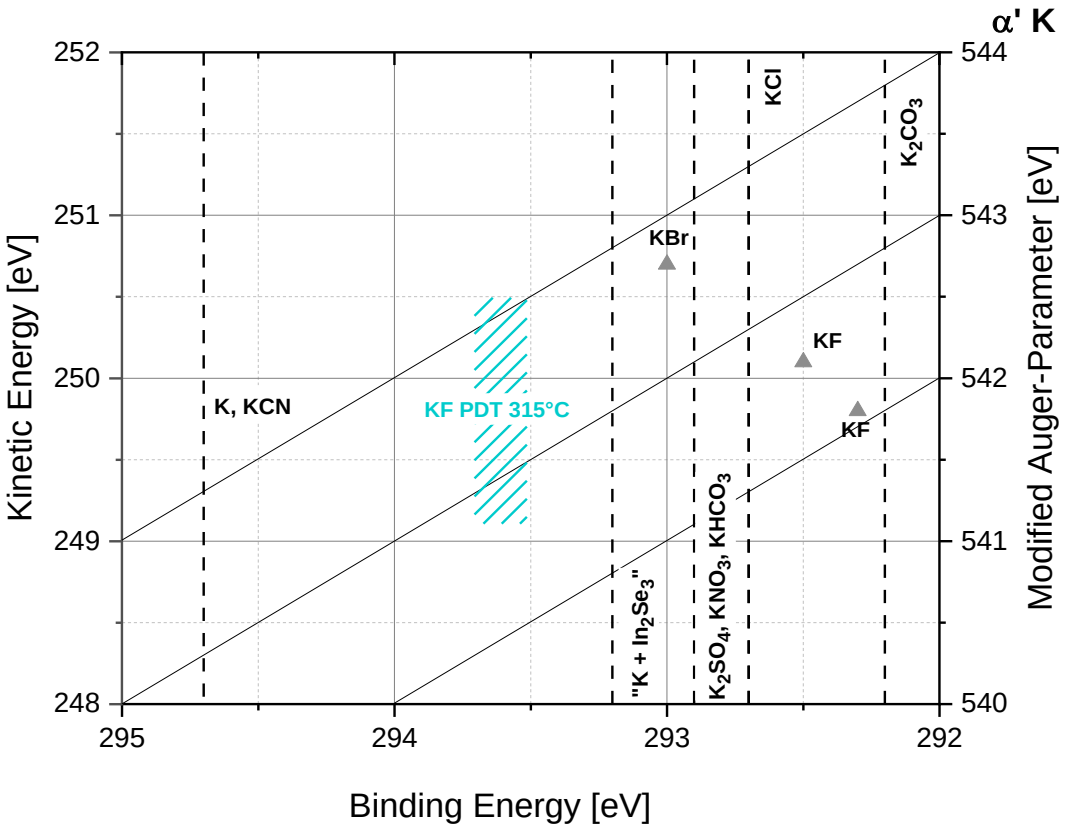

Figure 6.2.2.2 Wagner Plot of the modified K Auger parameter α'_K for the K species of the KF PDT 315 °C sample (blue dashed area). The gray triangles show the data points from literature for K in different chemical environments. The corresponding sources have been given in Chapter 6.1 in the text. Note, that for many compounds, no K LMM values were reported in literature, but only the K $2p_{3/2}$. These compounds are marked as dashed lines in the diagram.

The K species on the KF PDT 315 °C sample lies in closest distance to an "K + In_2Se_3" environment, as found by Lepetit et al. [36,123] on a CIGSe surface aftetr a KF PDT. They also observed a water-insoluble K species after a KF PDT and assumed its existence in an In_2Se_3 environment. Furthermore, they observed a second Se species besides Se(CIGSe), attributed to Se-In bonds. For the work in hand, the Se 3d signal also changes considerably on the rinsed KF PDT 315 °C sample. The Se 3d signal of the KF PDT 315 °C sample will therefore be analyzed in the following.

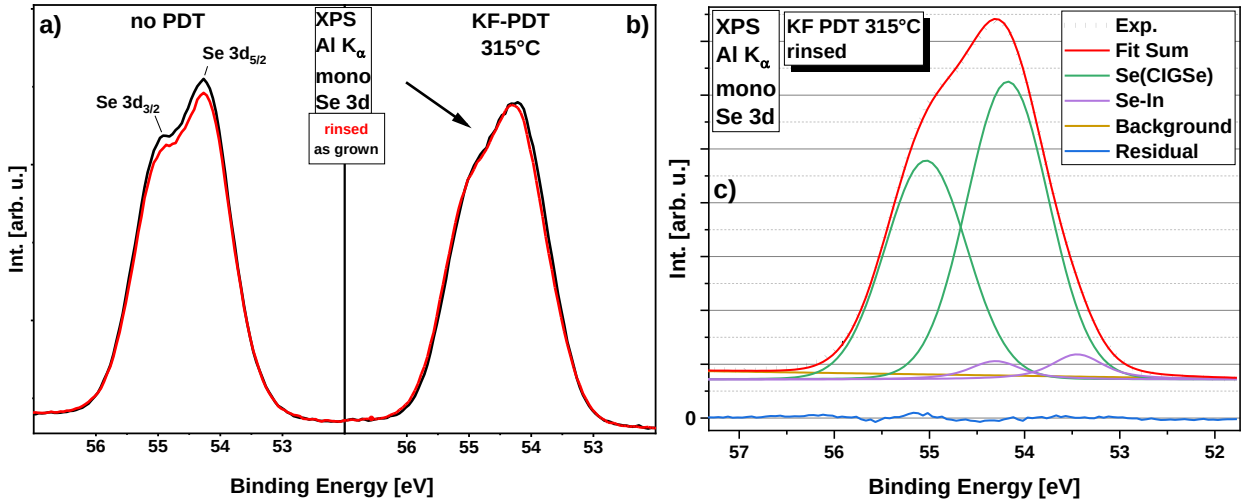

Figure 6.2.2.3 Se 3d spectra for a) the untreated reference (no PDT) and b) KF PDT 315 °C samples as-grown (black) and rinsed (red). c) Fit of Se 3d for the rinsed KF PDT 315 °C sample with two components. The different Se species found in the Se 3d fit are Se in a CIGSe environment (green), labeled „Se(CIGSe)“ and an additional Se species (pink) labeled „Se-In“, which is assumed to exist in an chemical environment similar to a Se-In component.

In Figure 6.2.2.3 a), the Se 3d signal is shown for the no PDT samples as-grown (black) and rinsed (red). The doublet peaks Se $3d_{3/2}$ and Se $3d_{5/2}$ can just be separated visually. For the KF PDT 315 °C samples b), the visual separation of Se $3d_{3/2}$ and Se $3d_{5/2}$ is not possible anymore (or only suggestible) and additional intensity is detected. This observation is marked with an arrow in Figure 6.2.2.3 b) and has already been reported for the as-grown KF PDT 315 °C sample (black) in Chapter 6.1.2 in Figure 6.1.2.10. A reason for this additional intensity between Se $3d_{3/2}$ and Se $3d_{5/2}$ can be a broader Se 3d signal or an additional Se species.

Furthermore, the low binding energy side of the Se $3d_{5/2}$ peak (at E_{Bin} ~ 54 – 53 eV) on the rinsed KF PDT 315 °C sample (red) is slightly flatter, than for the as-grown KF PDT 315 °C sample (black). This indicates that upon rinse the chemical environment for Se has changed slightly.

For the KF PDT 315 °C as-grown sample, only a variation of the FWHM of the Se 3d doublet peaks (compared to the FWHM of the no PDT Se 3d peaks) was enough, to explain the additional intensity between Se $3d_{3/2}$ and Se $3d_{5/2}$.

For the KF PDT 315 °C rinsed sample, however, a fit of the Se 3d signal with only one Se 3d doublet and varying FWHM or shape (to account for a not well-defined chemical environment) does not lead to satisfying results. A good fit was only possible by the introduction of a second Se species at lower binding energy. In Figure 6.2.2.3 c) the Se species at E_{Bin} = 54.18 eV (green) is ascribed to Se(CIGSe) and the second Se species at E_{Bin} = 53.45 eV (pink) is ascribed to Se-In bonds, as compared to values from Lepetit et al. ([123], E_{Bin} = 53.5 eV), Handick et al. ([38], E_{Bin} = 53.54 eV) or Miyake et al. ([124], E_{Bin} = 53.59 eV).

Not only the absolute values for E_{Bin} of Se 3d are similar to literature, but also the energetical distances between Se 3d of the Se-In species and the Se 3d of Se(CIGSe) species: In this work the energetical separation of Se $3d_{5/2}$ between Se-In and Se(CIGSe) is 0.73 eV, which compares well with 0.7 eV, detected in coevaporated In_2Se_3 [125], or with 0.6 eV, detected in Handick's work [38].

Therefore, the additional Se species at lower Se 3d binding energies could stem from In-Se bonds, which are chemically similar to In-Se bonds in In_2Se_3 or in a K-In-Se like component.

Together with the finding of a stable K species, which chemically can exist in an "In_2Se_3 + K" like environment (as found out before, in Figure 6.2.2.2), a K-In-Se like component could also exist on the KF PDT 315 °C sample. This means that the additional Se species, which is identified to be bound to In, should also be bound to K. Thereby, a new component containing Se, In, and K has formed on the rinsed KF PDT 315 °C sample surface.

In this respect, it is quite conspicuous that only for the KF PDT 315 °C sample a stronger In signal and weaker Cu- and Ga-signals are observed (see Figure 6.2.1.3), compared to the untreated sample. This underlines that a new In-containing species could have formed on the surface, with an In 3d binding energy equal to In(CIGSe).

Because of the processual similarities between the KF PDT 315 °C and the KF PDTs applied by Handick [38] and Lepetit [36], and the numerous similar experimental observations, the new chemical species on the rinsed KF PDT 315 °C sample can therefore be called "K-In-Se", as well.

6.2.3 Chemical impact of the rinsing step on the KF PDT 105 °C sample

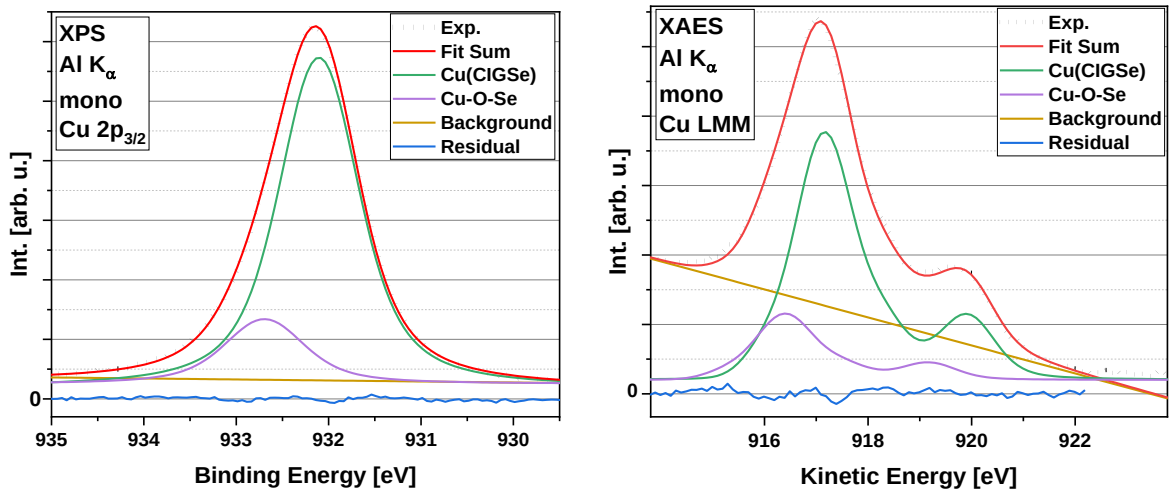

Figure 6.2.3.1 Peak-Fit of Cu $2p_{3/2}$ and Cu LMM Auger spectra of KF PDT 105 °C rinsed to distinguish between two different Cu species (purple and green).

The Cu $2p_{3/2}$ spectrum for the rinsed KF PDT 105 °C sample (Figure 6.2.3.1, left) shows an asymmetric shape with additional intensity at higher binding energies (E_{Bin} ~ 932.5 - 933.5 eV), and 2 Cu species with same width and shape (green and purple) can be fit into the signal. The same holds for the Cu LMM Auger spectrum, which was reproduced by two Auger signals of the reference sample, each of them being shifted and resized. The fit of the Cu LMM signal is shown in Figure 6.2.3.1, right. One must mention, however, that different chemical environments not only affect the line position of the Auger signal, but can also affect its shape. This means that it could be problematic to reproduce the Cu LMM signal of a KF PDT 105 °C sample with (a superposition of) the Cu LMM signal of a merely untreated, no PDT sample. This holds true especially for the Cu LMM Auger signal [98], since it involves the Cu 3d derived bands, which are part of the valence band and therefore distinctly impacted by the chemical environment.

Nonetheless, a qualitative comparison of the Cu LMM signals for the KF PDT 105 °C and no PDT sample (not shown) points out that an additional Cu species forms at lower kinetic energy than Cu(CIGSe). Thereby, the fit of the Cu LMM signal of KF PDT 105 °C with a superposition of no PDT-Cu LMM signals might be physically correct in this case.

All values for Cu $2p_{3/2}$ and Cu LMM of the rinsed samples were depicted in the Wagner plot of the modified Auger parameter α'_{Cu} in Figure 6.2.3.2. Reference values can be found in [92,94,98–100,102,109,118].

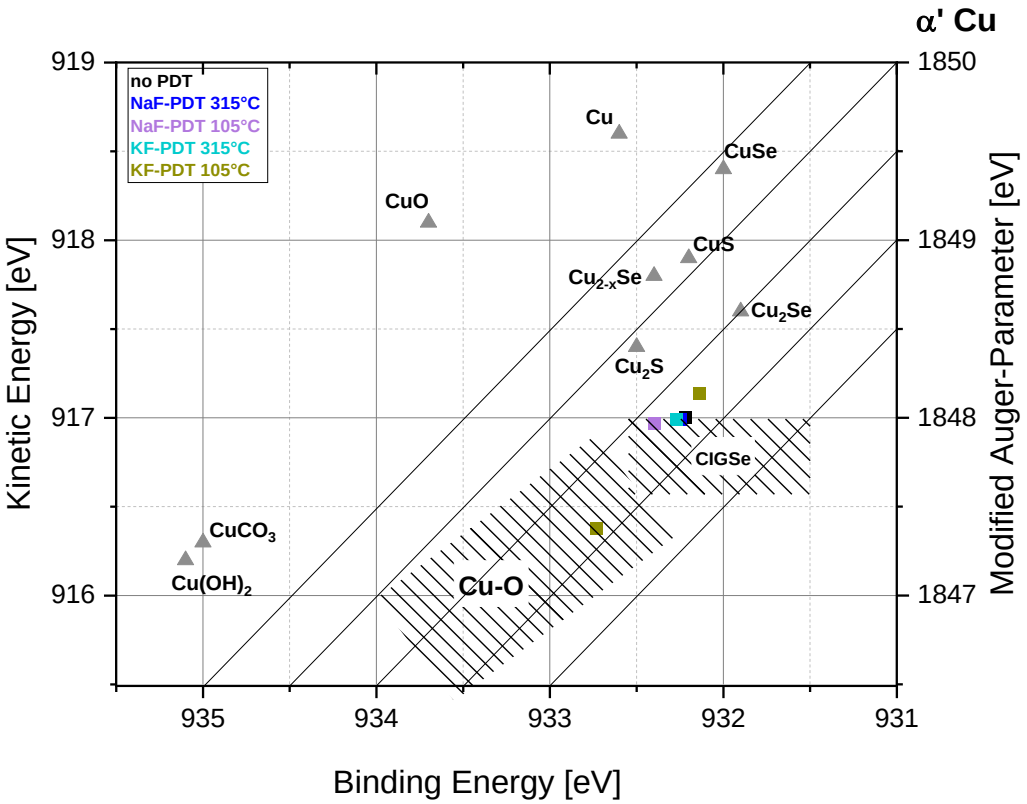

Figure 6.2.3.2 Wagner Plot of the modified Cu Auger parameter α'_{Cu} for the untreated, rinsed CIGSe surface (black) and the differently treated PDT CIGSe surfaces. The gray triangles show the data points from literature for Cu in different chemical environments.

In the Wagner plot two groups of different Cu species are visible, similar like for the as-grown samples. At α'_{Cu} ~ 1849.3 eV one finds Cu(CIGSe), as proposed for the as-grown samples. The additional Cu species in KF PDT 105 °C with α'_{Cu} ~ 1849.1 eV again might be Cu-O. Since O and Se are chemically similar, and the regions for Cu-O and Cu(CIGSe) overlap, the additional Cu species may be bound to O and to Se at the same time. Thereby, the additional Cu species on the KF PDT 105 °C sample can be denoted as Cu-O-Se.

Although the Wagner plot does not show any evidence for the formation of Cu-S bonds, a small fraction of the Cu at the surface can be bound to sulfur, which is supplied in the rinsing solution (aqueous Na_2S solution). This assumption is justified, since Cu and S show a high chemical affinity towards each other (which is reflected in the existence of a high number of Cu-S-minerals in natural deposit).

Subsequently, the S-related signals are analyzed in the following. It will be shown that a water-stable S species has formed, which indeed can be bound to Cu.

Figure 6.2.3.3 depicts the S LMM Auger spectra (left) and normalized Se 3p/ S 2p photoelectron spectra (right) for the untreated sample and the KF PDT 105 °C sample.

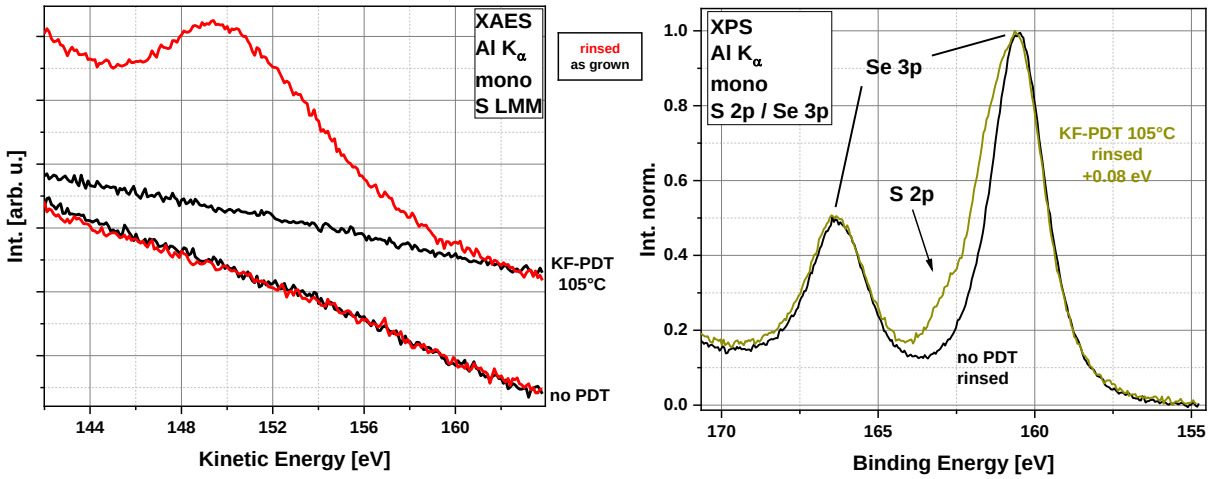

Figure 6.2.3.3 S LMM Auger signals (left diagram) for the untreated reference (no PDT) and KF PDT 105 °C sample, depicted as-grown (black) and rinsed (red). On the right, the normalized Se 3p/ S 2p photoelectron spectra are shown for the rinsed, untreated reference sample (no PDT, black) and the rinsed KF PDT 105 °C sample (dark yellow). Se 3p / S 2p spectra are normalized by setting the low binding energy background at ~155 eV to zero and the peak maximum to one. Additionally, the spectrum for the KF PDT 105 °C sample is shifted by +0.08 eV on the energy-axis to allow for a better comparison of the spectral shapes.

The KF PDT 105 °C sample, in rinsed condition, is the only sample, on which sulfur is detected. For all other samples, no S LMM signal is observed. S LMM Auger spectra are given exemplarily for the untreated reference and KF PDT 105 °C sample on the left in Figure 6.2.3.3. The S LMM Auger feature appears as a broad signal in the spectrum of the KF PDT 105 °C sample. Its position was read from the peak maximum in the spectrum and is E_{Kin} ~ 149.4 ± 0.5 eV. Unfortunately, no literature data for S LMM were found, except in the work of A. Epprecht, in which a KF+S PDT was applied to CIGSe samples. The rinsed samples showed a S LMM signal at E_{Kin} ~ 150.6 ± 0.5 eV, but no further characterization of the S species was made [94].

The S 2p signal is also detected and overlaps with the more intense Se 3p doublet (Figure 6.2.3.3, right). The S 2p signal creates additional intensity between at E_{Bin}~ 161 – 164 eV and the resulting Se 3p / S 2p spectrum (dark yellow) differs clearly from that of the no PDT sample (black). The measured Se 3p/ S 2p spectrum was fitted with a sum of the Se 3p (and Ga 3s) photoelectron signal of the no PDT sample and a S 2p doublet, with a spin-orbit coupling of 1.16 eV and an intensity ratio of 0.511 [126]. The fit is shown below in Figure 6.2.3.4. For S $2p_{3/2}$ one determines E_{Bin} ~ 161.5 eV ± 0.5 eV. To characterize the S species on the KF PDT 105 °C sample, literature values for different S species are included as gray boxes in the diagram.

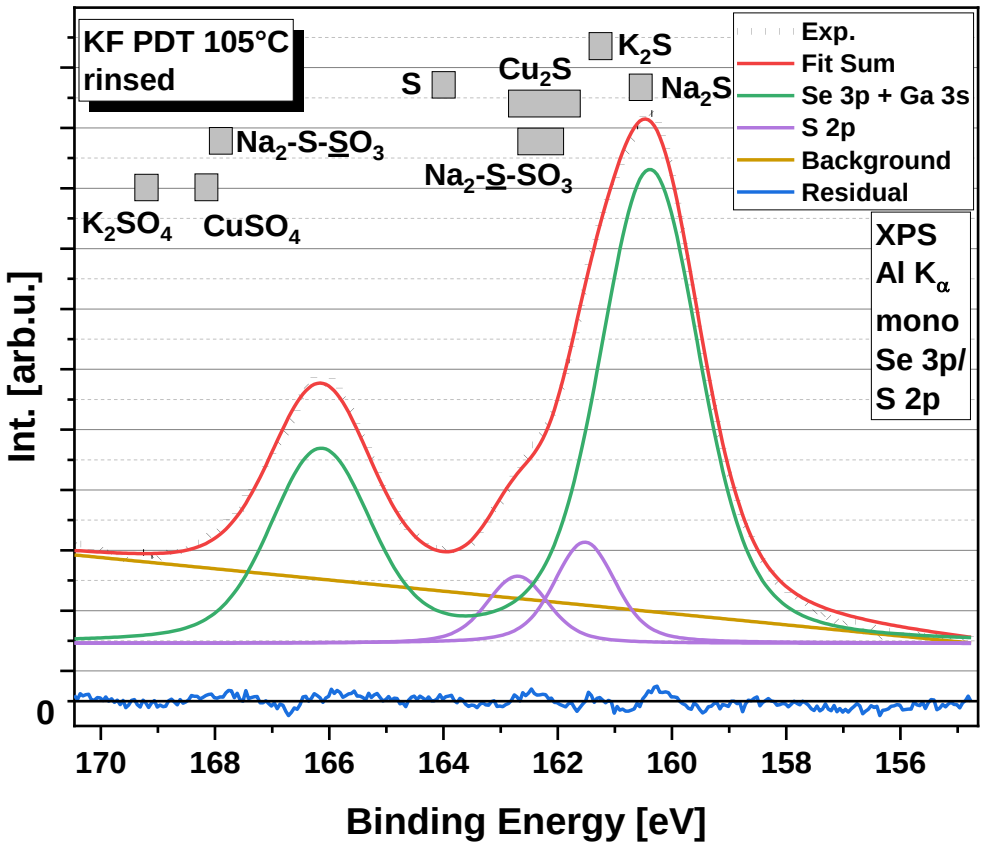

Figure 6.2.3.4 Fit of the Se 3p/ S 2p photoelectron spectrum for the rinsed KF PDT 105 °C sample. Boxes in gray mark binding energy regions of the S 2p signal for different S compounds, found in literature.

According to the binding energy of the S species, a partial overlap with Cu_2S is observed. K-S species can be excluded, since no K is found on the rinsed KF PDT 105 °C sample. The formation of elemental sulfur might also be excluded, since the difference in binding energy is too large. More likely, with regard to binding energy, could be a S species as thiosulfate ($S_2O_3^{2-}$). Then, however, it is questionable, which element present on the KF PDT 105 °C sample would be able to oxidize S(−II) to S(+II)? Since the O 1s signal decreases strongly after rinse, and also no F is detectable (not shown), chemically, there was no element with a sufficiently high redox potential left, which could oxidize S. Therefore, the S species might not be existent as a thiosulfate. S species in even higher oxidation states like sulfates (S(+VI)) lie too far away, at binding energies > 168 eV. Thus, all in all it seems most probable that Cu(I)-S species have formed [127–129].

An explanation, why a Cu-S species only forms on KF PDT 105 °C goes as follows: As it was shown in Chapter 6.1, the KF PDT 105 °C sample is the only sample, where Ga and In are removed from the surface, at the same time. The resulting surface is therefore Ga- and In-depleted (as pointed out in the summary of Chapter 6.1). The remaining Cu (and Se) atoms are thus coordinatively unsaturated, and only then will be able to react with new binding partners, e.g., sulfides.

To sum up, for the rinsed KF PDT 105 °C sample the formation of an insoluble, stable second Cu-component in an oxidic, sulfidic and/or selenic chemical environment (Cu-S-Se-O) is supposed. A more accurate identification is not possible so far from XPS results, because in metal salts O, S and Se show pronounced chemical similarities.

6.2.4 Remaining Na species on the CIGSe surface after the rinsing step

Besides a possible formation of new S-components, the rinse also deposits some additional Na onto the sample surfaces. A short characterization of the chemical state of Na is presented. For an overview, the Na 1s spectra for all samples are displayed, before and after rinsing, in Figure 6.2.4.1.

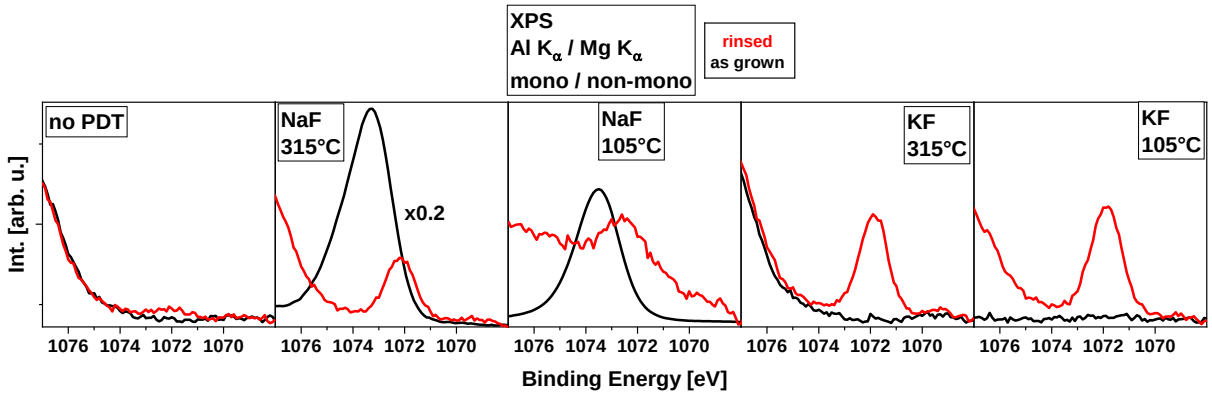

Figure 6.2.4.1 Na 1s spectra for all samples in as-grown condition (black) and after rinsing (red). All spectra are measured with Al K_α excitation, except for the NaF PDT 105 °C sample, which was measured with Mg K_α excitation. For a better comparison of absolute intensities, the scaling is equal in all diagrams.

After rinsing a Na 1s signal is detected on all samples. The Na 1s signal intensity (peak area) increases in the following order of samples: no PDT < NaF PDT < KF PDT. All Na 1s signals can be fitted with one single Voigt function, which is also equal in shape and width for the NaF PDT 315 °C, KF PDT 315 °C and KF PDT 105 °C sample. The Na 1s signal for NaF PDT 105 °C is wider and different in shape, possibly because of excitation with Mg K_α, rather than Al K_α (mono). Na 1s and Na KLL positions are presented in the Wagner plot for the modified Auger parameter α'_{Na} in Figure 6.2.4.2.

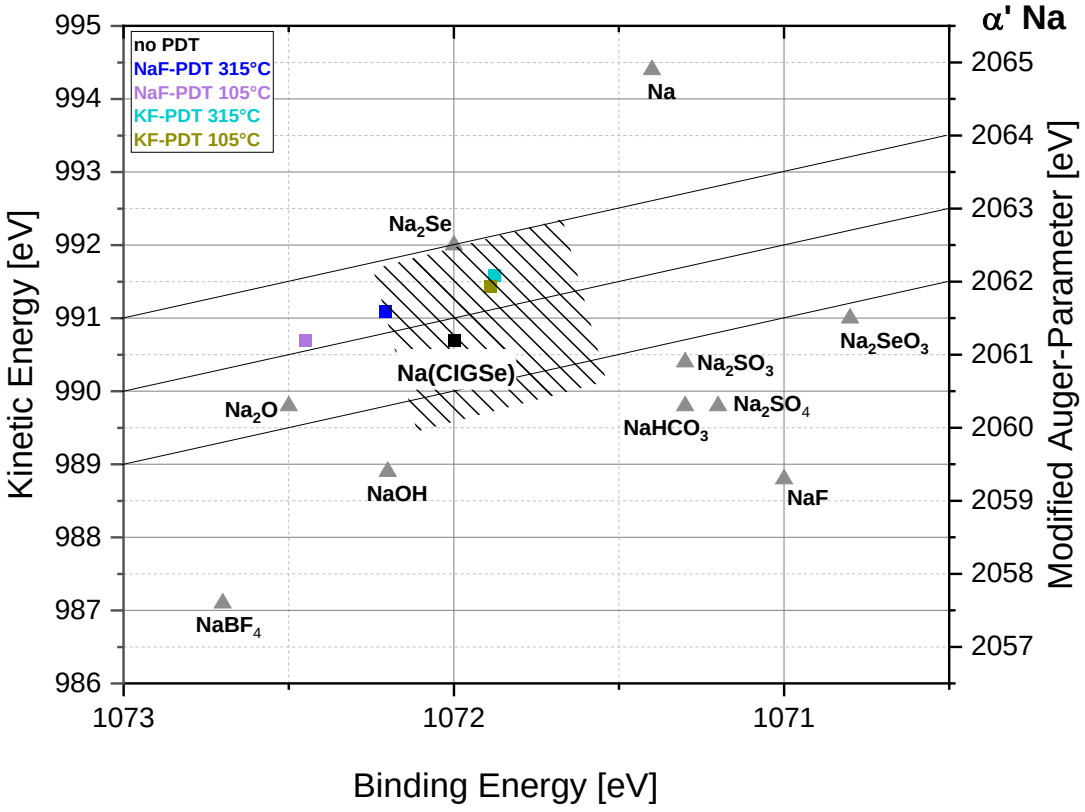

Figure 6.2.4.2 Wagner Plot of the modified Na Auger parameter α'_{Na} for the differently-treated, rinsed PDT CIGSe surfaces. Literature values for Na(CIGSe) are marked as a hatched area. The gray triangles show the data points from literature for Na in different chemical environments.

With α'_{Na} ~ 2063.3 ± 0.2 eV the Auger parameter is similar for all PDT samples and is slightly different for the untreated reference (α'_{Na} ~ 2062.7 eV). Upon comparison with literature values, all Na species should exist in an chemical environment, in which they are bound to oxygen and selenium. This Na species will be denoted as “Na-Se-O“. For NaF-treated samples, a distinct shift of Na 1s to higher binding energies is observed. Especially the NaF PDT 105 °C sample (pink) has “left“ the region where Na(CIGSe) is expected, and assume a more oxidic environment, like for Na_2O, for example. Yet, no high amounts of O were found, specifically on the NaF PDT 105 °C sample. The highest amounts of O (according to O 1s intensity) is found on the rinsed KF PDT 105 °C sample, in which Na 1s in turn, has one of the lowest binding energies.

One possible explanation might be a Na-Br-bond, since bromine is found on the rinsed NaF PDT 105 °C sample. The rinsed NaF PDT 105 °C sample is the only sample, which suffers from an unintended contamination with bromine. The bromine exists as a bromide species (Br^-) on the CIGSe surfaces in relative amounts of ~3 % and until now, no specific effect on device performance is observed.

6.2.5 Relative changes of CIGSe surface stoichiometry due to AlkF PDT and subsequent rinsing step and summary of reaction products

So far, it has been observed that the rinse has washed off most of the PDT reactants, and that a thin secondary component layer (in case of KF PDT), together with a Na-Se-O component, has formed on the surface. It is evaluated now, how the stoichiometry of the underlying CIGSe phase has changed. Like for the analysis of the as-grown samples, one will determine and compare peak areas from photoelectron signals appearing in the "Low binding energy region" at E_{Bin} ~ 80 – 0 eV. The estimated values are depicted below in Table 5.

	Peak-Areas [arb. u.]			Peak-Area Ratios	
Sample	**In $4d_{5/2}$**	**Ga $3d_{5/2}$**	**Se $3d_{5/2}$**	$\frac{Ga}{In}$	$\frac{Ga+In}{Se}$
no PDT	2733	525	4067	0.19 ± 0.01	0.80 ± 0.03
NaF 315	2976	498	4190	0.17 ± 0.01	0.83 ± 0.04
NaF 105	1163	275	1869	0.24 ± 0.02	0.77 ± 0.03
KF 315	3638	157	3759	0.04 ± 0.00	1.01 ± 0.05
KF 105	2053	398	2973	0.19 ± 0.01	0.82 ± 0.14

Table 5 Determined peak areas for In $3d_{5/2}$, Ga $3d_{5/2}$, Se $3d_{5/2}$ (solely the CIGSe part of the peak is included, secondary species are excluded here) and calculated peak area ratios for the untreated, rinsed sample and the rinsed PDT samples. Delta is the error margin of the corresponding ratios.

For the NaF PDT 315 °C sample a very slight Ga-depletion is determined, together with an In- and Se-enrichment. This sounds reasonable, since the Ga-F, which was formed during PDT, has decreased the amount of Ga(CIGSe) and has now been washed off the surface.

A similar trend is visible for the KF PDT 315 °C sample: A strong decrease is observed for Ga, a slight decrease for Se, and an enrichment of In.

The decrease of Se can be explained with formation of the additional Se species of the K-Se-In(-O)-component: Some amounts of Se(CIGSe) probably react to form Se/(K-In-Se(-O)). This part of Se(CIGSe) is therefore "consumed" within the KF PDT 315 °C so that the intensity for Se(CIGSe) decreases.

The increase in In 4d intensity can be explained as follows:

As less Ga atoms are present at the surface, inelastic scattering of In 4d photoelectrons by these Ga-atoms is decreased. Hence, more In 4d photoelectrons are detected. Alternatively, the In atom concentration could have increased at the surface, due to formation of the K-Se-In(-O) component.

On the NaF PDT 105 °C sample the Ga/In ratio and the (Ga+In)/Se ratio are (within the margin of error) comparable to the ratios of the untreated sample. Therefore, a nearly unchanged surface composition of the NaF PDT 105 °C sample is assumed.

The composition of the KF PDT 105 °C sample also seems to be "restored" after rinsing, and no relative changes compared to the untreated, rinsed sample are observed. The attenuation of the signal intensities for In, Ga and Se can be explained by the Cu-S-Se-O species, which lies on top the CIGSe surface. It must be stressed, however that this additional Cu species on

top (Cu-S-Se-O) has been disregarded in Table 5. Therefore, the Ga/In and (Ga+In)/Se ratios are similar to the untreated sample, but the Cu(CIGSe) amounts might be reduced due to formation of Cu-S-Se-O.

After completion of the chemical characterization of the rinsed samples, a summary of the most important results is attempted. For this purpose, a sketch is shown in Figure 6.2.5.1 that presents the determined components on the different sample surfaces.

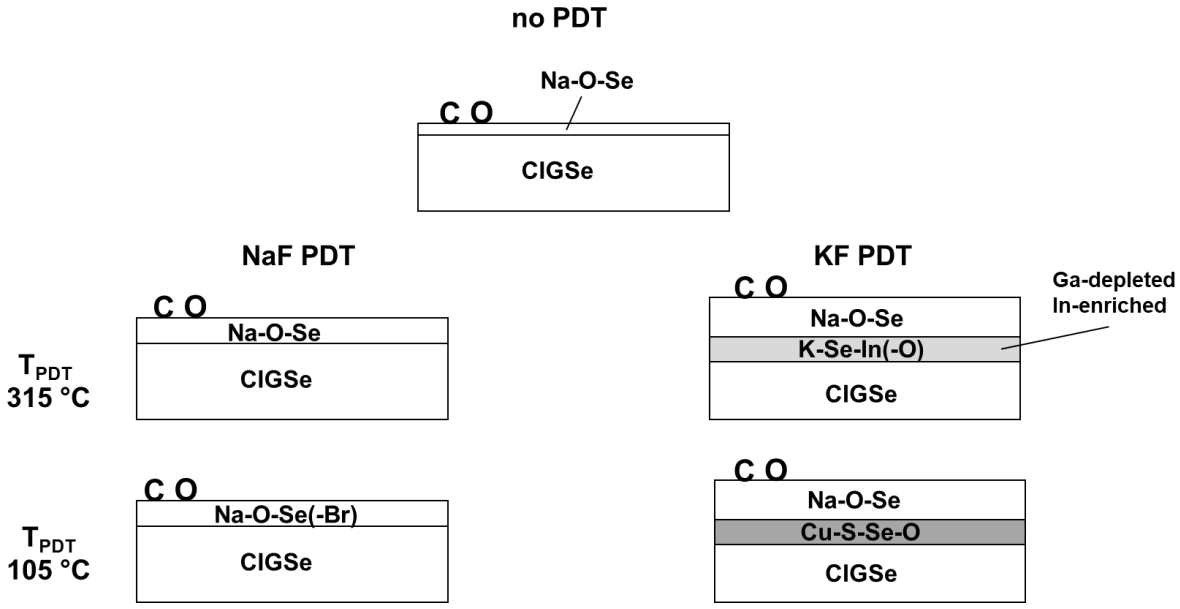

Figure 6.2.5.1 Summary of surface components on the untreated, rinsed reference sample ("no PDT") and different PDT-treated, rinsed samples. Note, that the sketch is simplified and does not represent the exact morphology of the different components on the CIGSe surface.

Rinsing the PDT samples with an aqueous Na_2S solution has a great impact on the chemical composition of the sample surfaces.

The rinse removes all fluorides from the surfaces like alkali fluorides, but also PDT reactants like Ga-F species and In-F species. At the same time, Na from the rinse is deposited on the CIGSe surface, where it probably exists, chemically bonded to Se and O. This Na-Se-O component covers the surface in different amounts in increasing order on the samples: no PDT < NaF PDT < KF PDT. Exclusively on the NaF PDT 105 °C sample, low amounts of bromide are detected, which could be part of the Na-O-Se component.

The composition of the NaF PDT sample surfaces is nearly unchanged, compared to an untreated (no PDT) sample, although high amounts of Ga-F species (relative to Ga(CIGSe)) were found especially on the NaF PDT 315 °C sample after PDT (see Figure 6.1.2.2, page 43).

In contrast, after a KF PDT the surface composition is altered dramatically, and also depends on T_{PDT}: For the KF PDT 315 °C sample the depletion in Ga at the CIGSe surface is very pronounced and a stable K species is observed, together with a new Se species, bounded to In. One suggests the formation of a component, in where these new species are combined, denoted as "K-Se-In(-O)". The exact stoichiometry and bonding situation, however, is not clear.

On the KF PDT 105 °C sample, Ga-F, as well as In-F species have been washed away during the rinse, so that in this case probably a Ga- and In-depleted CIGSe surface resulted. Together with S from the rinse, the (relatively) Cu- and Se-enriched surface forms a Cu-O-Se-S

secondary component. This Cu-rich secondary component is speculated to create the detrimental electrical effects, presented in Chapter 5.

Of course, the here presented sketch is only a very simplified depiction of the surface structure. For example, it is not clear, if the secondary components (Na-Se-O, K-Se-In(-O), Cu-S-Se-O) cover the surface homogeneously (thickness-variation, layer or island growth, …). Since the CIGSe surface is a polycrystalline surface, and the XPS technique measures the signal integrated over the whole CIGSe surface, one is not able to examine the exact chemical situation at the very different facets of the CIGSe surface.

7 Promotion of the chemical reactivity by elemental Se supply during the KF PDT

The simultaneous supply of alkali fluorides and Se during the PDT substantially contributes to the effectiveness of the PDT. Many research groups coevaporate Se during the PDT, but the exact explanation for the chemical role of Se has not been elucidated so far. One possible reason is as follows: With thermal desorption experiments it was shown, that a heated CIGSe surface decomposes under vacuum conditions by desorption of Ga- and In-selenides [130]. To deal with this problem, a low Se flux is applied when the CIGSe sample is still to be heated (e.g., during a PDT). It is then believed that a low Se flux impedes the desorption of selenides from the surface and thereby stops the degradation of the CIGSe sample. Like it was mentioned before, the effectiveness of this procedure has not been examined, yet.

Another observed Se-effect is, that, without a Se supply during PDT, the alkali diffusion into the CIGSe layer is pronouncedly impeded and the resulting cell efficiencies are slightly higher than those with Se. These observations have already been made at ZSW but are not explained, yet.

Therefore, a thorough explanation of the chemical involvement of Se in the PDT on the CIGSe surface is necessary. With a better understanding of the PDT-mechanism, it might be easier to explain, e.g., the formation of In-F species, which exceptionally arise on the KF PDT 105 °C sample. Hence, the effect of Se on both KF PDT samples will be evaluated, since KF PDTs lead to more drastic chemical changes of the CIGSe surface. The hope is that a KF PDT is more sensitive towards variations in the Se supply, than a NaF PDT. (This observation has also been made by R. Würz [131]) Following thereon, the chemical differences, which stem from different Se supplies, might be more pronounced for KF PDTs.

To investigate an extreme case, consequently KF PDTs with no Se supply at all will be examined. Small traces of coevaporated Se, however, cannot be fully excluded, since desorption of Se from hot parts of the deposition chamber cause a permanent small Se background pressure. This circumstance must be taken into account, although a liquid nitrogen cooling shroud was used in the PVD chamber.

Throughout the whole analysis of the new KF PDT samples without Se supply, the results and spectra of the KF PDT samples with Se supply from Chapter 6 are additionally presented, to precisely highlight the differences arising from Se.

7.1 Comparison of the reaction products after a KF PDT with or without Se supply (“as-grown” samples)

The KF PDT samples with and without Se supply were prepared in two different sample sets on two different preparation runs with a time lag of 1 year. Over this time period, the condition of the deposition chamber had changed, such as the residual gas composition, the composition of the material residue at the chamber walls or traces of water therein. All in all, however, the resulting CIGSe bulk compositions of the two sample sets are nearly identical, as verified by X-ray fluorescence measurements. Comparison of XPS measurements showed a slight decrease of Se-amount at the surface of the new samples (not shown). More important, however, is the decrease in intensity of the whole spectrum by ~50%. It is assumed that the reason for this decrease is a difference in the distance between sample and X-ray tube, since the X-ray tube was equipped with an additional pumping station in the meantime. Therefore, to better compare the signal intensities of the two sample sets to each other, the intensity of all spectra of the new sample set will be increased by a factor of 2.

For a first glance, the survey spectra of the KF PDT 315 °C and KF PDT 105 °C sample surfaces with and without Se in Figure 7.1.1.1 will be compared in the “as-grown“ state.

From now on, samples that underwent a standard PDT with Se supply will be marked with “w/ Se“. Samples that underwent a PDT without Se supply will be marked with “w/o Se“.

7.1.1 General difference in the chemical constitution of CIGSe surfaces after a KF PDT with or without Se supply

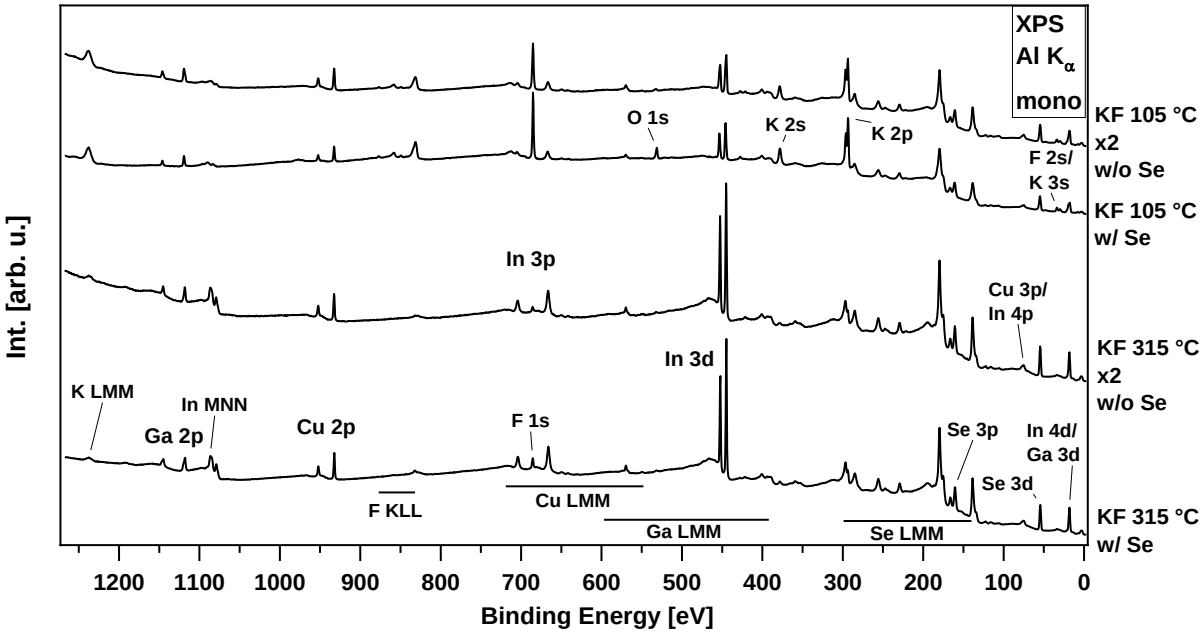

Figure 7.1.1.1 Al K_α excited survey spectra for KF PDT samples (as-grown) at T_{PDT} = 315 °C and 105 °C with and without Se supply during the PDT. All measured spectra of KF PDTs without Se are multiplied with a factor of 2. Prominent photoelectron and Auger lines from CIGSe- and KF-related elements are highlighted.

In Figure 7.1.1.1 it can be seen that for both T_{PDT}, the survey spectra of KF PDTs with and without Se are very similar. No additional photoelectron or Auger signals are detected on both samples without Se supply, compared to the respective sample with Se supply. For the KF PDT 315 °C w/o Se sample ~50 % less intensity for F 1s is detected than on the KF PDT 315 °C w/ Se sample. For the KF PDT 105 °C w/o Se sample ~10 % less K 2p intensity, ~ 25 % less F 1s intensity and ~80 % less O 1s intensity is detected than on the KF PDT 105 °C sample with Se supply.

Another noticeable difference is the inelastic background. For both KF PDT samples without Se, additional background intensity at E_{Bin} > 1070 eV is observed, in comparison to the KF PDT samples with Se.

For a more detailed comparison, the CIGSe core levels will be discussed in the following.

7.1.2 Detailed examination of the difference in the chemical structure after a KF PDT with or without Se supply

Analysis of Ga-related photoelectron and Auger signals

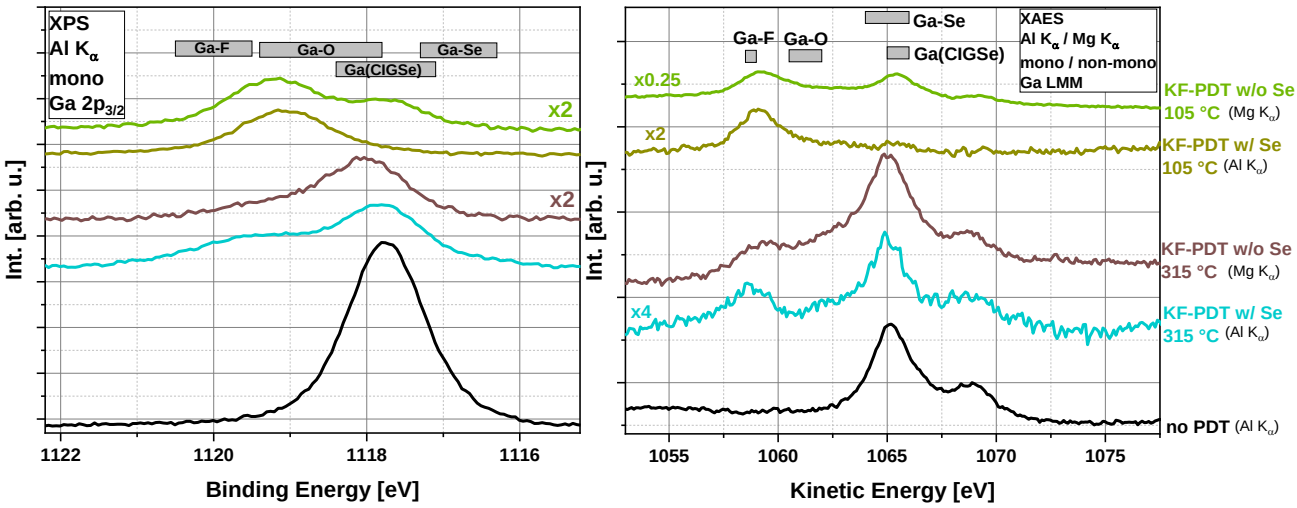

Figure 7.1.2.1 Ga $2p_{3/2}$ photoelectron spectra (left) and Ga LMM Auger spectra (right) for CIGSe samples (as-grown) which underwent KF PDTs at T_{PDT} = 315 °C and 105 °C and with different Se supplies. Note: All Ga $2p_{3/2}$ spectra were measured with Al K_α radiation, whereas the Ga LMM Auger spectra were measured by either Al K_α or Mg K_α radiation, depending on the sample. Gray bars represent binding energy ranges of different Ga-bonds according to literature data.

Figure 7.1.2.1 compares the Ga $2p_{3/2}$ photoelectron signals for KF PDTs with and without Se at different T_{PDT}. For the Ga $2p_{3/2}$ of the KF PDT 315 °C w/o Se sample surface a peak maximum at E_{Bin} ~ 1118 eV is observed and a slightly broader shoulder at higher binding energies, compared to the respective sample with Se. The shoulder at higher binding energies is less pronounced on the KF PDT 315 °C w/o Se sample. The signal can be fit with two Voigt-functions and a linear background, similar to the sample with Se (not shown). In both cases a Ga(CIGSe) species and a Ga-F species is found. The difference between the two samples is that, relatively and absolutely, lower amounts of Ga-F bonds (to Ga(CIGSe)) on the KF PDT 315 °C w/o Se sample are detected. A comparison of the corresponding Ga LMM Auger signals shows the same finding: Both Ga LMM spectra of the KF PDT 315 °C samples look similar, and two Ga species belonging to Ga(CIGSe) and Ga-F can be detected at E_{Kin} ~ 1065 and 1059 eV, respectively. For the KF PDT 315 °C w/o Se sample, however, the ratio of Ga-F to Ga(CIGSe) is smaller on the KF PDT 315 °C w/o Se sample than on the KF PDT 315 °C w/ Se sample. Again, the Ga LMM Auger signals were not precisely fit and it might be that some percent of Ga-O bonds are overlooked. Like for the samples with Se (Chapter 6), however it is assumed that the residual, unidentified Ga species make a small contribution, only.

On the KF PDT 105 °C samples (w/ and w/o Se) one also observes two different Ga-species at E_{Bin} ~ 1017.5 and 1019 eV, stemming from Ga(CIGSe) and Ga-F bonds, respectively. In addition, different ratios of Ga-F to Ga(CIGSe), are observed on the KF PDT 105 °C samples, depending on the Se supply: On the KF PDT 105 °C w/o Se sample, more Ga(CIGSe) (relative to Ga-F) is found than on the KF PDT 105 °C w/ Se sample. This trend can be observed in both spectra, Ga $2p_{3/2}$ and Ga LMM.

Despite these differences, for both KF PDTs at 315 °C (with and without Se), Ga-F is the minor species and Ga(CIGSe) is the major species. For both KF PDTs at 105 °C this ratio is reversed and Ga-F is the major species, while Ga(CIGSe) is the minor species.

Like for the samples with Se in Chapter 6, the photoelectron peak positions are determined by their fits and the position of the Ga LMM Auger signals is read from the spectra. The resulting data points for the modified Auger parameter α'_{Ga} for Ga are illustrated in the Wagner plot in Figure 7.1.2.2.

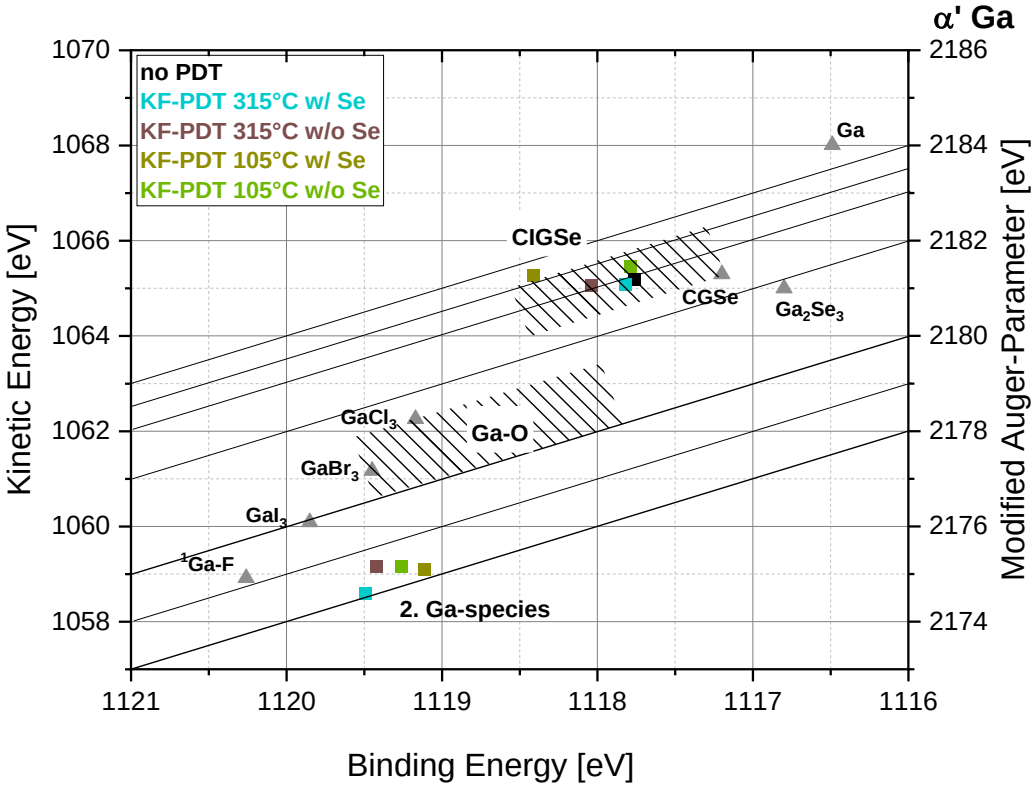

Figure 7.1.2.2 Wagner plot of the modified Auger parameter α'_{Ga} for the pristine CIGSe surface (black) and KF PDTs (as-grown) with or without Se supply. The data point marked with [1] belongs to a speculation found in literature. The shaded areas as well as the gray triangles show data points from literature for Ga in different bonding environments.

The Ga-F and Ga(CIGSe) species formed in KF PDTs without Se are chemically very similar to those species formed in a KF PDT with Se. This fact is independent of T_{PDT}. For Ga(CIGSe), α'_{Ga} decreases by ~0.4 eV from KF PDT 105 °C w/ Se to KF PDT 105 °C w/o Se. This can mainly be due to different amounts of fluoride at the surface, as will be seen in Chapter 7.1.5.

Analysis of Cu-related photoelectron and Auger signals

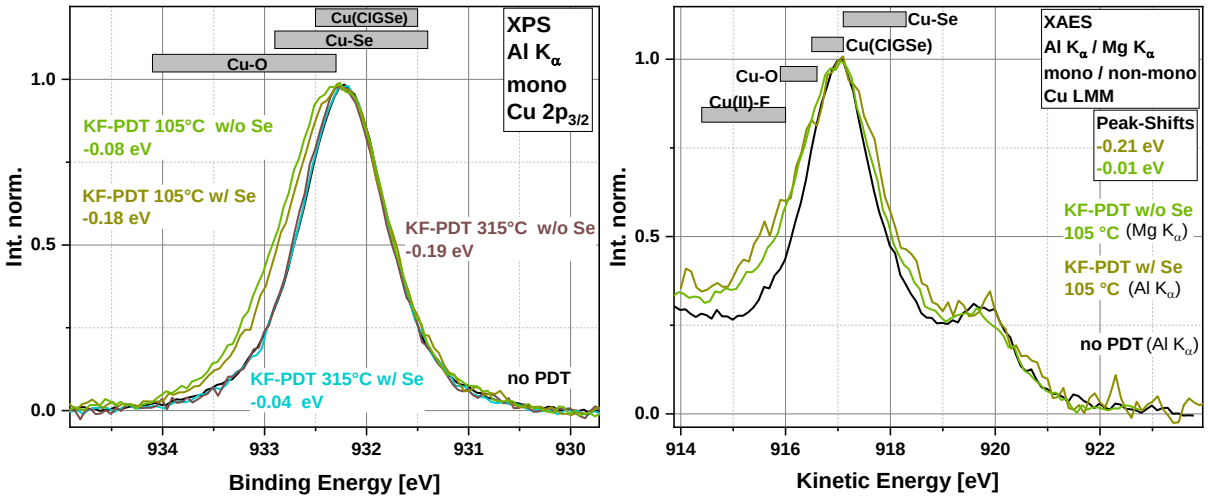

Figure 7.1.2.3 Cu $2p_{3/2}$ photoelectron spectra and Cu LMM Auger spectra for CIGSe samples which underwent KF PDTs (as-grown) at different T_{PDT}=315 °C and 105 °C and with and without Se supply. Cu $2p_{3/2}$ (Ga LMM) spectra are normalized by setting the low binding energy background at ~930 eV (high kinetic energy background at ~923 eV) to zero and the peak maximum to one. Additionally, the signals are shifted on the energy-axis to allow for a better comparison of the spectral shape. Respective shifts are given in the diagram. Gray bars represent binding energy ranges of different Cu-bonds according to literature data.

For both KF PDT 105 °C w/o Se samples, a broadening of the Cu $2p_{3/2}$ signal is observed (Figure 7.1.2.3, left), in which the broadening is slightly more pronounced for the KF PDT 105 °C w/o Se sample, than for the KF PDT 105 °C w/ Se sample. Possibly, an additional Cu-bond exists for the KF PDT 105 °C w/o Se sample, but in higher amounts (relative to Cu(CIGSe)) than for the KF PFT 105 °C sample. According to literature values, the additional Cu species can stem from Cu-O or Cu-Se-bonds, similar to the case of the sample with Se.

In the Cu LMM Auger spectra (Figure 7.1.2.3, right) also a broadening of the signal of both KF PDT 105 °C samples (with and without Se) is observed. The signal broadening can be due to an additional Cu species at lower kinetic energy, like Cu-O, which is in accordance with the Cu $2p_{3/2}$ spectrum. Moreover, because no satellite structure is observed in the Cu $2p_{3/2}$ spectrum at higher E_{Bin}, one can rule out the existence of Cu(II)-species.

In the Cu LMM Auger spectrum, however, the relative contributions of Cu(CIGSe) and Cu-O (or Cu-Se) are different than in the Cu $2p_{3/2}$ spectrum. This might be due to different depth-distributions of the additional Cu species throughout the surface region. Since Cu $2p_{3/2}$ photoelectrons are more surface sensitive than Cu LMM Auger electrons, higher amounts of the additional Cu species (relative to (Cu(CIGSe)) could exist at the upper most surface region for the KF PDT 105 °C w/o Se sample (compared to the KF PDT 105 °C w/ Se sample), and lower amounts somewhat deeper within the surface.

Both KF PDT 315 °C samples (with and without Se) show a similar shape in the Cu $2p_{3/2}$ spectra and are detected in the binding energy region for Cu(CIGSe). Therefore, it is assumed that no additional Cu species forms on the KF PDT 315 °C w/o Se sample, and also that the chemical environment of Cu is similar to that of the KF PDT 315 °C w/ Se sample.

To evaluate the exact position of the particular Cu species on the KF PDT 105 °C w/o sample, the Cu $2p_{3/2}$ signal was fitted with two Voigt-functions. For the fit of the Cu LMM Auger, the signal was reproduced by a sum of two Cu LMM spectra of the untreated Ar^+-ion cleaned reference sample (no PDT). These reference spectra were allowed to be resized and shifted

to reproduce the Cu LMM Auger signal of KF PDT 105 °C w/o Se. Additionally, a linear background was added. The resulting positions for Cu $2p_{3/2}$ and Cu LMM are displayed in the Wagner plot of the modified copper Auger parameter α'_{Cu} in Figure 7.1.2.4.

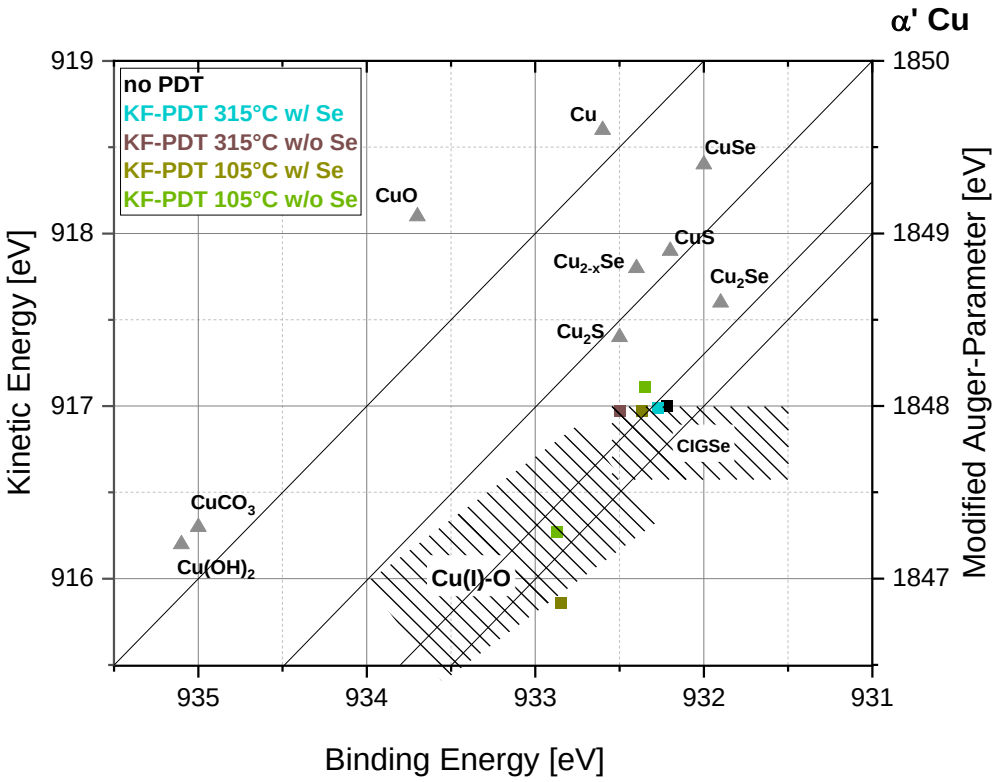

Figure 7.1.2.4 Wagner plot of the modified Auger parameter α'_{Cu} for the pristine CIGSe surface (black) and KF PDTs (as-grown) with and without Se supply. The shaded areas as well as the gray triangles show data points from literature for Cu in different bonding environments.

For the KF PDT samples w/o Se, a modified Auger parameter of α'_{Cu} = 1849.46 eV is calculated for the Cu(CIGSe) species. For the KF PDT samples w/ Se, a modified Auger parameter of α'_{Cu} = 1849.26 eV is calculated for the Cu(CIGSe) species. For these four samples, the main contribution is expected to be Cu in a CIGSe-like chemical environment.

The additional Cu species, which is observed on the KF PDT 105 °C samples, can be assigned to Cu-O bonds. Despite that α'_{Cu} = 1849.14 eV of the KF PDT 105 °C samples is similar to that of the Cu(CIGSe) species (α'_{Cu} ~ 1849.25 eV), the Cu $2p_{3/2}$ binding energy and Cu LMM Auger kinetic energy suggest Cu-O bonds. Therefore, the additional Cu species on the KF PDT 105 °C w/o Se sample might be a Cu-O-Se-like component, with slightly less amounts of O, compared to the KF PDT 105 °C w/ Se sample. This conclusion sounds reasonable, since the O 1s signal is much smaller on the KF PDT 105 °C w/o Se sample.

Analysis of In-related photoelectron and Auger signals

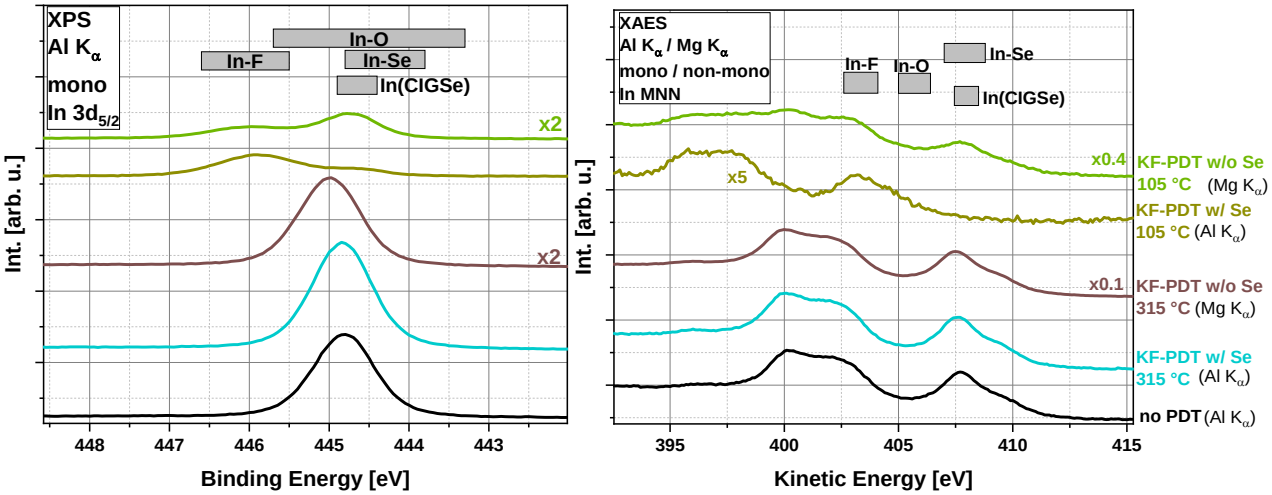

Figure 7.1.2.5 In $3d_{5/2}$ photoelectron spectra (left) and In MNN Auger spectra (right) for CIGSe samples which underwent KF PDTs at T_{PDT} = 315 °C and 105 °C and with different Se supplies. Note: All In $3d_{5/2}$ spectra were measured with Al K_α radiation, whereas the In MNN Auger spectra were measured by either Al K_α or Mg K_α radiation, depending on the sample. Gray bars represent binding energy ranges of different In-bonds according to literature data.

Figure 7.1.2.5 (left) compares the In $3d_{5/2}$ photoelectron signals of KF PDTs with and without Se supply. Peak-shape and –width of the two KF PDT 315 °C samples (with and without Se) are similar, and no additional In-components are observed. For both KF PDT 105 °C samples, additional In species are found at higher binding energies. In comparison to literature data In-O and In-F bonds may have formed. This was already observed for the KF PDT 105 °C w/ Se sample surface.

Like for Ga, the ratio of In(CIGSe) to the additional In species is different on the KF PDT 105 °C w/o Se sample, compared to the KF PDT 105 °C w/ Se sample. On the KF PDT 105 °C w/o Se sample, In(CIGSe) is detected as a major component, whereas for KF PDT 105 °C w/ Se, In-O and In-F are major components. A look at the In MNN signals (Figure 7.1.2.5, right) confirms this observation: For the KF PDT 105 °C w/o Se sample, In(CIGSe) is still visible in the spectrum at E_{Kin} ~ 408 eV and additional intensity is observed from E_{Kin} ~ 403 – 398 eV, compared to the In MNN signal of the KF PDT 105 °C w/ Se sample.

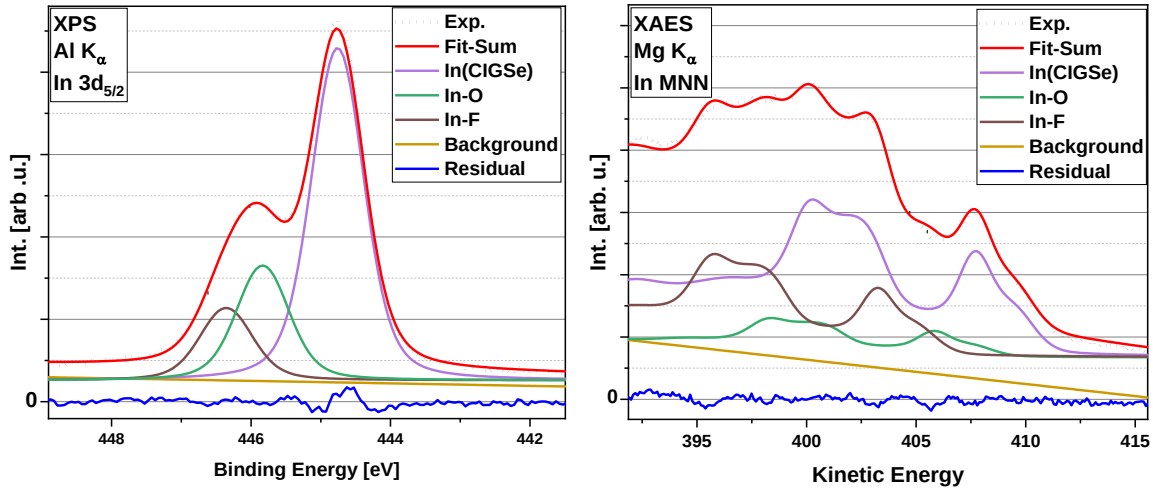

Figure 7.1.2.6 Peak-fit of In $3d_{5/2}$ photoelectron signal (left) and In MNN Auger spectra (right) of KF PDT 105 °C w/o Se to distinguish between the three different In species: In(CIGSe) (purple), In-O (green) and In-F (brown).

Therefore, a complete different In MNN shape results for the KF PDT 105 °C w/o Se sample (compared to KF PDT 105 °C w/ Se) and the fit of In MNN and In $3d_{5/2}$ are depicted in Figure 7.1.2.6.

The In $3d_{5/2}$ (Figure 7.1.2.6, left) signal can be fit with three Voigt-functions representing three In-components, which can be ascribed to In(CIGSe), In-O, and In-F in a ratio of 1 : 0.4 : 0.2. Three In-components can also be found in the In MNN Auger signal (Figure 7.1.2.6, right). The signal was reproduced by a superposition of the In MNN Auger spectrum of the untreated, Ar^+-ion cleaned reference sample (no PDT). The reference sample spectra were resized and shifted, and a linear background was added to reproduce the initial signal. According to literature values, the In species found from the fit of the In MNN spectrum also suggest formation of In(CIGSe), In-O and In-F. The ratio is 1 : 0.3 : 0.7. The two ratios evaluated with In $3d_{5/2}$ and In MNN are different, likely due to the different surface sensitivities of the two measurements. The data suggests that In-F exists mainly at the uppermost surface region as the In MNN measurement is more surface sensitive. To verify the chemical identification of In-O and In-F bonds, the corresponding positions of In $3d_{5/2}$ and In MNN for each sample are illustrated in the Wagner plot for In in Figure 7.1.2.7.

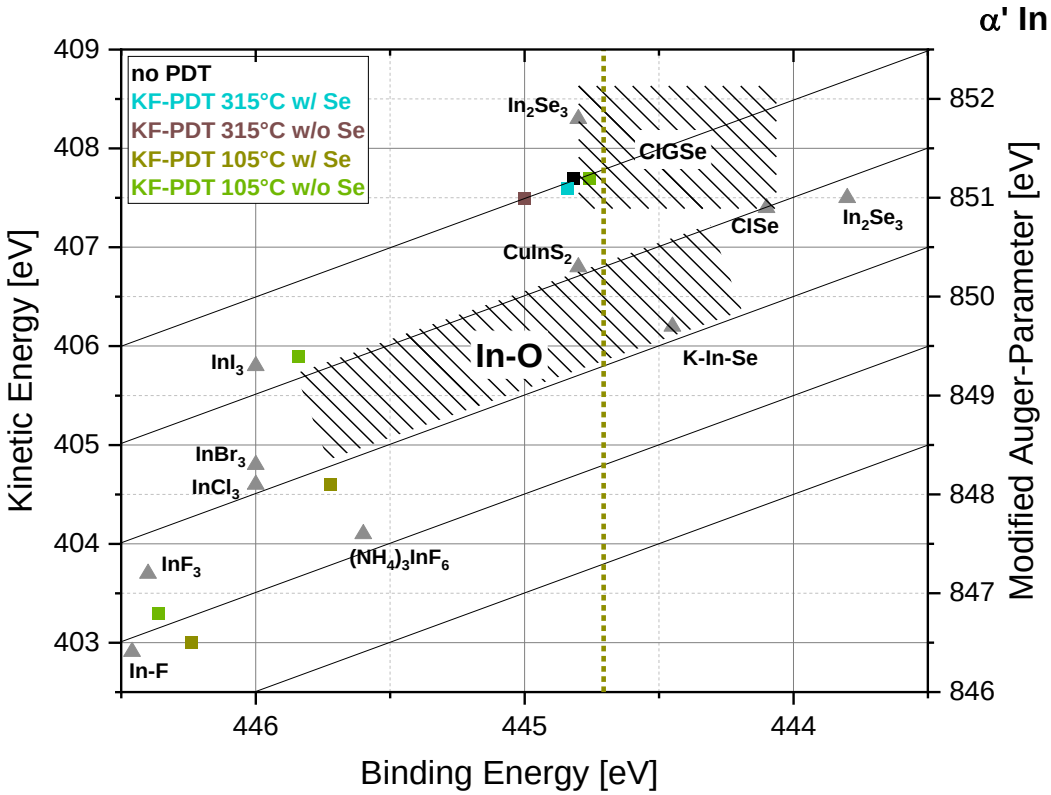

Figure 7.1.2.7 Wagner plot of the modified Auger parameter α'_{In} for the pristine CIGSe surface (black) and KF PDTs (as-grown) with and without Se supply. The shaded areas as well as the gray triangles show data points from literature for In in different bonding environments. For the KF PDT 105 °C w/ Se sample (dark yellow) no In(CIGSe) component was found in the In MNN Auger signal, as described earlier in Chapter 6.1. Therefore, only a dashed line is given at E_{Bin} ~ 444.7 eV.

The modified Auger parameter α'_{In} is very similar for all In(CIGSe) species. The data point for the KF PDT 315 °C w/o Se sample lies 0.2 eV away from the In(CIGSe)-region, possibly due to a different surface states induced band bending, which might change because of varying amounts of fluoride at the CIGSe surface. Nevertheless, the light blue data point for the KF PDT 315 °C w/o Se sample is ascribed to an In(CIGSe) species.

For the additional In species on the KF PDT 105 °C samples, two groups can be roughly observed: One In species at E_{Bin} ~ 445.7 – 445.9 eV and the other one at E_{Bin} ~ 446.2 – 446.4 eV.

The second In species is ascribed to In in an In-O-environment. These In-O environments can be found on both KF PDT 105 °C samples (w/ Se and w/o Se). Although these two data points lie a bit outside the range for literature values of In-O, an In-O environment is the only possible candidate in this region of the Wagner plot. The reason is that for other In-environments, such as In-Se or In-F, another kinetic energy was expected.

The third In species on KF PDT 105 °C w/o Se should also stem from In-F bonds, as was already determined for the KF PDT 105 °C w/ Se sample (in Chapter 6 on page 44 – 46). With a difference in α'_{In} of ~ 0.4 eV the chemical environments are comparable quite well and both lie near other values found in literature.

Analysis of Se-related photoelectron and Auger signals

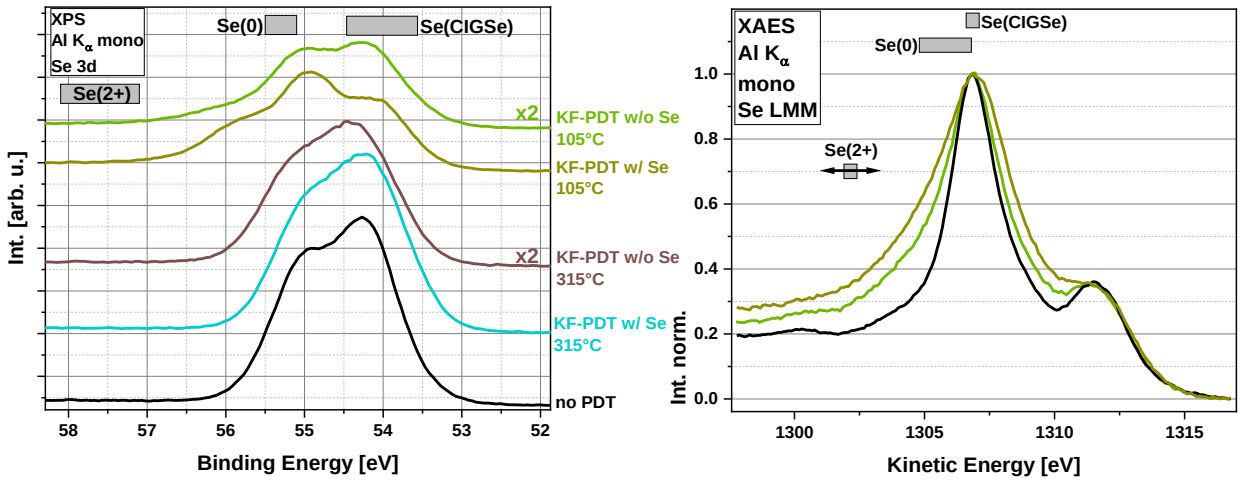

Figure 7.1.2.8 Al K_α excited Se 3d (left) and Se LMM Auger spectra (right) for as-grown CIGSe samples that underwent KF PDTs at T_{PDT} = 315 °C and 105 °C and with and without Se supply. The Auger spectra are normalized to zero at the high kinetic energy background and to one at peak maximum. Gray bars represent binding energy ranges of different Se-bonds according to literature data.

The Se 3d spectra in Figure 7.1.2.8, left, show that the KF PDT 315 °C samples are similar in width and shape and that they are broader than the Se 3d spectrum of the no PDT sample. This suggests that Se on the KF PDT 315 °C w/ Se and w/o Se samples might exist in a chemically not well-defined environment. However, for the KF PDT 105 °C samples (with and without Se), distinct differences in the peak shape are observed for the Se 3d spectra:

The Se 3d spectrum of the KF PDT 105 °C w/o Se sample shows additional intensity at higher binding energy with a shoulder at E_{Bin} ~ 56 eV and slightly more intensity at E_{Bin} ~ 55 eV, compared to the untreated sample. A fit of this Se 3d spectrum with two Voigt-functions reveals the formation on an additional Se species (along with Se(CIGSe)) at higher E_{Bin}. This the additional Se species at higher E_{Bin} is related to elemental Se upon comparison with literature data. Elemental Se was also detected on the KF PDT 105 °C w/ Se sample, as shown in Chapter 6 on page 47+48. However, compared to the KF PDT 105 °C w/ Se sample, the intensity at E_{Bin} ~ 55 and 56 eV is lower on the KF PDT 105 °C w/o Se sample. Therefore, less elemental Se is detected on the KF PDT 105 °C w/o Se sample than on the KF PDT 105 °C w/ Se sample. The Se LMM spectra in Figure 7.1.2.8, right support these findings: For both

KF PDT 105 °C samples (w/ Se and w/o Se), additional intensity is detected at $E_{Kin} \leq 1311$ eV. A fit of the Se LMM signals with a sum of two Se LMM signals for the no PDT samples (not shown) indeed reveals the formation of an additional Se species at lower E_{Kin}, which is ascribed to elemental Se. The fit of the Se LMM signal, however, was not very good, so that high error margins result for the position of the second Se species in the Se LMM spectrum.

The amount of elemental Se (Se(0)) on both KF PDT 105 °C samples (with and without Se) is quite different: Distinctly less Se(0) is observed on the KF PDT 105 °C w/o Se sample, than on the KF PDT 105 °C w/ Se sample. This of course makes sense, since no Se was supplied during the PDT. The question, however, arises: Why can Se(0) be detected at all? One reason could be desorption of Se from hot parts of the deposition chamber, like mentioned earlier in the introduction. Another possibility might be the chemical reaction of selenides (Se(2-)) to form Se(0). Since, formally, no reactant is available to oxidize Se(2-), this reaction might not be very probable, though.

To confirm that a Se(0) species is detected on the CIGSe surfaces, the determined positions for Se 3d and Se LMM are depicted in the Wagner plot for Se in Figure 7.1.2.9.

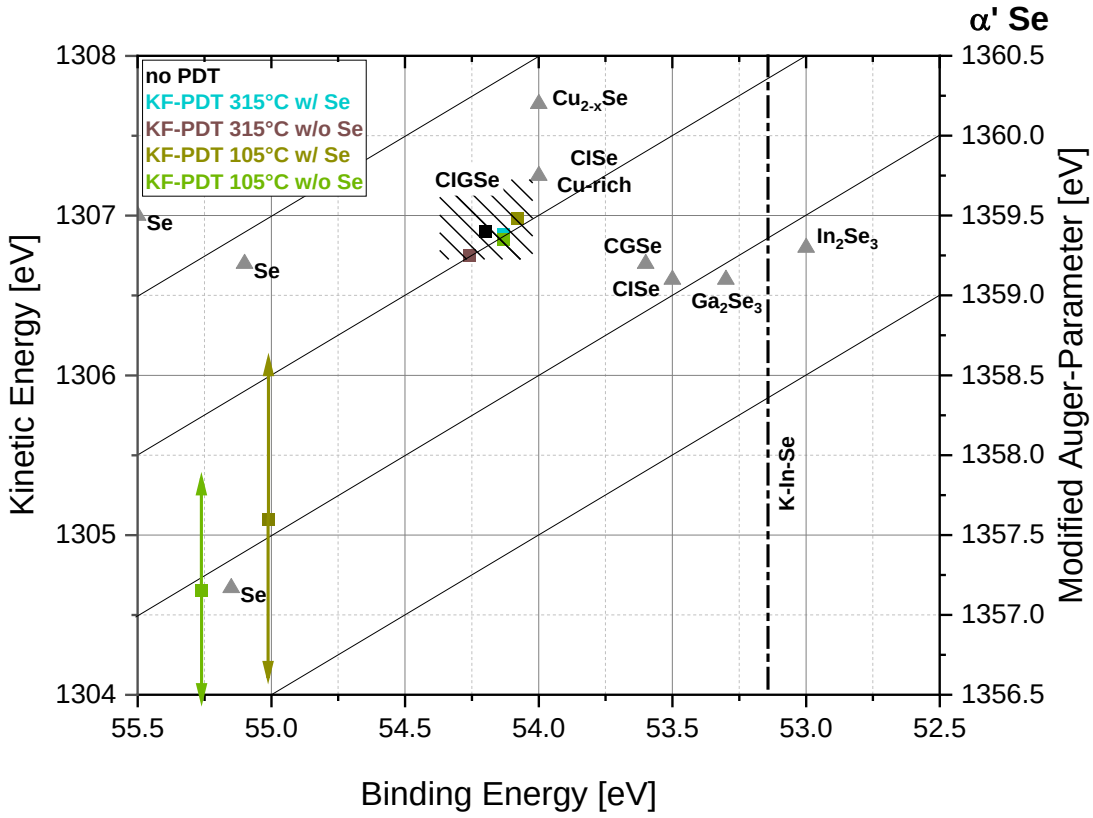

Figure 7.1.2.9 Wagner plot of the modified Auger parameter α'_{Se} for the pristine CIGSe surface (black) and KF PDTs (as-grown) with or without Se supply. The shaded areas as well as the gray triangles show data points from literature for Se in different bonding environments. The error margin for the additional Se species, found on both KF PDT 105 °C samples, is relatively high, due to difficulties with the fit of the spectrum.

All Se(CIGSe) species are chemically very similar and lie within the range of Se(CIGSe) species found in literature. The two additional Se species on the KF PDT 105 °C samples (with and without Se), located at $E_{Bin} > 55$ eV, only differ by 0.2 eV in α'_{Se}. Despite the high uncertainty for E_{Kin}, both points lie in proximity of Se(0), as found in literature. Oxidized Se species, such as Se(2+) appear at distinctly higher binding energies around 57 – 58 eV and can therefore be excluded as possible candidates for the here-found additional Se species.

7.1.3 Comparison of the non-CIGSe related elements after a KF PDT with or without Se supply

Analysis of K-related photoelectron and Auger signals

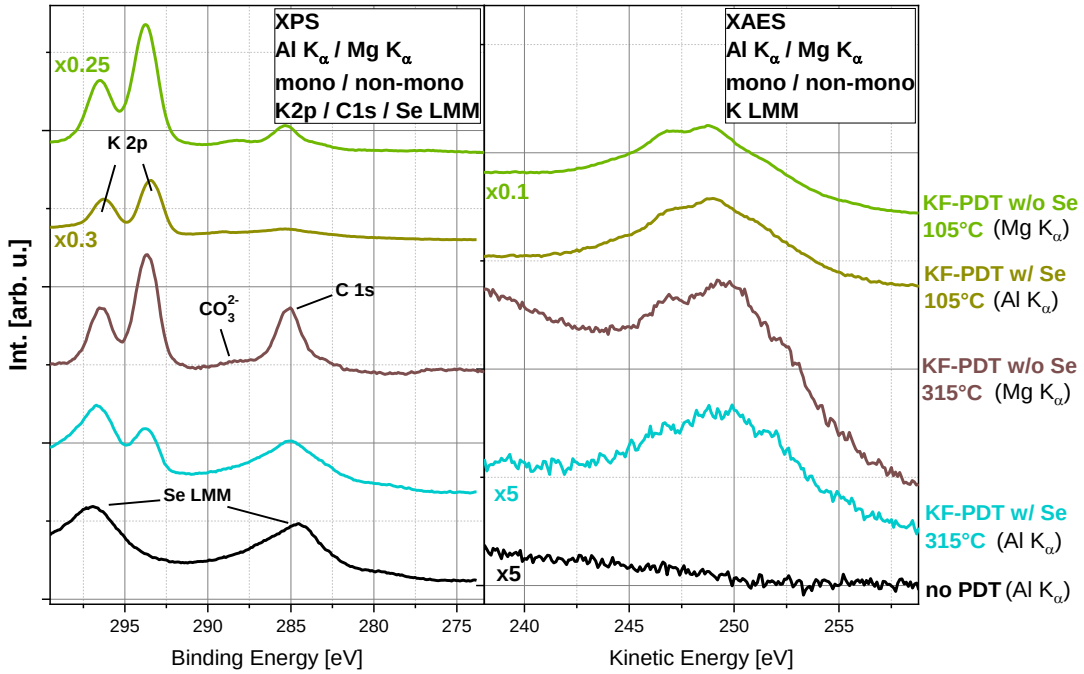

Figure 7.1.3.1 Al K_α or Mg K_α excited K 2p photoelectron spectra (left) and K LMM Auger spectra (right) for as-grown CIGSe samples, which underwent KF PDTs at T_{PDT} = 315 °C and 105 °C and with different Se supplies.

For all KF PDT samples the K $2p_{3/2}$ signal is clearly visible at E_{Bin} ~ 293.5 eV (Figure 7.1.3.1, left). On the Al K_α-excited samples KF PDT 315 °C w/ Se and KF PDT 105 °C w/ Se, however, the K 2p and C 1s signals are overlapped by the Se LMM Auger signal. Especially for the KF PDT 315 °C w/ Se sample (light blue), this Se LMM Auger signal is very intense, so that it partially masks the K 2p signal. On the Mg K_α excited samples KF PDT 315 °C w/o Se and KF PDT 105 °C w/o Se, the K 2p and C 1s signals are uniquely identifiable, though.

When comparing the signal intensities, it is found that the K 2p intensities are higher on the KF PDT 105 °C samples (both, with and without Se supply) than on the respective KF PDT 315 °C samples.

All K 2p signals can be fitted with one doublet; for the Al K_α excited spectra the Se LMM signal was subtracted prior to the fit.

The K LMM Auger spectra look similar with slight differences in shape. Like for the K 2p signals, the intensity for K LMM on the KF PDT 105 °C samples (both, with and without Se supply) is higher than on the respective KF PDT 315 °C samples. This is illustrated in a lower SNR for the KF PDT 315 °C samples (light blue and brown) in Figure 7.1.3.1, right.

To be able to compare the K 2p intensities throughout all KF PDT samples, only Al K_α-excited survey spectra were analyzed (different to the spectra shown in Figure 7.1.3.1). The peak areas for KF PDT 315 °C w/ Se, KF PDT 315 °C w/o Se, KF PDT 105 °C w/ Se and KF PDT 105 °C w/o Se appear in the ratio 1.3 : 1 : 8 : 5. More K on samples at low T_{PDT} is reasonable, since less desorption of K should take place. Moreover, the K 2p signal intensity for samples with Se supply is higher, compared to samples without Se supply.

The position of the K 2p and K LMM Auger signals are illustrated in the Wagner plot for the modified Auger parameter for α'_K potassium in Figure 7.1.3.1.

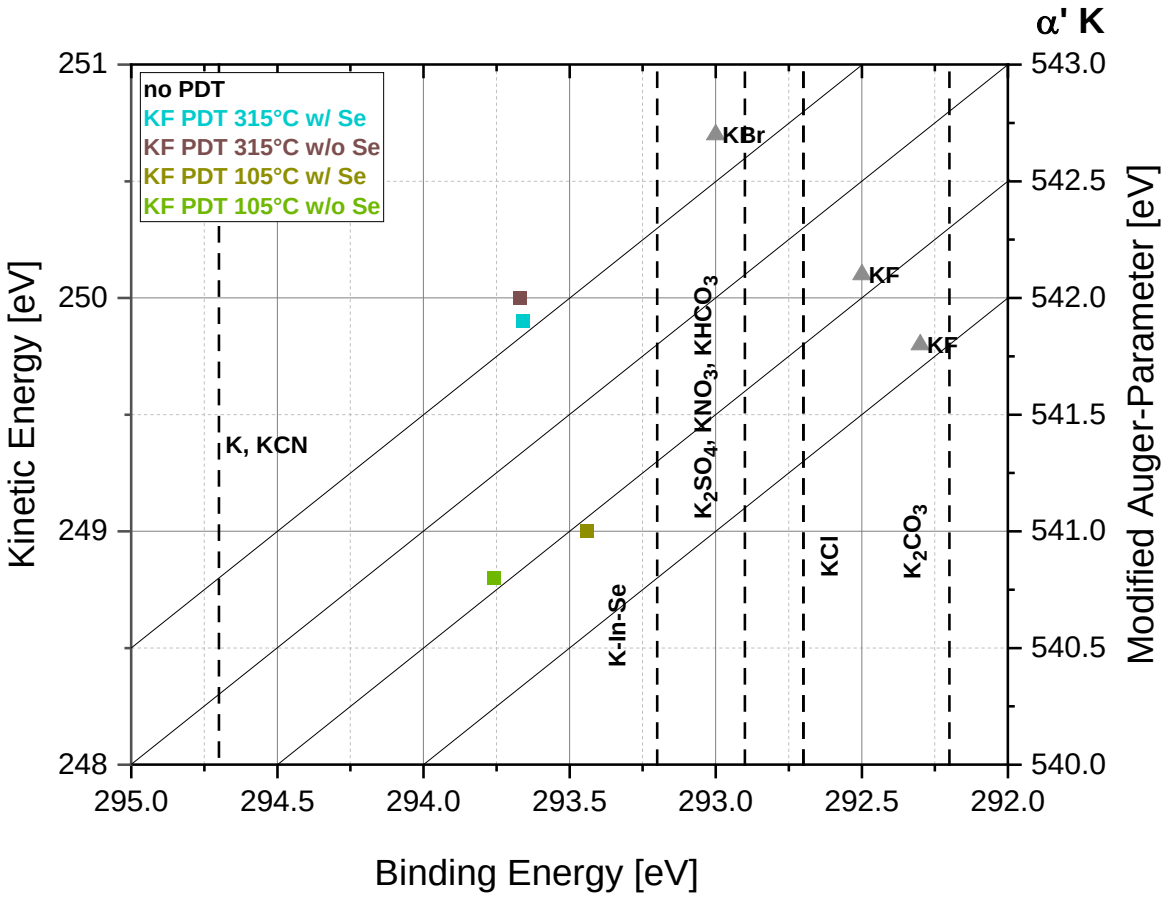

Figure 7.1.3.1 Wagner plot of the modified Auger parameter α'_K for the pristine CIGSe surface (black) and KF PDTs (as-grown) with or without Se supply. The gray triangles show data points from literature values for K in different bonding environments. For many K species only the binding energy is given but no data for K LMM were found in literature. These K species are marked as dashed lines.

For the KF PDT 315 °C samples (with Se and without Se) α'_K ~ 543 eV and both data points lie very close to each other. For the KF PDT 105 °C samples (with Se and without Se) α'_K ~ 542.5 eV and again, their α'_K values are very similar (comparing the samples with and without Se). On both KF PDT samples w/o Se (315 °C and 105 °C, brown and light green) it can be evaluated that K-F bonds have formed, similar to both KF PDT samples w/ Se (315 °C and 105 °C, light blue and dark yellow), as was shown in Chapter 6.1 on page 54. For the KF PDT 315 °C samples (with and without Se), the K-F species resemble more a K-Br component, which could be interpreted that K is bounded to less fluorine atoms, because of a smaller amount of fluorine at the surface. This is in accordance with the amount of fluorine derived from the F 1s spectra in Figure 7.1.3.2.

Analysis of C-related photoelectron signals

Figure 7.1.3.1 shows the C 1s peak, which is clearly visible in case of the Mg K_α excited samples KF PDT 315 °C w/o Se and KF PDT 105 °C w/o Se. An asymmetric C 1s signal is detected for the KF PDT 315 °C w/o Se sample with the peak maximum at E_{Bin}~285.0 eV and additional intensity at E_{Bin}~288.0 eV. According to literature values, the signal at E_{Bin}~285.0 eV stems from hydrocarbon or polymeric carbon and the additional intensity at E_{Bin}~288.0 eV

indicates C as carbonate species (CO_3^{2-}) [132]. For the KF PDT 105 °C w/o Se sample, also an asymmetric C 1s signal is observed with the peak maximum at E_{Bin}~285.3 eV and a second C 1s signal, clearly detectable at E_{Bin}~288.2 eV. These two C 1s signals are ascribed to hydrocarbons or polymeric carbon and carbonate.

The intensity of the main C 1s signal at E_{Bin}~285 eV decreases from the KF PDT 315 °C w/o Se sample to the KF PDT 105 °C w/o Se sample. This decrease can be due to a thicker KF cover layer on the KF PDT 105 °C w/o Se sample, as will be shown further below. The intensity of the C 1s signal at E_{Bin}~288 eV (carbonate) increases from the KF PDT 315 °C w/o Se sample to the KF PDT 105 °C w/o Se sample. A reason for this increase might be a higher amount of carbonate species, due to higher amounts of oxygen on the KF PDT 105 °C w/o Se sample, than on the KF PDT 315 °C w/o Se sample, as will also be shown further below.

Since the other samples were measured with Al K_α radiation, the C 1s signal is strongly overlapped by the Se LMM Auger and can therefore not be analyzed easily.

Analysis of F-related photoelectron and Auger signals

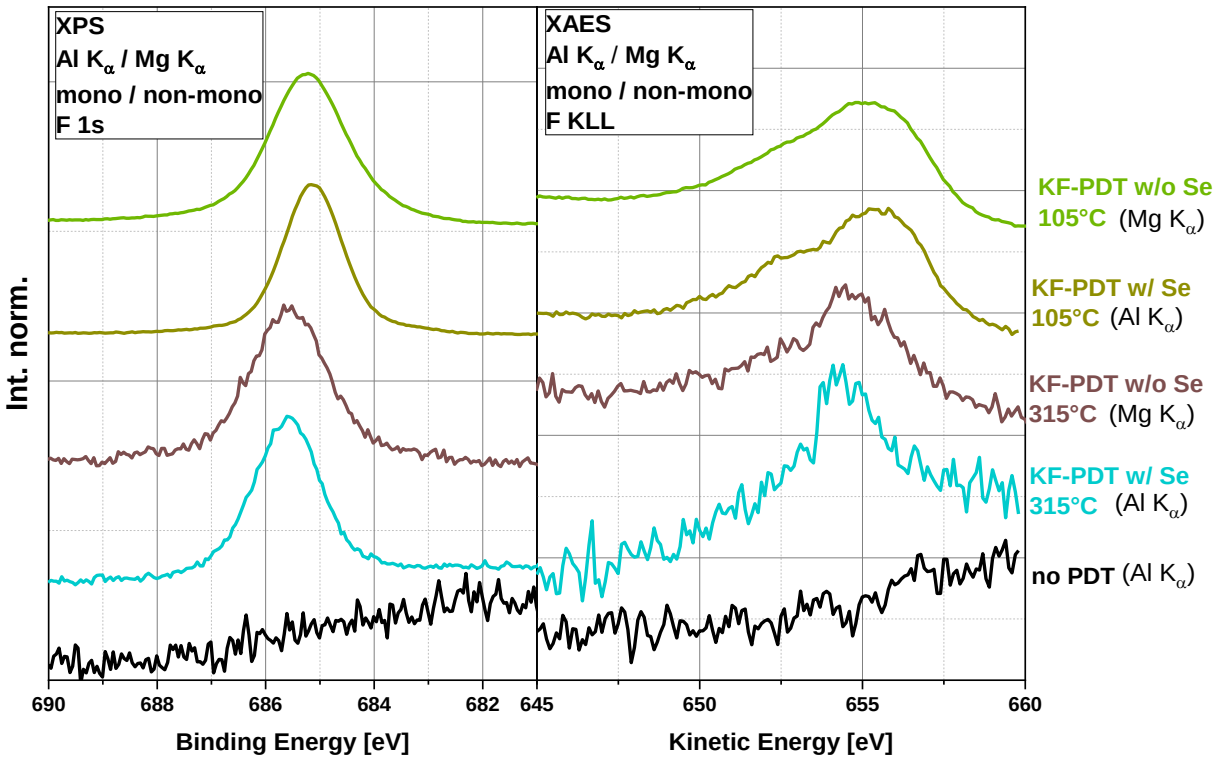

Figure 7.1.3.2 Al K_α or Mg K_α excited, normalized F 1s photoelectron spectra (left) and F KLL Auger spectra (right) for as-grown CIGSe samples which underwent KF PDTs at T_{PDT} = 315 °C and 105 °C and with and without Se supplies. F 1s (F KLL) spectra were normalized by setting the low binding energy background (high kinetic energy background) to zero and the signal maximum to one.

The F 1s signals (Figure 7.1.3.2, left) for the samples without Se show different peak-widths and –shapes than the samples with Se. For both samples, KF PDT 315 °C w/o Se and KF PDT 105 °C w/o Se, the F 1s signal can be fit with one F-component. The F 1s binding energies for the KF PDT 315 °C samples (with and without Se) are nearly identical. For the KF PDT 105 °C samples (with and without Se), the F 1s binding energies are also very similar, and differ by only 0.1 eV. Therefore, it is assumed that the same F-species have formed on

both KF PDT 315 °C sample surfaces (w/ Se and w/o Se) and similarly, the same F-species have formed on both KF PDT 105 °C sample surfaces (w/ Se and w/o Se). Upon comparison with the findings for F-components on KF PDT samples with Se (see Chapter 6.1), it is concluded that that mainly F-K bonds form, possibly together with some F-Ga and/or F-In bonds.

For the F KLL spectra, the shapes of all four signals are similar to each other. Different additional intensities arise as a "shoulder" at E_{Kin} ~ 652 eV, but it can be concluded that the main F-species on all four samples (KF PDT at 315 °C and 105 °C, with Se and without Se supply) are similar to each other and can be ascribed to F-K bonds. Their integral amounts, however, do vary from sample to sample, as will be shown: To compare the integral amount of F on the different samples, the F 1s signal intensities are taken from the Al K_α excited survey spectra and are compared. F 1s peak area ratios of 1 : 0.5 : 6.6 : 5.2 for KF PDT 315 °C w/ Se, KF PDT 315 °C w/o Se, KF PDT 105 °C w/ Se and KF PDT 105 °C w/o Se are determined, respectively.

The F 1s peak intensity ratio is qualitatively similar and in the same order of magnitude as the ratio found for the K 2p signal intensities: Higher F 1s (K 2p) intensities for the KF PDT 105 °C samples are observed than for the KF PDT 315°C samples, and slightly less intensity is observed for a KF PDT without Se, compared to a KF PDT with Se. The qualitative coincidence of the peak area ratios for F 1s and K 2p might confirm that most of the K- and F-atoms exist in K-F-components.

Analysis of O-related photoelectron signals

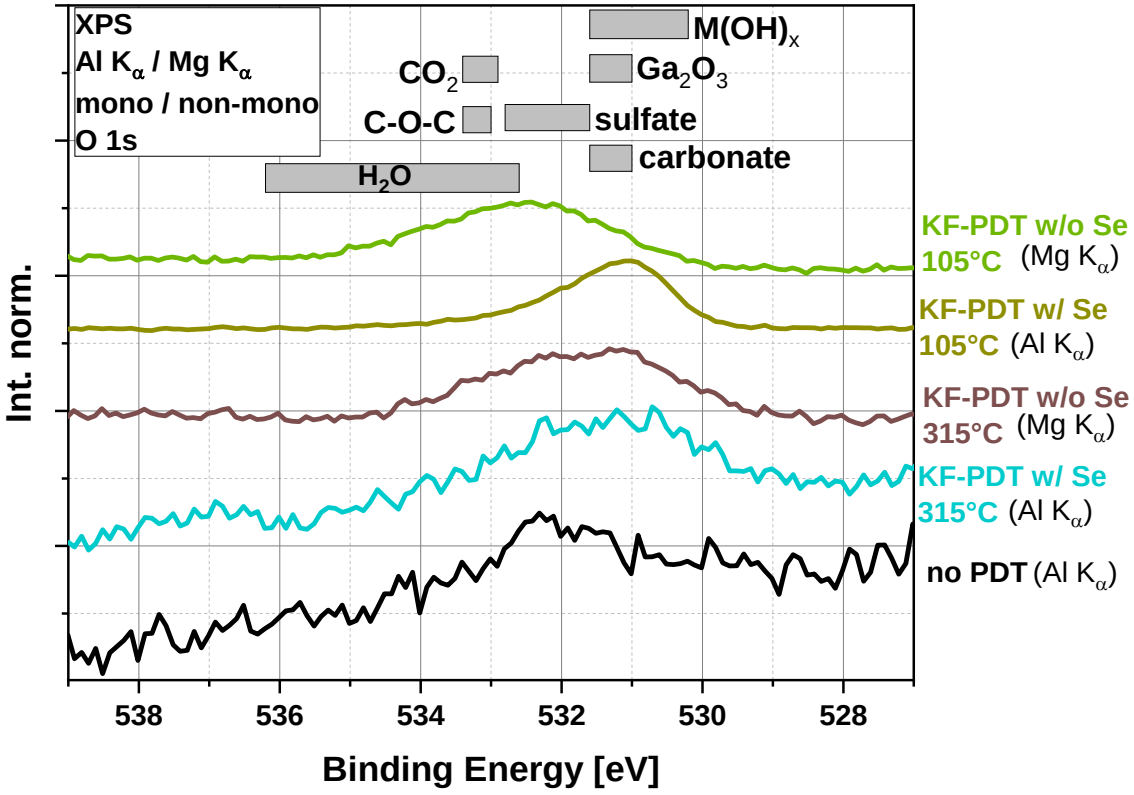

Figure 7.1.3.3 Al K_α or Mg K_α excited, normalized O 1s photoelectron spectra for as-grown CIGSe samples, which underwent KF PDTs at T_{PDT} = 315 °C and 105 °C and with and without Se supply. The spectra were normalized by setting the low binding energy background to zero and the peak maximum to one.

A broad O 1s signal appears on both KF PDT 315 °C samples (w/ Se and w/o Se) in the same binding energy region (Figure 7.1.3.3). Therefore, chemically similar O-components could exist on both KF PDT 315 °C samples (with and without Se). The definite identification of certain O species is difficult, because too many different O-components fall within the binding energy range of E_{Bin} ~ 531 – 533 eV, as stated before in Chapter 6.1.

The KF PDT 105 °C w/o Se sample shows an O 1s signal, which is broader, different in shape and shifted to higher binding energies, compared to the O 1s signal of the KF PDT 105 °C w/ Se sample. The chemical environment for O on the KF PDT 105 °C w/o Se sample should therefore be pronouncedly different to O on the KF PDT 105 °C w/ Se sample.

The ratio of the O 1s peak areas for the different samples was estimated with the O 1s signals from Al K_α-excited survey spectra. The O 1s peak area ratio for no PDT, KF PDT 315 °C w/ Se, KF PDT 315 °C w/o Se, KF PDT 105 °C w/ Se and KF PDT 105 °C w/o Se is 1 : 13 : 8 : 63 : 16. Again, like for K 2p and F 1s, higher amounts of O (K, F) are observed on the low T_{PDT} samples and also (relatively) higher amounts of O for a KF PDT with Se supply. The relative amounts of K, F and O on the different KF PDT samples therefore correlate. Since KF is highly hygroscopic, the O on the samples could stem from residual water exposure during the sample transfer.

To summarize the chemical analysis of the CIGSe surfaces after KF PDTs with different Se supply, all discovered chemical bonds and species are presented in Figure 7.1.3.4. No attempt to quantify the additional Cu-, In-, Ga- or Se-bonds was made, as some more analysis of the surface will follow in the next chapters. All chemical components, which are detected on the KF PDT sample with Se supply (left side in Figure 7.1.3.4) have also been detected on the respective KF PDT sample without Se supply (right side in Figure 7.1.3.4). In case of the KF PDT samples with Se supply, no carbonate species was detected, which might be due to technical reasons: The C 1s spectra of KF PDT samples with Se supply were measured with Al K_α radiation, and therefore a spectral overlap with the strong Se LMM signal impeded the analysis of these signals.

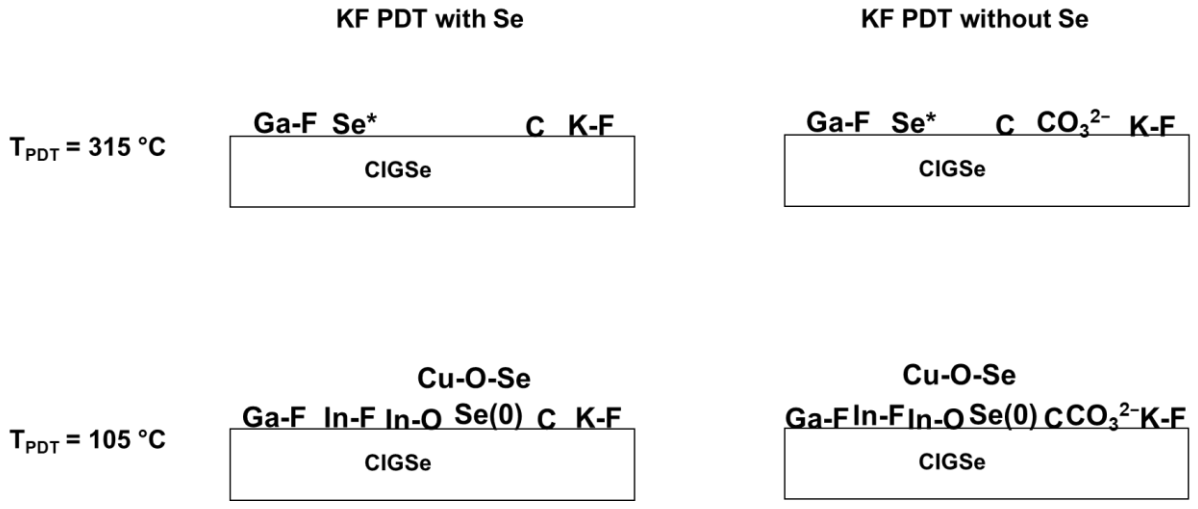

Figure 7.1.3.4 Summary of the found chemical bonds between the constituents of the as-grown CIGSe surfaces before (no PDT) and after different KF PDTs. The denotation "Se*" on the KF PDT 315 °C samples labels a chemically not well-defined environment for the Se atoms, rather than an additional Se species.

7.1.4 Relative changes in CIGSe stoichiometry due to KF PDTs with or without Se supply

The “Low binding energy region“ of the XPS spectrum was analyzed to evaluate changes in composition of the underlying CIGSe phase. Photoelectrons from signals in the “Low binding energy region“ all have a similar inelastic mean free path, so that their sensitivity on surface adsorbates is nearly equal. This makes the analysis of this part of the spectrum so convenient.

Again, like in Chapter 6.1.4, no absolute CIGSe stoichiometries were calculated, but the ratio of different peak areas was compared from sample to sample. Generally, no absolute stoichiometries of the CIGSe surface with XPS data were calculated in this work, because the error margin for such calculations is too high, so that unreliable values would result. For a reliable calculation of absolute stoichiometries a very specific layer model would be needed, the values for the photoionization cross sections must be well known and excellent numbers for the IMFP are required. This, however, is not the case.

The calculation of the peak area ratios is identical to the one used before in Chapter 6.1.4.1. Figure 7.1.4.1 shows the examined range of the spectrum for the different KF PDT samples, in which the In- Ga- and Se-signals were analyzed.

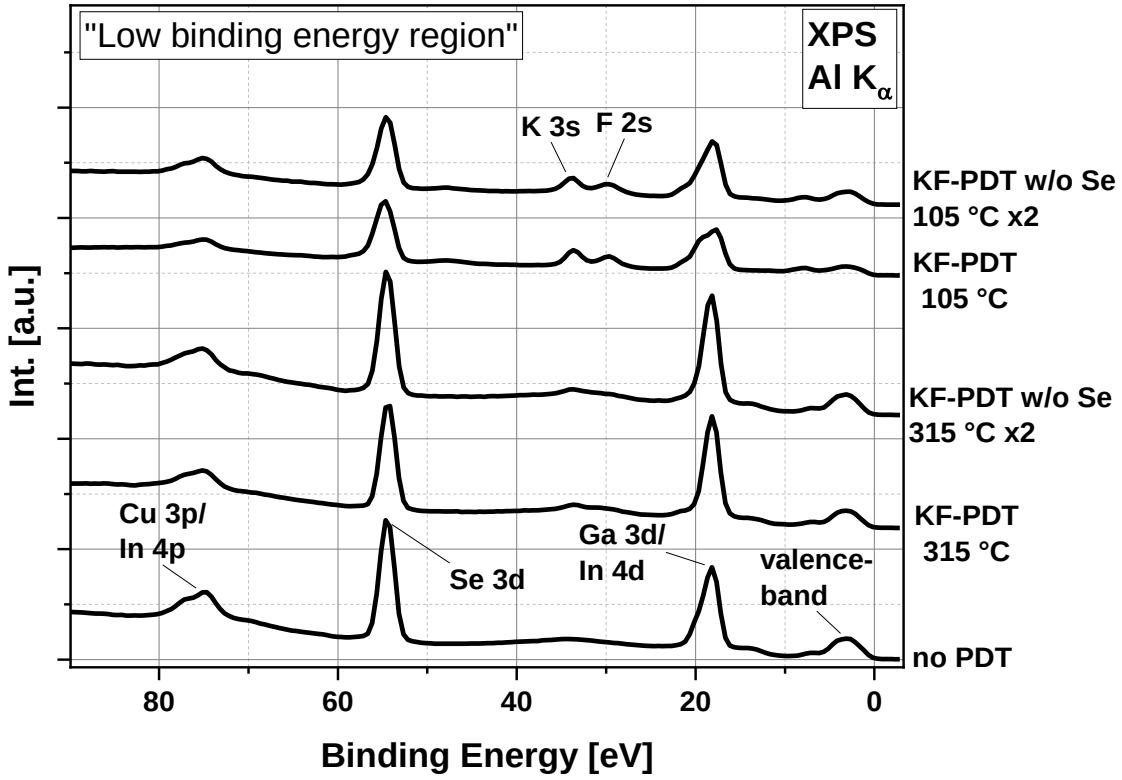

Figure 7.1.4.1 Al K_α or Mg K_α excited photoelectron spectra in the binding energy range from 80 to 0 eV for CIGSe samples which underwent KF PDTs at T_{PDT} = 315 °C and 105 °C and with different Se supplies. The In-, Ga- and Se-signals appearing in this region are analyzed to determine changes in the stoichiometry of the underlying CIGSe phase.

For the evaluation, the peak areas of the Se 3d, Ga 3d and In 4d photoemission lines are determined by fitting the signals with Voigt-functions. Only the CIGSe-contribution of the signal is taken and contributions of secondary species to the integral peak area are left out. The reason for this approach is that Ga atoms, which, e.g., are bound to F, do not belong to Ga in a pure CIGSe environment anymore and therefore are not taken into account, when the

composition of CIGSe is evaluated, specifically. Again, the analysis of the Cu 3p line is left out, since it is overlapped by a broad In 3d line, which complicates the determination of the Cu 3p peak area. The determined peak areas for Se 3d, Ga 3d, and In 4d and the corresponding area ratios are presented in Table 6. With these values, the peak area ratios are calculated. With these ratios it is evaluated, how the CIGSe stoichiometry changes, compared to the untreated sample. For the KF PDT samples without Se, the peak area values are multiplied by 2, to account for the lower irradiation intensity, as stated in the beginning of Chapter 7.

Sample	Peak-Areas [arb. u.]			Peak-Area Ratios	
	In $4d_{5/2}$	Ga $3d_{5/2}$	Se $3d_{5/2}$	$\frac{Ga}{In}$	$\frac{Ga+In}{Se}$
no PDT	2865	557	4186	0.19 ± 0.01	0.82 ± 0.03
KF 315 w/ Se	3964	162	3892	0.04 ± 0.00	1.06 ± 0.05
KF 315 w/o Se x2	2946	232	3286	0.08 ± 0.01	0.97 ± 0.04
KF 105 w/ Se	946	501	1557	0.53 ± 0.04	0.93 ± 0.14
KF 105 w/o Se x2	1494	436	1862	0.29 ± 0.04	1.04 ± 0.08

Table 6 Determined peak areas for In $3d_{5/2}$, Ga $3d_{5/2}$, Se $3d_{5/2}$ and for the untreated CIGSe surface (no PDT) and the different KF PDT with or without Se supply. With the estimated peak areas, respective peak area ratios are calculated.

The changes for the peak areas and -ratios are as follows for the KF PDT 315 °C samples (w/ Se and w/o Se): The In $4d_{5/2}$ area increases from no PDT to the KF PDT 315 °C samples. The increase of In $4d_{5/2}$ from no PDT to KF PDT 315 °C w/Se (2865 to 3964) is stronger than from no PDT to KF PDT 315 °C w/o Se (2865 to 2946). In contrast, the Ga $3d_{5/2}$ area decreases from no PDT to the KF PDT 315 °C samples. A strong decrease is observed from no PDT to KF PDT 315 °C w/ Se (557 to 162), and a mediocre decrease is observed from no PDT to KF PDT 315 °C w/o Se (557 to 232). Therefore, the Ga/In peak area ratio for both KF PDT 315 °C samples is smaller than for the no PDT sample (0.19) and the Ga/In peak area ratio is smaller for the KF PDT 315 °C w/ Se sample (0.04) than for the KF PDT 315 °C w/o Se (0.08) sample. This seems reasonable, since more Ga-F bonds are detected on the KF PDT 315 °C w/ Se sample than on the KF PDT 315 °C w/o Se sample (as seen in the chapters before), and thus less Ga(CIGSe) should remain. The Se $3d_{5/2}$ peak areas decrease from no PDT to the KF PDT 315 °C samples. A stronger decrease in Se $3d_{5/2}$ peak area is observed from no PDT to KF PDT 315 °C w/o Se (4186 to 3286), than from no PDT to KF PDT 315 °C w/ Se (4186 to 3892). This is reasonable, since no Se is supplied during the KF PDT 315 °C w/o Se and thus a part of the Se of the CIGSe surface can desorb or react. Nonetheless the (Ga+In)/Se ratio for KF PDT 315 °C w/ Se (1.06) is higher than the (Ga+In)/Se ratio for KF PDT 315 °C w/o Se (0.97), and thus shows a stronger deviation from the (Ga+In)/Se ratio of the no PDT sample (0.82). In summary, the underlying CIGSe layer of the KF PDT 315 °C w/o Se sample is less Ga-depleted and more Se-depleted than the KF PDT 315 °C w/ Se sample.

Next, the results for the KF PDT 105 °C samples (w/ Se and w/o Se) are presented: The In $4d_{5/2}$ area decreases from no PDT to the KF PDT 105 °C samples. The decrease of In $4d_{5/2}$ from no PDT to KF PDT 105 °C w/ Se (2865 to 946) is *stronger* than from no PDT to KF PDT 105 °C w/o Se (2865 to 1494). The Ga $3d_{5/2}$ area also decreases from no PDT to the KF PDT 105 °C samples. In contrast (to In $4d_{5/2}$), the decrease of Ga $3d_{5/2}$ from no PDT to KF PDT 105 °C w/ Se (557 to 501) is *weaker* than from no PDT to KF PDT 105 °C w/o Se (557 to 436). Therefore, a different behavior of the In $4d_{5/2}$ and Ga $3d_{5/2}$ peak areas is observed on the KF PDT 105 °C samples: For the In $4d_{5/2}$ peak area, a stronger decrease (compared to

no PDT) is observed on the KF PDT 105 °C w/ Se sample (2865 to 946), whereas for the Ga $3d_{5/2}$ peak area, a stronger decrease (compared to no PDT) is observed on the KF PDT 105 °C w/o Se sample (557 to 436). This suggests that the reactivities of In and Ga (towards KF) depend differently on Se supply. The Ga/In peak area ratio of the KF PDT 105 °C w/o Se sample (0.29) deviates less from the Ga/In peak area ratio of the no PDT sample (0.19), than the KF PDT 105 °C w/ Se sample (0.53). This suggests that the overall chemical transformation of the CIGSe surface is less pronounced in case of a KF PDT 105 °C w/o Se. For the (Ga+In)/Se-ratio of the KF PDT 105 °C w/o Se sample (1.04) a value is determined, which deviates stronger from the (Ga+In)/Se-ratio of the untreated reference (0.82), than from the KF PDT 105 °C w/ Se (0.93) sample. Therefore, the KF PDT 105 °C w/o Se sample might be slightly depleted in Se, compared to the KF PDT 105 °C w/ Se sample. Together with the results for the Ga/In-ratio, the CIGSe surface in case of the KF PDT 105 °C w/o Se sample seems more Ga-depleted and less In depleted, compared to the KF PDT 105 °C w/ Se sample.

7.1.5 Estimation of the adsorbate layer thickness on the CIGSe surface after KF PDTs with or without Se supply

For the estimation of the thickness of a potential adsorbate layer covering the CIGSe surface, the model and procedure was applied as introduced in Chapter 6.1.5. The resulting estimated values for the adsorbate layer thicknesses are given in Figure 7.1.5.1.

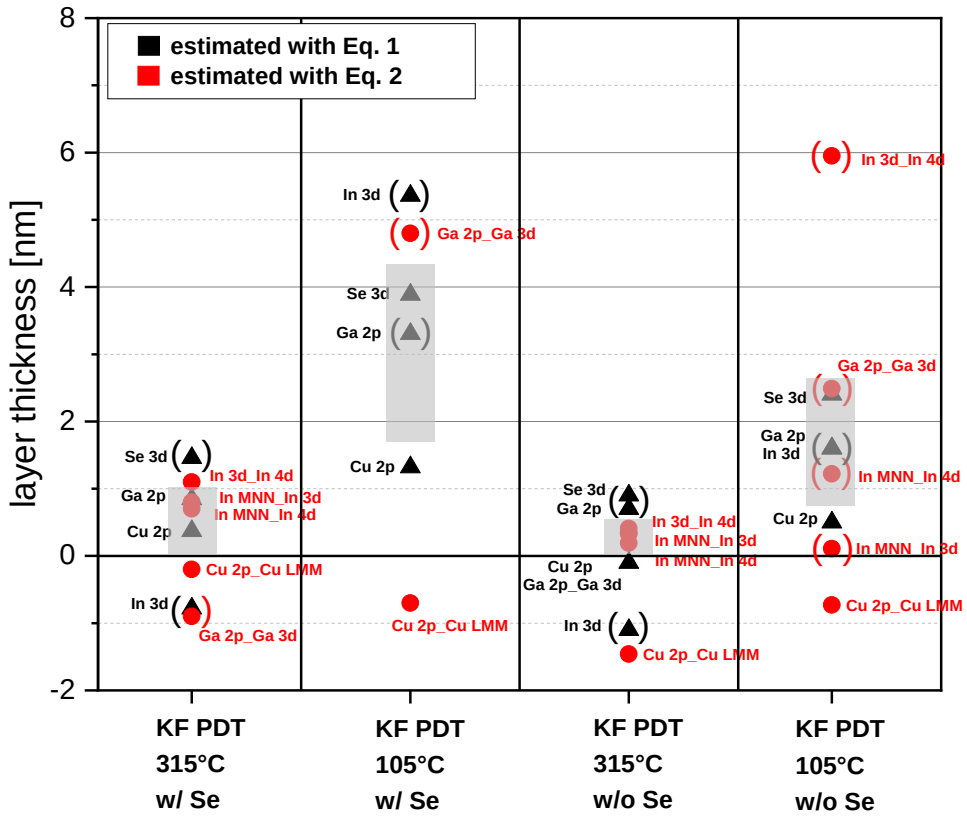

Figure 7.1.5.1 Adsorbate layer thicknesses d, estimated with the help of the attenuation of the respective photoelectron and Auger signals, shown for the different KF PDT CIGSe surfaces. The d-values were estimated with different equations (illustrated in black and red), according to a procedure explained in Chapter 6.1.5. The explicit photoelectron or Auger lines, with which d was determined, are depicted next to the data point. Especially for equation 2, two different photoelectron lines were taken. Values with expectably high uncertainty (mainly because of the existence of secondary components of the respective element) or outliers are set into brackets. The explanation for the exclusion of some estimated d-values is given in the text. The gray shaded areas mark the range, in which the thickness of the adsorbate layer is expected.

For both KF PDT 315 °C samples, the same d-values (Ga 2p, In 3d, Se 3d) were excluded for the estimation of d, since the same secondary components form, which complicate the estimation. For the KF PDT 315 °C w/o Se sample, the outlier at negative d-values (d ~ −1.5 nm) stems from Cu-related signals. Since no chemical reaction of Cu on the KF PDT 315 °C w/o Se sample is observed, it is unclear, why an obviously wrong d-value results. Despite this fact, an adsorbate layer thickness d to be < 0.5 nm is estimated for the KF PDT 315 °C w/o Se sample. Figure 7.1.5.1 shows that the estimated d-values for the KF PDT 315 °C w/o Se sample are slightly smaller, compared to the KF PDT 315 °C w/ Se sample.

For the KF PDT 105 °C w/o Se sample, a pronounced spread in d-values is visible. Again, Ga- and In-related signals for the estimation of d are excluded, so that only Se- and Cu-related signals are taken into account. Since the formation of a second Cu species is expected, the

signal intensity for Cu is not attenuated, but increased, so that the resulting mean d-value for both Cu-signals (Cu 2p and Cu 2p_Cu LMM) is negative (d_{mean} ~ −0.1 nm). The only reliable signal to determine the thickness might be Se, with which d ~ 2.4 nm is estimated. Since most of the other d-estimates are < 2 nm, an assumption of d ≤ 2nm for the KF PDT 105 °C w/o Se sample is made. Therefore, a thinner adsorbate layer is estimated on the KF PDT 105 °C w/o Se sample than on the KF PDT 105 °C w/ Se sample. This is in accordance with the different amounts of K and F found on the several samples, as shown before in Chapter 7.1.3. Comparing the different T_{PDT}, again, thicker adsorbate layers are detected on the KF PDT 105 °C samples, than on the KF PDT 315 °C samples, due to a weaker desorption at lower T_{PDT}.

7.1.6 Depth distribution of Ga-F and In-F secondary species within the CIGSe surface region and summary of the results

Like in Chapter 6.1.6, the rough location of Ga-F and In-F species within the surface region will be examined. The procedure and the analyzed photoelectron signals are the same like in Chapter 6.1.6. The respective peak-area ratios Ga-F : Ga(CIGSe) and In-F : In(CIGSe) are shown in below Table 7 and 8.

Sample	Ga $2p_{3/2}$ Ga-F : Ga(CIGSe)	Ga $3d_{5/2}$ Ga-F : Ga(CIGSe)
no PDT	0 : 1	0 : 1
KF 315 w/ Se	0.70 : 1.00	0.75 : 1.00
KF 315 w/o Se	0.25 : 1.00	0.30 : 1.00
KF 105 w/ Se	9.0 : 1.0	0.4 : 1.0
KF 105 w/o Se	2.0 : 1.0	0.4 : 1.0

Table 7 Peak area ratios of fitted Ga-F and Ga(CIGSe) contributions in Ga $2p_{3/2}$ signals and in Ga $3d_{5/2}$ signals. The peak area of Ga(CIGSe) is set to 1. The Ga $2p_{3/2}$ photoelectron has a much lower kinetic energy than the Ga $3d_{5/2}$ photoelectrons and therefore is much more surface sensitive.

After a KF PDT at 315 °C w/o Se supply during PDT, the ratio of formed Ga-F species to Ga from CIGSe is lower, than after a KF PDT at 315 °C with Se supply during PDT. Hence, Se strongly affects the formation of Ga-F bonds at the surface. The lower Ga-F to Ga(CIGSe) ratio exists throughout the whole, here-examined, depth of the CIGSe layer, as it does not change when measuring deeper “into“ the surface (with Ga $3d_{5/2}$).

For the KF PDT 105 °C w/o Se samples, a similar observation is made for the KF PDT 315 °C samples: Less Ga-F (relative to Ga(CIGSe)) is observed on samples without Se supply at the outermost surface, as derived with Ga $2p_{3/2}$. However, the Ga-F to Ga(CIGSe) ratio deeper within the surface region, as derived with Ga $3d_{5/2}$, is similar for both, KF PDT 105 °C w/ Se and KF PDT 105 °C w/o Se sample, i.e., Ga-F exists only at the outmost surface region. Table 8 adds another interesting observation for the KF PDT 105 °C w/o Se sample:

Sample	In $3d_{5/2}$ In-F : In(CIGSe)	In $4d_{5/2}$ In-F : In(CIGSe)
KF 105 w/ Se	4.8 : 1.0	0.5 : 1.0
KF 105 w/o Se	0.22 : 1.00	0.08 : 1.00

Table 8 Peak area ratios of fitted In-F and In(CIGSe) contributions in In $3d_{5/2}$ signals and in In $4d_{5/2}$ signals. The peak area of In(CIGSe) is set to 1.

On the KF PDT 105 °C w/o Se sample, for both signals, In $3d_{5/2}$ and In $4d_{5/2}$, the In-F to In(CIGSe) ratio is lower than on the KF PDT 105 °C w/ Se sample. This means that the In-F amount (partly to In(CIGSe)) is lower, also deeper within the surface region. This finding is different to that for Ga-F on the KF PDT 105 °C w/o Se sample, as seen before. Therefore, for the formation of In-F it might make a bigger difference, if Se is available at the reaction site or not, than for the formation of Ga-F.

Summary of all findings for the as-grown KF PDT sample surfaces without Se supply during PDT

The most important results from Chapter 7.1.1 to 7.1.6, which characterize the KF PDT as-grown surfaces chemically, are summarized in the sketch in Figure 7.1.6.1. For a better visibility, the relative quantities of K-F, C, O, and Se(0), presented in Figure 7.1.6.1, are also given in Table 9.

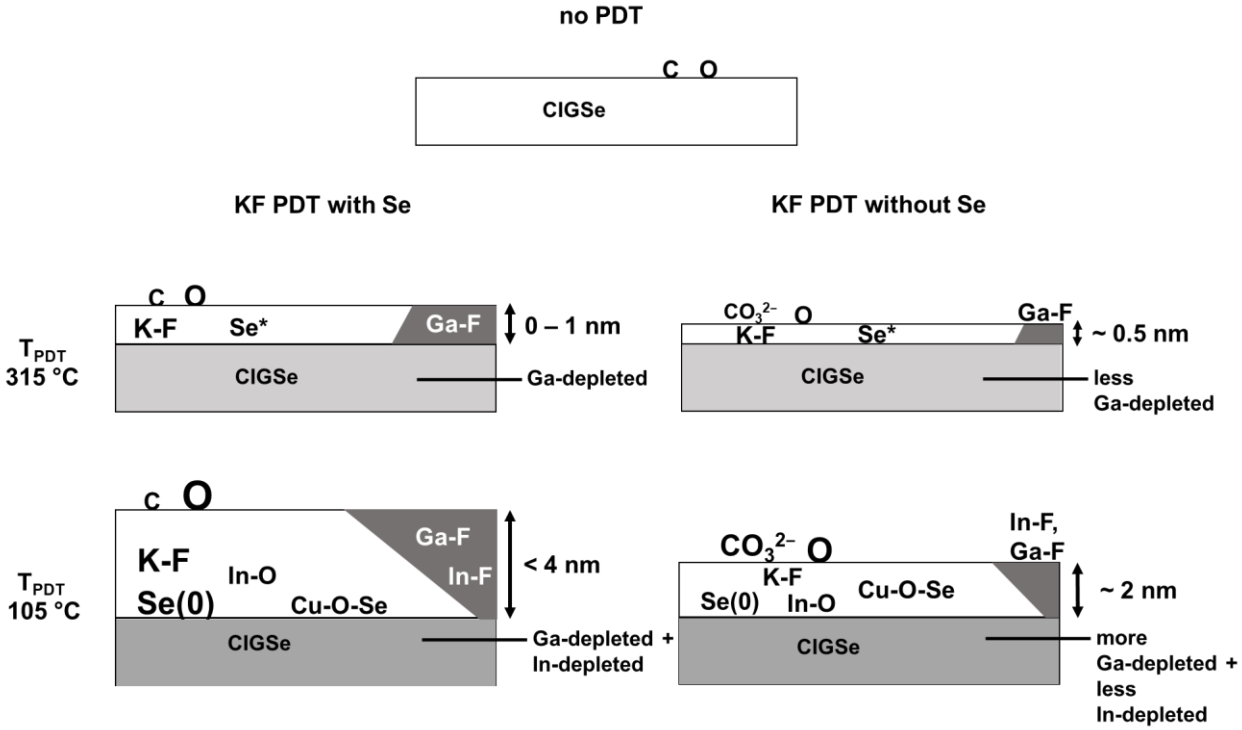

Figure 7.1.6.1 Simplified sketch of the analyzed samples and detected components. The font sizes for O, K-F, Se(0) and CO_3^{2-} indicate quantitative changes from sample to sample. No quantitative statements regarding CIGSe-related components (from sample to sample) are provided. „Se*“ on the KF PDT 315 °C samples (with and without Se) labels a chemically not well-defined environment for the Se atoms, rather than an additional Se species. Dark gray trapezia should schematically illustrate the distribution of Ga-F and In-F throughout the adsorbate layer. In this depiction, the horizontal width of the trapezia should imply the concentration of Ga-F (or In-F) at a certain z-position in the adsorbate layer.

	K-F	C	O	Se(0)
no PDT		+	+	
KF PDT 315 °C w/ Se	++	+	++	
KF PDT 315 °C w/o Se	+	+	+	
KF PDT 105 °C w/ Se	++++	+	+++	++
KF PDT 105 °C w/o Se	+++	++	++	+

Table 9 Relative K-F, C, O and Se(0) -quantities on the differently treated CIGSe surfaces directly after PDT. “+” marks the existence of the respective element and the number of “+” indicates the amount. The relative quantities are given for the respective element from sample to sample, and no comparison between KF, C, O, and Se(0)-quantities on the same sample was made.

Distinct differences which arise due to a KF PDT without Se are thinner cover layers on the CIGSe surface and therefore mainly less K, F, and O. This thinner cover layers could result from a faster desorption of K and F in the absence of Se. This observation is made for both KF PDT temperatures, i.e., 315 °C and 105 °C. For the KF PDT 315 °C w/o Se sample, lower

amounts of Ga-F are observed and therefore the underlying CIGSe layer is less Ga-depleted (also resulting from the analysis of the low binding energy region in Chapter 7.1.4). The question, however, is, if these lower amounts of Ga-F are a consequence of the absence of Se, or just a consequence of the thinner K-F cover layer and thereby a lower K- or F-concentration at the surface? Both facts are possible reasons and can therefore not be ruled out. For the KF PDT at 105 °C w/o Se sample the situation is different: Lower amounts of K-F are detected and consequently Ga-F and In-F are observed. The relative ratio of Ga-F to In-F, however, has changed, and more Ga-F than In-F forms, compared to a KF PDT 105 °C with Se. The resulting, underlying CIGSe layer therefore becomes more Ga-depleted and less In-depleted on the KF PDT 105 °C w/o Se sample, than on the KF PDT 105 °C w/ Se sample. The formation reactions of Ga-F and In-F consequently depend on the concentration of Se supplied during the PDT. Condensing the most important results from Chapter 7.1, the formation of Ga-F and In-F is promoted in the presence of Se, and without Se supply during PDT the CIGSe surface is less changed in its composition.

7.2 Impact of the aqueous Na_2S rinsing step on KF-treated CIGSe surfaces with or without Se supply ("rinsed" samples)

Distinct chemical differences are noticed on the CIGSe surface, when a KF PDT is applied with no Se supply. In Chapter 7.1 before, a reduced reactivity of the KF on the CIGSe surface is observed within a KF PDT without Se, compared to a KF PDT with Se, and so the formation of lower amounts of Ga-F and In-F species is observed. Thereby, lower amounts of Ga(CIGSe) and In(CIGSe) have reacted to form Ga-F and In-F bonds, and so that the resulting CIGSe surfaces became less Ga-depleted and/ or In depleted. The arising question is how the subsequent rinsing of the KF PDT samples further influences this chemical change. As it will be shown, mainly the amounts of secondary components like K-In-Se and Cu-S-Se-O will change, leading to a different surface composition. This different surface composition in turn will slightly alter the electronic properties of the rinsed surfaces.

Chapter 7.2 is divided into four sub-chapters, starting with Sub-Chapter 7.2.1, which will compare the KF PDT 315 °C samples with and without Se after the rinsing process. Similarly, Sub-Chapter 7.2.2 will present the chemical differences of the KF PDT 105 °C samples with and without Se after the rinse. Sub-Chapter 7.2.3 will determine differences in the resulting CIGSe stoichiometry and summarize the results of the comparison. At last, the impact of the Se supply on the electronic properties is determined with UPS measurement in Sub-Chapter 7.2.4.

7.2.1 Formation of secondary components during KF PDT 315 °C with and without Se supply

The analysis of the KF PDT 315 °C w/o Se rinsed sample reveals that the formed chemical species are similar to those on the KF PDT 315 °C w/ Se rinsed sample surface. It will be shown that in both cases a Na-Se-O-like and a K-Se-In(-O) component are found. Their quantities on both samples are different, however. The analysis starts with the identification of a possible K-In-Se(-O) component. Figure 7.2.1.1 compares the fit of the Se 3d signals for both KF PDT 315 °C samples.

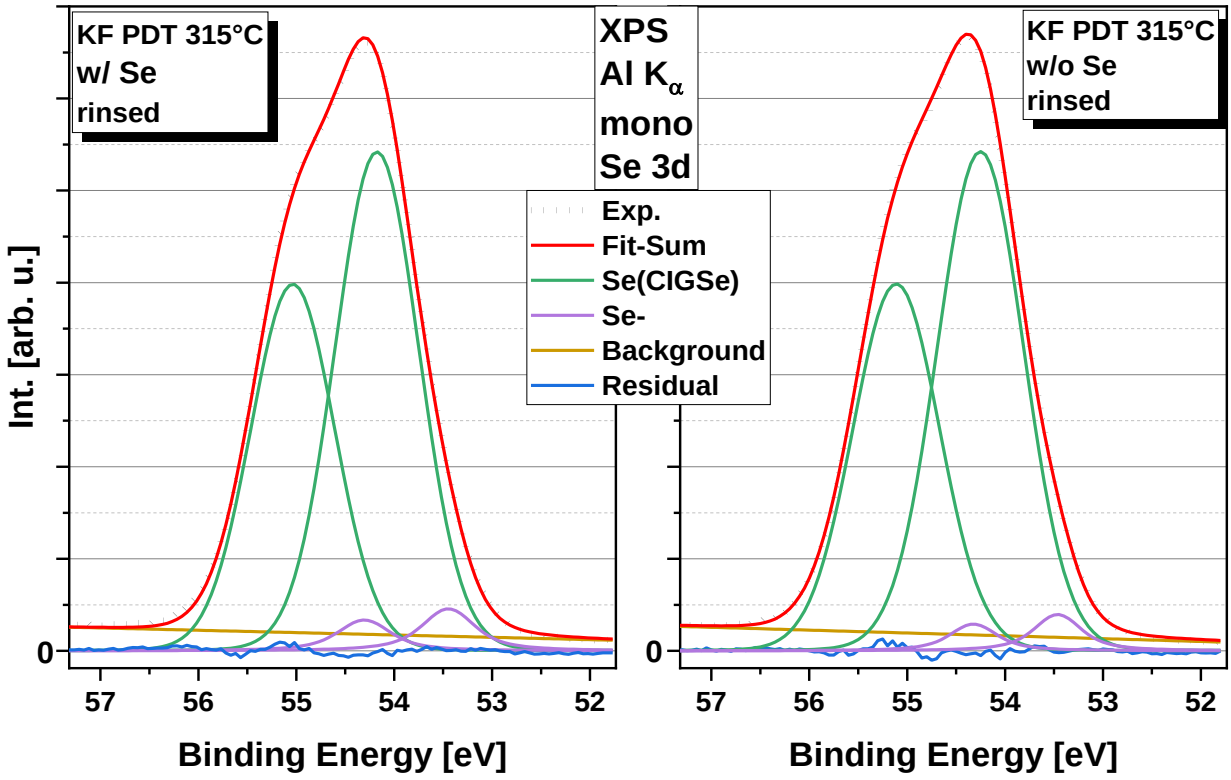

Figure 7.2.1.1 Fit of the Se 3d signal for the rinsed KF PDT 315 °C sample with Se supply (left) and without Se supply (right) with two components.

For the KF PDT 315 ° C w/o Se sample (Figure 7.2.1.1 right), a very similar fit of the Se 3d signal can be made, like for the KF PDT 315 °C w/ Se sample (left). Again, an additional Se species (purple) appears at lower binding energy, at E_{Bin} ~ 53.5 eV. The intensity for this additional Se species is slightly lower on the KF PDT 315 °C w/o Se sample. However, this difference is almost unnoticeable and possibly not statistically significant. When the two spectra are plotted directly on top of each other, only very faint differences are visible (not shown). Similarly, to the sample with Se supply, the additional Se species on the KF PDT 315 °C w/o Se sample is identified as Se-In bonds. Comparison with literature values of a coevaporated In_2Se_3 phase or even a KF PDT of an In_2Se_3 layer confirm this result [38,125].

Next, the K-related signals of the rinsed KF PDT 315 °C samples (w/ Se and w/o Se) are compared, to evaluate, if a missing Se supply influences the amount or chemical nature of K on the rinsed CIGSe surface.

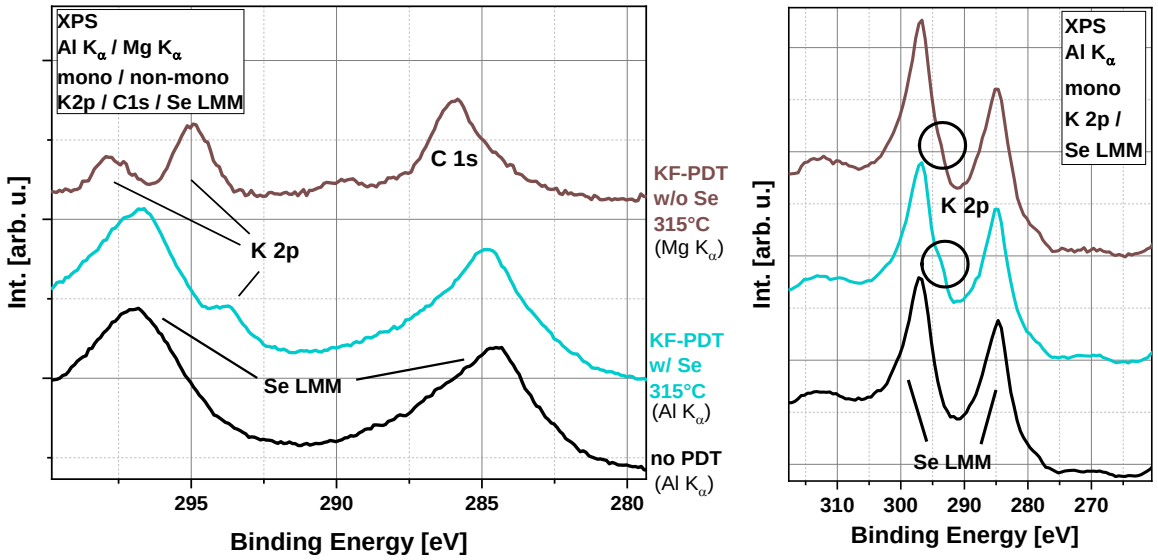

Figure 7.2.1.2 K 2p signals measured with Al K_α and Mg K_α radiation (left) and K 2p signals taken as excerpts from survey spectra measured solely with Al K_α radiation (right). The spectral resolution in the survey spectra excepts (right) is lower, therefore the K 2p signals only appear as a „shoulder“ on the Se LMM Auger at E_{Bin} ~ 293 eV (encircled). All K 2p signals are superimposed by strong Se LMM Auger signals when measured with Al K_α radiation.

In Figure 7.2.1.2 left, the K 2p signals are detected for both KF PDT 315 °C samples, with and without Se supply during PDT. The KF PDT 315 °C w/ Se sample (light blue) was measured with Al K_α radiation, therefore the K 2p signal is superimposed by a strong Se LMM Auger signal. Nevertheless, the K $2p_{3/2}$ peak is visible at E_{Bin} ~ 293 eV. The KF PDT 315 °C w/o Se sample (brown) was measured with Mg K_α radiation, so no Se LMM signal appears in this spectrum and K $2p_{3/2}$, as well as K $2p_{1/2}$ become visible. Because of charging of the KF PDT 315 °C w/o Se sample during the measurement with Mg K_α radiation, the whole spectrum is shifted to higher binding energies by about 1.5 eV. Overall, it is found that K exists on both KF PDT 315 °C samples (w/ Se and w/o Se).

To estimate the relative amounts of K on both KF PDT 315 °C samples, K 2p spectra, measured with the same radiation are displayed in Figure 7.2.1.2, right. The K 2p signals appear as additional intensity on the Se LMM Auger signals at E_{Bin} ~ 293 eV and create a “shoulder“ on the Se LMM Auger signal (encircled part of the spectrum). This “shoulder“ at E_{Bin} ~ 293 eV appears more pronounced for the KF PDT 315 °C w/ Se sample, than for the KF PDT 315 °C w/o Se sample. On the latter, the “shoulder“ is almost not visible, but it does exist. It can be speculated, whether these small visual differences stem from an effectively lower K $2p_{3/2}$ signal intensity on the KF PDT 315 °C w/o Se sample, or, from a small chemical shift of K $2p_{3/2}$ to higher binding energies (without any decrease in K $2p_{3/2}$ signal intensity). Nonetheless, a decreased K $2p_{3/2}$ intensity could be interpreted as lower amounts of K on the KF PDT 315 °C w/o Se sample, than on the KF PDT 315 °C w/ Se sample, and hence lower amounts of an insoluble, water-stable K component. This assumption sounds reasonable, since lower amounts of KF were also found before, on the as-grown KF PDT 315 °C w/o Se sample, than on the KF PDT 315 °C w/ Se sample (shown in Chapter 7.1). It will be illustrated in the following that the assumption of lower amounts of K on the KF PDT 315 ° C w/o Se sample (compared to the sample with Se) is in agreement with other photoelectron signals.

So far, it has been determined that a Se-In species exists on the KF PDT 315 °C w/o Se sample, similar to the sample with Se, and that a water-stable K species has formed. Next, the intensities of the CIGSe core levels are analyzed, especially with respect to Indium. If a new Se-In species evolved, one might notice this circumstance in the In 3d signals. Figure 7.2.1.3

illustrates the CIGSe core levels for both KF PDT 315 °C samples (w/ Se and w/o Se) and the untreated (but rinsed) reference sample.

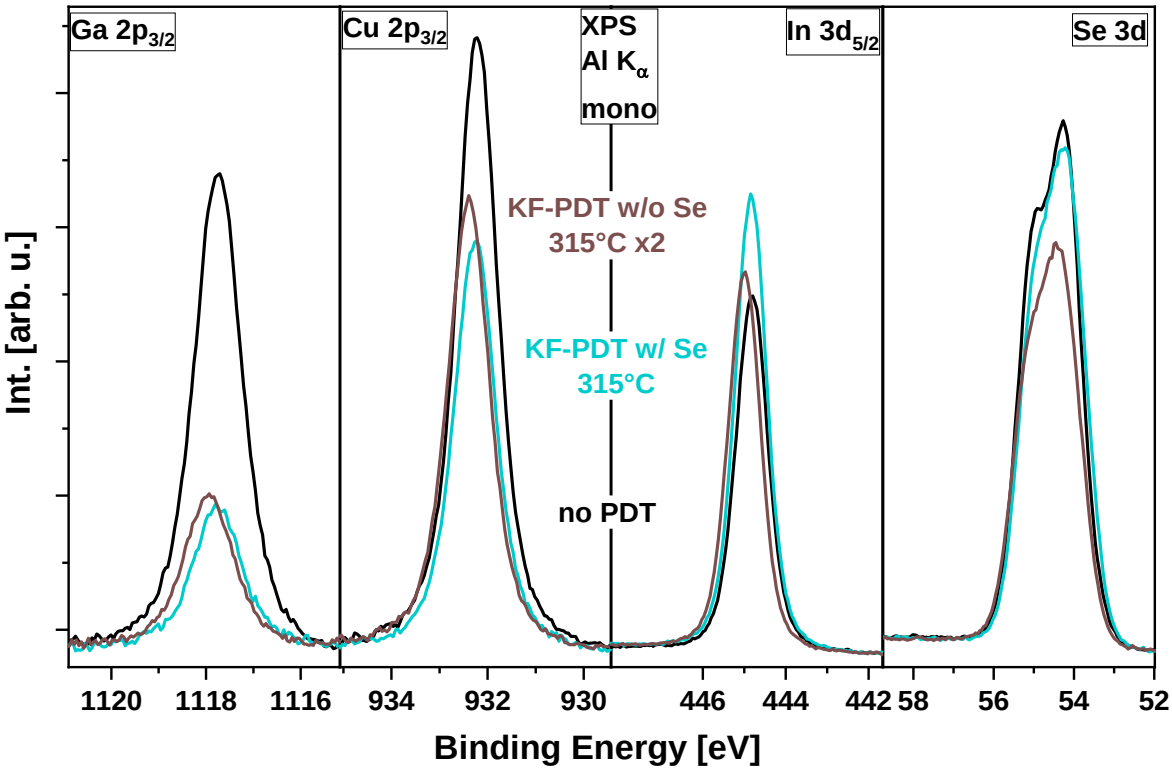

Figure 7.2.1.3 Al K_α excited CIGSe core-level spectra for the untreated rinsed surface (black) and the rinsed KF PDT 315 °C surfaces with (light blue) and without Se supply (brown) during PDT.

First, the In $3d_{5/2}$ signals and their different intensities are discussed: For the KF PDT 315 °C w/ Se sample (light blue) the In $3d_{5/2}$ intensity is higher than for the untreated reference sample (black). In section 6.2 this was interpreted as an indication of a newly formed In species with an In $3d_{5/2}$ binding energy equal to that of In in CIGSe (In(CIGSe)). Together with the finding of a new Se species, which consists of Se-In bonds, as shown in the beginning of this chapter, it is assumed that the additional intensity of the In 3d signal stems from the formation of a new In-Se species. For the KF PDT 315 °C w/o Se sample, however, the In $3d_{5/2}$ intensity is lower, than for the KF PDT 315 °C w/ Se sample. It is therefore suggested that on the KF PDT 315 °C w/o Se sample, also an In-Se component has formed, but in lower amounts than on the KF PDT 315 °C w/ Se sample. Since also lower amounts of K are found, on the sample without Se than on the sample with Se (as it was presented before), it can be speculated that K is chemically bound to In-Se. Therefore, similar to the sample with Se, a K-In-Se(-O) component could have formed on the KF PDT 315 °C w/o Se sample, but in lower amounts. Although there is no direct experimental proof of the K-In-Se(-O) species, the existence of different amounts of such a layer can be confirmed with the attenuation of the Ga 2p and Cu 2p signals in Figure 7.2.1.3: The K-In-Se(-O) layer covers the CIGSe surface and, together with other surface adsorbates like Na-Se-O, attenuates the Ga 2p and Cu 2p signals (compared to the untreated sample). This attenuation is slightly more pronounced for the KF PDT 315 °C w/ Se sample (light blue), for which a thicker K-In-Se(-O) cover layer is estimated. The Se(CIGSe) contributions of the Se 3d signal intensities, however, do not completely follow this trend: The Se 3d signal attenuation of the KF PDT 315 °C samples (w/ Se and w/o Se), compared to the untreated sample, is less pronounced, than for Ga 2p and Cu 2p. This is reasonable, because Se 3d photoelectrons are less surface sensitive, than Ga 2p or Cu 2p photoelectrons. The intensity of Se 3d for KF PDT 315 °C w/ Se (light blue), however, is not

lower than the Se 3d intensity for KF PDT 315 °C w/o Se (brown), although a thicker K-In-Se(-O) cover layer should exist on the former.

An explanation for this observation can be as follows: A Na-containing component was found to be an additional adsorbate, covering the surface. Chemical analysis of the Na species (not shown) affirms a component comparable to Na_2O or Na_2Se, for now described as Na-Se-O. Furthermore, a comparison of Na 1s spectra reveals (not shown) that the Na amount is slightly higher on the KF PDT 315 °C w/o Se sample than on the sample with Se. It is speculated that the Na-Se-O component might be chiefly adsorbed on Se-terminated surfaces. Thereby, somewhat higher amounts of Na caused an unexpectedly stronger attenuation of the Se 3d signal for the KF PDT 315 °C w/o Se sample. This attenuation of the Se 3d signal would then be stronger, than one might expect, according to the integral thickness of adsorbate layer covering the surface. Thereby, the stronger Se 3d attenuation of the CIGSe signal on the KF PDT 315 °C w/o Se sample (compared to the sample with Se) could be explained.

To briefly summarize the results for the KF PDT 315 °C samples, an additional Se species on the KF PDT 315 °C w/o Se sample has been detected, similar to that on the KF PDT 315 °C w/ Se sample, but yet in tendentially lower amounts, than on the sample with Se. Also, assumingly less of a water-stable K-component is found, and the increase in In signal intensity is less pronounced for the KF PDT 315 °C w/o Se sample, than for the KF PDT 315 °C w/ Se sample. It can be concluded that a lower amount of a K-In-Se(-O) component has formed on the KF PDT 315 °C w/o Se sample, than on the KF PDT 315 °C w/ Se sample. In addition to it, slightly higher amounts of Na have been detected on the KF PDT 315 °C w/o Se sample, than on the KF PDT 315 °C w/ Se sample, probably as a Na-Se-O component covering the surface, together with K-In-Se(-O).

It must be stressed that this interpretation is just one possibility to draw a complete picture of the chemical changes on the KF PDT 315 °C sample surfaces, and to explain all observations made in the spectra. Other models do also exist; without any claim for correctness, however, the author of the work in hand believes that the here-presented model of a K-In-Se(-O) component suits best, especially for the interpretation of the data for the here-examined ZSW samples.

7.2.2 Formation of secondary components and chemical reaction products during KF PDT 105 °C with and without Se supply

Similar to the results before for the high T_{PDT} samples, lower amounts of a Cu-S-Se-O secondary component are observed, but comparable amounts of a Na-Se-O-like component on the KF PDT 105 °C w/o Se sample, compared to the KF PDT 105 °C w/ Se sample.

The comparison is started by discussing the Cu $2p_{3/2}$ and Cu LMM spectra of the rinsed KF PDT 105 °C samples with and without Se in Figure 7.2.2.1.

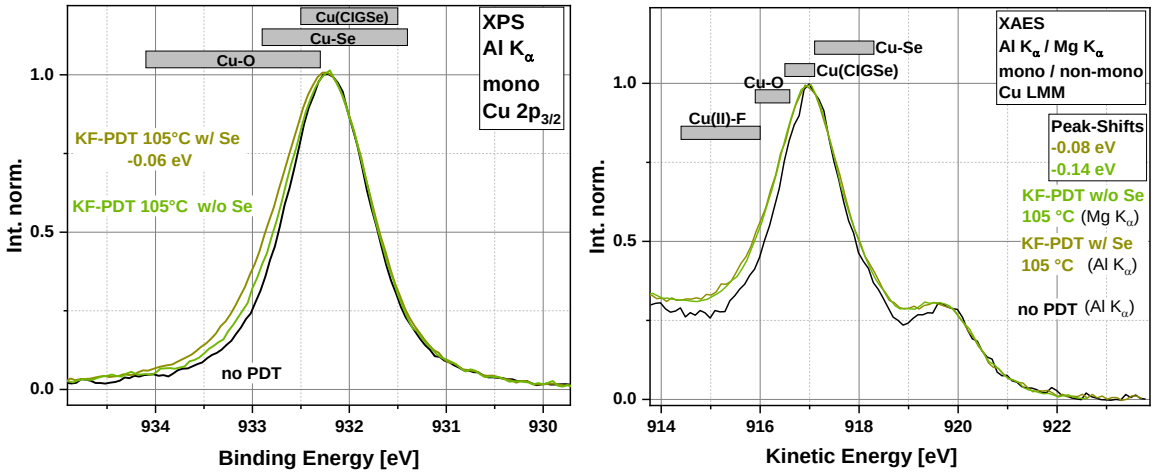

Figure 7.2.2.1 Normalized Cu $2p_{3/2}$ photoelectron spectra (left) and Cu LMM Auger spectra (right) for the untreated reference sample (no PDT, black) and the KF PDT 105 °C samples with different Se supply. The Cu $2p_{3/2}$ (Cu LMM) spectra were normalized by setting the low binding energy background (high kinetic energy background) to zero and the signal maximum to one. For a better comparison of the spectral shapes, the spectra are shifted on the x-axis. Respective shifts are given in the diagram. Gray bars indicate binding energy ranges for common Cu-bonds found in literature.

In the normalized Cu $2p_{3/2}$ spectra in Figure 7.2.2.1 (left), both KF PDT 105 °C samples show a spectrally broadened signal, compared to the no PDT sample. The broadening is less pronounced for the KF PDT 105 °C w/o Se sample than for the KF PDT 105 °C w/ Se sample. It is therefore concluded that less of a secondary Cu species, appearing at higher binding energies, forms on the KF PDT 105 °C w/o Se sample compared to the sample with Se. A different signal (compared to no PDT) is also observed in the Cu LMM Auger spectra. Additional intensity is detected at E_{Kin} ~ 919 eV and at E_{Kin} < 917 eV. Both observations indicate the existence of an additional Cu species at lower kinetic energy. The spectral shape of both KF PDT 105 °C Auger signals is equal, indicating that, in contrast to Cu $2p_{3/2}$, the second Cu LMM component has equal relative weight for both KF PDT 105 °C samples. The latter can be attributed to the different surface-sensitivity of the respective photo- or Auger electron giving a different relative weight of surface and bulk species in the spectra.

The Cu $2p_{3/2}$ and Cu LMM spectra of the KF PDT 105 °C w/o Se sample were fitted in the same way as the spectra from the KF PDT 105 °C w/ Se sample in Chapter 6.2. This way, the modified Auger parameter α'_{Cu} of the different Cu species on the KF PDT 105 °C samples (with and without Se supply) was determined and is depicted in the Wagner plot in Figure 7.2.2.2.

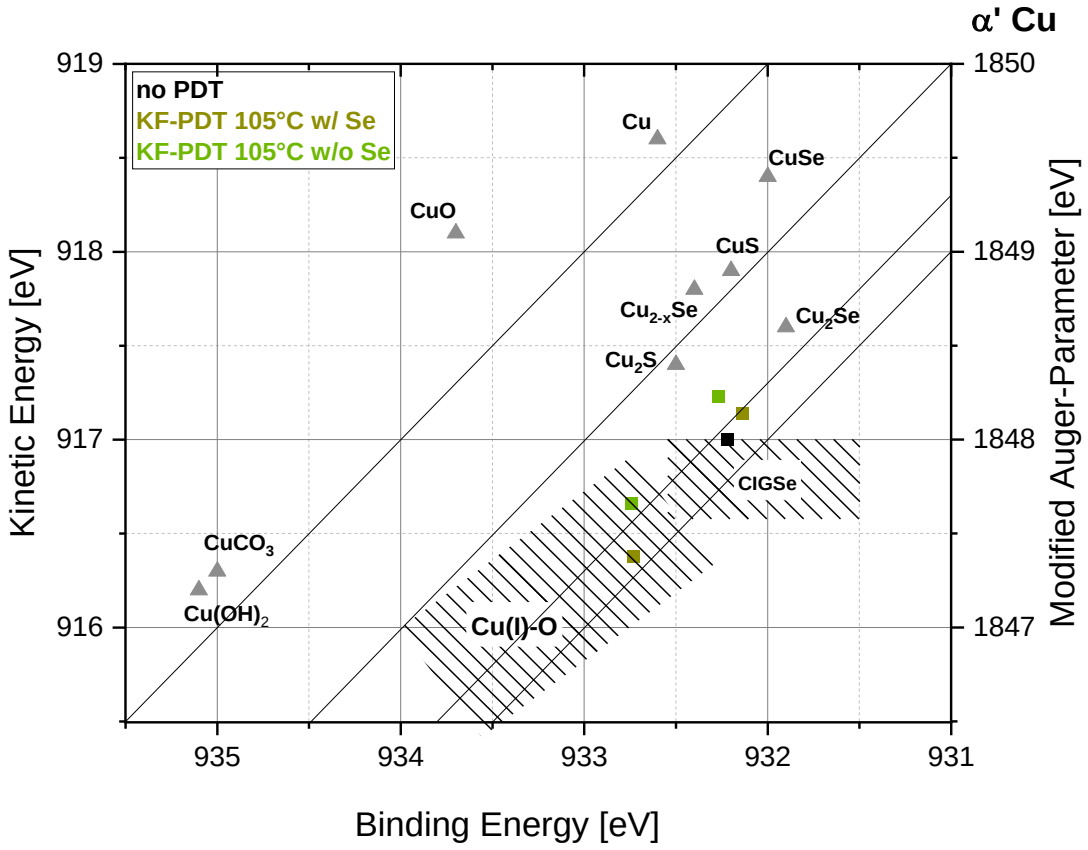

Figure 7.2.2.2 Wagner plot of the modified Auger parameter α'_{Cu} for the rinsed, untreated sample (no PDT, black) and KF PDT 105 °C samples with different Se supply. The shaded areas as well as the gray triangles show data points from literature for Cu in different bonding environments.

On the KF PDT 105 ° C w/o Se, sample two Cu species have been found. One Cu species, which is the main component, belongs to Cu(CIGSe) with an Auger parameter α'_{Cu} = 1849.5 eV. Compared to literature values for Cu(CIGSe) this data point shows a higher kinetic energy. The other Cu species on the KF PDT 105 °C w/o Se sample (α'_{Cu} = 1849.4 eV) lies within the range of Cu-O bonds, but is also near the Cu(CIGSe) region. This could mean that the additional Cu species on the KF PDT 105 °C w/o Se sample possesses Cu-O bonds, but not as pronounced, as for the KF PDT 105 °C w/ Se sample. Figuratively, the additional Cu species on the KF PDT 105 °C w/o Se sample is bound to a lower number of oxygen atoms, than to selenium atoms, and thus resembles more a Cu-atom in an CIGSe environment. This additional Cu species will be called Cu-O-Se from now on.

Both Cu species of the KF PDT 105 °C w/o Se sample (light green) are shifted by 0.1 – 0.4 eV to higher kinetic energies in the Wagner plot, compared to the respective Cu species of the KF PDT 105 °C w/ Se sample (dark yellow). Therefore, a stronger band bending on the KF PDT 105 °C w/o Se sample may also be the reason for the different α'_{Cu} values of similar Cu-bonds in the Wagner plot.

To conclude the results for Cu, Cu(CIGSe) was found as major component and a Cu-Se-O as a minor component on the KF PDT 105 °C w/o Se sample, likewise as for the KF PDT 105 °C w/ Se sample, but presumably in lower amounts.

Again, also sulfur is found on the sample surface after the rinse, as it is the case for the rinsed KF PDT 105 °C w/ Se sample. In the following, the chemical environment of S is analyzed and

it is found that S could be bonded to Cu. Figure 7.2.2.3 shows the S LMM and S 2p / Se 3p spectra for the respective samples.

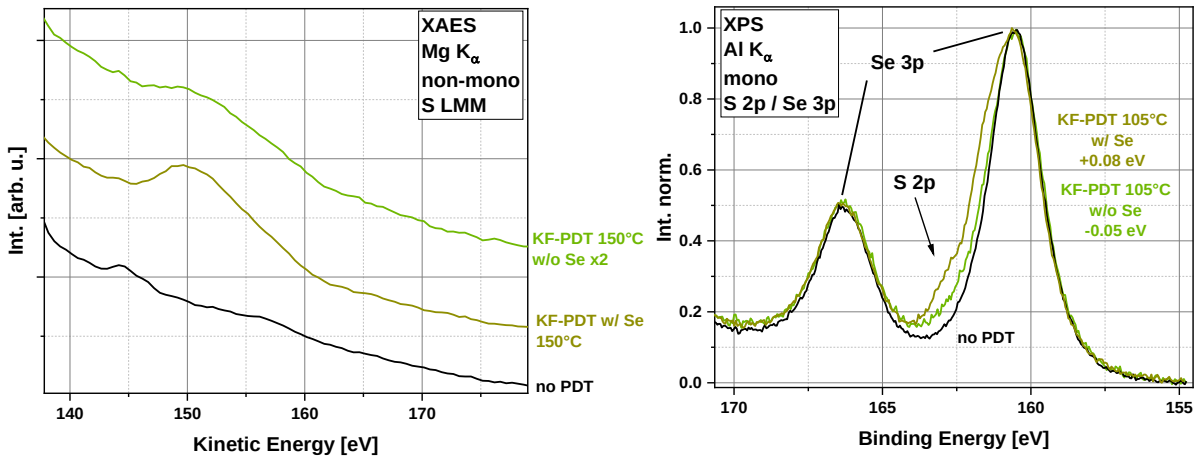

Figure 7.2.2.3 S LMM Auger spectra (left) and normalized S 2p / Se 3p spectra for the untreated reference sample (no PDT, black) and the KF PDT 105 °C samples with different Se supply. The S 2p / Se 3p spectra were normalized by setting the low binding energy background to zero and the signal maximum to one. To allow for a better comparison of spectral shapes, the signals are shifted on the x-axis. Respective shifts are given in the diagram.

A clear S LMM Auger signal is visible on both KF PDT 105 °C samples (with and without Se supply) at E_{Kin} ~ 152 eV in Figure 7.2.2.3, left. For the KF PDT 105 °C w/o Se sample a lower intensity for the S LMM signal is observed. The S 2p photoelectron signals (Figure 7.2.2.3 right) are strongly overlapping with the Se 3p doublet. The S 2p signal appears at E_{Bin} ~ 162 – 164 eV and creates additional intensity at the left shoulder of Se $3p_{3/2}$. For the S 2p photoelectron signal the same observation is made like for the S LMM Auger signal: The S 2p doublet is less intense on the KF PDT 105 °C w/o Se sample, than on the KF PDT 105 °C w/ Se sample. With a fit of the S 2p signal, the accurate position of S $2p_{3/2}$ can be determined and the S species formed on the surface can be identified.

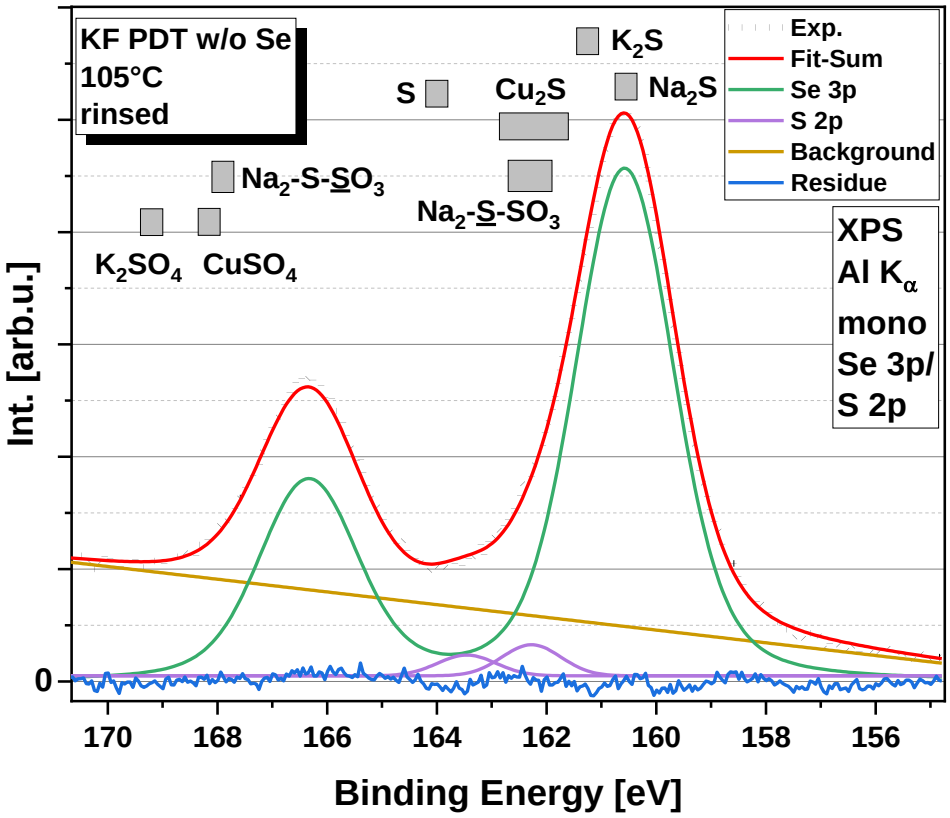

Figure 7.2.2.4 Fit of the Se 3p/ S 2p photoelectron spectrum for the rinsed KF PDT 105 °C w/o Se sample. Boxes in gray mark binding energy regions of the S 2p signal for different S-compounds, found in literature.

In Figure 7.2.2.4 it is shown that a small S 2p contribution (purple) and a strong Se 3p contribution (green) can be fitted from the signal. The S $2p_{3/2}$ peak is found at E_{Bin} ~ 162.2 eV. As already described in Chapter 6.2, no literature values for S LMM Auger signals could be found, therefore the S species has to be characterized by its S 2p binding energy.

Comparing the S 2p binding energy with literature values (depicted as gray boxes in Figure 7.2.2.4), the S species on the KF PDT 105 °C w/o Se sample matches the binding energy region of a transition metal sulfide (e.g., Cu_2S, with oxidation state −II) quite well.

At the same time, the existence of S in oxidation states +I and +V, e.g., as a thiosulfate ion $S_2O_3^{2-}$, might also be possible. S in the oxidation state +I might result from an oxidation of S^{2-} ions by O_2, which is present in the water of the Na_2S solution. However, if the reaction of S^{2-} ions to form $S_2O_3^{2-}$ took place on the CIGSe surface though, one would also detect S species on the other PDT samples, which is not the case. Moreover, for a thiosulfate ion, an additional S 2p signal is expected at E_{Bin} ~ 167.8 eV, representing the highly oxidized S(+V) atom in the SO_3 group of the thiosulfate ion. This signal, however, is absent. Therefore, the S species cannot exist as thiosulfate ion. Interestingly, S species are only detected on sample surfaces, which are Cu-rich (the KF PDT 105 °C samples). Because of the very low solubility product of Cu_2S it thus stands to reason that S^{2-} will mainly react with Cu(I) ions, rather than react with traces of O_2. Concluding the analysis of the S-related signals, S on the KF PDT 105 °C samples should therefore be bound to Cu, and furthermore, less S is detected on the KF PDT 105 °C w/o Se sample, than on the KF PDT 105 °C w/ Se sample.

In the analysis of Cu-related signals before, it was figured out that lower amounts of a Cu secondary component exist on the KF PDT 105 °C w/o Se sample than on the KF PDT 105 °C w/ Se sample. Together with the finding of a S species, which is probably bound to Cu, and is

also detected in lower amounts on the KF PDT 105 °C w/o Se sample, it is concluded that less Cu-O-S-Se is formed on the KF PDT 105 °C w/o Se sample than on the KF PDT 105 °C w/ Se sample.

This result is comparable to the result for the amount of the K-component on the KF PDT 315 °C w/o Se sample: Both secondary species form in lower amounts during a KF PDT without Se supply.

Different from this observation is the relative amount of the Na-component, which is found after the rinse: For the high T_{PDT} KF PDTs more Na and O is detected on KF PDT samples without Se supply (see Chapter 7.2.1). In this chapter, for the low T_{PDT} samples, less Na and O is detected on KF PDT samples without Se supply. Figure 7.2.2.5 illustrates this finding:

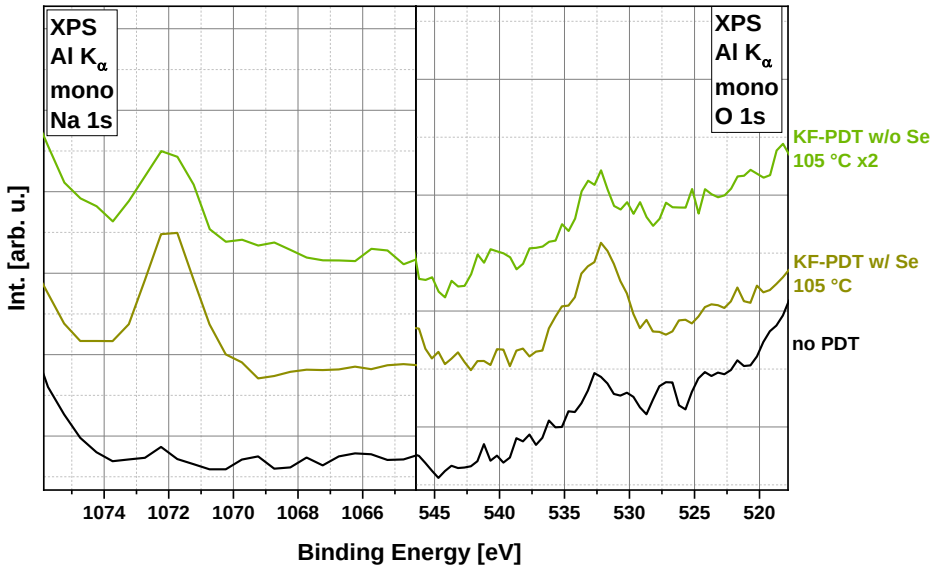

Figure 7.2.2.5 Na 1s (left) and O 1s (right) photoelectron spectra for the untreated reference cell (no PDT, black) and both KF PDT 105 °C samples with different Se supply. Both spectra are excerpts of a survey spectrum. Therefore, energy resolution and SNR might be comparably low.

A clear Na 1s signal is detected for both KF PDT 105 °C samples at E_{Bin} ~ 1072 eV. The Na 1s signal is less intense for the KF PDT 105 °C w/o sample than for the KF PDT 105 °C w/ Se sample. The same observation is made for the intensities of the O 1s signals, which appear at E_{Bin} ~ 532 eV. The energy resolution and the SNR of the spectra are low, compared to other spectra. This is because the spectra are excerpts of a survey spectrum. A chemical analysis of the Na species (not shown) on the KF PDT 105 °C w/o Se sample reveals that Na is present in a CIGSe-like environment, similarly to the Na species on the KF PDT 105 °C w/ Se sample. Because of its electropositive character, Na will mainly bind to Selenium at the surface and form Na-Se bonds. Furthermore, because of its high affinity to oxygen, it will also form bonds to oxygen atoms at the surface. Therefore, the Na component on the surface will be denoted as Na-Se-O, similar to the Na component on the other KF PDT 105 °C w/ Se sample.

According to the lower Na 1s and O 1s intensities (see Figure 7.2.2.5) on the KF PDT 105 °C w/o Se sample, it is assumed that less of a Na-Se-O like component formed on the KF PDT 105 °C w/o Se sample, than on the KF PDT 105 °C w/ Se sample.

To complete the chemical characterization of the KF PDT 105 °C w/o Se sample, some remaining traces of elemental Se were found on the surface after the rinse. The Se 3d spectra for both KF PDT 105 °C samples (with and without Se) are shown in the following in Figure 7.2.2.6.

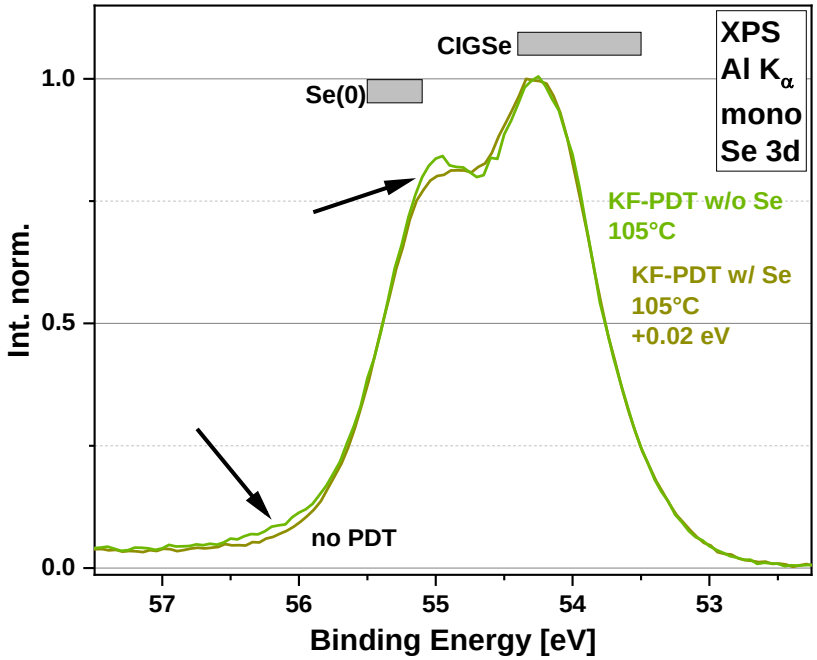

Figure 7.2.2.6 Normalized Se 3d spectra for the KF PDT 105 °C samples with and without Se supply. The spectra were normalized by setting the low binding energy background to zero and the signal maximum to one. For a better comparison of the spectral shapes, the spectrum of the KF PDT 105 °C w/ Se sample has been shifted by 0.02 eV to higher binding energy. Gray boxes indicate binding energy ranges for Se in different chemical environments. The arrows mark the position, where additional intensity is detected on the sample without Se (light green), compared to the sample with Se (dark yellow).

The KF PDT 105 °C w/o Se sample shows additional intensity at E_{Bin} ~ 55 and 56 eV, compared to the KF PDT 105 °C w/ Se sample. A fit of the Se 3d spectrum reveals an additional Se species at higher binding energies, which is ascribed to elemental Se, after comparison to literature values. Since no Se was supplied during PDT, it appears unusual that elemental Se is existent on the sample. It is speculated that this elemental Se stems from the excess Se, which is offered after completion of the CIGSe growth and that the rinse was too short, to sufficiently remove it. Therewith, the reason for the detection of elemental Se on the KF PDT 105 °C w/o Se sample might lie in experimental issues.

For now, the chemical characterization of the two KF PDT samples without Se at 315 °C and 105 °C has nearly been finished. Before summarizing the results in a sketch, it will be analyzed, how the stoichiometry of the underlying CIGSe phase has changed after the rinsing.

7.2.3 Relative changes of CIGSe surface stoichiometry due to KF PDTs with and without Se supply and summary

To evaluate the stoichiometry of the CIGSe phase, the “Low binding energy region“ was analyzed, similar to Chapter 7.1.4. The LBEE includes the photoelectron signals Se 3d, In 4d, Ga 3d, Cu 3p, and In 4p. Since Cu 3p is overlapping with the broad In 4p signal, the analysis of the Cu 3p signal is left out. For the evaluation of relative stoichiometries the peak areas of the aforementioned photoelectron signals were determined and the peak area ratios Ga/In and (Ga+In)/Se are calculated. The values are depicted in Table 10, below. To estimate relative changes, the respective Ga/In and (Ga+In)/Se ratios of the different samples were compared to the ratio of the untreated sample (no PDT). Only the contributions of the CIGSe component in the respective signal was taken to estimate the peak area.

Sample	Peak-Areas [arb. u.]			Peak-Area Ratios	
	In $4d_{5/2}$	Ga $3d_{5/2}$	Se $3d_{5/2}$	$\frac{Ga}{In}$	$\frac{Ga+In}{Se}$
no PDT	2733	525	4067	0.19 ± 0.01	0.80 ± 0.03
KF 315 w/ Se	3638	157	3759	0.04 ± 0.00	1.01 ± 0.05
KF 315 w/o Se x2	3130	180	3246	0.06 ± 0.00	1.02 ± 0.06
KF 105 w/ Se	2053	398	2973	0.19 ± 0.01	0.82 ± 0.05
KF 105 w/o Se x2	1872	418	3300	0.22 ± 0.02	0.69 ± 0.05

Table 10 Determined peak areas for In $3d_{5/2}$, Ga $3d_{5/2}$, Se $3d_{5/2}$, and calculated peak area ratios for the differently treated, rinsed CIGSe samples.

With Ga/In = 0.06, the Ga/In ratio of the KF PDT 315 °C w/o Se sample is higher than for the KF PDT 315 °C w/ Se sample, which is reasonable and can be explained as follows: In Chapter 7.1 a lower reactivity of KF has been observed, as well as lower amounts of Ga-F on the KF PDT 315 °C w/o Se samples, than on the respective sample with Se. Therefore, lower amounts of Ga(CIGSe) have reacted to form Ga-F bonds on the sample without Se, than on the sample with Se. Since Ga-F components like GaF_3 are water-soluble, the Ga-F bonds are washed away during rinse. Therefore, the CIGSe layer on the KF PDT 315 °C w/o Se sample should be less depleted in Ga, than the CIGSe layer on the KF PDT 315 °C w/ Se sample. This is the case, as can be read from the Ga/In ratio: The Ga/In ratio of the KF PDT 315 °C w/o Se sample deviates less from the Ga/In ratio of the untreated sample (0.06 vs. 0.19), than the Ga/In ratio of the KF PDT 315 °C w/ Se sample (0.04 vs. 0.19).

The (Ga+In)/Se ratios for both KF PDT 315 °C samples are nearly equal and higher than for the untreated reference cell. The relative Se amount within the CIGSe layer should therefore be similar on both KF PDT 315 °C samples (with and without Se supply).

For the KF PDT 105 °C w/o Se sample, a slight increase in the Ga/In ratio is observed (0.22 vs. 0.19), which lies within the error margin.

Concerning the relative Se-amounts, the (Ga+In)/Se ratio is lower on the KF PDT 105 °C w/o Se sample (0.69), than on the KF PDT 105 °C w/ Se sample (0.82). This increase stems from a more intensive Se 3d signal on the KF PDT 105 °C w/o Se sample, than on the KF PDT 105 °C w/ Se sample. As also traces of elemental Se are found on this sample (probably due to a too short rinsing time), the rinse may also not have removed any Se(CIGSe), so that the remaining Se(CIGSe) amount is slightly higher on the KF PDT 105 °C w/o Se sample.

A summary for the chemical differences between the KF PDT samples with and without Se supply is illustrated in Figure 7.2.3.1.

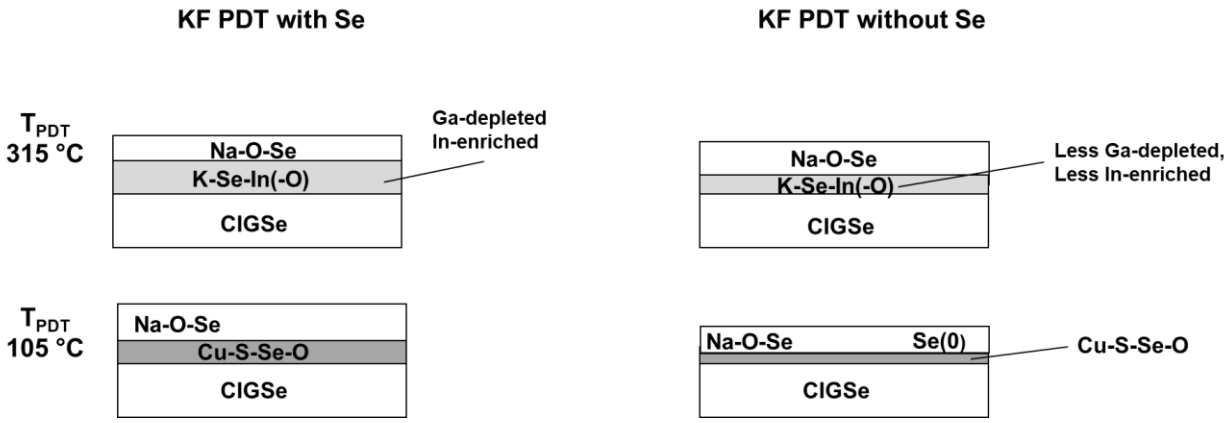

Figure 7.2.3.1 Summary for the comparison rinsed samples after a KF PDT with and without Se supply at T_{PDT} = 315 °C and T_{PDT} = 105 °C as a sketch. Note, that this sketch is very simplified, and does not take the morphology of the surface into account. It is not clear, e.g., if the adsorbate layer is homogeneously covering the surface or appears in the form of islands, which has a tremendous impact on the PDT, as well.

Without a Se supply, the KF PDT alters the CIGSe surface in a different way, than with Se supply:

For the KF PDT 315 °C w/o Se sample (Figure 7.2.3.1 upper row, right), the Ga-depletion of the surface is less pronounced, than for the KF PDT 315 °C w/ Se sample (Figure 7.2.3.1 upper row, left). On the sample without Se, lower amounts of a K species were detected, as well as a decreased intensity for In-related signals, than on the sample with Se. The Se species indicating In-Se bonds is also detected on the KF PDT 315 °C w/o Se sample. Together with the aforementioned findings, the formation of a species, in which In, Se, K and possibly O (because of the high oxophilic character of K) are bound together. Despite the exact composition and bonding motifs are not clear, the additional elements are summarized as “K-Se-In(-O)“. This species is suggested to form in lower amounts on the KF PDT 315 °C w/o Se sample, than on the KF PDT 315 °C w/ Se sample. At the same time, however, higher amounts of a Na-Se-O component were detected on the KF PDT 315 °C w/o Se sample, than on the KF PDT 315 °C with Se sample.

The surface of the KF PDT 105 °C w/o Se sample (Figure 7.2.3.1 lower row, right) was also found to be Cu-rich, similar to the surface of the KF PDT 105 °C w/ Se sample (Figure 7.2.3.1 lower row, left). An additional Cu species was also detected on the KF PDT 105 °C w/o Se sample and exists in a chemical environment between S, Se and O. As the exact stoichiometry of this Cu species is not known, it is described as “Cu-S-Se-O“, equally to the Cu species on the KF PDT 105 °C w/ Se sample. Differently, however, to the sample with Se supply, lower amounts of the Cu-S-Se-O species were detected on the sample without Se. This can be explained with the lower (relative) amounts of In-F on the as-grown KF PDT 105 °C w/o Se sample (than on the KF PDT 105 °C w/ Se sample, see Figure 7.1.2.5 left, page 93). Thereby, less In-F is washed away during the rinse, and the resulting surface is therefore less (relatively) enriched in Cu on the KF PDT 105 °C w/o Se sample. Consequently, the amount of Cu-S-Se-O is lower on the sample without Se (than on the sample with Se).

Moreover, some elemental Se is detected on the KF PDT 105 °C w/o Se sample (which might be due to an unintended insufficient rinsing) and lower amounts of Na-O-Se are detected, than on the KF PDT 105 °C w/ Se sample.

Summing up the comparison, K-Se-In(-O) and Cu-S-Se-O do also form on KF PDTs without Se supply, but in lower amounts than on a sample with Se supply.

After pointing out the chemical differences between KF PDTs with and without Se supply, the differences of the electronic properties of the surfaces will be evaluated. Thereby, He II excited UPS spectra of KF PDT CIGSe surfaces without Se supply are displayed in Figure 7.2.4.1 (next page) and are compared with the respective KF PDT CIGSe surfaces with Se supply and some untreated reference samples.

7.2.4 Changes of the valence band structure at the CIGSe surface due to KF PDTs with or without Se supply

As it was mentioned before, a sample charging of the KF PDT 315 °C w/o Se sample occurred while it was measured with Mg K_α radiation. The same problem is observed for the UPS measurement. This shift of the spectrum complicates the determination of the VBM severely. To overcome this problem, the UPS spectra of KF PDT 315 °C samples in "as-received" condition were analyzed, different to all other spectra examined in this work.

For a better comparison, a reference sample in "as-received" condition is also included for the KF PDT 315 °C samples (black), and a reference sample in "Ar^+ ion-cleaned" condition is included for the KF PDT 105 °C samples (gray). These UPS spectra are displayed in Figure 7.2.4.1, below.

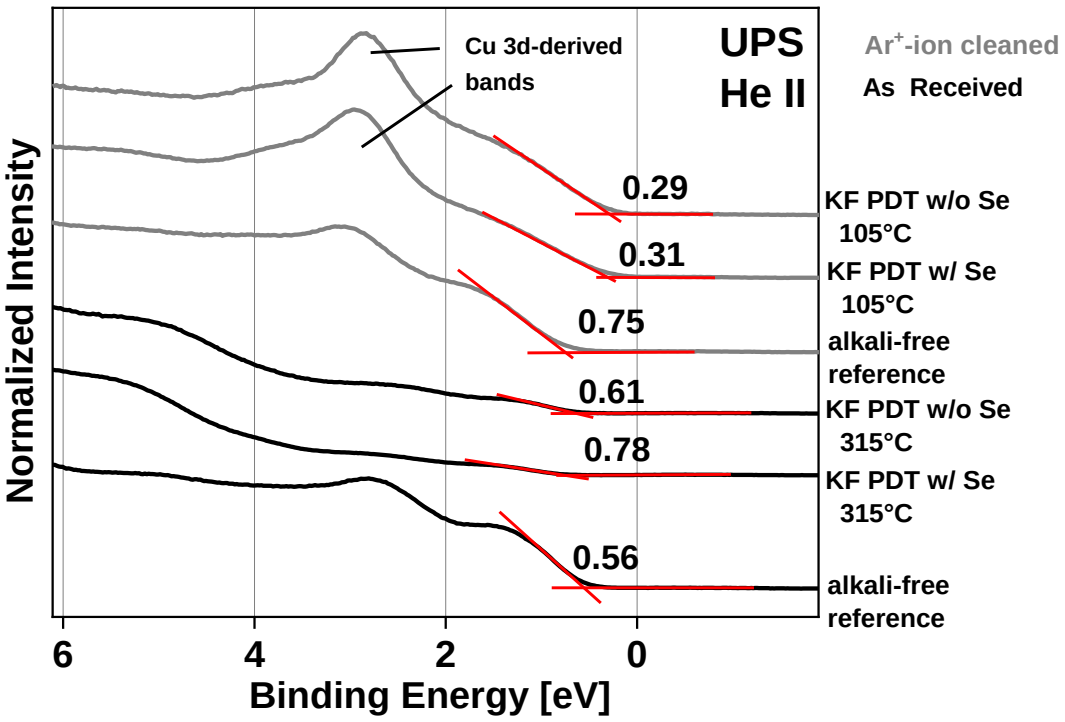

Figure 7.2.4.1 He II-excited UPS spectra of the CIGSe references and KF PDTs at T_{PDT} = 315 °C and 105 °C, with different Se supplies. For the KF PDT 315 °C samples, the "as-received" samples were compared, together with a reference in "as-received" condition (black). For the KF PDT 105 °C samples, the "Ar^+ ion-cleaned" samples were compared, together with a reference in "Ar^+ ion-cleaned" condition (gray). The binding energy is given with respect to the Fermi energy of a Au foil reference (not shown). Linear extrapolations of the leading edge are drawn for the determination of the valence band maxima (VBM). VBM values are given in eV with an error margin of ± 0.1 eV.

To determine the position of the valence band maximum (VBM) with respect to the Fermi Level (E_F), a linear extrapolation was drawn (red) for the leading edges for each spectrum.

For the evaluation of the KF PDT 315 °C samples, solely the spectra in black are compared, and for the evaluation of the KF PDT 105 °C samples, solely the spectra in gray are compared. The VBM position of the alkali-free reference samples do differ from each other (0.75 vs. 0.56 eV), because the Ar^+-ion cleaning removes some surface adsorbates and thus slightly changes the band bending at the surface.

For both KF PDT 315 °C surfaces (with and without Se supply), a downshift of the VBM (i.e. away from the Fermi level) is observed compared to the VBM of the reference surface. The magnitude of downshift for the VBM (rel. to E_F) from the reference sample to the KF PDT 315 °C w/ Se sample is comparable for the “as-received“ samples (shown here in Figure 7.2.4.1) and for the “Ar^+ ion-cleaned“ samples (shown earlier in Figure 5.4.1 in Chapter 5). This downward shift of the VBM on the KF PDT 315 °C w/ Se sample is explained by the formation of a K-In-Se(-O) like component on the CIGSe surface, like it was figured out in Chapter 6.

For the KF PDT 315 °C w/o Se sample, however, this downward shift of the VBM is less pronounced (+0.05 eV), than for the KF PDT 315 °C w/ Se sample and even lies within the error margin of this measurement (± 0.1 eV). It can therefore be speculated, if there is a “true“ downshift of the VBM on the KF PDT 315 °C w/o Se sample (rel. to the reference) or not. Nevertheless, this observation is in accordance with the chemical result that less of a K-In-Se(-O) like component has formed on the KF PDT 315 °C w/o Se sample, than on the KF PDT 315 °C w/ Se sample. Vice versa, this observation also indicates that mainly the K-In-Se(-O) component is responsible for the VBM downshift.

Another interesting observation is made for the Cu 3d-related bands at E_{Bin} ~ 3 eV: The intensity of Cu 3d-related bands is much lower on the KF PDT 315 °C samples (with and without Se), than on the reference sample. This reduced intensity can be explained with an attenuation of Cu 3d photoelectrons by the K-In-Se(-O) layer on top of the CIGSe surface. Since a reduced Cu 3d-intensity is observed for both KF PDT 315 °C samples, this confirms the formation Cu-free or Cu-poor component (such as K-In-Se(-O)) on both KF PDT 315 °C samples.

Next, the electronic properties of the KF PDT 105 °C sample surfaces (with and without Se supply) are compared:

The VBM on both KF PDT 105 °C samples show no difference. In both cases (with and without Se) a comparably high upward shift of the VBM towards the Fermi energy is detected, compared to the VBM position of the reference sample. Although it is anticipated that less of a Cu-secondary component (Cu-S-Se-O) forms on the KF PDT 105 °C w/o Se sample, than on the KF PDT 105 °C w/ Se sample, their impact on the electrical properties is equally strong.

Summing up, for the position of the VBM (rel. to E_F) it makes a big difference in case of a KF PDT at 315 °C, if Se is supplied during PDT or not. For the KF PDT 315 °C w/ Se sample, a clear downshift of the VBM of ~0.2 eV is observed, whereas for the KF PDT 315 °C w/o Se sample no, or at least a very weak downshift of ~0.05 eV is observed. For the KF PDT 105 °C samples it makes no difference for the position of the VBM (rel. to E_F), if Se is supplied during PDT or not. Reasons for this different behavior are not found. The author of the work in hand assumes that different growth modes of the secondary component (K-In-Se(-O) or Cu-S-Se-O) might play a role.

Finally closing Chapter 7, it has been found out that the reactivity of KF is drastically altered, when no Se is supplied during the PDT. The CIGSe surfaces are less Ga- and In-depleted and lower amounts of secondary components form after a rinse. Nevertheless, the impact on electronic properties of the CIGSe surface is still distinctively pronounced. However, new questions arise, concerning the exact chemical dependence of Ga-F or In-F formation on Se supply or the effectiveness of the Se supply at different PDT temperatures.

8 Concluding Discussion and Outlook

The work in hand compared the chemical and electrical effects of a NaF PDT and KF PDT on CIGSe layers and complete -solar cells. For this purpose, specially tailored CIGSe solar cells and layers with a defined structure and composition were manufactured and analyzed. The chosen CIGSe solar cell structure served as a simple model for more complex CIGSe material systems applied in the industrial production. With the use of alkali-free substrates, single stage grown CIGSe, a proven wet-chemical treatment and under exclusion of surface contaminations, a well-defined system with less degrees of freedom was established, enabling a promising in-depth electrical and chemical analysis. The here-found results serve as a basis to understand more complex industrial CIGSe solar cells, and to make more targeted improvements possible.

At first, the device properties of complete solar cells were compared, to establish a general comparison between NaF PDT and KF PDT cells. Then, for the most noticeable differences, the specific chemical causes were investigated via XPS measurements. Following these issues, further questions arose, concerning the molecular mechanism of the PDT. Therewith, the chemical role of Selenium was unraveled in the last section.

The comparison of the NaF PDT and KF PDT cells started with the dependence of device performances on PDT temperature (T_{PDT}), an important process parameter of the PDT. A steady increase of the cell efficiency with increasing T_{PDT} is observed for NaF PDT cells, resulting in higher efficiencies than for the untreated, alkali-free reference cell. For KF PDT cells an increase in efficiency was also observed for $T_{PDT} > 150$ °C, however, for $T_{PDT} < 150$ °C a strong drop in efficiency is observed, resulting in lower efficiencies, than for the untreated reference cell.

Only very few examples are reported, in which an alkali PDT leads to efficiencies lower than an untreated cell [36,86,88,133]. The question is, if a KF PDT at $T_{PDT} < 150$ °C solely deteriorates the electrical properties of the CIGSe layer, or has a more extensive impact on e.g., the chemistry at the interfaces? Therewith, at first some properties of complete cells are checked: The alkali concentration within the CIGSe layer is higher in both, NaF PDT and KF PDT cells, than for the untreated cells. Moreover, the K-concentration after a KF PDT is even higher than the Na-concentration after a NaF PDT. The integral alkali supply should therefore be sufficient. Another important electrical property is the charge carrier density N_A, derived from C-V measurements. The N_A of both, NaF PDT and KF PDT cells is higher than the N_A of the untreated reference cell. Therefore, electrical properties, such as the electrical conductivity (σ) of the CIGSe material might also be sufficiently high (as σ rises proportionally with N_A), enabling a good charge carrier transport. These findings are the “typical“ effects of alkali metals as dopants in CIGSe solar cells, as reported in numerous studies before. Therefore, at a first glance, no indications exist, why especially the KF PDT cell at $T_{PDT} < 150$ °C should be deteriorated.

A closer inspection of the KF PDT with $T_{PDT} < 150$ °C cells exhibits strong deviations of the I-V curves from the ideal diode shape. EQE measurements show a dramatically decreased quantum yield over the whole spectral range of the cell. Both observations suppose a heavily deteriorated p/n-junction and/or a massively increased number of deep-level defects in the absorber layer.

Comparable findings are made e.g., when the CIGSe layer is contaminated with traces of Fe^{2+} [134] or Ni^{2+} [135]. For these cells, the current breaks down over the entire spectral range, similar to what is observed for the low T_{PDT} KF PDT cells, resulting in very bad devices. Therefore it

must be considered, which reason for the efficiency drop is more likely: An increased number of deep-level defects within the CIGSe layer or a degraded p/n-junction?

An increased number of deep-level defects might be ruled out, since alkali metal ions like Na^+ and K^+ are chemically completely different to transition metal ions like Fe^{2+} or Ni^{2+}: Generally, transition metal cations can form diverse coordination polyhedra, depending on their oxidation state, are capable of existing in a variety of bonding motifs, regularly exhibit magnetism, and show a pronounced redox activity. Alkali metal cations, however, are quite limited in their ability to form multiple bonds, mainly show diamagnetism, remain as monovalent cations, and show no pronounced redox behavior. These differences come alive especially in solution but are still perceptible in solid state. Therefore, alkali metal ions like Na^+ and K^+ behave chemically different in the CIGSe bulk, than Fe^{2+} and Ni^{2+} ions and thus, should not be able to introduce deep-level defects in the CIGSe layer.

On one hand, since Na^+ and K^+ ions improve the electrical properties of the CIGSe layer, (as it is observed for NaF PDT cells, and high T_{PDT} KF PDT cells), how, on the other hand, K^+ ions should be able to deteriorate the electrical properties (in low T_{PDT} KF PDT cells)? Since it is the same chemical K species, which diffuses into the CIGSe bulk regime at high and low T_{PDT}, the formation of deep-level defects especially at $T_{PDT} < 150$ °C is ruled out.

Consequently, the main reason for non-ideal diode behavior, massive current loss, and subsequently performance decline, must be a degraded p/n-junction in low T_{PDT} KF PDT cells.

The following question was, how a low T_{PDT} KF PDT can lead to the degradation of the p/n-junction? As the p/n-junction is the interface between CIGSe and CdS and the CdS layer is grown onto the CIGSe layer, the CIGSe surface plays a special role in this context. As the CIGSe surface is the substrate for the subsequent CdS growth, its chemical nature distinctly influences the resulting interface. UPS measurements of rinsed CIGSe surfaces reveal a strong upward-shift of the VBM by −0.44 eV on the KF PDT 105 °C sample, compared to the untreated and rinsed CIGSe sample surface. This drastic electronic transformation at the surface of the KF PDT 105 °C sample might be responsible for the breakdown of the p/n-junction and the drop in efficiency: A strong reduction of the band bending at the CIGSe surface due to the KF PDT 105 °C could lead to an unfavorable band alignment at the CdS/CIGSe interface and thus to a strong increase in charge carrier recombination.

To obtain a complete picture of the specific situation at the different surfaces, the NaF PDT and KF PDT CIGSe samples were characterized chemically with XPS. For this purpose, in sum four different samples with different PDTs were analyzed: Two NaF PDTs at T_{PDT} = 315 °C and 105 °C, and analogously two KF PDTs at T_{PDT} = 315 °C and 105 °C. Therewith, a direct comparison of a NaF PDT to a KF PDT is possible, and the influence of the PDT temperature can also be investigated. To our knowledge, this is the first time, a mere alkali fluoride PDT is performed and analyzed on an alkali-free grown single stage CIGSe layers. The subsequent processing step after the PDT is the rinsing treatment. The rinsing treatment happens prior the CdS deposition and therefore also influences the properties of the p/n-junction. The effects of the rinsing step are therefore analyzed, as well.

The results partly coincide with findings from other, different CIGSe studies in literature: The PDT and subsequent rinsing modify the CIGSe sample surface pronouncedly and lead to an altered surface constitution. A NaF PDT leads to less pronounced chemical changes on the CIGSe surface, than a KF PDT [136]. Ga-F bonds are observed on all sample surfaces after PDT, but only in case of a KF PDT, a Ga-depleted surface results after rinsing. This higher reactivity of KF, compared to NaF, is explained with the lower lattice energy for KF (816 kJ/mol), than for NaF (920 kJ/mol). Therewith, the reaction of fluoride with the constituents of the CIGSe surface can take place faster in case of KF. For both NaF PDTs

(T_{PDT} = 315 °C and 105 °C) no significant change of the CIGSe surface composition resulted. After rinsing, only 5-10% of a Na species are found on the surfaces, which can be a component like Na_2O or Na_2Se, possibly also containing C. These minor changes of the surface composition after a NaF PDT explain the only small shifts of the VBM position (rel. to E_F), compared to the VBM position of the untreated sample surface, as found by UPS.

The enhanced reactivity for KF, however, leads to a totally different surface chemistry, depending critically on PDT temperature: At T_{PDT} = 315 °C a strong depletion of Cu and Ga at the surface is observed, together with the formation of a second Se species, a water-insoluble K species and a distinctively increased intensity for In-related signals. The question arose, how to interpret these specific findings?

In a HAXPES measurement of NaF+KF PDT CIGSe surfaces Handick et al. also found a second Se species at lower Se 3d binding energy, as well as a second In species at lower binding energy [38]. Chemically, these additional Se and In species were very similar to the In- and Se species of an In_2Se_3 reference sample, which underwent a KF PDT. Additional XES measurements of the Se $M_{4,5}$ transition revealed the existence of two Se species, one in a CIGSe-like environment, and the other Se species in an In_2Se_3 + KF PDT environment. Therefore, the new Se species, which is detected at lower Se 3d binding energy by Handick et al. should stem from a new type of Se-In bonds. Consequently, although not a combined NaF+KF PDT was conducted in this work, it is possible that the additional Se species on the KF PDT 315 °C sample also belongs to Se-In bonds.

Lepetit et al. [123] also observed an additional Se species due to a KF PDT at lower Se 3d binding energy and identified these Se species upon comparison with literature as Se-In bonds. To verify this finding, a KF PDT was applied under simultaneous evaporation of elemental In and Se [137]. Therewith, the chemical reaction of In with KF and Se was specifically promoted. As a result, the intensity of the new Se species at lower Se 3d binding energy increased, which corroborates that the new Se species must consist of Se-In bonds.

Because the work in hand applies a similar KF PDT and also detects a new Se species at lower Se 3d binding energies, this new Se species should also represent a new type of Se-In bonds. This finding is also underpinned by the fact that the In-related signal intensity strongly increases on the KF PDT 315 °C sample. At the same time, Ga and Cu related signals decrease, which is another hint for a new layer on top of the CIGSe surface.

The findings for Se and In signals on the KF PDT 315 °C sample have now been discussed. Subsequently, the K-related signals will be addressed and compared to literature.

The observations for K-related signals on the KF PDT 315 °C sample are similar to those found in literature: A water-insoluble, chemically stable K species forms on the CIGSe surface. With Raman spectroscopy measurements Lepetit et al. [123] found that, structurally, the In-Se species that forms after KF PDT at the CIGSe surface, is substantially affected by the existence of K. Because of the similar KF PDT processes of Lepetit and the work in hand, it is therefore assumed that the new In-Se species is affected by K, as well.

Briefly summarizing all findings for the KF PDT 315 °C sample, the formation of a new Se species can be claimed. This new Se species should be bound to In, which is chemically similar to In in CIGSe. Moreover, K is also involved in the formation of a new In-Se species, so that chemically it becomes water-insoluble. The exact composition and binding situation between Se, In, and K, however, remains unclear, and it is not known, what role oxygen might play on the surface. Furthermore, it is not clear, if just loose atomic bonds exist between these elements, or a complete phase has formed. Therefore, just a formula can be resumed in which the concerned elements are given: K-In-Se(-O).

Nevertheless, this “loose“ arrangement of atoms, bonds or domains, however, might be sufficient, to create a beneficial band alignment between the modified CIGSe surface and CdS, so that charge carrier recombination at the interface is greatly reduced.

In this respect, also similar observations for the electrical properties at the surface are made on our samples and Handick´s samples, when a KF PDT is applied:

Handick et al. [8] found that the downward shift of the VBM at the surface is more intense after a NaF+KF PDT, than after a NaF PDT. They explained this observation with a possible formation of a K-In-Se or In-Se component after a NaF+KF PDT, which has a higher band gap, than the nearly unchanged CIGSe surface, after a NaF PDT. [8]. For the work in hand, this observation is also made, but to a lower extent: The downward shift of the VBM (rel. to E_F) is more pronounced for the KF PDT 315 °C sample, than for the NaF PDT 315 °C sample. Again, this is another hint which implies that a K-In-Se(-O) like component has formed on the KF PDT 315 °C sample surface.

So far, for the KF PDT 315 °C sample the possible formation of a K-In-Se component has been detected on the CIGSe surface, whereas for the NaF PDT 315 °C sample no Na-In-Se component has been found.

To conclude the comparison of the KF PDT 315 °C and NaF PDT 315 °C samples, the existence or absence of these secondary components can be explained with thermodynamic calculations by Malitckaya et al. [39] They found different solubilities of a hypothetical $KInSe_2$ or $NaInSe_2$ phase in $CuInSe_2$ bulk material. At T = 315 °C the solubility of $KInSe_2$ in $CuInSe_2$ is lower than the solubility of $NaInSe_2$ in $CuInSe_2$. Therefore, Na should be „dissolved in the $CuInSe_2$ matrix as $Na_xCu_{1-x}InSe_2$ e.g., whereas for K a phase segregation occurs and $KInSe_2$ coexists on the $CuInSe_2$ surface (in this work a $Cu(In,Ga)Se_2$ surface). Although this is a very general explanation, it confirms the findings for the KF PDT 315 °C and NaF PDT 315 °C samples.

Again, it must be mentioned that for the first time this circumstance has now been proven for an alkali-free grown, single stage CIGSe absorber surface, which underwent a mere NaF PDT or KF PDT.

Next, the results for the low T_{PDT} KF PDT at 105 °C are evaluated, for which the cell properties have deteriorated dramatically. After the KF PDT 105 °C, Ga-F bonds, as well as In-F bonds are found as products of reaction on the CIGSe surface. The detection of In-F bonds is very surprising, since they are only found on the KF PDT 105 °C sample surface. After the rinse, Ga-F and In-F components are washed away, since they are soluble in water, and a Ga- and In-depleted surface resulted. Hence, the CIGSe component is destroyed at the surface and mainly Cu and Se remained and form a Cu-S-Se-O secondary component with sulfur from the Na_2S rinse. This Cu-O-Se-S component is not soluble in water and can be viewed as a precipitate on top of the underlying CIGSe layer.

Raman measurements of a complete KF PDT 105 °C solar cell showed characteristic vibrational modes for a Cu-Se secondary phase besides the mode of $Cu(In,Ga)Se_2$ [138]. Thereby, the existence of a Cu-Se secondary component at the CIGSe surface is supported by Raman measurements.

Again, like for the K-In-Se(-O) species on the KF PDT 315 °C samples, the exact composition and binding situation in the Cu-Se-S-O species (on the KF PDT 105 °C samples) is not clear. It is not known if just loose Cu-bonds or isolated Cu-phases exist, which cover the CIGSe surface. It can just be stated that a Cu-rich surface has been formed upon KF PDT 105 °C in which S, Se and oxygen are bound to Cu. This Cu secondary component has detrimental electrical effects, as the strong upward shift of the VBM (rel. to E_F) points out. Therewith, the

formation of the Cu secondary component is the chemical reason for the huge efficiency drop for KF PDT 105 °C cells.

A similar observation was made by Lepetit et al. [36]: Upon a KF PDT of multi-stage CIGSe layers, he also received cells with completely degraded properties. As for the work in hand, not only V_{OC} and FF decreased, but also the j_{SC} dropped significantly. As causes for this behavior, Lepetit also observed the formation of a second Cu species on the KF PDT surface and identified it as $Cu_{2-x}Se$. This confirms that the Cu-S-Se-O component, found on the KF PDT 105 °C sample surface, must be responsible for the efficiency drop. It must be mentioned, however that Lepetit performed a KF PDT at T_{PDT} = 350°C on a CIGSe layer with higher Cu content than used in standard CIGSe layers, whereas for the work in hand a KF PDT was performed at T_{PDT} = 105 °C on a Cu-poor grown CIGSe layer. Nonetheless, both situations lead to the formation of a Cu-secondary component at the CIGSe surface.

Another indirect hint for the formation of a Cu-secondary component at the CIGSe surface yielded a test of different rinsing agents and their effect on cell efficiency (presented in chapter 5.3). Indeed, rinsing a KF PDT 105 °C sample with KCN solution, instead of Na_2S solution, increases the PCE from 0.4 to 7.2 %. As common, cyanide ions are suitable ligands to dissolve Cu(I)-components under formation of soluble $[Cu(CN)_2]^-$ complex anions and hence dissolve the Cu-secondary component at the CIGSe surface. Thereby, only a weak deterioration of the cell efficiency, compared to the alkali-free reference cell (10 %), is observed. Yet, this explanation is very implicit and still has to be vetted.

So far, it is concluded that the simultaneous depletion of Ga and In on the KF PDT 105 °C sample led to a (relatively) Cu-enriched CIGSe surface. Thereby, it is important to mention that the KF PDT 105 °C sample is the only sample, on which In-F bonds are detected, together with Ga-F bonds (which are washed away in the rinse, so that a Ga- and In-depletion results). However, it is not trivial that the formation of these In-F bonds (together with Ga-F bonds) takes place exclusively on the KF PDT 105 °C sample surface. An explanation, including not yet validated assumptions could go as follows:

Indium is a less reactive metal than gallium. In order to enable a reaction of In from CIGSe with NaF or KF, a higher reactivity of the alkali fluoride is needed. This higher reactivity is established by an increased concentration of NaF or KF on the CIGSe surface, as well as by a faster dissociation of NaF or KF into Na^+/K^+ and F^- ions (because only the ions are able to react with CIGSe).

For a higher concentration of alkali fluoride, lower T_{PDT} (in our case 105 °C) are needed, because at lower T_{PDT} the desorption of the alkali fluoride into the gas phase is slower. For KF a faster dissociation into ions is expected, compared to NaF, because the lattice energy of KF is lower than of NaF. Combining both aspects, only in case of the KF PDT 105 °C sample, the concentration of KF on the CIGSe surface is high enough, and, at the same time the dissociation of KF into K^+ and F^- is pronounced enough, to increase its reactivity. It is the effective balance between these two aspects, which determine the reactivity of the alkali fluoride at a certain T_{PDT}. For the here-examined T_{PDT} range and the given values for the lattice energies for NaF and KF, the highest alkali fluoride reactivity is found on the KF PDT 105 °C sample. For this reason, KF on the KF PDT 105 °C sample not only reacts with Ga to form Ga-F bonds, but also with In to form In-F bonds.

Indirect proofs of this model can be made, when the concentration of KF on the CIGSe surface is varied, e.g., by varying the KF rate during PDT (not shown):

When the KF rate during a KF PDT 105 °C is reduced, the concentration of KF on the CIGSe surface is reduced. Thereby, the reactivity of KF decreases, so that less (or even no) In-F

bonds form, the surface becomes Ga-depleted, but only scarcely In depleted (after rinse) and no (relatively) Cu-enriched surface formed, with detrimental electrical properties. Thereby, the efficiency drop should be less pronounced. This, however, is exactly the observation, which is made (not shown), when a KF PDT 105 °C is applied with reduced KF rate (from 0.3 to 0.03 Å/s) during PDT: The efficiency of the resulting cell “rises“ from 1 to 9%.

Vice versa, the model can also be proven indirectly on the KF PDT 315 °C sample: By increasing the KF rate during KF PDT 315 °C, the concentration of KF on the CIGSe surfaces increases. Thereby, the reactivity of KF increases, so that Ga-F, as well as In-F bonds form, the surface becomes Ga-depleted and In depleted (after rinse) and a (relatively) Cu-enriched surface forms, with detrimental electrical properties. Thereby, the efficiency should decrease distinctly. Again, this is the observation, which is made (not shown), when a KF PDT 315 °C is applied with increased KF rate (from 0.3 to 0.9 Å/s) during PDT: The efficiency of the resulting cell “drops“ from 13 to 9%.

These observations serve as first hints that the “alkali fluoride reactivity model“ is correct. Consequently, the formation of In-F bonds (in addition to Ga-F bonds) can now be regarded as the “true“ origin of the efficiency drop on KF PDT 105 °C CIGSe solar cells.

To finalize the results for NaF and KF PDTs, it can be appreciated that with a precise chemical analysis of the sample surfaces with XPS, one was successful in explaining the observed electrical trends with T_{PDT}.

The observations made in Chapter 6 show that the PDT on CIGSe surfaces involves a complex chemical mechanism with yet unexplained details. Another unexplained detail is the purpose of the Se supply during PDT. On KF PDTs without Se supply, the following observations are made: The amount of K incorporated in the CIGSe layer is two orders of magnitude lower, when a KF PDT at 315 °C is applied with no Se supply at all. At the same time, the cell parameters improve slightly, though [139].

Consequently, Se somehow plays a very special role and is inevitable for the effectiveness of the PDT. To corroborate this special role of Se on the PDT, KF PDTs without Se supply were conducted in Chapter 7, and the results were compared with those of normal KF PDTs from Chapter 6 (with Se supply). The following findings were made: In case of a KF PDT without Se supply, smaller amounts of KF are detected and the CIGSe surface is covered with a thinner layer of adsorbates. At the same time less reactants like Ga-F, In-F, Se(0), or Cu-Se-S-O are detected, than on a KF PDT sample with Se supply (see Figure 7.1.6.1, page 108). After rinse, the KF PDT 315 °C w/o Se surface is less Ga-depleted and less of a K-In-Se(-O) component forms, than on the KF PDT 315 °C w/ Se sample. For the rinsed KF PDT 105 °C w/o Se sample, also lower amounts of the Cu-Se-S-O secondary component are detected, than on the KF PDT 105 °C w/ Se sample.

Summing up these results, without Se, the amount of KF on the CIGSe surface is lower, and therewith, the reactivity of KF on the CIGSe surface might be lower. This explains the lower amounts of reactants and consequently a less chemically changed surface composition (after rinse), compared to a KF PDT with Se supply.

Vice versa, the existence of Se during PDT seemingly increases the amount of KF on the surface and thereby increases the reactivity of KF. Consequently, Se could function as a “cover“ impeding the desorption of KF off the CIGSe surface into the gas phase, so that more KF is available for the chemical reactions. In this respect, it is rather the colligative property of Se (together with KF) on the CIGSe surface, which plays an important role, than the specific chemical properties of Se.

Nonetheless, one could also imagine a specific chemical impact of Se on the PDT mechanism. This means that Se might be catalytically active and promote the reaction between CIGSe and KF to form Ga-F and In-F. This aspect seems reasonable, since in organoselenium chemistry, some Se-compounds are known to possess catalytic properties [140]. This holds true especially for essential seleno-proteins, where selenocysteine works as a key catalytic group [141,142].

Chemically, the dependence of the PDT on Se is not trivial. For the formation of Ga-F or In-F species, formally no Se is needed. The formation of these fluorides can be understood as a metathetical reaction, shown for CIGSe with an exemplary composition in Eq.12 (and for now leaving out the formation of secondary components like K-In-Se):

$$CuIn_{0.5}Ga_{0.5}Se_2 + 1.5\ KF \rightarrow CuIn_{0.5}Ga_{0.5}Se_{1.25}F_{1.5} + 0.75\ K_2Se \qquad \text{(Eq.12)}$$
$$\downarrow$$
$$CuIn_{0.5}Se_{1.25} + 0.5\ GaF_3 + 0.75\ K_2Se$$

In such a reaction the CIGSe surface and KF partly "exchange“ their cations and anions. This means that the fluoride anions will leave KF and react with the positively charged cations of the CIGSe surface, in this case Ga. A part of the K cations in KF will react with the negatively charged anions in CIGSe, which is Se. Depending on the stability of these intermediates, they will decay into end products, which are then detected by XPS. These reactions formally run without elemental Se, as can be understood by the reaction equations above.

The chemical properties of the surface of a material, however, deviate greatly from that of the bulk material. Surfaces in general exhibit very special sites for chemical reactions with a variety of exotic electronic properties. This peculiarity in fact just enables their catalytic capabilities and make unusual chemical reactions possible. In a same way, it is believed that the CIGSe surface and elemental Se will behave in their very special way to enable a chemical reaction with alkali fluorides. No previous attempts to unravel the specific chemical role of selenium have been published so far. Summing up the results for KF PDT without Se, the work in hand marks the first effort in this matter.

For now, still a number of open questions exists, which will have to be tackled with future experiments. For example, an interesting observation was made concerning the relative amounts of Ga-F species to In-F species on the KF PDT 105 °C samples with and without Se: Upon a KF PDT 105 °C w/o Se, less In-F species (relative to Ga-F species) are detected. This means that the formation of In-F species more critically depends on Se, than the formation of Ga-F species. Another example might be the existence of selenium fluorides like SeF_4 or SeF_6. It is anticipated by the scientific community that these species form during PDT. However, because of their high vapor pressure and due to their low concentration, they have not been detected, so far. With specially tailored experiments like Temperature Programmed Desorption (TPD) one might be able to prove their existence. Thereby, the role of Se during PDT on the CIGSe surface remains very versatile and complex.

All in all, the work in hand has revealed the chemical differences of a NaF PDT and KF PDT on alkali-free grown CIGSe layers, has explained the impact of PDT temperature and its consequences for the electrical cell properties, and has given first insights into the exact chemical role of Se during PDT.

To give a more general outlook, the work in hand has focused more on the chemical composition of the CIGSe surface. However, SEM images reveal that the morphology of the alkali fluoride (and Se) on the CIGSe surface also plays a significant role. Depending on the growth mode of the alkali fluoride and Se on the CIGSe surface, differently patterned nano-

structures evolve, which can alter the chemical reactivity of the surface [143]. Several experiments with varying alkali fluoride rates during PDT (not included in this work but mentioned before) have shown that the rate of alkali fluoride coevaporation is also a critical process parameter, with tremendous impact on resulting cell efficiency.

Even in a simplified CIGSe system as in the work in hand, unexpected electrical trends appeared and resulted from a complex chemical interplay between the here-examined parameters: PDT temperature, alkali fluoride, and Se supply. For industrial CIGSe production processes, the PDT parameters have to be optimized even more carefully, in respect of a higher complexity and assumingly more “hidden” parameters.

Ongoing effort must be put into these aspects to be able to implement substantial improvements, boosting further the efficiency of CIGSe solar cells.

References

[1] Klimaschutzpaket der EU-Kommission, https://www.bundesregierung.de/breg-de/themen/europa/fit-for-55-eu-1942402, accessed 17 August 2022.

[2] Die Evolution der gemeinsamen Energieaußenpolitik der EU, https://www.bpb.de/themen/wirtschaft/energiepolitik/152502/die-evolution-der-gemeinsamen-energieaussenpolitik-der-eu/, accessed 17 August 2022.

[3] Russland und die Europäische Union, https://www.bpb.de/themen/europa/russland/47974/russland-und-die-europaeische-union/, accessed 17 August 2022.

[4] A. M. Gabor, J. R. Tuttle, D. S. Albin, M. A. Contreras, R. Noufi, A. M. Hermann, *Appl. Phys. Lett.* **1994**, *65 (2)*, 198–200. DOI: 10.1063/1.112670.

[5] D. Rudmann, Da Cunha, M. Kaelin, F. Kurdesau, H. Zogg, A. N. Tiwari, G. Bilger, *Appl. Phys. Lett.* **2004**, *84 (7)*, 1129–1131. DOI: 10.1063/1.1646758.

[6] Solar Frontier achieves CIS thin-film lab efficiency record of 23.35%, https://www.pv-tech.org/solar-frontier-achieves-cis-thin-film-efficiency-record-of-23-35/, accessed 19 August 2022.

[7] A. Czudek, A. Urbaniak, A. Eslam, R. Wuerz, M. Igalson, *phys. stat. sol. (RRL)* **2022**, *16 (1)*, 2100459. DOI: 10.1002/pssr.202100459.

[8] E. Handick, P. Reinhard, J.-H. Alsmeier, L. Köhler, F. Pianezzi, S. Krause, M. Gorgoi, E. Ikenaga, N. Koch, R. G. Wilks, S. Buecheler, A. N. Tiwari, M. Bär, *ACS Appl. Mater. Interfaces* **2015**, *7 (49)*, 27414–27420. DOI: 10.1021/acsami.5b09231.

[9] F. Pianezzi, P. Reinhard, A. Chirilă, B. Bissig, S. Nishiwaki, S. Buecheler, A. N. Tiwari, *Phys. Chem. Chem. Phys.* **2014**, *16 (19)*, 8843–8851. DOI: 10.1039/c4cp00614c.

[10] D. A. Cusano, *Solid-State Electron.* **1963**, *6 (3)*, 217–232. DOI: 10.1016/0038-1101(63)90078-9.

[11] P. N. Keating, *J. Phys. Chem. Solids* **1963**, *24 (9)*, 1101–1106. DOI: 10.1016/0022-3697(63)90023-4.

[12] W. D. Gill, R. H. Bube, *Journal of Applied Physics* **1970**, *41 (9)*, 3731–3738. DOI: 10.1063/1.1659500.

[13] K. W. Böer, *Phys. Rev. B* **1976**, *13 (12)*, 5373–5385. DOI: 10.1103/PhysRevB.13.5373.

[14] S. Wagner, J. L. Shay, P. Migliorato, H. M. Kasper, *Appl. Phys. Lett.* **1974**, *25 (8)*, 434–435. DOI: 10.1063/1.1655537.

[15] W. E. Devaney, R. A. Mickelsen, W. S. Chen, *Proceedings of the 18th IEEE PV Specialists Conference* **1985**, 1733.

[16] R. Scheer, *Chalcogenide photovoltaics: Physics, technologies, and thin film devices,* Wiley Online Library, Wiley-VCH, Weinheim **2011**.

[17] D. Abou-Ras, D. Rudmann, G. Kostorz, S. Spiering, M. Powalla, A. N. Tiwari, *Journal of Applied Physics* **2005**, *97 (8)*, 84908. DOI: 10.1063/1.1863454.

[18] M. Nakamura, K. Yamaguchi, Y. Kimoto, Y. Yasaki, T. Kato, H. Sugimoto, *IEEE J. Photovoltaics* **2019**, *9 (6)*, 1863–1867. DOI: 10.1109/JPHOTOV.2019.2937218.

[19] Avancis GmbH, Weltrekordwirkungsgrad für CIGS Solarmodule: NREL zertifiziert einen Aperturwirkungsgrad von 19,64 % **2021**, https://www.avancis.de/wirkungsgrad-weltrekord-fuer-cigs-solarmodule-von-1964/.

[20] ZSW Stuttgart, Schichtaufbau eines CIGS-Solarmoduls im Rasterelektronenmikroskop (REM), https://www.zsw-bw.de/forschung/photovoltaik/themen/duennschichtsolarzellen-und-module.html#c460, accessed 5 September 2022.

[21] S. Minoura, T. Maekawa, K. Kodera, A. Nakane, S. Niki, H. Fujiwara, *J. Appl. Phys.* **2015**, *117 (19)*, 195703. DOI: 10.1063/1.4921300.

[22] T. Tinoco, C. Rincón, M. Quintero, G. S. Pérez, *physica status solidi (a)* **1991**, *124 (2)*, 427–434. DOI: 10.1002/pssa.2211240206.
[23] A. Urbaniak, M. Igalson, F. Pianezzi, S. Bücheler, A. Chirilă, P. Reinhard, A. N. Tiwari, *Solar Energy Materials and Solar Cells* **2014**, *128*, 52–56. DOI: 10.1016/j.solmat.2014.05.009.
[24] Hedström et al., *Conf. Rec. 23rd IEEE PVSC* **1993**, 364.
[25] M. Ruckh, et al., *24th IEEE PVSC* **1994**, 156.
[26] A. Laemmle, R. Wuerz, T. Schwarz, O. Cojocaru-Mirédin, P.-P. Choi, M. Powalla, *Journal of Applied Physics* **2014**, *115 (15)*, 154501. DOI: 10.1063/1.4871457.
[27] C. Heske, R. Fink, E. Umbach, W. Riedl, F. Karg, *Appl. Phys. Lett.* **1996**, *68 (24)*, 3431–3433. DOI: 10.1063/1.115783.
[28] D. Rudmann, G. Bilger, M. Kaelin, F.-J. Haug, H. Zogg, A. N. Tiwari, *Thin Solid Films* **2003**, *431-432*, 37–40. DOI: 10.1016/S0040-6090(03)00246-3.
[29] H. Stange, S. Brunken, H. Hempel, H. Rodriguez-Alvarez, N. Schäfer, D. Greiner, A. Scheu, J. Lauche, C. A. Kaufmann, T. Unold, D. Abou-Ras, R. Mainz, *Appl. Phys. Lett.* **2015**, *107 (15)*, 152103. DOI: 10.1063/1.4933305.
[30] D. Rudmann, A. F. da Cunha, M. Kaelin, F.-J. Haug, H. Zogg, A. N. Tiwari, *Mat. Res. Soc. Symp. Proc.* **2003**, *763 (B1.9.1)*.
[31] A. Laemmle, R. Wuerz, M. Powalla, *Phys. Status Solidi RRL* **2013**, *7 (9)*, 631–634. DOI: 10.1002/pssr.201307238.
[32] A. Chirilă, P. Reinhard, F. Pianezzi, P. Bloesch, A. R. Uhl, C. Fella, L. Kranz, D. Keller, C. Gretener, H. Hagendorfer, D. Jaeger, R. Erni, S. Nishiwaki, S. Buecheler, A. N. Tiwari, *Nat. Mater.* **2013**, *12 (12)*, 1107–1111. DOI: 10.1038/nmat3789.
[33] P. Jackson, R. Wuerz, D. Hariskos, E. Lotter, W. Witte, M. Powalla, *Phys. Status Solidi RRL* **2016**, *10 (8)*, 583–586. DOI: 10.1002/pssr.201600199.
[34] P. Jackson, D. Hariskos, R. Wuerz, O. Kiowski, A. Bauer, T. M. Friedlmeier, M. Powalla, *phys. stat. sol. (RRL)* **2015**, *9 (1)*, 28–31. DOI: 10.1002/pssr.201409520.
[35] C. P. Muzzillo, *Solar Energy Materials and Solar Cells* **2017**, *172*, 18–24. DOI: 10.1016/j.solmat.2017.07.006.
[36] T. Lepetit, S. Harel, L. Arzel, G. Ouvrard, N. Barreau, *Prog Photovolt Res Appl* **2017**, *25 (12)*, 1068–1076. DOI: 10.1002/pip.2924.
[37] A. Chirilă, P. Reinhard, F. Pianezzi, P. Bloesch, A. R. Uhl, C. Fella, L. Kranz, D. Keller, C. Gretener, H. Hagendorfer, D. Jaeger, R. Erni, S. Nishiwaki, S. Buecheler, A. N. Tiwari, *Nature materials* **2013**, *12 (12)*, 1107–1111. DOI: 10.1038/nmat3789.
[38] E. Handick, P. Reinhard, R. G. Wilks, F. Pianezzi, T. Kunze, D. Kreikemeyer-Lorenzo, L. Weinhardt, M. Blum, W. Yang, M. Gorgoi, E. Ikenaga, D. Gerlach, S. Ueda, Y. Yamashita, T. Chikyow, C. Heske, S. Buecheler, A. N. Tiwari, M. Bär, *ACS Appl. Mater. Interfaces* **2017**, *9 (4)*, 3581–3589. DOI: 10.1021/acsami.6b11892.
[39] M. Malitckaya, H.-P. Komsa, V. Havu, M. J. Puska, *J. Phys. Chem. C* **2017**, *121 (29)*, 15516–15528. DOI: 10.1021/acs.jpcc.7b03083.
[40] D. Kreikemeyer-Lorenzo, D. Hauschild, P. Jackson, T. M. Friedlmeier, D. Hariskos, M. Blum, W. Yang, F. Reinert, M. Powalla, C. Heske, L. Weinhardt, *ACS Appl. Mater. Interfaces* **2018**, *10 (43)*, 37602–37608. DOI: 10.1021/acsami.8b10005.
[41] T. M. Friedlmeier, P. Jackson, A. Bauer, D. Hariskos, O. Kiowski, R. Wuerz, M. Powalla, *IEEE J. Photovoltaics* **2015**, *5 (5)*, 1487–1491. DOI: 10.1109/JPHOTOV.2015.2458039.
[42] A. Lämmle, *PhD thesis,* Karlsruhe Institute of Technology (KIT), Karlsruhe **2014**.
[43] T. P. Weiss, S. Nishiwaki, B. Bissig, R. Carron, E. Avancini, J. Löckinger, S. Buecheler, A. N. Tiwari, *Adv. Mater. Interfaces* **2018**, *5 (4)*, 1701007. DOI: 10.1002/admi.201701007.
[44] S. S. Lin, J. G. Lu, Z. Z. Ye, H. P. He, X. Q. Gu, L. X. Chen, J. Y. Huang, B. H. Zhao, *Solid State Commun.* **2008**, *148 (1-2)*, 25–28. DOI: 10.1016/j.ssc.2008.07.028.

[45] T. Kodalle, M. D. Heinemann, D. Greiner, H. A. Yetkin, M. Klupsch, C. Li, P. A. van Aken, I. Lauermann, R. Schlatmann, C. A. Kaufmann, *Sol. RRL* **2018**, *2 (9)*, 1800156. DOI: 10.1002/solr.201800156.
[46] R. V. Forest, B. E. McCandless, X. He, A. A. Rockett, E. Eser, K. D. Dobson, R. W. Birkmire, *Journal of Applied Physics* **2017**, *121 (24)*, 245102. DOI: 10.1063/1.4986635.
[47] J. Nishinaga, T. Nagai, T. Sugaya, H. Shibata, S. Niki, *Appl. Phys. Express* **2018**, *11 (8)*, 82302. DOI: 10.7567/APEX.11.082302.
[48] A. Czudek, A. Eslam, A. Urbaniak, P. Zabierowski, R. Wuerz, M. Igalson, *J. Appl. Phys.* **2020**, *128 (17)*, 173102. DOI: 10.1063/5.0025183.
[49] A. Vilalta-Clemente, M. Raghuwanshi, S. Duguay, C. Castro, E. Cadel, P. Pareige, P. Jackson, R. Wuerz, D. Hariskos, W. Witte, *Appl. Phys. Lett.* **2018**, *112 (10)*, 103105. DOI: 10.1063/1.5020805.
[50] N. Taguchi, S. Tanaka, S. Ishizuka, *Appl. Phys. Lett.* **2018**, *113 (11)*, 113903. DOI: 10.1063/1.5044244.
[51] M. Chugh, T. D. Kühne, H. Mirhosseini, *ACS Appl. Mater. Interfaces* **2019**, *11 (16)*, 14821–14829. DOI: 10.1021/acsami.9b02158.
[52] P. Würfel, U. Würfel, *Physics of solar cells from basic principles to advanced concepts,* 3rd ed., Wiley-VCH Verlag GmbH & Co. KGaA, Weinheim **2016**.
[53] U. Wuerfel, A. Cuevas, P. Wuerfel, *IEEE J. Photovoltaics* **2015**, *5 (1)*, 461–469. DOI: 10.1109/JPHOTOV.2014.2363550.
[54] M. Morkel, L. Weinhardt, B. Lohmüller, C. Heske, E. Umbach, W. Riedl, S. Zweigart, F. Karg, *Appl. Phys. Lett.* **2001**, *79 (27)*, 4482–4484. DOI: 10.1063/1.1428408.
[55] D. Abou-Ras, T. Kirchartz, U. Rau, *Advanced Characterization Techniques for Thin Film Solar Cells*, Wiley-VCH Verlag GmbH & Co. KGaA, Weinheim, Germany **2011**.
[56] A. Luque, S. Hegedus, *Handbook of photovoltaic science and engineering,* 2nd ed., Wiley, Chichester, West Sussex, U.K **2011**.
[57] A. Einstein, *Annalen der Physik* **1905**, *322*, 132–148.
[58] M. O. Krause, J. G. Ferreira, *J. Phys. B: At. Mol. Phys.* **1975**, *8 (12)*, 2007–2014. DOI: 10.1088/0022-3700/8/12/013.
[59] H. Kuhlenbeck, *Berichte der Bunsengesellschaft für physikalische Chemie* **1993**, *97 (9)*, 1168. DOI: 10.1002/bbpc.19930970925.
[60] J. F. Moulder, J. Chastain, *Handbook of X-ray Photoelectron Spectroscopy: A Reference Book of Standard Spectra for Identification and Interpretation of XPS Data*, Physical Electronics Division, Perkin-Elmer Corporation **1992**.
[61] M. P. Seah, W. A. Dench, *Surf. Interface Anal.* **1979**, *1 (1)*, 2–11. DOI: 10.1002/sia.740010103.
[62] P. Auger, *J. Phys. Radium* **1925**, *6 (6)*, 205–208. DOI: 10.1051/jphysrad:0192500606020500.
[63] G. Moretti, *Journal of Electron Spectroscopy and Related Phenomena* **1998**, *95 (2-3)*, 95–144. DOI: 10.1016/S0368-2048(98)00249-7.
[64] C. D. Wagner, L. H. Gale, R. H. Raymond, *Anal. Chem.* **1979**, *51 (4)*, 430A-433A. DOI: 10.1021/ac50040a704.
[65] L. Weinhardt, D. Hauschild, C. Heske, *Adv. Mater.* **2019**, *31 (26)*, e1806660. DOI: 10.1002/adma.201806660.
[66] M. Haschke, J. Flock, *Röntgenfluoreszenzanalyse in der Laborpraxis*, Wiley-VCH Verlag GmbH & Co. KGaA, Weinheim, Germany **2017**.
[67] C.B.Honsberg and S.G.Bowden, Air Mass - Photovoltaics Education Website **2019**, https://www.pveducation.org/pvcdrom/properties-of-sunlight/air-mass, accessed 11 September 2022.
[68] C. Heske, G. Richter, Z. Chen, R. Fink, E. Umbach, W. Riedl, F. Karg, *J. Appl. Phys.* **1997**, *82 (5)*, 2411–2420. DOI: 10.1063/1.366096.

[69] D. W. Niles, M. Contreras, K. Ramanathan, R. Noufi, in *Conference record of the Twenty Fifth IEEE Photovoltaic Specialists Conference - 1996: Hyatt Regency Crystal City, Washington, DC, May 13 - 17, 1996*, IEEE Service Center, Piscataway, NJ **1996**.
[70] *Photoelectronic properties of semiconductors* (Ed: Richard H. Bube), Vol.5, Cambridge University Press (CUP), Cambridge **1992**.
[71] A. Czudek, A. Urbaniak, A. Eslam, R. Wuerz, M. Igalson, *IEEE J. Photovoltaics* **2020**, *10 (6)*, 1926–1930. DOI: 10.1109/JPHOTOV.2020.3014865.
[72] A. F. Holleman, E. Wiberg, N. Wiberg, *Lehrbuch der anorganischen Chemie,* 102nd ed., De Gruyter, Berlin **2007**.
[73] S. M. Sze, K. K. Ng, *Physics of semiconductor devices,* 3rd ed., Wiley-Interscience online books, Wiley-Interscience, Hoboken, NJ **2007**.
[74] J. W. Orton, P. Blood, *The electrical characterization of semiconductors: Measurement of minority carrier properties,* Techniques of physics, Vol.13, Acad. Pr, London **1990**.
[75] J. T. Heath, J. D. Cohen, W. N. Shafarman, *J. Appl. Phys.* **2004**, *95 (3)*, 1000–1010. DOI: 10.1063/1.1633982.
[76] T. Eisenbarth, T. Unold, R. Caballero, C. A. Kaufmann, H.-W. Schock, *J. Appl. Phys.* **2010**, *107 (3)*, 34509. DOI: 10.1063/1.3277043.
[77] A. Bosio, A. Romeo, *Thin Film Solar Cells: Current Status and Future Trends,* Energy Science, Engineering and Technology, Nova Science Publishers Incorporated, Hauppauge **2010**.
[78] Z.-K. Yuan, S. Chen, Y. Xie, J.-S. Park, H. Xiang, X.-G. Gong, S.-H. Wei, *Adv. Energy Mater.* **2016**, *6 (24)*, 1601191. DOI: 10.1002/aenm.201601191.
[79] A. O. Pudov, A. Kanevce, H. A. Al-Thani, J. R. Sites, F. S. Hasoon, *J. Appl. Phys.* **2005**, *97 (6)*, 64901. DOI: 10.1063/1.1850604.
[80] S. S. Hegedus, W. N. Shafarman, *Prog. Photovoltaics Res. Appl.* **2004**, *12 (23)*, 155–176. DOI: 10.1002/pip.518.
[81] Lothar Weinhardt, *Elektronische und chemische Eigenschaften von Grenzflächen und Oberflächen in optimierten Cu(In,Ga)(S,Se)2 Dünnschichtsolarzellen, Doctoralthesis,* Universität Würzburg, Würzburg **2005**.
[82] J. Lehmann, S. Lehmann, I. Lauermann, T. Rissom, C. A. Kaufmann, M. C. Lux-Steiner, M. Bär, S. Sadewasser, *Journal of Applied Physics* **2014**, *116 (23)*, 233502. DOI: 10.1063/1.4903976.
[83] T. Gleim, C. Heske, E. Umbach, C. Schumacher, W. Faschinger, C. Ammon, M. Probst, H.-P. Steinrück, *Appl. Phys. Lett.* **2001**, *78 (13)*, 1867–1869. DOI: 10.1063/1.1358366.
[84] T. Gleim, C. Heske, E. Umbach, C. Schumacher, S. Gundel, W. Faschinger, A. Fleszar, C. Ammon, M. Probst, H.-P. Steinrück, *Surf. Sci.* **2003**, *531 (1)*, 77–85. DOI: 10.1016/S0039-6028(03)00439-4.
[85] D. Hauschild, D. Kreikemeyer-Lorenzo, P. Jackson, T. M. Friedlmeier, D. Hariskos, F. Reinert, M. Powalla, C. Heske, L. Weinhardt, *ACS Energy Lett.* **2017**, *2 (10)*, 2383–2387. DOI: 10.1021/acsenergylett.7b00720.
[86] P. Pistor, D. Greiner, C. A. Kaufmann, S. Brunken, M. Gorgoi, A. Steigert, W. Calvet, I. Lauermann, R. Klenk, T. Unold, M.-C. Lux-Steiner, *Appl. Phys. Lett.* **2014**, *105 (6)*, 63901. DOI: 10.1063/1.4892882.
[87] M. Mezher, L. M. Mansfield, K. Horsley, M. Blum, R. Wieting, L. Weinhardt, K. Ramanathan, C. Heske, *Appl. Phys. Lett.* **2017**, *111 (7)*, 71601. DOI: 10.1063/1.4998445.
[88] M. Mezher, L. M. Mansfield, K. Horsley, W. Yang, M. Blum, L. Weinhardt, K. Ramanathan, C. Heske, *ACS Appl. Energy Mater.* **2019**, *2 (12)*, 8641–8648. DOI: 10.1021/acsaem.9b01565.

[89] I. Majumdar, *Photoelectron spectroscopic studies of alkali-treated Cu(In,Ga)Se2 absorbers and simulation studies of solar cell performances, Doctoralthesis*, Freie Universität Berlin, Berlin **2019**.
[90] J. J. Yeh, I. Lindau, *Atomic Data and Nuclear Data Tables* **1985**, *32 (1)*, 1–155. DOI: 10.1016/0092-640X(85)90016-6.
[91] U. Rau, H. W. Schock, *Appl. Phys. A* **1999**, *69 (2)*, 131–147. DOI: 10.1007/s003390050984.
[92] D. Schmid, M. Ruckh, H. Schock, *Appl. Surf. Sci.* **1996**, *103 (4)*, 409–429. DOI: 10.1016/S0169-4332(96)00099-2.
[93] A. Kylner, *J. Electrochem. Soc.* **1999**, *146 (5)*, 1816–1823. DOI: 10.1149/1.1391849.
[94] Adrian Epprecht, *Impact of post-deposition treatments on the chemical and electronic structure of Cu(In,Ga)Se2 thin-film solar cells*. Master Thesis, Karlsruhe **2017**.
[95] J. L. Bourque, M. C. Biesinger, K. M. Baines, *Dalton Trans.* **2016**, *45 (18)*, 7678–7696. DOI: 10.1039/c6dt00771f.
[96] G. Cossu, G. M. Ingo, G. Mattogno, G. Padeletti, G. M. Proietti, *Appl. Surf. Sci.* **1992**, *56-58*, 81–88. DOI: 10.1016/0169-4332(92)90219-N.
[97] G. Schön, *Journal of Electron Spectroscopy and Related Phenomena* **1973**, *2 (1)*, 75–86. DOI: 10.1016/0368-2048(73)80049-0.
[98] M. C. Biesinger, *Surf. Interface Anal.* **2017**, *49 (13)*, 1325–1334. DOI: 10.1002/sia.6239.
[99] F. M. Capece, V. Castro, C. Furlani, G. Mattogno, C. Fragale, M. Gargano, M. Rossi, *Journal of Electron Spectroscopy and Related Phenomena* **1982**, *27 (2)*, 119–128. DOI: 10.1016/0368-2048(82)85058-5.
[100] J. Haber, T. Machej, L. Ungier, J. Ziółkowski, *Journal of Solid State Chemistry* **1978**, *25 (3)*, 207–218. DOI: 10.1016/0022-4596(78)90105-6.
[101] D. Cahen, P. J. Ireland, L. L. Kazmerski, F. A. Thiel, *J. Appl. Phys.* **1985**, *57 (10)*, 4761–4771. DOI: 10.1063/1.335341.
[102] M. Romand, M. Roubin, J. P. Deloume, *Journal of Electron Spectroscopy and Related Phenomena* **1978**, *13 (3)*, 229–242. DOI: 10.1016/0368-2048(78)85029-4.
[103] P. Woidy, A. J. Karttunen, M. Widenmeyer, R. Niewa, F. Kraus, *Chemistry (Weinheim an der Bergstrasse, Germany)* **2015**, *21 (8)*, 3290–3303. DOI: 10.1002/chem.201406136.
[104] J. C. Klein, C. P. Li, D. M. Hercules, J. F. Black, *Appl Spectrosc* **1984**, *38 (5)*, 729–734. DOI: 10.1366/0003702844555016.
[105] D. Briggs, *Surf. Interface Anal.* **1981**, *3 (4)*, v. DOI: 10.1002/sia.740030412.
[106] G. van der Laan, C. Westra, C. Haas, G. A. Sawatzky, *Phys. Rev. B: Condens. Matter* **1981**, *23 (9)*, 4369–4380. DOI: 10.1103/PhysRevB.23.4369.
[107] S. W. Gaarenstroom, N. Winograd, *J. Chem. Phys.* **1977**, *67 (8)*, 3500–3506. DOI: 10.1063/1.435347.
[108] J. C. C. Fan, J. B. Goodenough, *Journal of Applied Physics* **1977**, *48 (8)*, 3524–3531. DOI: 10.1063/1.324149.
[109] D. Cahen, P. J. Ireland, L. L. Kazmerski, F. A. Thiel, *J. Appl. Phys.* **1985**, *57 (10)*, 4761–4771. DOI: 10.1063/1.335341.
[110] L. L. Kazmerski, O. Jamjoum, P. J. Ireland, S. K. Deb, R. A. Mickelsen, W. Chen, *Journal of Vacuum Science and Technology* **1981**, *19 (3)*, 467–471. DOI: 10.1116/1.571040.
[111] M. K. Bahl, R. L. Watson, K. J. Irgolic, *J. Chem. Phys.* **1980**, *72 (7)*, 4069–4077. DOI: 10.1063/1.439634.
[112] Y. Kawamoto, K. Ogura, M. Shojiya, M. Takahashi, K. Kadono, *Journal of Fluorine Chemistry* **1999**, *96 (2)*, 135–139. DOI: 10.1016/S0022-1139(99)00068-8.
[113] V. M. Bermudez, *Appl. Surf. Sci.* **1997**, *119 (1-2)*, 147–159. DOI: 10.1016/S0169-4332(97)00190-6.

[114] C. D. Wagner, *Faraday Discuss. Chem. Soc.* **1975**, *60*, 291. DOI: 10.1039/DC9756000291.
[115] D. Braunger, D. Hariskos, G. Bilger, U. Rau, H. W. Schock, *Thin Solid Films* **2000**, *361-362*, 161–166. DOI: 10.1016/S0040-6090(99)00777-4.
[116] D. W. Niles, K. Ramanathan, F. Hasoon, R. Noufi, B. J. Tielsch, J. E. Fulghum, *J. Vac. Sci. Technol., A* **1997**, *15 (6)*, 3044–3049. DOI: 10.1116/1.580902.
[117] J. Sterner, J. Malmström, L. Stolt, *Prog Photovolt Res Appl* **2005**, *13 (3)*, 179–193. DOI: 10.1002/pip.595.
[118] A. Kylner, *J. Electrochem. Soc.* **1999**, *146 (5)*, 1816–1823. DOI: 10.1149/1.1391849.
[119] G. Hanna, S. Schleussner, G. Bilger, H.W. Schock, U. Rau, J.H. Werner, *Proceedings of the 3rd World Conference on Photovoltaic Energy Conversion* **2003**.
[120] Y. Hashimoto, N. Kohara, T. Negami, M. Nishitani, T. Wada, *Japanese Journal of Applied Physics* **1996**, *35*, 4760–4764. DOI: 10.1143/JJAP.35.4760.
[121] L. C. Olsen, F. W. Addis, L. Huang, W. N. Shafaman, P. Eschbach, G. J. Exarhos, 458–461. DOI: 10.1109/PVSC.2000.915869.
[122] D. Hariskos, *ICPS-Messungen an gebrauchten Rinse-Lösungen*. private communication, ZSW Stuttgart **2022**.
[123] T. Lepetit, S. Harel, L. Arzel, G. Ouvrard, N. Barreau, *IEEE J. Photovoltaics* **2016**, *6 (5)*, 1316–1320. DOI: 10.1109/JPHOTOV.2016.2589365.
[124] I. Miyake, T. Tanpo, C. Tatsuyama, *Japanese Journal of Applied Physics* **1984**, *23 (Part 1, No. 2)*, 172–178. DOI: 10.1143/JJAP.23.172.
[125] B. Canava, J. Vigneron, A. Etcheberry, J. Guillemoles, D. Lincot, *Applied Surface Science* **2002**, *202 (1-2)*, 8–14. DOI: 10.1016/S0169-4332(02)00186-1.
[126] Thermo Scientific, XPS Reference, Table of Elements **2022**, https://www.jp.xpssimplified.com/elements/sulfur.php.
[127] C. D. Wagner, J. A. Taylor, *Journal of Electron Spectroscopy and Related Phenomena* **1982**, *28 (2)*, 211–217. DOI: 10.1016/0368-2048(82)85044-5.
[128] X.-R. Yu, F. Liu, Z.-Y. Wang, Y. Chen, *Journal of Electron Spectroscopy and Related Phenomena* **1990**, *50 (2)*, 159–166. DOI: 10.1016/0368-2048(90)87059-W.
[129] B. J. Lindberg, K. Hamrin, G. Johansson, U. Gelius, A. Fahlman, C. Nordling, K. Siegbahn, *Phys. Scr.* **1970**, *1 (5-6)*, 286–298. DOI: 10.1088/0031-8949/1/5-6/020.
[130] D. Hariskos, *Desorptionsexperimente an thermisch aufgeheizten CIGSe-Proben unter Vakuumbedingungen*. mündlich, ZSW Stuttgart **2022**.
[131] R. Wuerz, *NaF and KF PDTs without Se supply*. mündlich, ZSW Stuttgart **2022**.
[132] A. Shchukarev, D. Korolkov, *Open Chemistry* **2004**, *2 (2)*, 347–362. DOI: 10.2478/BF02475578.
[133] H. ElAnzeery, F. Babbe, M. Melchiorre, A. Zelenina, S. Siebentritt, *IEEE J. Photovoltaics* **2017**, *7 (2)*, 684–689. DOI: 10.1109/JPHOTOV.2017.2651802.
[134] R. Wuerz, A. Eicke, F. Kessler, F. Pianezzi, *Sol. Energy Mater. Sol. Cells* **2014**, *130*, 107–117. DOI: 10.1016/j.solmat.2014.06.038.
[135] P. Jackson, P. Grabitz, A. Strohm, G. Bilger, H. W. Schock, *19th European Photovoltaic Solar Energy Conference, Paris, France* **2004**, p. 1936.
[136] P. Reinhard, B. Bissig, F. Pianezzi, E. Avancini, H. Hagendorfer, D. Keller, P. Fuchs, M. Döbeli, C. Vigo, P. Crivelli, S. Nishiwaki, S. Buecheler, A. N. Tiwari, *Chem. Mater.* **2015**, *27 (16)*, 5755–5764. DOI: 10.1021/acs.chemmater.5b02335.
[137] I. Khatri, M. Sugiyama, T. Nakada, *Prog Photovolt Res Appl* **2017**, *25 (10)*, 871–877. DOI: 10.1002/pip.2892.
[138] Maxim Guc, *Raman-Messungen an KF PDT 105°C CIGSe Solarzellen*. personal communication, ZSW Stuttgart **2021**.
[139] Roland Wuerz, *Alkali-Diffusion im CIGSe durch PDTs ohne Se-Angebot*. mündlich, Stuttgart **2022**.

[140] F. V. Singh, T. Wirth, *Catal. Sci. Technol.* **2019**, *9 (5)*, 1073–1091. DOI: 10.1039/C8CY02274G.
[141] H. J. Reich, R. J. Hondal, *ACS chemical biology* **2016**, *11 (4)*, 821–841. DOI: 10.1021/acschembio.6b00031.
[142] *Selenium: Chemistry, analysis, function and effects Chapter 1* (Ed: V.R. Preedy), Food and nutritional components in focus, Vol.9, Royal Society of Chemistry, Cambridge **2015**.
[143] P. Reinhard, B. Bissig, F. Pianezzi, H. Hagendorfer, G. Sozzi, R. Menozzi, C. Gretener, S. Nishiwaki, S. Buecheler, A. N. Tiwari, *Nano Lett.* **2015**, *15 (5)*, 3334–3340. DOI: 10.1021/acs.nanolett.5b00584.

Eidesstattliche Erklärung

Bei der vorliegenden Dissertation zu dem Thema

Chemical and Electrical Impact of Alkali Fluoride Post Deposition Treatments on Cu(In,Ga)Se_2 Solar Cells

handelt es sich um meine eigenständig erbrachte Leistung.

Ich habe nur die angegebenen Quellen und Hilfsmittel benutzt und mich keiner unzulässigen Hilfe Dritter bedient. Insbesondere habe ich wörtlich oder sinngemäß aus anderen Werken übernommene Inhalte als solche kenntlich gemacht.

Die Arbeit oder Teile davon habe ich bislang nicht an einer Hochschule des In- oder Auslands als Bestandteil einer Prüfungs- oder Qualifikationsleistung vorgelegt.

Die Richtigkeit der vorstehenden Erklärungen bestätige ich.

Die Bedeutung der eidesstattlichen Versicherung und die strafrechtlichen Folgen einer unrichtigen oder unvollständigen eidesstattlichen Versicherung sind mir bekannt.

Ich versichere an Eides statt, dass ich nach bestem Wissen die reine Wahrheit erklärt und nichts verschwiegen habe.

Stuttgart, 30.08.2022

Ort und Datum

Danksagung

So wie bei jeder anderen Doktorarbeit, hat zum Gelingen dieser Arbeit eine Vielzahl von Menschen beigetragen. Ich möchte mich daher bei allen bedanken, die mich auf diesem Weg begleitet haben:

Mein herzlichster Dank gilt Prof. Dr. Clemens Heske, der mein Erstbetreuer war, und von dem ich eine Menge gelernt habe. Clemens stand bei jeder wissenschaftlichen Fragestellung unangefochten zur Verfügung und hat mir auch viele organisatorische Tipps gegeben, wie man eine Doktorarbeit plant, anfertigt und letztendlich auch durchhält. Weiterhin war es sehr erfrischend, die sehr Solarzellen-lastige Forschung am ZSW „durch die Brille“ eines Chemieprofessors zu sehen. Das hat immer wieder neue Denkanstöße gegeben, und wichtige, grundlegende Fragen aufgeworfen, die sonst übersehen worden wären. Als externer Doktorand und vor allem aufgrund der Corona-Pandemie waren die meisten Treffen leider auf virtuelle Meetings beschränkt, bei denen m.E. der zwischenmenschliche Aspekt viel zu kurz kommt. Ich wäre gerne öfter persönlich nach Karlsruhe gekommen um meine Betreuung etwas mehr „live“ zu erleben. Trotz dieser Umstände habe ich enorm viel „mitgenommen“: Ich danke Clemens für die Spektroskopie-Vorlesung im SS 2020, den wertvollen Kontakt zu anderen CIGSe-Experten (Dirk und Lothar), und dass ich an der XPS-Kammer im MFE-Lab mitarbeiten durfte. So sind auch schöne Daten rausgekommen, die ja schließlich den Kernteil der Doktorarbeit ausmachen. Danke Dir dafür!

Prof. Dr. Michael Powalla gebührt ebenso mein größter Dank. Ohne seine „Connection“ wäre der Kontakt zu Clemens Heske vielleicht nie zu Stande gekommen und ich hätte nicht in Chemie promovieren können am KIT. Danke Dir! Auch Michael stand jederzeit zur Verfügung, wenn es um neue wissenschaftliche Fragen oder der thematischen Ausrichtung der Versuche ging. Ich bin weiterhin dankbar für die 3½-jährige Doktorandenstelle am ZSW und der reichhaltigen Forschungsinfrastruktur, mit der ich dort meine Zellen untersuchen konnte.

Roland Würz hat mich auf jedem Schritt und Tritt meiner Doktorarbeit begleitet und durch einen erfolgreichen DFG-Antrag meine Finanzierung am ZSW gesichert. Wir pflegten eine enge Zusammenarbeit am ZSW und waren beide für die Solarzellen-Präparation an der Solamo-Anlage verantwortlich. Ich danke Roland ganz herzlich, dass er mir von Tag Eins an alles gezeigt hat, mich mit ausreichend Literatur versorgt hat und stets für Nachfragen und Erklärungen offen war. Ich danke Dir für deine Geduld, wenn ich manchmal mehrmals nachfragen musste, und dass du meine zeitweise Schusseligkeit nicht zu übelgenommen hast. Auch weiß ich sehr zu schätzen, dass du mir immer genügend Freiraum gegeben hast, selbst zu entscheiden, wann ich welche Aufgabe erledige und wie ich meine Prioritäten setzte. Ich habe es genossen, von dir zu lernen, mit dir zu diskutieren und zusammen mit dir Versuche zu machen. Du bist ein hilfsbereiter und zuverlässiger Mensch. Danke für deine Zeit!

Dirk Hauschild habe ich zu verdanken, dass meine ganzen Proben sorgfältig mit XPS und UPS untersucht wurden. In drei Mess-Serien haben er und ich immer eine ganze Armada an Messungen im MFE-Lab durchgeführt, die den Großteil dieser Arbeit ausmachen. Und das geschah ausgerechnet mitten in der Corona-Pandemie, in der man jeden (Mess-)Tag bangen musste, dass das KIT sofort alle Labore schließt. Ich danke dir, Dirk, allerherzlichst, dass du alles darangesetzt hast, so schnell wie möglich alle Proben durchzumessen. Sei es tagsüber im Labor oder selbst nachts und morgens früh von zu Hause aus; Danke für diese enorme Einsatz- und Aufopferungsbereitschaft! Weiterhin stand Dirk auch für jede Frage bezüglich der Auswertung der Daten zu Verfügung und er hat mir beigebracht, worauf es bei XPS-Messungen am CIGSe besonders ankommt. Danke Dir!

Lothar Weinhardt war ebenfalls Teil des engeren Betreuungsteams und hat in jedem Meeting wertvolle Tipps zur Auswertung der XPS und UPS-Daten gegeben. Weiterhin stand er auch (so wie Dirk und Clemens) immer zur Verfügung, wenn ich Fragen bezüglich aller Spektroskopie-Themen hatte. Ich danke Lothar außerdem für das Gegenlesen aller Poster, dem Paper und auch Abschnitten dieser Arbeit und war immer wieder (positiv) überrascht, aus welchem neuen Blickwinkel man die Materie betrachten kann. Danke für Deinen Support!

Wie schon erwähnt, war auch die Forschungsinfrastruktur am ZSW wichtig, um eine erfolgreiche Doktorarbeit zu schreiben. Diese wird hauptsächlich durch die dortigen Mitarbeiter bestimmt:

Wolfram Hempel danke ich für die Durchführung der SIMS-Messungen, Dominik Bagrowski für das Aufbringen des Gridkontaktes und Philipp von Bismarck danke ich für die ein oder andere Hilfe am RFA-Gerät. Weiterhin danke ich euch für die lustigen Unterhaltungen, die wirklich grottenschlechten Witze und die mittäglichen Spaziergänge in die Schwabengalerie. Euer Büro war mit Abstand das coolste, und ich kam sehr gern einfach zum Verweilen bei Euch vorbei. Irgendwie war nur Erwin schon länger nicht mehr da; dachte, den seh ich nochmal… Mit dem richtigen Humor kann man alles durchstehen. Danke für Euren Frohsinn!

Sasa Milisavljevic bin ich aufgrund großer technischer Unterstützung ebenfalls zum besten Dank verpflichtet und soll ihm auch beste Grüße von meiner Stehleuchte im Wohnzimmer ausrichten. Ihr geht es wieder besser.

Dimitrios Hariskos und Wolfram Witte danke ich, respektive, für das Rinsing der XPS-Proben und für die Raman-Messungen, und ebenso für die interessanten Gespräche fachlicher, wie „nebensächlicher“ Natur. Alles Gute Euch!

Ana Kanevce danke ich für die ausführlichen Erklärungen zu QE- und CV-Messungen, und für die Hilfe bei den IV(T) und Suns-V_{OC} Messungen. Dank Ihr konnte ich ein tieferes Verständnis für die elektrische Charakterisierung von Solarzellen aufbauen und dieses auch anwenden. Darüberhinaus war es auch sehr hilfreich, dass sich Ana zusammen mit uns die Versuchsergebnisse der Warschauer angeschaut hat, und mir diese sehr anschaulich vermitteln konnte. Danke, dass ich Dich immer fragen konnte, und alles Gute für Deine Zukunft!

Mario Zinßer und Tim Helder waren meine (Doktoranden-)Mitstreiter und als ausgesprochene Theoretiker hatten sich unsere Arbeiten eher selten überschnitten. Ich habe trotzdem gerne mit Euch diskutiert und besonders die letzte Diskussion über den „wahren“ Einfluss von E-Feldern in der Solarzelle (oder doch nicht?!), wird mir lange in Erinnerung bleiben. Herr Würfel lässt grüßen. ;-)

Christine Böhmerle und Daniela Müller danke ich für die stets zuverlässigen CdS-Dips an der Nassbank. Danke Euch!

Mit Hendrik Pfeifer und Abdul Azzam verbringe ich auch außerhalb des ZSW gerne viel Zeit. Trotzdem: Danke für Eure Aufmunterung während der Doktorarbeit, für „strategische Lebens-Beratungen“ und auch die ein oder andere Schachpartie. Das hat meine Laune immer wieder aufgebessert und mir neue Kraft gegeben.

Besonders jedoch dem ganzen MAT-Team am ZSW bin ich dankbar für ein wirklich angenehmes Arbeitsumfeld, freundlichen, lockeren Kollegen und den respektvollen Umgang miteinander.

Thomas Ruppert danke ich herzlich für Tipps und Hilfe bezüglich des Layouts und der Formatierung einer Doktorarbeit speziell für die Chemie am KIT, und dass er mir bei Unklarheiten in der Prüfungsordnung weitergeholfen hat. Danke Dir!

Eine Doktorarbeit ist an sich schon ein gewaltiger Kraftakt, den man über mehrere Jahre hinweg bewältigen muss. Besonders viel Energie hat mich (so wie den Rest der Welt) die Corona-Pandemie gekostet. Ich bin daher meiner Freundin Johanna Waack sehr dankbar, dass sie mich nicht „allein“ gelassen hat hier in Stuttgart, sondern mich oft aus dem Rheinland besuchen kam, auch für längere Zeit. So habe ich es immer wieder geschafft, mich zu motivieren und ich war nicht komplett „mit meinen Gedanken“ allein. Ich glaube, das hat mir im Endeffekt auch geholfen, meine Arbeit durchzuziehen. Vielen Dank, Johanna!

Ebenso muss ich mich bei meinen Eltern bedanken, dass sie zweifellos an mich glauben und mich in allen Lebenslagen unterstützen; auf jede mögliche Art und Weise. Auch wenn sie jetzt sagen, dass das alle Eltern machen, bin ich sehr froh, dass ich Euch hab. Danke für alles und auch danke, dass ich noch zwei Geschwisterchen hab. Meine Brüder Kevin und Dominik stellen wichtige Bezugspersonen für mich dar, auch wenn wir beruflich oder von den Interessen her sehr unterschiedlich sind. Es ist immer wieder schön, euch zu sehen, und zu wissen, dass es euch gutgeht!

Einen anderen wichtigen Teil von Menschen, ohne die es wirklich trostlos geworden wäre, sind meine Freunde, die mir ebenfalls immer wieder Kraft und Zuspruch während der Doktorarbeit gegeben haben. Zu nennen wären die „Kölner Chaoten“ Daniel Werner, Nikolay Barashkov, Peter Mons und Nico Ballas. Mit euch gehe ich meinen Weg schon seit Studienbeginn 2012 und die Zeit mit Euch ist eine riesen Bereicherung! Ich bin froh, dass wir uns kennen und bestimmt noch viel miteinander erleben werden.

Mit Andreas Schubert verbinde ich eine Reihe toller Erlebnisse. Angefangen bei den ersten Konzertbesuchen in 2012, „wunderschönen“ Radtouren in die Walachei, als auch nicht zuletzt die interessanten „Musikveranstaltungen mitten im Nirgendwo“: Das gab mir immer wieder Kraft für meine Arbeit, wenn ich Zwischendurch mal was Ausgefallenes erleben konnte. Danke Dir!

Alexander Riegel konnte ich immer wieder mal „konsultieren“ wenn chemische Kenntnisse aus dem Grundstudium gefragt waren. Gerne bin ich mit dir durch Andernach spaziert, während du u. a. Quantenchemie II mit mir aufgefrischt hast. Noch viel dankbarer bin ich über deine Literatur-Recherche über den Alkalifluorid-PDT. Danke für das ganze Zusammengesuche. Eine wirklich bemerkenswerte Leistung, wenn man bedenkt, dass du fachlich garnichts mit CIGSe zutun hast!

Tobias Bergen danke ich für die alljährlichen Radtouren mitten durch den Wald, auch mal abseits der geplanten Wege. Danke für die spontanen Besuche, und dass du mich aufgemuntert hast, wenn ich etwas unglücklich war.

Raiko Hahn war eigentlich mein erster Tutor zu Beginn des Studiums, ist dann aber nach Freiburg gezogen, um dort seine Doktorarbeit zu verwirklichen. Durch ihn habe ich erkannt, dass man auch südlich von Bonn promovieren kann und das auch Früchte trägt. Danke für diese Einsicht!

Zuletzt möchte ich mich noch bei Ernst Mermagen und Adrian Hühn bedanken, guten Freunden, die ich während der Promotion etwas seltener gesehen habe, aber die mich aufgemuntert haben, auch wenn ich nur Schlechtes von meiner Arbeit zu berichten hatte. Danke Euch!

List of Publications

- **A. Eslam**, R. Würz, D. Hauschild, L. Weinhardt, W. Hempel, M. Powalla, C. Heske, „Impact of substrate temperature during NaF and KF post-deposition treatments on chemical and optoelectronic properties of alkali-free Cu(In,Ga)Se_2 thin-film solar cell absorbers“, *Thin Solid Films 739*, 138979, **2021**.

- A. Czudek, **A. Eslam**, A. Urbaniak, P. Zabierowski, R. Würz, M. Igalson; „Evolution of the electrical characteristics of Cu(In,Ga)Se_2 devices with sodium content“, *J. Appl. Phys. 128*, 173102, **2020**.

- A. Czudek, A. Urbaniak, **A. Eslam**, R. Würz, M. Igalson, „Dependence of the Magnitude of Persistent Photoconductivity on Sodium Content in Cu(In,Ga)Se2 Solar Cells and Thin Films“, *IEEE J. Photovoltaics 10 (6)*, 1926, **2020**.

- A. Czudek, A. Urbaniak, **A. Eslam**, R. Würz, M. Igalson, „Potassium versus Sodium in Cu(In,Ga)Se_2 - Similarities and Differences in the Electrical Characteristics of Solar Cells and Thin Films after NaF or KF Postdeposition Treatment“, *Phys. Stat. Sol. (RRL) 16*, 2100459, **2022**.

- N. Humberg, R. Bretel, **A. Eslam**, E. Le Moal, M. Sokolowski, „Hydrogen-Bonded One-Dimensional Chains of Quinacridone on Ag(100) and Cu(111): The Role of Chirality and Surface Bonding“, *J. Phys. Chem. C 124*, 24861, **2020**.

- A. S. Jenniches, J. Bahr, D. Püschner, T. Kellner, S. Hütgens, K. Gratzfeld, F. Spahlholz, **A. Eslam**, A. Lützen, „Influence of Different Substitution Patterns on the 2D Crystalline Aggregation of Small Molecules on HOPG Surfaces“, *Langmuir 38*, 6602, **2022**.